COMPUTATIONAL VISCOELASTIC DAMAGE MODELING OF COMPOSITE MATERIALS IN EXTRUSION DEPOSITION ADDITIVE MANUFACTURING

by

Miguel A. Ramirez

A Dissertation

Submitted to the Faculty of Purdue University

In Partial Fulfillment of the Requirements for the degree of

Doctor of Philosophy

School of Aeronautics and Astronautics

West Lafayette, Indiana

August 2021

THE PURDUE UNIVERSITY GRADUATE SCHOOL

STATEMENT OF COMMITTEE APPROVAL

Dr. R. Byron Pipes, Chair

School of Aeronautics and Astronautics

Dr. Wenbin Yu

School of Aeronautics and Astronautics

Dr. Tyler N. Tallman

School of Aeronautics and Astronautics

Dr. Vikas Tomar

School of Aeronautics and Astronautics

Dr. Evan J. Pineda

NASA Glenn Research Center

Approved by:

Dr. Gregory A. Blaisdell

Dedicated to my family

ACKNOWLEDGMENTS

I would like to express tremendous gratitude and appreciation to my advisor and mentor, Dr. R. Byron Pipes for guiding me through my research and graduate studies. Throughout the years, I have always known your invaluable advice and experience will successfully guide me to this point. I am extremely grateful to have been given the opportunity to work on this exciting research problem, and have the opportunity to lead the way, knowing I always have your continuous support. With your leadership, I always felt I can exercise my creativity and grow as a scholar. Most importantly, you have ingrained the qualities of a passionate researcher and level of confidence that will indubitably last forever.

I would like to thank the members of my dissertation committee: Dr. Wenbin Yu, Dr. Vikas Tomar, Dr. Tyler Tallman, and Dr. Evan Pineda. I will always appreciate the technical advice and perspective you have provided for which has been influential to this dissertation. I would like to express my deepest thanks to my colleague and friend, Dr. Sergey Kravchenko. Our profound technical discussions of damage mechanics, mechanics, and general philosophical discussions have been instrumental in my scholarly and professional development as well as this dissertation, I have always been able to count on you even during turbulent times.

I would like to thank Dr. Eduardo Barocio for being an exemplary figure within the additive manufacturing group, I will always be appreciative for your help throughout the years for which has been crucial to this dissertation. Thanks to Dr. Bastian Brenken and Dr. Anthony Favaloro for providing your knowledge, tools, and perspective for which has been very helpful throughout the years. I would like to express deep gratitude to Jung-Ting Tsai for our many profound discussions, collaboration, and support throughout these years. Many thanks to the additive group members for which have been very supportive throughout the years: Pasita Pibulchinda, Vasudha Kapre, Akshay Jacob Thomas, Jorge Ramirez, Sushrut Karmarkar, and Alfredo Ocegueda. I would also like to thank Dr. Orzuri Rique Garaizer, for your technical perspective and always being supportive throughout the years. To my friend and colleague, Julio Hernandez, I want to thank you for always selflessly lending your support, I have always enjoyed our profound discussions throughout our academic journey. To Dr. Ronald Sterkenburg and Dr. Garam Kim, thank you for always lending your support for some of the projects in this dissertation. Thanks to Dr. Ben Denos for your perspective and advice on composites testing. My warm gratitude goes to Bill Applegate for

always providing support in the lab and making my time at the composites manufacturing and simulation center enjoyable. A warm thank you to: Himal Agrawal, Sadat Ahsan, Subramanian Chidambaram, Brian Hogle, Warren Katz, Dillon Prach, for your friendship and support throughout my time at Purdue University.

A special thanks to my supervisor at NASA Glenn Research Center, Nelson Morales, for providing me the opportunity to further learn and grow my skills as well as lending your support on the exciting and challenging problems I was able to tackle. I would also like to thank Ariel Dimston, I have always enjoyed learning from you and sharing my knowledge and passion with you. I would also like to express my gratitude to Dr. Louis Ghosn for always providing the opportunity to learn and grow my expertise on damage tolerance, I have always enjoyed our discussions. Thank you to Dr. Matthew Appleby, Jerald Thompson, Ian Haskin, Elliot Schmidt, Amy Stalker, David Myers, and everyone at the LMM0 branch for making my time there enjoyable.

To my friends, thank you for always being standing beside me and providing motivational support: Kenny Fernandez, Ahlam Abuawab, Kevin Fox, and Jamil Sanders. I will be forever grateful to all of my professors throughout my academic career, some of whom deserve special recognition: Dr. Deborah Chung for instilling in me a passion to perform research and being the exemplary figure I truly admire, Dr. Gregory Denbeaux for providing the opportunity to conduct research early in my undergraduate studies, and Dr. Jonathan Petruccelli for opening the doors to conduct exciting research. I would like to express my heartfelt gratitude to the faculty and staff at the University at Albany: Maritza Martinez, Mayra Santiago, and Patrick Romain. With their support, I have been able to exercise my true potential and excel during my undergraduate studies. Deep gratitude towards Dr. Chris Fernando, for always being encouraging and supportive.

To my wonderful family: my mother Niurka Ramirez, my two sisters Meybelle Houellemont and Carolina Ramirez, my uncle Ramon Ramirez, my Aunt Inez Ramirez, my cousins Stephany Ramirez, Anthony Ramirez, and Jeremy Ramirez. Without your unconditional support and perpetual love, this would not have been possible.

This work has been supported by the Purdue Doctoral Fellowship, Purdue Forever Fellowship, and sponsored by the U.S. Department of Energy, Institute for Advanced Composites Manufacturing Innovation (IACMI). My sincere gratitude is given to these institutions for their financial support throughout my graduate studies and research.

TABLE OF CONTENTS

LIST OF TABLES

LIST OF FIGURES

ABSTRACT

Extrusion deposition additive manufacturing (EDAM) is a material extrusion method within the additive manufacturing technique, this method utilizes a screw and heaters to drive molten short fiber polymer composite through an orifice. The use of short fiber composite for EDAM has enabled large-scale 3D printing of tools and molds for traditional composite manufacturing processes, and structures. Additive manufactured (AM) short fiber composites (SFC) are both anisotropic and viscoelastic, with mechanical properties exhibiting strong non-linear behavior and temperature dependence. This means that the material processing history impacts the final residual stress and deformation states in a printed part. To simulate the in-manufacturing and in-service complex behavior of an AM SFC part, a homogenized physics-informed material model is required to be able to capture non-linear behavior stemming from sub-scale damage mechanisms. With this in mind, a viscoelastic damage model is developed within a thermodynamically consistent framework.

Damage refers to failure mechanisms associated with fracture; these mechanisms act to degrade the stiffness of the material. The proposed material model is developed under the continuum damage mechanics and thermodynamics frameworks; therefore, thermodynamic-consistency in enforced and representative orthotropic damage variables describe anisotropic damage nature. A damage surface is defined using the energy-norm, which is related to the thermodynamic forces conjugated to the damage variables, hardening function, and material-dependent coefficients. Temperature-dependent material parameters are used to capture experimentally observed attributes of the stress versus strain. Two approaches are presented, a model calibrated using simple uniaxial tensile experiments conducted at ambient and elevated temperatures. The second approach considers the unilateral effect alongside extensive nonlinear behavior under shear by utilizing the sign of the normal strains to evolve normal damage variables that are dissociated into tensile and compressive modes, and using independent shear damage variables, respectively.

The material model is implemented as a user-defined material subroutine and exercised in the commercial finite element analysis software Abaqus/Standard. The performance of an additive manufacturing mold using the modified Additive3D framework is presented to demonstrate the viability of predicted progressive damage at elevated temperature for a compression molding tool.

1. INTRODUCTION

1.1 Background

1.1.1 Extrusion Deposition Additive Manufacturing (EDAM)

Extrusion deposition additive manufacturing (EDAM) is a material extrusion process which is an additive manufacturing technique, and according to ASTM 5290 [1], it is understood as a process of joining materials to make parts from 3D models in a layer-by-layer fashion. Commonly, composite feedstock materials in the form of unidirectional long discontinuous fiber or short randomly oriented fiber pellets are used for producing 3D printed parts. The feedstock is processed at the melt temperature of the polymer and extruded from a nozzle through application of pressure developed from a processing screw and melt pump. One of the main differences between EDAM and other forms of material extrusion processes is the use of an injection-molding like screw used for processing the feedstock pellets. The use of a screw significantly increases the amount of material extruded per unit time; this benefit is realized as parts become large since the time required to print a part can be substantially reduced depending on the allowable layer time. A converging conical nozzle is commonly used in EDAM systems, nozzles of this type produce cylindrically shaped extruded beads; however, when a bead compactor is utilized, such as a tamper or roller, the extruded bead is approximately elliptical. The extruded bead exits the nozzle at the molten temperature and atmospheric pressure, and it is exposed to either an open or closed environment, a heated chamber can be used to create a closed-like environment. In both environments, the extruded bead loses heat from conduction, convection, and radiation heat transfer; however, the extent of heat losses will be different. In either approach, a heated build plate can be used, and this can reduce the heat loss that occur through conduction between the deposited beads and the plate. Another aspect of EDAM deals with the first layers, the first printed layer does not adequately bond or stick to the build plate and this can cause the part to slide, to mitigate slippage, an adhesive or constraining technique is required. Continuous deposition of the molten material is guided by a machine code that commands the movement of either the nozzle system, print bed, or both. Moreover, the machine code contains includes a series of temporal and spatial commands for which dictates where and when the molten material will be deposited; in addition, optional feature commands can be recorded in the event series such as the type of feature is being printed (i.e.,

infill or perimeter) and the status of the nozzle. A notable advantage of the additive manufacturing process is the ability to design a wide variety of complex shapes and infill structure with ease; however, an understanding of material behavior and slicing capabilities are some of the things required for successful use of the technology. Another important advantage is the waste reduction; for instance, the designed part is printed near shape so that very little machining is required to obtain desired surface smoothness or size. With this in mind, industrial-scale parts can be printed without significant waste, this has the potential to save time and allow for simplified designs such as elimination of non-critical joints. Overall, the ability to rapidly prototype large-scale printed structures through EDAM in an economical fashion and its potential for high temperature tooling are appealing abilities for the aerospace industry.

In recent years, large-scale EDAM systems have become available. The technology has been shown to print short fiber composite parts or molds on the scale of meters in a short amount of time. Figure 1 depicts two large-scale EDAM systems; namely, the Large Scale Additive Manufacturing (LSAM) and Big Area Additive Manufacturing (BAAM), produced by Thermwood© and Cincinnati Inc., respectively. The technical details of these machines can be found in [2] and [3] for Thermwood© and Cincinnati Inc., respectively. In contrast to their pure polymeric counterparts, processed short fiber composite pellets have the following advantages which make them attractive for EDAM: (i) enhanced mechanical performance (ii) lower distortion or part warpage due to its coefficient of thermal expansion and (iii) enhanced in-plane thermal conductivity [4]. A printed part with a material that has a low CTE tends to have lower internal residual stresses caused by thermal gradient, this in turn reduces part deformation as a result of thermal gradients; evidently, this is appealing for the production of large-scale parts in open environments. Notable applications of this technology involve 3D printing of a 25% wt. short carbon fiber reinforced polyether sulfone (PESU) fuselage skin mold using an LSAM system [5] and a proof-of-concept composite hull using a BAAM system [6], these 3D printed structures are shown in Figure 2. These printed structures have bolstered the economic claims that can be accomplished through additive manufacturing by demonstrating the ability to curtail manufacturing lead times and lower overall cost of production. For example, the proof-of-concept hull project, based on the collaboration between Oak Ridge National Laboratory and the Navy's Disruptive Technology Laboratory, reported a 90% reduction in production cost and reduced lead time from several months to days [6]. By the same token, the composite tooling case study between

traditional fused deposition modeling (FDM) and BAAM approaches described by Post et al. [7] best exemplifies the economics of EDAM. Specifically, the FDM printed tool required 478 hours and $31.4K whereas the BAAM printed tool required only 11 hours and $1.87K, the printed mold weighed approximately 65 pounds.

(a) (b)

Figure 1 (a) Thermwood© Large Scale Additive Manufacturing system [2] (b) Cincinnati Inc. Big Area Additive Manufacturing system [3]

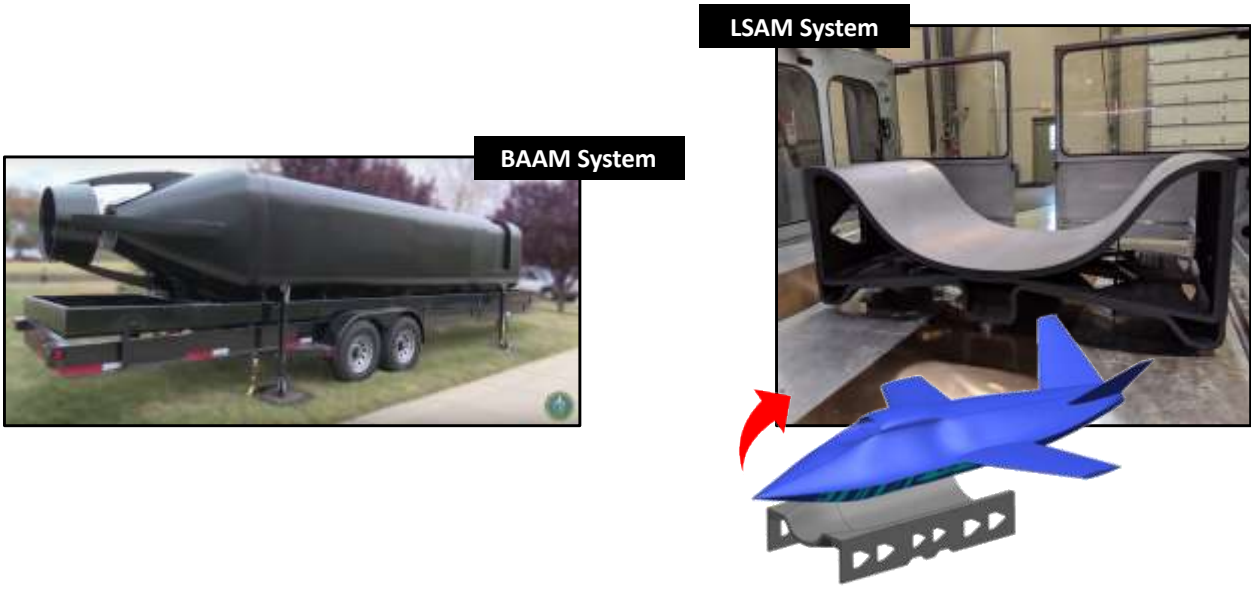

Figure 2 A 3D printed composite submersible hull [6] (left) and 3D printed composite fuselage skin mold [5] (right)

While large-scale additive manufacturing has promising applications, an understanding of the complex physics involved during and post-processing has somewhat remained empirical and so has been the choice of processing parameters. A Composite Additive Manufacturing Research Instrument (CAMRI) was developed to investigate and observe the composite material extrusion deposition process at a smaller-scale relative to the aforementioned systems, this has been for the purpose of developing and validating material models which is briefly discussed in 1.1.2. The system is custom designed by the additive manufacturing team at the composites manufacturing and simulation center (CMSC) at Purdue University; moreover, this integrated system functions in a similar manner to the aforementioned large-scale EDAM systems. The CAMRI system uses a combination of instruments (e.g., injection-molding style screw, heaters, gear pump, tamper) to melt the composite feedstock and extrude it through a convergent zone nozzle, some of the design elements and assembly are shown in Figure 3. For comprehensive details on the performance and attributes of the CAMRI system, the interested reader is referred to Barocio [8]. This EDAM system can be used for processing thermoplastics and fiber reinforced thermoplastics.

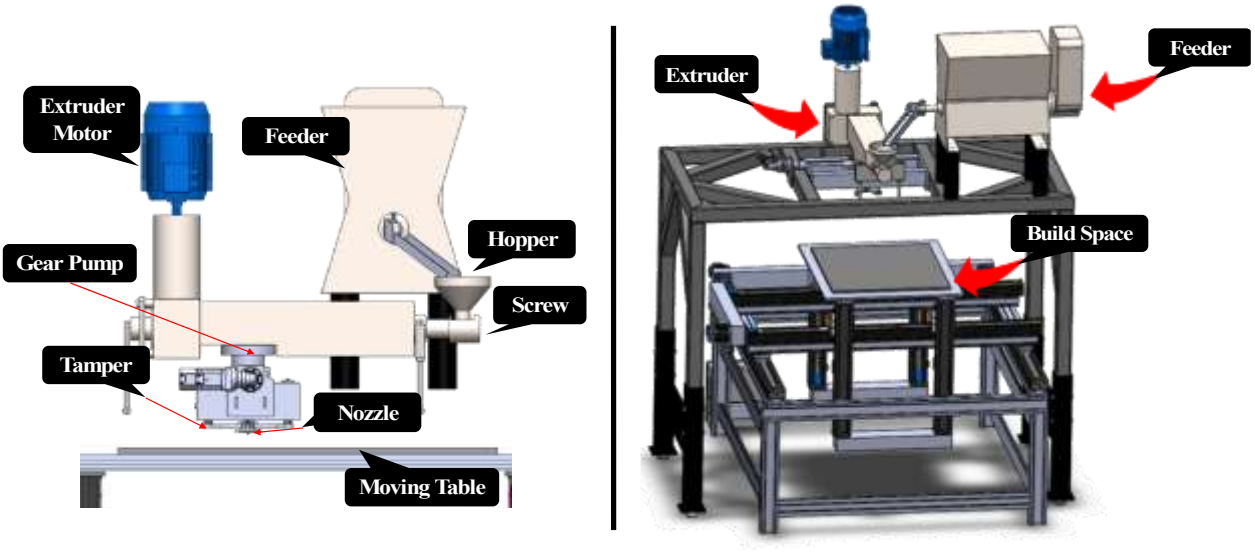

Figure 3 Composite Additive Manufacturing Research Instrument

The general procedure for designing and manufacturing a 3D printed mold is discussed below alongside some general considerations during these stages of design. Five main steps are needed for production of a short fiber composite mold, namely, (i) a Computer Aided Design (CAD) geometry file exported with a slicer compatible extension such as ".stl," (ii) slicing of CAD

geometry which is translated into a ".gcode" file, (iii) printing of the sliced geometry dictated by the gcode commands, (iv) post-annealing of printed part to reduce process-induced residual stresses, and (v) machining step to smoothen the surface. Figure 4 below depicts these steps for a composite NACA air inlet duct mold [9], the last step can be omitted as coatings are usually applied when wear resistance and surface quality need to be improved.

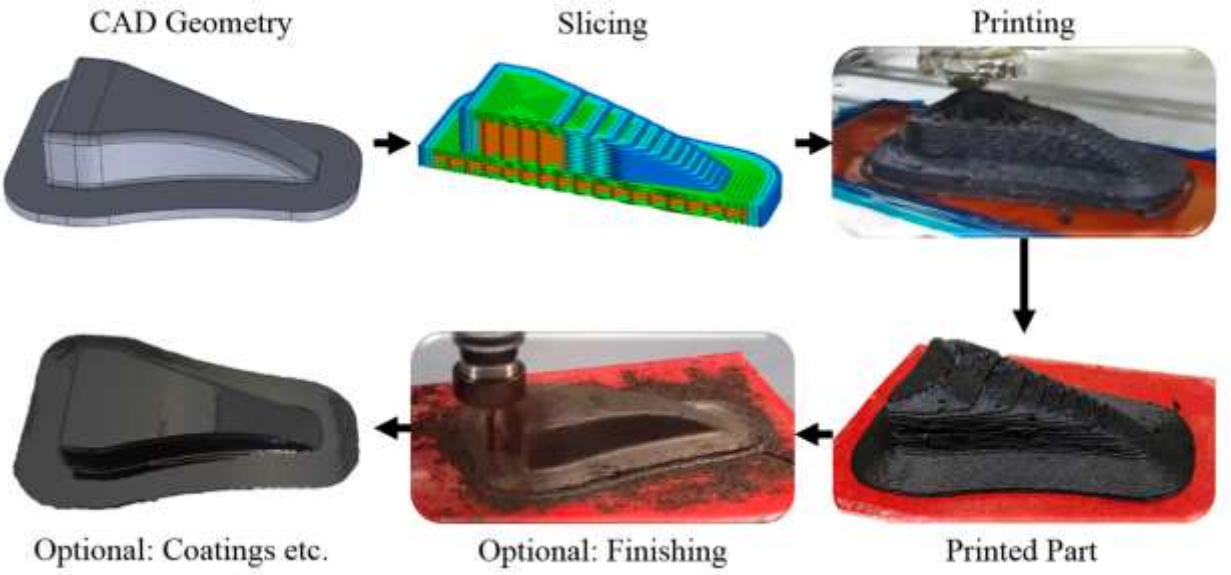

Figure 4 Production cycle of EDAM [9]

In the first step, CAD geometries are slightly oversized (i.e., approximately a fraction of a bead width) to allow for post-machining of the desired net-shape. Surface roughness of printed structures is inherent to the 3D printing process; hence, some form of machining is required if smooth surfaces are needed. Moreover, surface roughness of printed parts is defined by its surface texture (i.e., surface topography), this results from the semi-roundness of a bead as shown in Figure 5. Noteworthy to mention, as the layer height increases, the surface roughness, in general, increases [10]. EDAM systems typically have bead heights between 1.5mm and 5.08mm, though these can be slightly altered depending on the flow mechanics; nevertheless, highly complex designs will need to account for this if smooth surfaces are required in difficult to reach locations. For composite materials, the slicing step requires some knowledge of composite mechanics so as to not induce a highly unbalanced design which will intentionally warp the printed part. Furthermore, layer times are an important consideration during the slicing step and should be specified appropriately so as to not induce severe thermal gradients or material sagging. These

considerations during the slicing step are not exhaustive and the main point here is that the slicing strategy directly affects the performance and outcome of a printed part; therefore, some understanding of process-structure-performance relationship is needed to support the efficiency gained through additive manufacturing. During the print stage, the first layer or two are usually sacrificial layers since the bead quality is impacted by the imperfections of the print bed, these layers are either removed during machining or accounted for during the model design stage. Furthermore, long periods of dwell time should be avoided since thermoplastics degrade with time at high temperatures, this degradation causes a significant increase in viscosity which may halt the printing process. Annealing of the printed part should be performed if feasible, this step requires an oven to bring the temperature of the part slightly below its glass transition temperature for amorphous thermoplastic composites. During this phase, some residual stress induced during processing can be relaxed. The relaxation phenomenon is a property of the polymer since it is viscoelastic. Machining should be performed after the annealing phase since the internal stresses will have to re-equilibrate as material is removed. Moreover, it is generally not recommended to remove significant amounts of material during a single pass. If the void volume fraction is significant within the material, the post-machined part may have surface cavities as a result of the air pocket within the bead. A coating material can be used to achieve the desired surface quality, the type of coating can be chosen so as to improve the wear resistant of the printed part.

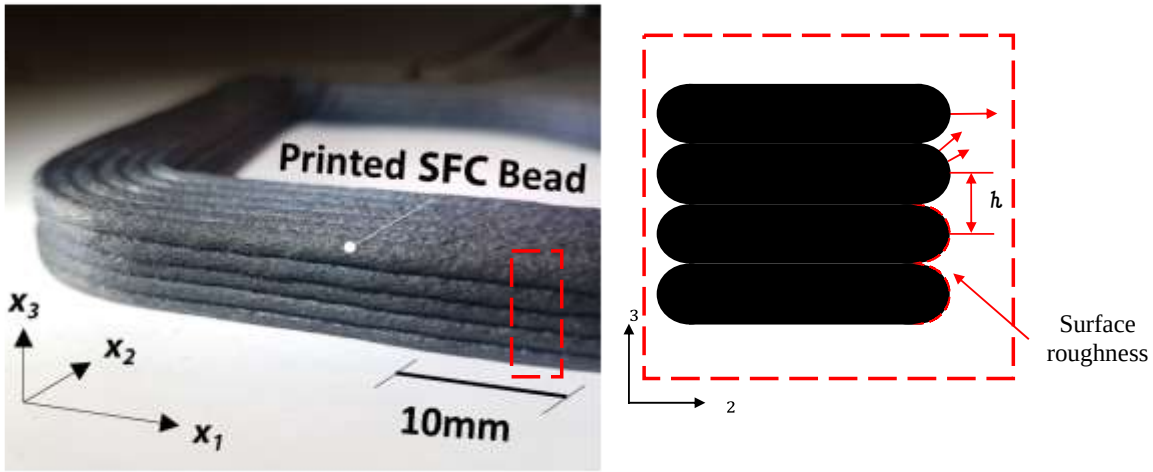

Figure 5 Illustration of a printed composite part and surface roughness

1.1.2 Virtual Design of EDAM Parts

Virtual design of EDAM parts includes both the Design For Additive Manufacturing (DFAM) process and computational simulations. Gibson, Rosen, and Stucker [11] define DFAM as "maximizing product performance through the synthesis of shapes, sizes, hierarchical structures, and material composition, subject to the capabilities of AM technologies." Product performance can be measured in terms of part deformation and part integrity and these metrics depend on both the EDAM process and part-level structure (i.e., infill structural details). In practice, maximizing product performance requires iteration of the virtual design process accomplished by modifying the geometry and slicing method, see Figure 6. With today's available CAD software, designers have access to extensive tools to create highly complex structures with precise dimensions, however, dimensional compensation based on a printed bead's cross-section should be considered beforehand; especially, for directions which are in-plane transverse to the print direction, specifically, certain dimensions should be an integer multiple of the bead's width and its height an integer multiple of the bead's height. With this in mind, changes made to the infill structure, such as infill orientation, may need geometrical compensation to achieve the slightly oversized shaped intended for minimal machining. Efficient additive manufacturing process designs minimize time and cost of production, this implies that optimal process designs should be sparsely filled whenever possible and quickly printed. Internal structure of sparsely filled geometries should not be random and should account for the anisotropy of the printed short fiber composite; in general, the print direction has the greatest stiffness and strength relative to its in-plane and stacking directions. In-service loads that produce highly stressed regions should take advantage of the print direction properties whenever possible or filled adequately to prevent excessive deformation or damage. Neither should the print speed be tuned arbitrarily fast nor should it be the chief objective, an extremely fast print speed translates to a short layer time; the time it takes for the system to complete a layer. When the layer time is extremely short, material sagging becomes pronounced because of the lack of cooling time the layer experiences. In other words, very short cooling times do not allow the printed short fiber composite to develop enough stiffness to significantly resist gravitational deformation. On the contrary, neither should the layer time be extremely long as severe thermal gradients can promote significant residual stresses on a part. Therefore, the efficiency of the design process is constrained by the material behavior, likewise, minimization of

time and cost depend on the material behavior. Striking the balance between optimal process design variables and material behavior is facilitated by the virtual design process in contrast to the traditionally empirical trial and error fashion of printing a part. On the performance side, it is important to predict whether the intended structure can withstand the required service loads for a sustained period of time. Simulation tools that provide this capability allows the designer to modify the 3D printed shape for maximum performance; thus, taking advantage of the additive manufacturing capabilities and attributes.

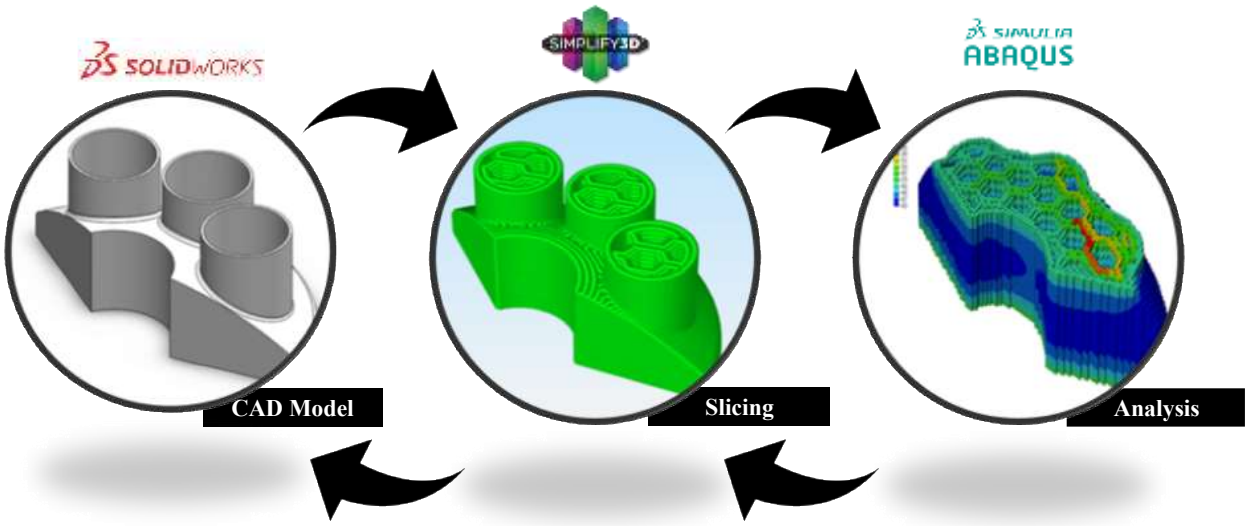

Figure 6 Virtual design for EDAM process

A couple of exemplary examples of the virtual design process is found in [12], one of which is a virtual design exercise of an automotive air inlet, shown in Figure 7b. The simulation framework used for the study is Additive3D, this framework is discussed in 1.1.2. The automotive air inlet is made from prepreg, depicted in Figure 7a, a fibrous material pre-impregnated with resin which is processed inside an autoclave. Two analyses are required to understand the implications of process and structure design choices, the first is the EDAM process simulation and the second is the performance simulation. Figure 8a illustrates the elements that inform the EDAM process simulations, these are the machine code, AM system card, and digital material card. The machine code is used for specifying the orientation states within the simulation, the AM system card for identifying appropriate boundary conditions, and the digital material model for the correct material properties. Furthermore, the EDAM process simulation is a sequentially-coupled thermal-stress

finite element analysis and its inputs depend on the EDAM system considered. For example, the CAMRI and LSAM systems extrude bead profiles of different dimensions because of the different nozzle sizes, consequently, the bead's microstructure and performance will be different, and this is captured using different digital material cards.

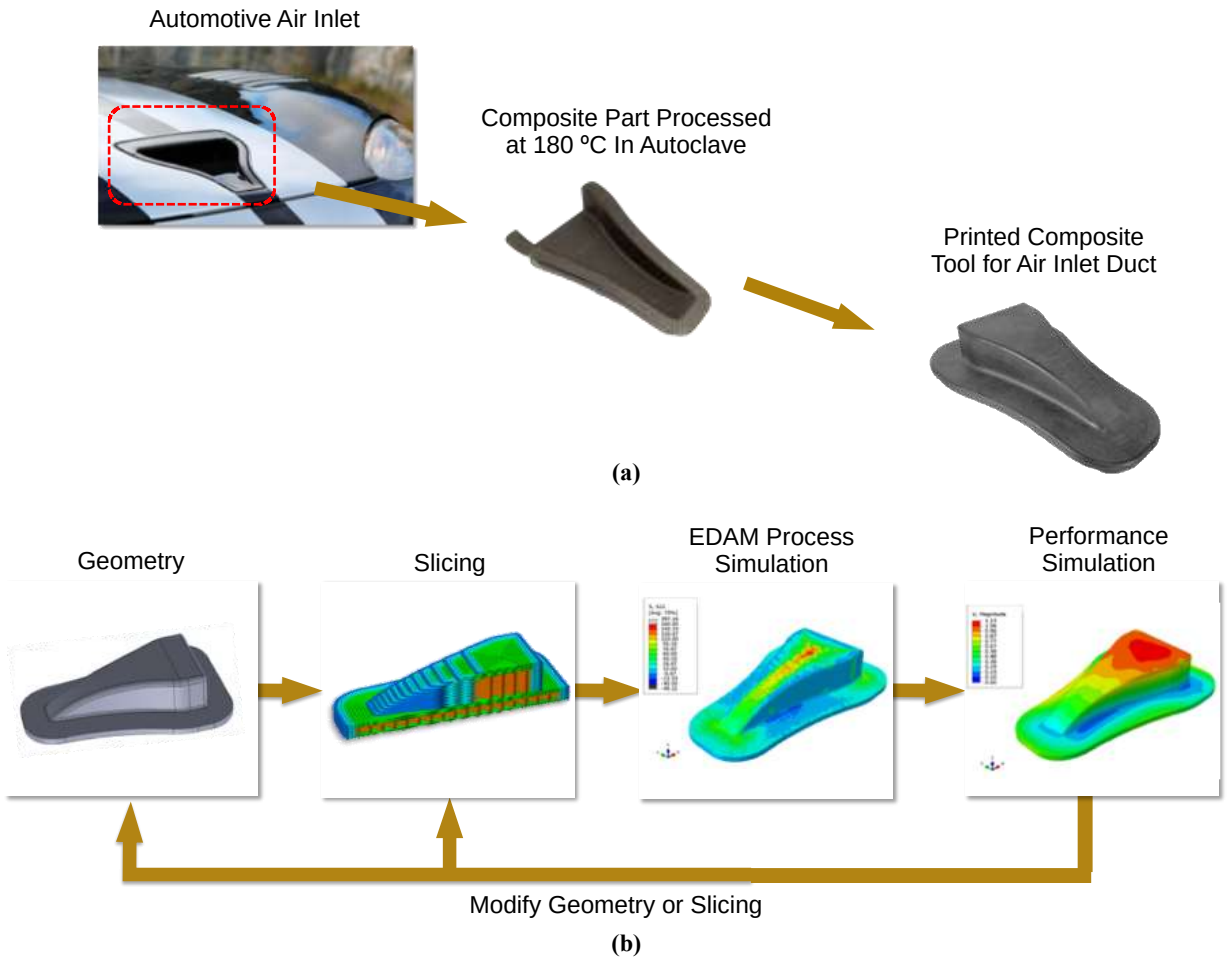

Figure 7 (a) Automotive air inlet fiber reinforced composite produced using an 3D printed short fiber composite autoclave mold (b) Virtual design process for NACA duct air inlet autoclave mold [12]

Figure 8b and Figure 8c illustrate the workflow for the performance simulation. Residual stresses can be mapped onto a conformal mesh of the geometry, and the final stress state can be investigated after the in-service loads are specified. The deformed shape of the tool during service-use can be plotted and compared with the nominal shape profile. Tool shape compensation can then be made to achieve the desired design shape.

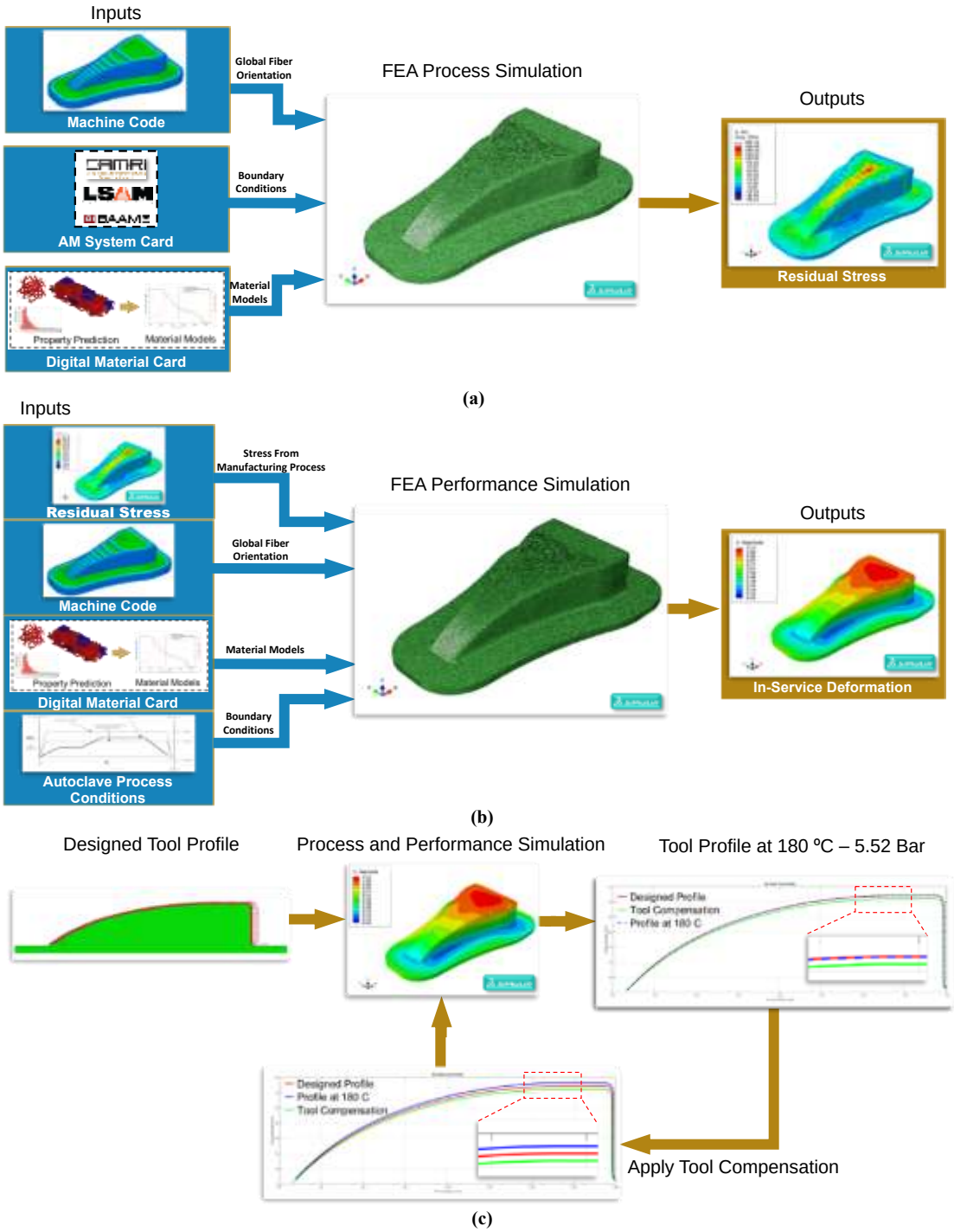

Figure 8 (a) EDAM process simulation workflow for a NACA duct autoclave short fiber composite mold (b) Performance analysis of composite NACA duct mold (c) Geometrical compensation of NACA duct composite mold [12]

1.1.3 Computational Modeling of EDAM Process using Additive3D

Computational modeling of the EDAM process has been implemented in Abaqus/Standard (Implicit) via a set of user-defined subroutines, this framework is known as Additive3D [13]. Process and performance simulations are sequentially coupled thermal-stress analyses, these analyses require nine user-defined subroutines. The Additive3D workflow virtually reflects the design for additive manufacturing process by simulating the physics of the process to understand stress and deformation development. While the framework and workflow discussed in 1.1.1 are essential for improving the efficiency of additive manufacturing designs, it does not capture damage-based degradation as a result of the accumulated residual stress build-up or in-service conditions. Nevertheless, it remains relevant to discuss some of the elements of the framework to understand how damage mechanics can be implemented without extensive modification to the framework.

Additive3D contains nine user-defined subroutines utilized for the sequential thermomechanical analysis, Table 1 summarizes the subroutine descriptions. The mesh of the geometry is constructed by executing an in-house python script which generates a non-conformal voxel mesh based on the tool path in the machine code file, the resulting mesh only contains elements that will be activated in the analysis. The continuous deposition of molten material in the additive manufacturing process is imitated in Abaqus/Standard through the use of progressive element activation; specifically, the activation time of the element is computed based on the event series and an initially dormant element becomes active after the activation time is reached by using the UEPActivationVol subroutine. Moreover, this subroutine requires machine code information, denoted as the event series, alongside a searching algorithm that will check if an element is active or dormant at any given time during the deposition process. The event series usually contains information about the temporal and spatial history of the nozzle, and user-defined indicators that will aid in modeling certain phenomena. The order of subroutine execution begins with the ORIENT subroutine, it is called at the first integration point of an element. The searching algorithm is executed, and the activation time and local orientations is stored in a global array; specifically, by using the UEXTERNALDB subroutine. Subsequent integration point calls from ORIENT, all calls to SDVINI and UEPActivationVol extract required input information from the global array. For complex 3D printed geometries with internal infill walls, UFIELD is implemented to

approximate differences in convection properties between infill exposed surfaces and external surfaces. UMATHT is used for defining the thermal constitutive behavior of the short fiber composite in addition to internal heat generation, it is called at all material points of an element with user-defined thermal material behavior. UMDFLUX is implemented to capture the heat losses that result from an air cooled mechanical bead compactor or tamper when in use. UEXPAN is used for defining incremental thermal strains that are a function of temperature, predefined field variables, and state variables, this subroutine allows for capturing strain changes resulting from material phase changes such as crystallization for semi-crystalline polymers. UMAT is used for defining the mechanical constitutive behavior of the short fiber composite and it is called at all integration points for user-defined material behavior. For a comprehensive review of these subroutines, the pseudocode algorithm, and implementation, the motivated reader is referred to [8], [13]–[18]. Based on the functions of the subroutines, only the UMAT requires modification to include thermoviscoelastic damage mechanics.

Table 1 Abaqus/Standard (Implicit) user-defined subroutines for the EDAM process simulations, H denoting heat transfer analysis and M denoting mechanical analysis, modified from [13]

User subroutine	**Analysis**	**Description**
UEXTERNALDB	H & M	Called at the beginning of an analysis to allocate global arrays to facilitate relevant information transfer between subroutines
ORIENT	H & M	Assigns local element orientations based on principal directions of the local event series coordinate system. A
SDVINI	H & M	Called after ORIENT at the beginning of analysis. Stores and shares activation time and other initial conditions to other subroutines
UEPACTIVATIONVOL	H & M	Called at the beginning of increment to activate dormant elements by setting the activated volume fraction to one.
UFIELD	H only	Called as needed and used for assigning feature-based convection properties to nodes
UMATHT	H only	Called to perform phase change (i.e., crystallization for semi-crystalline polymers, melting, and bonding) and heat transfer calculations
UMDFLUX	H only	Uses event series to implement heat losses from mechanical bead compactor (e.g., tamper)
UEXPAN	M only	Used for phase transfer computations in mechanical analysis, crystallization and melting, and computes thermal crystallization strains
UMAT	M only	Implements thermoviscoelasticity

The UMAT and UMATHT are the subroutines that require material input parameters whenever a new short fiber composite is introduced, the set of material parameters are organized into a single file denoted as the material card. The other subroutines deal with machine-relevant information. A brief description of the relevant equations used for modeling heat and thermoviscoelasticity is discussed for the purpose of identifying relevant material-dependent parameters that must be considered for new material systems. It is noteworthy to mention that these material parameters or properties are not readily available in a database or in the literature; therefore, most if not all 3D printed short fiber composite require some form of characterization either experimentally or through validated micromechanical models.

The variables involved in the heat transfer formulation are density, ρ, heat capacity, C_p, thermal conductivity tensor, k_i for $i = 1,2,3$, heat generation, Q, time, t, and temperature, T. Moreover, heat generation is present for semi-crystalline polymers like polyphenylene sulfide (PPS) because of its exothermic crystallization kinetics phenomenon, and it is omitted for amorphous polymers such as PESU. Furthermore, the variables involved in the convection formulation are the effective material conductivity, k_{eff}, parallel to the surface normal, n, film coefficient, h, emissivity, ε, Boltzmann constant, σ_B, ambient temperature with respect to convection, $T_{\infty 1}$, and mean temperature of the boundaries in proximity to the surface, $T_{\infty 2}$. For a fiber reinforced amorphous polymer, the essential heat transfer variables that need characterization are: $C_p(T)$, k_i, ρ, ε, h.

$$\frac{\partial}{\partial x_1}\left(k_1(T)\frac{\partial T}{\partial x_1}\right)+\frac{\partial}{\partial x_2}\left(k_2(T)\frac{\partial T}{\partial x_2}\right)+\frac{\partial}{\partial x_3}\left(k_3(T)\frac{\partial T}{\partial x_3}\right)+Q=\frac{\partial}{\partial t}\left(\rho C_p(T)T\right)$$
(conduction)

$$q=-k_{eff}\frac{\partial T}{\partial n}\Big|_{surface}= h\left(T|_{surface}-T_{\infty 1}\right)+\varepsilon\sigma_B\left(T^4|_{surface}-T_{\infty 2}^4\right) \quad (1)$$
(convection/radiation)

Polymer diffusion is an important phenomenon that affects the performance of 3D printed parts, it plays an essential role in the adhesion of bead-to-bead interfaces. A non-isothermal autohesion model, developed by Yang and Pitchumani [19], then modified by Barocio [8] to include crystallinity, is used for quantifying the temporal evolution of the mode-I critical energy release rate, $G_{IC}(t)$. The ratio between the temporal energy release rate its maximum possible

energy release rate, $G_{IC\infty}$, is coined as the degree of bonding, D_b as shown in Eq. (2). The degree of bonding is a scalar value that ranges between 0 and 1, with a value of 0 denoting no bonding and a value of 1 signifying complete bonding. The model includes a welding time parameter, t_w, to quantify the degree of bonding, and it is defined using the Arrhenius equation, $t_w(T) = Ae^{E_A/RT}$. The essential variables needed to describe the degree of bonding are the pre-exponential factor, A, and the activation energy, E_A. These variables are obtained through mode-I fracture experiments of 3D printed double cantilever beam samples. The mechanical properties of the interfaces are influenced by the degree of bonding; likewise, damage behavior is assumed to be coupled to this parameter. While it is important to study the coupling nature of these two phenomena, it is assumed the beads adhere to one another completely, this assumption is reasonable for thermally annealed specimens and geometries as this allows for accelerated polymer diffusion.

$$D_b(t) = \frac{G_{IC}(t)}{G_{IC_\infty}} = \sqrt{\int_0^{t_c} \frac{d\tau}{t_W\big(T(\tau)\big)}}, \qquad t_c \in \{t \mid X < X^{crit}\} \tag{2}$$

The time-dependence of the short fiber composite is modeled with a thermoviscoelastic material description, the generalized Maxwell model is used alongside the reduced time variable. The material model is derived using a combination of rheological elements such as springs and dashpots, and when a 3D state of stress is considered, the time-dependent stresses are represented by the hereditary integral shown below. Here, the stiffness tensor, $C_{ij}(T, X, t-\tau)$ depends on temperature, T, crystallinity for semi-crystalline polymers, X, and time, t, moreover, the stiffness tensor is also defined with a Prony series. Time, t, is substituted with the reduced time variable, ξ, to represent the change in material behavior at different temperature, it is characterized by an empirical William-Landel-Ferry (WLF) or Arrhenius equation. The stiffness tensor is described using a Prony series, and each component of the stiffness tensor requires the constants of the Prony series. The material parameters that are required are the stiffness weights and the corresponding relaxation constants, these can be obtained from stress relaxation experiments. The number of constants in the reduced time expression depend on the model; for example, the WLF relation requires two constants obtained from thermoviscoelastic experiments. Additional details of the required material parameters and characterization for the heat transfer, degree of bonding, and thermoviscoelasticity models, the reader is referred to Barocio [8] and Brenken [14].

$$\sigma_i = \int_0^t C_{ij}(T, X, t-\tau)\frac{\partial \varepsilon_j^{eff}}{\partial \tau} d\tau\,, \qquad i,j = 1,2,\ldots,6 \tag{3}$$

1.1.4 EDAM Short Fiber Composite Heterogeneity Hierarchy

From a material modeling perspective, there are three length-scales which are most relevant for the analysis of EDAM behavior. Namely, these are the microscale, mesoscale, and macroscale. At the smallest length-scale, there are microscopic features, invisible to the human eye, at larger length-scales. Noteworthy to mention, modeling very small features for mesoscale or macroscale analyses can present a significant challenge. Most often, homogenization and localization approaches are used for transferring information from one length-scale to another, this is illustrated in Figure 9. Homogenization is a powerful tool that allows for effective material description based on microscopic descriptors, this approach is typically used to reduce computational expense at the cost of smearing microscopic or local stress and strain fields. This approach is used throughout this work to model anisotropic material behavior in a computationally inexpensive way.

The microscale is the origin of material heterogeneity, it contains microscopic features considered fundamental to the effective behavior of the material. The heterogeneity of a printed bead microstructure contains fibers or inclusions, matrix, fiber/matrix interfaces, and voids. Fibers are typically cylindrical; however, peculiarities in fiber production may yield other shapes such as the kidney-bean shaped fibers. The microstructure of a short fiber composite is an amalgamation of these micro-constituents, this ensemble is most often quantitatively characterized by its fiber length, fiber shape and size, fiber volume fraction, fiber orientation, matrix volume fraction, void volume fraction, and void size and shape. Each microstructural characteristic (e.g., fiber length, fiber orientation) has a distribution of values and this distribution does change with processing conditions. For example, modifying the nozzle size or geometry can significantly alter the fiber orientation tensor [20], mesoscale and macroscale performance are then affected. For anisotropic modeling, these microscopic features and characteristics should be considered.

The mesoscale contains features on the length-scale of a printed bead, also, each bead contains a significant quantity of micro-constituents. The printed bead and bead-to-bead interfaces are the relevant characteristics at this length-scale. The microscale heterogeneity of the material propagates to the mesoscale and it produces anisotropic material behavior. Moreover, at the

mesoscale, the role of interfaces is important, and its behavior should be incorporated into models. Due to the anisotropic nature of the material, the direction of beads or infill structure will have an impact on the final deformation state. Since the effective anisotropic response depends on the microscopic details, it requires characterization or analysis efforts when a new microstructure is obtained. This is an important point of consideration for EDAM material cards that incorporate effective mesoscale material properties, significant characterization efforts or validated micromechanical analyses are required for significant changes to the microstructure. Despite this reality, the processing conditions responsible for significantly altering the microstructure are kept the same and this translates to an effective mesoscale mean response that remains the same from batch-to-batch but with variability present. In this dissertation, the effective mesoscale properties of the short fiber composite are of interest and microscale characterization and analyses are only considered to inform mesoscale models or procure homogenized composite properties.

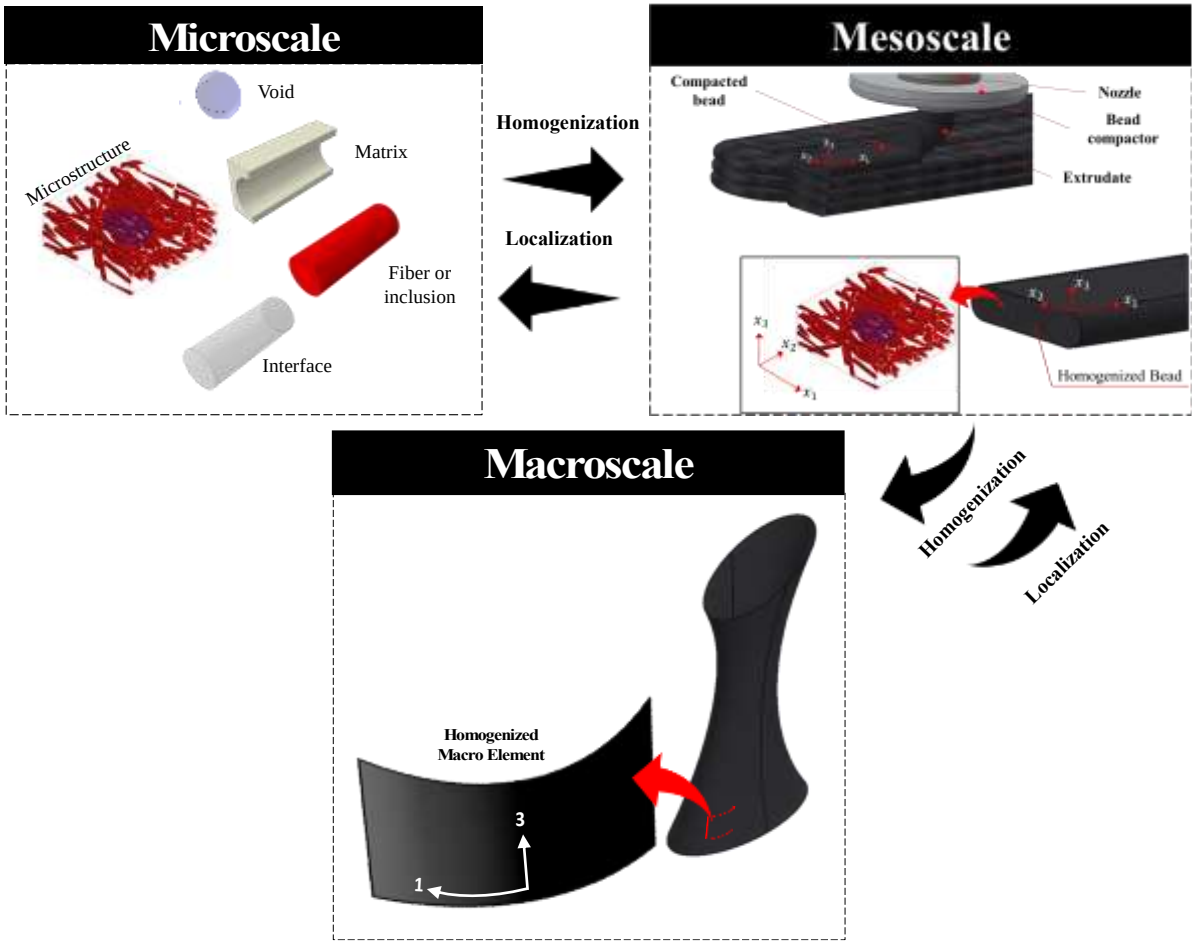

Figure 9 Depiction of the EDAM relevant multiscales

The macroscale is considered for printed structures that are relatively large compared to the length-scale of a printed bead. At this scale, a computational analysis of large-scale structures may require further homogenization, this means that mesoscale details are smeared. Like homogenization, localization can be performed and is accomplished by using the macroscopic fields to predict mesoscopic or microscopic fields (i.e., local fields such as stress or strain within the representative volume). When high fidelity is warranted, traversing across the multiscale ladder is possible with homogenization/localization analyses. A brief review of multiscale analysis is discussed in 2.3.3. Figure 9 contains the torch design as an example of a macroscale structure relative to the other length-scales. The torch geometry is the largest known 3D printed structure produced with an LSAM by Dimensional Innovations© for the Las Vegas Raiders stadium [21]. The outer section of the torch structure is made of 225 assembled 3D printed blocks composed of 20% wt. carbon fiber reinforced polycarbonate, each block weighing approximately 158.8 kilograms (350 pounds).

1.1.5 Damage and Failure in EDAM Materials and Structures

Damage and failure during EDAM has been observed and reported by Talagani et al. [22] and Compton et al. [23], both publications investigate the same material, carbon fiber reinforced acrylonitrile butadiene styrene (ABS), printed on the BAAM. In their study, the failure event is shown through images of processing-induced delaminations. Delamination of the printed car chassis is shown in Figure 10, from the images at the center and right. A visible dark region is evident in the center image and this is evidence of delamination during the EDAM process; additionally, a flat yellow object was inserted between the crack surfaces on the image on the right-hand side. The authors also show a micrographic image of the printed bead's cross-section along the print direction, the image shows initial cracks as a dark band at the edge of the bead along its stacking interface, as well as dark irregular shaped intrabead regions denoted as voids. Motivated by the car chassis problem, Talagani et. al. [22] investigate the effects of process-induced residual stresses on structural distortion, multiscale damage and interface fracture in the BAAM process via a fully coupled thermo-mechanical finite element analysis. The coupled analysis utilized a temperature field based on the physical print to inform the mechanical analysis. Also, the thermal constitutive properties and thermal portion of the coupled analysis were validated using measured temperatures of a printed wall. A voxelized mesh model of the car chassis is constructed from

inputs of the BAAM machine code, additionally, the local element orientations are specified from the same machine code inputs. The input properties required for the mechanical constitutive law were obtained by reverse engineering micro-constituent properties and microstructural characteristics (e.g., fiber orientation tensor), then a homogenization step is performed using the Mori-Tanaka scheme. The macro stress and strain field were utilized in a localization step to determine element failure using multiscale damage and linear fracture mechanics, specifically, intrabead damage and interbead fracture within an element. The specifics of the damage model equations, theory, and calibration were not discussed in the article.

Figure 10 Micrograph of extruded carbon fiber ABS with initial flaws (left), car chassis section with delamination printed on the BAAM system (center), interior of car chassis displaying delamination (right) [22]

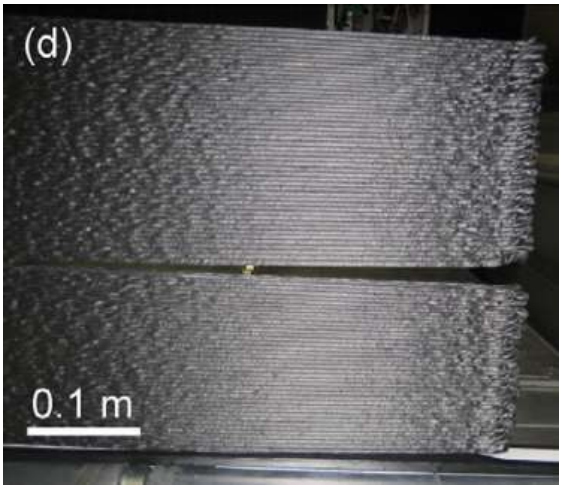

Figure 11 Warping and interbead cracking for a carbon fiber reinforced ABS wall printed on the BAAM system [23]

Compton et al. [23], while motivated by the same printed car chassis problem, investigated printed thin walls by measuring its thermal evolution, for the purpose of developing a 1D transient thermal model. Six thin walls were printed to study the effects of layer time on the steady-state top layer temperature, warping, and delamination. The steady-state top layer temperature, denoted as T_{top}, is defined as the temperature of the last deposited bead before the subsequent layer is added. Three of the six walls were printed with an 11mm thickness and the remaining three with 20mm thickness; additionally, the length and height were 1.542m and 0.358m, respectively. For each wall of a given thickness, three layer times were imposed, categorized as short, intermediate, and long layer times. The authors show a plot of the steady-state top layer temperature with respect to the layer time with reference horizontal dashed lines indicating the temperature at the ABS glass transition and the ambient. One notable discovery was that delamination of the wall occurred for the cases with long layer times, while only warping occurred for intermediate layer times. Furthermore, delaminations occurred when the steady-state top layer temperature dropped significantly below the glass transition temperature.

1.2 Problem Statement and Objective

As discussed earlier, the computational framework and workflow used for process and performance analysis of 3D printed short fiber composites utilizes a thermoviscoelastic material model to understand part deformation and residual stresses, the material model does not take into account nonlinearity in material behavior as a result of accumulated micro-damage. The reported continuum and fracture mechanics based damage approach used for simulating failure sites of EDAM printed structures have not been adequately described to enable its implementation in similar thermomechanical models; therefore, the approach is questionable especially for different load cases. Furthermore, a framework or workflow that describes the damage model, proposes characterization experiments, and outlines material model calibration procedure has not been previously developed for this application. The interaction between creep and damage has not been captured in the previously developed additive manufacturing performance simulation approaches. In addition, the reported methodologies cannot accurately capture progressive damage and ultimate failure of a 3D printed part at elevated temperatures. Also, an understanding of anisotropic material behavior at elevated temperatures that are below the glass transition are lacking in the literature for a wide-range of 3D printed short fiber composites. With this in mind, the dearth of

experimental data poses a challenge for assessing how well a proposed material model can represent its behavior. Even though micromechanical approaches aimed at estimating material properties and behavior are possible, it is computationally expensive, and often requires difficult to characterize micro-constituent properties.

In this dissertation, these challenges are solved by developing a temperature-dependent viscoelastic continuum damage model that is capable of capturing anisotropic damage. The developed damage model is compatible with the additive3D framework since a similar hereditary integral is used. Experimental characterization of the viscoelastic properties remain the same as discussed in [14], except with less reliance on micromechanical predictions to obtain missing elastic properties. Experimental data under tension, compression, and shear are procured to calibrate the material model parameters and capture the experimental nonlinear trends at room and elevated temperatures. Finally, the material model is exercised to demonstrate its ability to predict time-dependent damage and structural performance of a 3D printed tool. The objective of this dissertation is to develop the framework and workflow for characterizing a thermoviscoelastic damage model for 3D printed short fiber composites.

1.3 Dissertation Outline

Chapter 2 provides a literature review of the relevant fields needed to develop the thermoviscoelastic damage model to accurately represent the short fiber reinforced thermoplastic. The classification of is discussed and the behavior of thermoplastics are illustrated to highlight notable aspects of mechanical behavior such as intrinsic and extrinsic yield points, proportional limit, strain softening or hardening. Further, these mechanical attributes are assumed to exists for reinforced thermoplastics and are considered when selecting an appropriate anisotropic viscoelastic damage theory. Viscoelastic properties are briefly discussed to explain the difference between creep and relaxation phenomenon as well as illustrate the temporal behavior associated with polymers. The rheological model and its mathematical representation used for describing viscoelastic behavior in Additive3D are reviewed for identifying the required mathematical formulation to develop a compatible thermoviscoelastic damage formulation. Previous work on damage mechanisms of short fiber composites is mentioned to facilitate appropriate selection of the anisotropic damage theory. Moreover, the taxonomy of computational progressive fracture and

damage mechanics is provided to identify the most viable approach for the adopted simulation framework.

In Chapter 3, a thermoviscoelastic damage model is derived from fundamental thermodynamic equations. The theory accounts for damage in the constitutive law through introduction of a damage effect tensor, this is accomplished by employing the energy equivalence principle used in continuum damage mechanics. The damage effect tensor can be either formulated direction or through a dyadic product of its second-order damage or integrity tensors. Directional damage variables represent the different damage modes associated with anisotropic material behavior. The constitutive properties are derived from the Helmholtz free energy and thermodynamic consistency is enforced through the Clausius-Duhem inequality. The inequality ensures entropy remains positive for the thermodynamics of irreversible processes. The free energy function is shown to exhibit relaxed and unrelaxed parts, this is true for the derived stresses which resembles the Prony series discussed in Chapter 2. A damage surface and potential are postulated, these are formulated in strain-space to exploit the temporal driving force stemming from viscoelastic behavior. The thermodynamic force conjugated to the damage variables and a temperature-dependent isotropic hardening/softening law are used for describing the thermodynamically allowable material state by which no damage occurs. The viscoelastic damage model is numerically formulated for its implementation into the implicit finite element method with the updated stresses and Jacobian defined as required by the user material subroutine.

In Chapter 4, the material properties for a 3D printed short fiber composite are experimentally obtained and the material behavior analyzed to assess trends of the mechanical attributes discussed in Chapter 2. The experimental set-up, apparatus, and methodology are discussed. Stress relaxation experiments are performed to both characterize the viscoelastic properties of the composite using the methodology described by Brenken [14] and determine the elevated temperature cases with the allotted time-scale for which viscoelastic stress relaxation is minimal to allow nonlinear behavior to be dominated by damage. Transient heat transfer analyses are performed to predict required thermal soak time to achieve a core temperature equal to the ambient within the environmental chamber. Microstructural images and characterization is made for the short fiber composite to highlight the microstructural features common to 3D printed composites. The strain fields for all mechanical tests were obtained using the digital image correlation method, and most thermoelastic properties for the orthotropic short fiber composite

were extracted. Uniaxial tensile, compression, and shear deformations were considered for this work. Scanning electron microscopy is performed to investigate the post-mortem fracture surfaces of mechanical coupons at room temperature and elevated temperature.

In chapter 5, the stress relaxation experiments, and mechanical properties obtained in Chapter 4 are used for characterizing the viscoelastic model parameters as well as calibrating the damage properties. A proposed procedure for calibrating the damage model according to tension and compression stress versus strain experiments is made under the assumption plastic deformation is insignificant for brittle behavior. Model parameters are studied to illustrate the change in predicted material response and assess its ability to capture the experimental trends. Two types of approaches are taken to reflect the softening regime, the first assumes instantaneous fracture once the damage critical value is reached and the other assumes no further hardening occurs which accelerates the rate of damage past the ultimate stress point. The material model accounts for the stacking direction nonlinear behavior by assuming an independent set of parameters which are assumed to be interfacial properties. Creep and creep-induced damage is presented to highlight the capability of predicting time-dependent damage.

In Chapter 6, the viscoelastic damage model is integrated into the Additive3D framework to the provide simulated progressive damage performance capability. The design for additive manufacturing process is demonstrated using the modified framework by designing a u-shaped mold similar to the LSAM large-scale mold geometry shown in Chapter 1. Process simulations are conducted to illustrate the stress analysis of the printed part for the characterized material model. Secondly, the mold is subjected to a compression load exerted by an aluminum plunger to reflect a compression molding load case. A sequentially coupled thermal-stress analysis is performed for the performance analysis of the mold to represent a load case with spatially varying temperature and damage behavior. A physical mold is printed and tested under a similar condition, comparison and contrast is made between the model and experiment.

Chapter 7 concludes the dissertation with recommendations for future work.

2. LITERATURE REVIEW

2.1 Thermoviscoelasticity Background

2.1.1 Classification of Polymers and Mechanical Behavior

In general, most polymers are categorized as either thermoplastic or thermoset. The physical difference between a thermoplastic and a thermoset lies in its bonding behavior between molecular chains. Thermosets have primary and secondary bonds between chains; however, thermoplastics only exhibits secondary bonds. The bonding structure and morphology of the chains influences the thermal, mechanical, and processing behavior. Thermoplastics can be further classified as either semi-crystalline or amorphous, semi-crystalline polymers exhibit diffraction patterns which are indicative of short range order. The crystallization percentage directly influences the mechanical properties of the thermoplastic and should be considered in modeling approaches. The noteworthy distinction between both classes of polymers is based on its processing; specifically, thermoplastic polymers can be melted or molded by raising the temperature to its melt point. On the other hand, thermosetting polymers cannot be melted or molded rather they undergo an irreversible cross-linking phenomenon. The cross-linking nature of thermosets also influence the mechanical properties of the polymer or composite. Amorphous thermoplastics are simple to model relative to semi-crystalline thermoplastics and thermosets since modeling nonlinear mechanical behavior does not require crystallization or cross-linking material models. For this work, only reinforced amorphous thermoplastics polymers are considered.

Uniaxial tensile tests are one of the common methods used for assessing the performance of polymers, guides such as the ASTM D638 [24] provide a standard approach for testing many different classes of polymers. Four types of uniaxial tensile behavior can be observed from a variety of polymers, as shown in Figure 12a., these are either:

- Brittle – Fracture occurs with little elastic deformation and without significant plastic deformation
- Semi-ductile – Fracture occurs with some plastic deformation
- Ductile – Significant plastic formation is observable whereby sustained loads are accompanied by irreversible strains

- Elastomer – Usually exhibits high flexibility such as rubbers and behave highly nonlinear

PESU, an amorphous thermoplastic polymer of interest, is known to behave in a ductile and high softening manner; moreover, the polymer has a Young's modulus of 2.6GPa, yield stress of 82MPa, and elongation at break of 40% [25]. Commercial polymers may however behave differently than its base polymer despite having the same basic chemical structure, the reason for this is due to additives. Additives are composed of a substance or solvent added to a polymer to modify the properties of a polymer to meet a specified need or application; for example, typical additives are lubricants, plasticizers, stabilizers, and reinforcements. With this in mind, a base polymer such as PESU can behave in a glassy brittle manner depending on the types of additives used.

Figure 12b illustrates Considère construction which is often used for the interpretation of the yield and flow phenomenon in a tensile test, especially for ductile behavior. The proportional limit denotes the transition between linear elastic and nonlinear behavior. The extrinsic yield point is defined as the tangent to the nonlinear curve through the point $\varepsilon = -1\%$ or $\varepsilon = 0\%$ if an extension ratio is used, and it is obtained from manipulation of the true stress, nominal stress, and engineering strain relations [25]. The intrinsic yield point is often taken as the proportional limit stress or the first peak in the stress versus strain diagram [26]. Both intrinsic or extrinsic yield points are methods used for identifying the yield point in the stress-strain diagram, and either definition can be adopted depending on the application; nevertheless, the intrinsic yield point is adopted most often. The intrinsic yield point may change with temperature or strain rate as shown in Figure 13a; however, Brinson and Brinson [26] mention that care must be taken to ensure interpretations are taken from isochronous stress-strain plots. Polymers are also known to exhibit unilateral tension and compression behavior, an example is shown in Figure 13b based on the work of Rybicky and Kanninen [27]. With these observations in mind, it reasonable to expect fiber reinforced polymer composites to exhibit similar behavior.

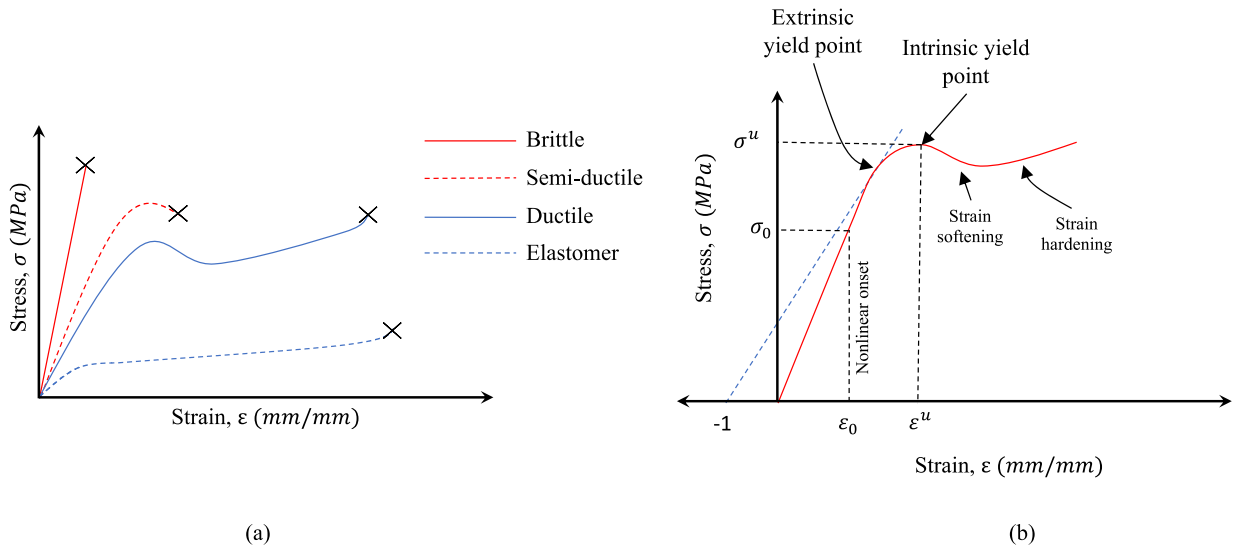

(a) (b)

Figure 12 (a) Typical stress-strain response of various polymers, modified from [26] (b) Considère's construction adopted from (Kinloch and Young, 1995) [28]

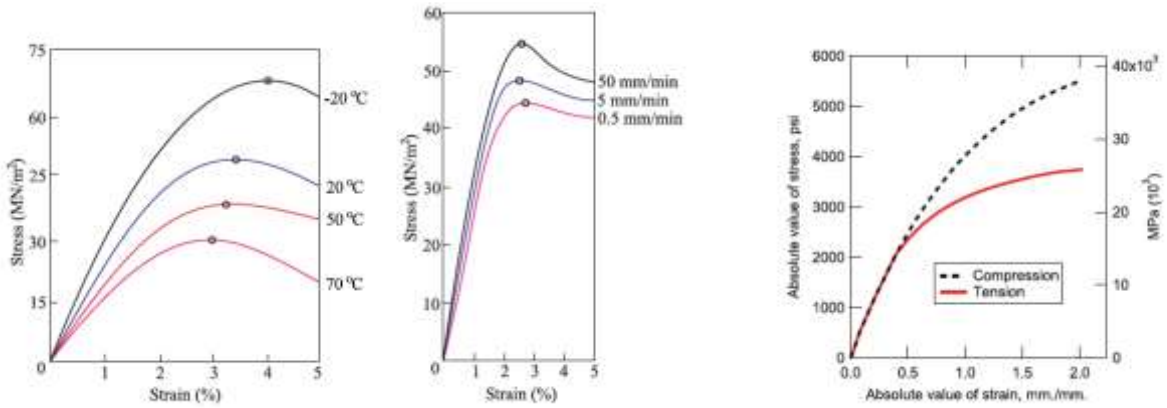

(a) (b)

Figure 13 (a) An example of temperature effect (left) and strain rate (right) on the stress-strain response of a typical polymer (Brinson and Brinson, 2008 [29]), and (b) Unilateral response of polypropylene (Rybicky and Kanninen, 1973) [27]

2.1.2 Viscoelastic Properties of Polymers

Viscoelasticity refers to nature of a material that behaves both elastic and viscous when subjected to a deformation state. Elastic behavior is defined as the ability to resist deformation without energy dissipation such that the original shape is recoverable upon load relief. On the other hand, viscous behavior is best described as the ability to resist flow, Newtonian or non-Newtonian fluids are known to exhibit viscous behavior. Polymers are materials that behave both in an elastic

and viscous manner. Furthermore, viscoelastic materials exhibit time-dependent behavior and in polymers it is caused by its unique molecular structure. Other materials, such as metals, also behave in a time-dependent manner depending on environmental factors (e.g., moisture, temperature etc.); however, the nano-scale mechanisms that trigger time-dependent behavior in metals and polymers are not the same. Therefore, the methodologies used for characterizing time-dependent behavior in metals do not generally apply to polymers.

Relaxation and creep tests are the two fundamental methods used for characterizing the viscoelastic behavior of polymers. Viscoelastic materials increase their deformation with time under a constant stress state whereas the stresses decrease with time under a constant strain input. A relaxation test places a viscoelastic material under a constant uniaxial strain, ε_0, that is applied in a quasi-static fashion. It is also assumed the viscoelastic material does not have a previous stress or strain history, or has at least been relieved through some form of annealing. Under this condition, the stress output, $\sigma(t)$, is depicted in Figure 14a on the right-hand side. From such observations, it becomes evident that the modulus $E(t)$, also referred to as relaxation modulus, is time dependent as shown in Eq. (4) below. By the same token, a uniaxial quasi-statically applied constant stress, σ_0, produces the time varying strain, $\varepsilon(t)$, illustrated in Figure 14b, this is known as the creep test with $D(t)$ denoting the creep compliance. Thermoset and semi-crystalline polymers are known to have equilibrated properties; for example, the stress relaxation test will decay toward a non-zero constant value and the creep test will plateau to an equilibrated strain value. These equilibrated values are related to equilibrated modulus or compliance. Amorphous thermoplastics do not behave the same way in the long-term, and its relaxation modulus inevitably decays to null while its creep compliance perpetually increases. The viscoelastic properties of EDAM short fiber composites are examined via relaxation experiments; hence, the relaxation modulus is recorded as a function of time at any given temperature.

$$E(t) = \sigma(t)/\varepsilon_0, \qquad D(t) = \varepsilon(t)/\sigma_0 \tag{4}$$

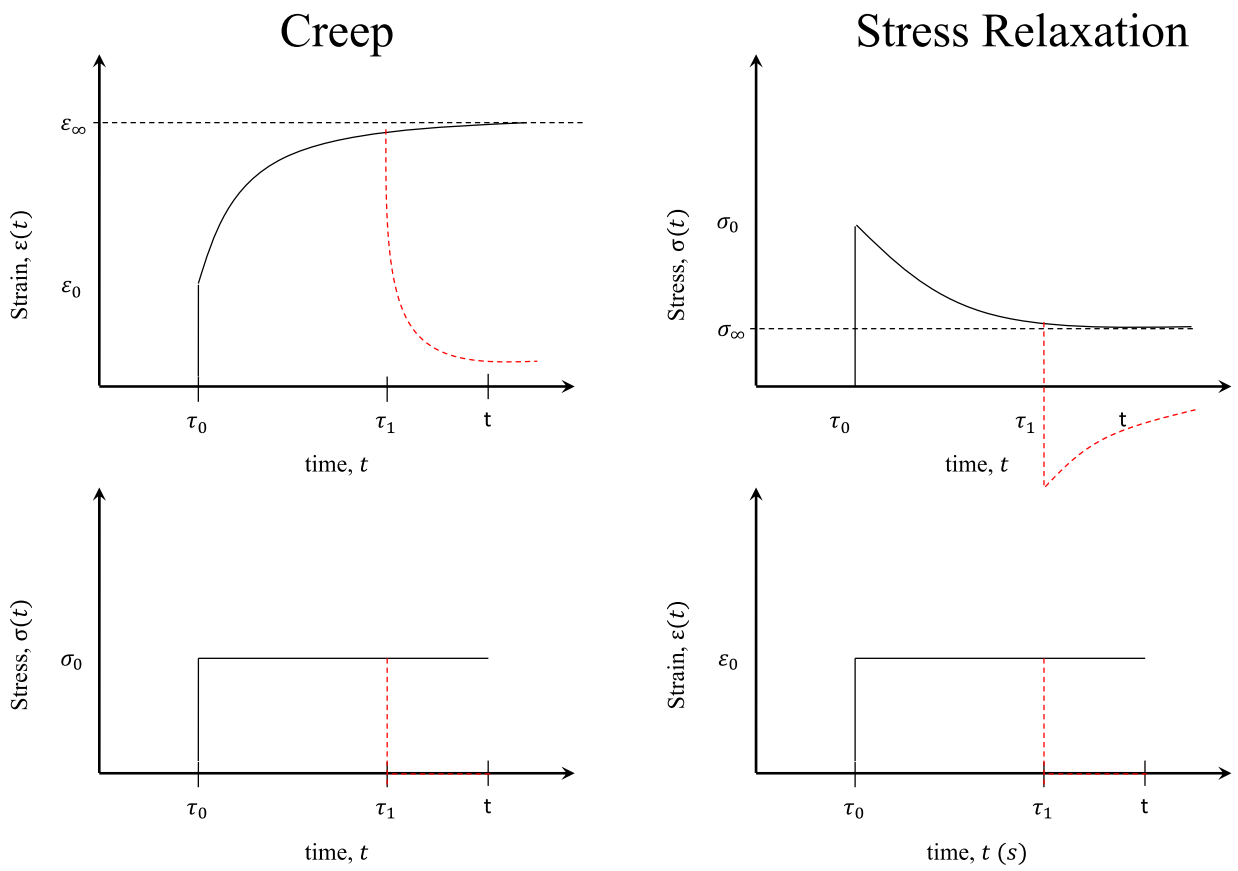

Figure 14 Creep test with stress input function (left), and stress relaxation test with strain input function (right) [30]

Isochronous modulus versus temperature plots can be extracted from relaxation tests. These plots offer the perspective of understanding the polymer phases at different temperatures, specifically, the modulus trend with temperature provides insight into glassy, transitioning, rubbery and/or flow phases. From the relaxation experiment, the stress value taken at 10 seconds or any other suitable time is divided by the applied strain for each temperature run, then the modulus is plotted as a function of temperature. Isochronous plots are also useful for determining if the mechanical response of the polymer is linear or nonlinear. The requirement of linearity restricts the modulus response to be independent of strain, the same independent requirement holds for the compliance and stress. To test for linearity using the relaxation test, three experiments are conducted at constant temperature. Each test is performed at different strain levels well within the linear elastic regime so as to not induce nonlinear response as a result of damage or plasticity. For each experiment, the stress is taken at three stress values are taken at times, t_1, t_2, and t_3. Then,

each stress value that corresponds for example to t_1 is plotted with respect to the corresponding strain input. If the stress-strain points follow a linear trend, then the material is said to be linear viscoelastic; however, this does not prove or justify neglecting aging or that the viscoelastic material is time-translational invariant. Linear viscoelastic tests based on isochronous plots determine if relaxation modulus or creep compliance is solely a function of time and not dependent on strain or stress level, respectively.

2.1.3 Rheological Elements and Models

Rheological elements and models are useful for describing viscoelastic material behavior based on the observed response, rheological models are phenomenological approaches aimed at describing time-dependent phenomena. Two of the common elements used for deriving rheological models are the helicoidal spring and dashpot. The spring is assumed to be perfectly linear elastic and massless whereas the dashpot is an ideal viscous element, their mathematical representations are shown in Eq. (5) where E represents the linear elastic stiffness and η the viscosity coefficient. The aforementioned elements are not exhaustive, and many types of rheological models can be developed based on numerous combinations of rheological elements. The two well-known rheological models are the Maxwell model and the Kelvin model, in the context of amorphous thermoplastics, the Maxwell model is briefly discussed; however, the reader is referred to Brinson and Brinson [29] and Marques and Creus [31] for a review of these models.

The Maxwell model combines a spring and dashpot element in series as shown in Figure 15. When a deformation is applied to the series model, the forces must be equivalent for each element; however, the strains are additive. With this in mind, the differential equation in Eq. (6) can be formed and solved for to obtain the temporal stress function. For stress relaxation problems, a unit step in strain, $\varepsilon(t) = \varepsilon_0 H(t)$, is imposed on the system, with $H(t)$ denoting the Heaviside function. The differential equation, Eq. (6), is solved by taking the Laplace transform of both sides and solving for $\mathcal{L}^{-1}\{\mathcal{L}\{\sigma(t)\}\}$; also, keeping in mind the definition of the Dirac delta function, $\delta(t) = dH/dt$, one can arrive at Eq. (7) where $\tau = \eta/E$. The time-varying modulus, defined in Eq. (8), resembles the modulus behavior of amorphous thermoplastics such that at time $t_0 = 0$, the instantaneous modulus is $E(t_0) = E$ then decays to null at $t = \infty$. The relaxation time, τ, is the time required for the modulus to decay by $1/e$.

$$\sigma(t) = E\varepsilon(t) \text{ (Spring model/Hooke's model)}$$
$$\dot{\varepsilon}(t) = \sigma(t)/\eta \text{ (Dashpot model/Newton equation)} \quad (5)$$

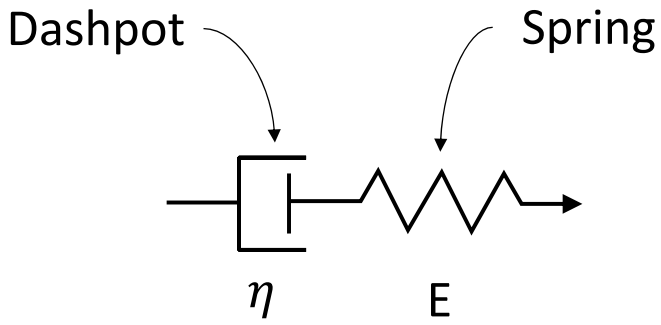

Figure 15 Maxwell rheological model

$$\dot{\sigma} + \frac{E}{\eta}\sigma = \dot{\varepsilon} \quad (6)$$

$$\sigma(t) = \varepsilon_0 E e^{-t/\tau} \quad (7)$$

$$E(t) = E e^{-t/\tau} \quad (8)$$

While the Maxwell model is useful for conceptually understanding viscoelastic behavior, it is generally not pragmatic for representing real viscoelastic materials. Nevertheless, it serves as the fundamental building block for development of generalized models that are more appropriate for modeling viscoelastic behavior. The generalized Maxwell model is developed by considering M^{th} Maxwell systems (i.e., spring-dashpot in series) in parallel, then solving each individual differential equations and using superposition will produce the series model shown in Eq. (9) for the stress relaxation strain input condition [32]. The summation in Eq. (10) is deemed the relaxation modulus, this is also known as the Prony series. Brinson and Brinson [32] note that the Prony series is not referenced to a mechanical model and it is also used for describing the relaxation stiffness of a viscoelastic material. It is noteworthy to mention that such an exponential series can be obtained through from thermodynamic derivation. Similar to the single Maxwell system, the time-dependent modulus in the Prony series approaches zero for an infinite time. For solids that possess an equilibrated modulus, E^e, at $t = \infty$, an additional spring element in parallel can be

added to the generalized Maxwell model; consequently, this addition produces the relaxation modulus shown in Eq. (11). Even though ideal amorphous thermoplastics are best characterized by Eq. (10), a low equilibrated modulus value can be included to alleviate potential numerical issues in computational analysis. The relaxation modulus model in Eq. (11) has been used for EDAM process and performance simulations in the work of Brenken [14].

$$\sigma(t) = \varepsilon_0 \sum_{m=1}^{M} E_m e^{-t/\tau_m} \tag{9}$$

$$E(t) = \sum_{m=1}^{M} E_m e^{-t/\tau_m} \tag{10}$$

$$E(t) = E^e + \sum_{m=1}^{M} E_m e^{-t/\tau_m} \tag{11}$$

The output of stress or strain for viscoelastic solids can be obtained by solving the general differential equations if the input function is specified, such an approach is difficult to implement in computational frameworks. The Boltzmann superposition principle if often used for three-dimensional stress analysis problems that involve strain or stress temporal input functions, it is an integral expression that is also recognized as Duhamel's integral. Integral expressions are appealing for numerical analysis as opposed to differentiation, derivatives are the limits of the difference quotient, by which you may have a large quantity divided by a small quantity which can cause numerical instability. The Boltzmann superposition principle assumes the strain response is superposable, this means that an arbitrary stain input, shown in Figure 16, can be specified as step-wise strain defined in Eq. (12). Since the stress relaxation response for any step in strain may be defined as $\sigma(t) = \varepsilon_n E(t - t_n)H(t - t_n)$, it follows that the stress response is then defined by the summation shown in Eq. (13). Duhamel's integral is obtained by multiplying and dividing Eq. (13) by the time increment, $\Delta\tau$, and taking the limit as the time increment approaches zero as shown in Eq. (14). Duhamel's integral shown in Eq. (15) is also referred to as the hereditary integral or the Boltzmann superposition integral. Lastly, the integral is only applied

to linear viscoelastic materials because of the superposition and proportionality assumptions, where proportionality is deduced from isochronous stress-strain behavior tests.

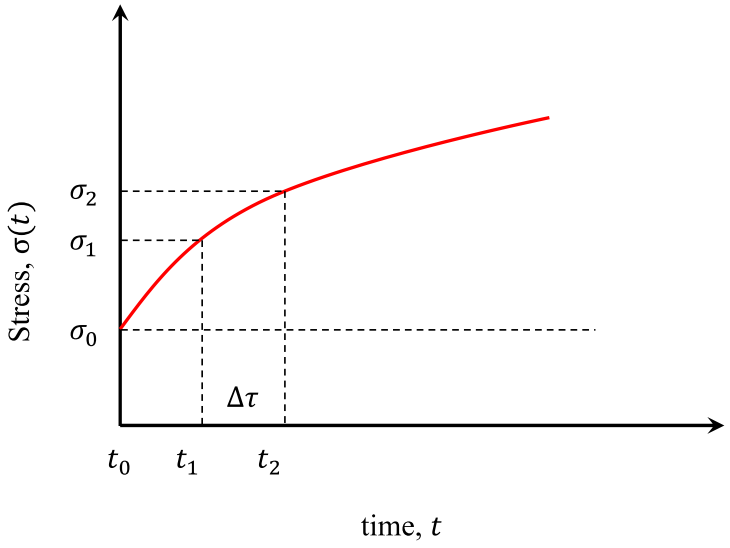

Figure 16 Arbitrary strain input modified from [30]

$$\varepsilon(t) = \varepsilon_0 H(t) + (\varepsilon_1 - \varepsilon_0)H(t - t_1) + \cdots + (\varepsilon_n - \varepsilon_{n-1})H(t - t_n) \tag{12}$$

$$\sigma(t) = \varepsilon_0 E(t)H(t) + (\varepsilon_1 - \varepsilon_0)E(t - t_1)H(t - t_1) + \cdots + (\varepsilon_n - \varepsilon_{n-1})E(t - t_{n-1})H(t - t_{n-1}) \tag{13}$$

$$\sigma(t) = \varepsilon_0 E(t)H(t) + \lim_{\substack{n\to\infty \\ \Delta\tau\to 0}} \sum \frac{(\varepsilon_n - \varepsilon_{n-1})}{\Delta\tau} E(t - t_n)H(t - t_n)\Delta\tau \tag{14}$$

$$\sigma(t) = \int_0^t E(t - \tau)\frac{d\varepsilon(\tau)}{d\tau} d\tau \tag{15}$$

The hereditary integral above is derived considering isothermal conditions. However, Non-isothermal conditions are often encountered in applications of viscoelastic materials, this is the case for extruded viscoelastic materials in the EDAM process. Moreover, viscoelastic materials have temperature-dependent constitutive relations, it must be included for transient thermal problems. When the effect of temperature is accounted for in viscoelastic models, the model is denoted as thermoviscoelastic. Therefore, to properly account for thermal effects, the hereditary

integral must be changed or modified to account for the temperature variable. For thermoviscoelastic models, temperature is assumed to affect time and time is substituted with an expression that relates to temperature. The reasoning for this assumption has been subject to experimental and theoretical investigation for decades [33]. Thermoviscoelastic models use the hereditary integral in the form shown below in Eq. (16) where ξ denotes a reduced time which depends of temperature, T, and time t.

$$\sigma(t,T) = \int_0^t E(t-\tau,T)\frac{d\varepsilon(\tau)}{d\tau}d\tau$$
$$\sigma(\xi) = \int_0^t E(\xi-\xi')\frac{d\varepsilon(\tau)}{d\tau}d\tau \tag{16}$$

The physical significance of the variable ξ is related to the mechanics of polymeric chains and their relaxation mechanisms; however, its mathematical definition, provided in Eq. (17), is based on phenomenological behavior at the macroscale which reasonably represents this phenomena. According to Klompen and Govaert [34], time-dependent behavior of thermoviscoelastic materials is caused by molecular transitions and changes in temperature appear to accelerate or decelerate molecular transitions which affects relaxation time. Assumptions made on relaxation time are classified as either thermorheologically simple or complex. The former assumes the material exhibits only one active molecular transition which means that all relaxation times are affected by temperature in the same way; on the other hand, thermorheologically complex refers to multiple relaxation mechanisms that lead to multiple relaxation times [33]–[35]. The thermorheologically simple assumption implies time-temperature superposition principle (TTSP) is valid; practically, this means that the log-log plot of relaxation modulus versus time (i.e., in relaxation tests) can be superposed by vertically and/or horizontally shifting each individual short-term isothermal curve to generate a continuous master curve at the chosen reference temperature. For a short introduction to the history and development of time-temperature superposition for polymers, the reader is referred to the Brinson and Brinson [33] section on the kinetic theory of polymers. Horizontal shifts are those along the time axis, shown in Figure 17, and vertical shifts are along the modulus or compliance axis. The notation used for horizontal shifting is a_T, and b_T for vertical shifting. The horizontal shift factors can be calculated, usually in the melt stage, if knowledge of viscosity as a function of temperature is known [36], and if the

vertical shifted factor is assumed negligible (i.e., $b_T = 1$) then the relation $a_T = \eta_0(T)/\eta_0(T_{ref})$ can be used where η_0 represents the viscosity, T is the temperature and T_{ref} is the reference temperature. Despite this definition which is related to polymer mechanics, thermoviscoelastic characterization of thermoplastic composite, from the glassy state to the rubbery state, often entails empirical shifting isothermal curves to produce a master curve. The empirical shifting process can be done through optimization routines that attempts to find the optimal shift factor that produces the best overlap between the isothermal curves [37]. For example, Ropers et al. [38] characterized the thermoviscoelastic properties of a thermoplastic composite by empirically shifting the dynamic moduli along the time axis to achieve a continuous master curve. Horizontal shift factors are often described by an empirical equation that is a function of temperature, the function is obtained by plotting a_T against temperature and fitting its trend using the Arrhenius equation, William-Landel-Ferry (WLF) equation, and/or a modified WLF equation [39], these equations are provided in Eq. (18). The equations can be defined in a continuous or piece-wise way. It is noteworthy to mention that the WLF equation is valid for temperatures above the glass transition temperature [33]; however, it can be used for temperatures below T_g if the error between data and WLF trend is not significant. Although, it may be more appropriate to use either an Arrhenius relation or modified WLF equation for predicting the shift factor trend below the glass transition. When vertical shift factors are assumed negligible, the horizontal shift factor is then what defines the acceleration or deceleration of relaxation; hence, it defines the value of the reduced time variable ξ in the thermoviscoelastic model.

$$\xi(t) = \int_0^t \frac{d\tau}{a_T(T(\tau))} \tag{17}$$

$$\begin{aligned} \log_{10} a_T &= \frac{E_a}{2.303R}\left(\frac{1}{T} - \frac{1}{T_{ref}}\right) \text{ (Arrhenius equation)} \\ \log_{10} a_T &= \frac{-C_1(T-T_{ref})}{C_2+(T-T_{ref})} \text{ (WLF equation)} \\ \log_{10} a_T &= \frac{-C_1\left(T-T_{ref}\right)^c}{C_2+\left(T-T_{ref}\right)^c} \text{ (Modified WLF)} \end{aligned} \tag{18}$$

Significant errors may develop if vertical shifting is not accounted for during development of the master curve [33]. One way to account for vertical shifting is to use the Bueche-Rouse

theories [40], [41] that define the vertical shift factor as $b_T = T_{ref}\rho_{ref}/T\rho$, where ρ is the density. Depending on the polymer system, modified theories can be used [36], [42]. In practice, thermoviscoelastic characterization of thermoplastic composites may yield discrepancies between instantaneous modulus measured from a dynamic mechanical analyzer (DMA) and the Young's modulus measured via mechanical testing systems at the same temperatures, Hobbiebrunken et al. [43] and Deng et al. [44] both have observed and reported such discrepancy and accounted for it by shifting the moduli versus temperature curve obtained from DMA based on mechanical test data. Although this type of vertical shifting is reasonable under the assumption that factors such as the type of DMA machine, clamps and/or test parameters only affect the magnitudes of elastic modulus and not the temperature dependency, it requires further investigation to assess the validity of such shifting [44].

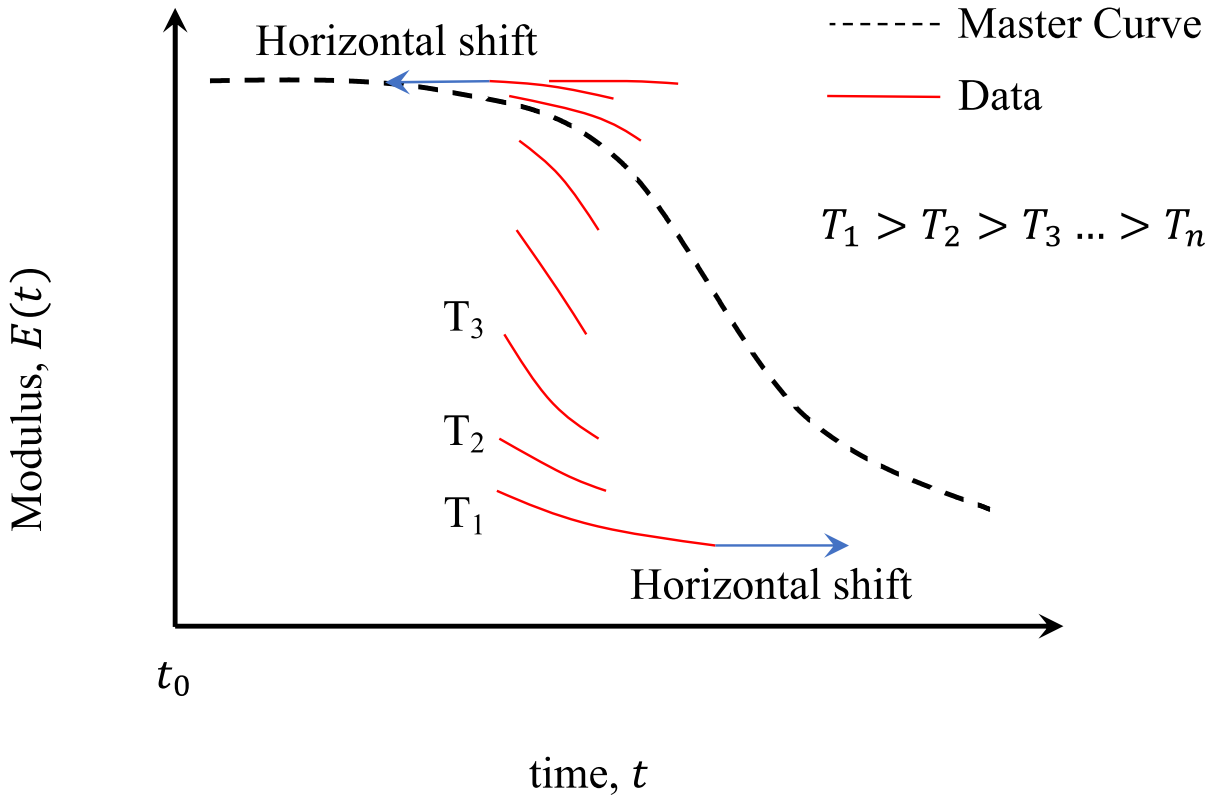

Figure 17 Horizontal shifting for thermorheologically simple material under time-temperature superposition principle (TTSP)

2.2 Damage and Failure in Heterogenous Short Fiber Composites

In general, 3D printed short fiber composites are anisotropic materials; however, we can approximate the material behavior as orthotropic which is defined as having three planes of symmetry. An orthotropic approximation implies the composite material is characterized by nine elastic properties. For 3D printed composites, these orthogonal planes of symmetry are the 1, 2, and 3 planes; moreover, these correspond to the print, in-plane transverse to the print, and stacking directions, respectively. Here, the 1, 2, and 3 directions are the material coordinate directions which is sometimes interchanged with the principal directions not to be confused with the eigenvectors obtained from the eigenvalue analysis of the stress or strain tensor. The different mechanical properties for 3D printed composites along these directions have been reported by Duty et al. [45] a z-tamped 13% wt. carbon fiber reinforced acrylonitrile butadiene styrene. The tensile strength and stiffness values along the print direction are greater than the tensile strength and stiffness along transverse directions. The reason for the anisotropic behavior is due to the microstructural morphology; for example, Tekinalp et al. [46] experimentally observed most of the fibers collimated along the print direction. Additionally, scanning electron microscopy (SEM) images of the tensile fracture surface along the print direction illustrated fibers sticking out from the fractured matrix surface and regions from which fibers were pulled out.

The print direction tends to exhibit mostly fiber pull-out, fiber/matrix interfacial debonding, and matrix cracking. The transverse directions tend to be dominated by matrix damage mechanisms such as matrix micro-cracks. In a relevant study on the effect of fiber direction and temperature on the tensile properties of short fiber reinforced polyphenylene sulfide, Takahashi et al. [47] observed different fracture modes for tensile coupons loaded along the 0° direction and 90° direction using SEM.

Short fiber composites manufactured using other fabrication processes such as injection molding can provide insights into the types of damage mechanisms that may occur in 3D printed composites as a result of its microstructural morphology. The micro-structural characteristics, such as the distributions of fiber volume fraction, fiber length, fiber orientation, void volume fraction, void size and shape, determine the elastic, strength and failure properties of the composite. These microstructural features influence the initiation and evolution of microscopic damage. Based on the observations made by several authors [48]–[57], fiber breakage, fiber/matrix interface debonding, and matrix micro-cracking are the micro-damage mechanisms responsible for the

failure process in these composites. Although fiber fracture is a contributing damage mechanism along directions with high fiber collimation, it can depend on the fiber critical length [58] and may not be the dominant mechanism in composites with significantly short fibers [50], [52], [59], [60]. Huang and Talreja described the general progressive damage process in four stages which are (i) the matrix debonds from the fiber ends early in the loading stage, (ii) matrix cracking and fiber/matrix interface debonding induced from stress concentrations at the debonded fiber end site, (iii) coalescence of matrix micro-cracks to form a macroscopic crack, and (vi) unstable propagation of macroscopic crack that leads to failure. The decohesion described in stages 1 and 2 relating to debonding of the fiber ends and fiber/matrix interface failure was originally categorized by Nath et al. [61] into three modes which was further explained by Sirivedin et al. [62], these modes are summarized below.

1. Mode α (penny-shaped crack) – Localized matrix yielding at the intact interface in the vicinity of the stress concentration associated with the fiber end. Penny-shaped interface cracks are said to form from this mode.
2. Mode β (cylindrical crack) – As a result of weak fiber/matrix interface, a cylindrical interface crack (i.e., this may be envisioned as a crack in the shape of a sleeve) initiates at the fiber end and propagates along the interface. The cylindrical interface crack evolves from the penny-shaped crack that initiated at the fiber end; moreover, this crack remains closed as tensile loading progresses such that frictional stress transfer between the fiber and matrix may take place across the crack faces.
3. Mode γ (conical crack) – When the fiber/matrix interface is strong, a conical crack forms from the debonded fiber end at an angle θ_c relative to the fiber axis. A conical crack can open as load progressive resulting in traction free surfaces. Like the cylindrical crack, the conical crack evolves from the penny-shaped crack.

2.3 Computational Progressive Damage and Failure Analysis

2.3.1 Continuum Damage Mechanics and Discrete Damage Mechanics

Many approaches exist for modeling the progression of damage in a material system within a computational framework, a taxonomy of the various computational approaches is provided by Forghani et al. [63] as shown in Figure 18. While each approach is capable of modeling progressive

damage and deterioration of the material system, each approach is based on different sets of assumptions. The main difference between the holistic approaches; namely, continuum and discrete damage approaches is in the representation of the displacement discontinuity as noted by Rose, Dávila, and Leone [64]. In continuum models, the displacement discontinuity is represented with local volumetric stiffness degradation variables which may be defined as a soft discontinuity. On the other hand, models based upon the explicit kinematics of the displacement jump are denoted as a hard discontinuity. While some of the limitations of continuum models are its inability to capture the local effects of stress redistribution or capture the realistic crack pattern, it can capture the overall nonlinear response and it is generally computationally efficient for large-scale computational analysis. In this work, continuum models are of interest due to the computational efficiency it offers in the finite element method. Discrete damage models are usually implemented as cohesive element or cohesive surface models, discrete models often are used for capturing delamination behavior in composites. In 3D printed materials, delamination occurs at the bead-to-bead interfaces. Discrete models present implementation challenges in processing and performance simulations; therefore, continuum approaches exists as an approximate solution. It is noteworthy to mention, Yuan and Fish et al. [65] used continuum damage mechanics to model interfacial damage in laminates and they proved it may be a viable alternative to interfacial damage modeling.

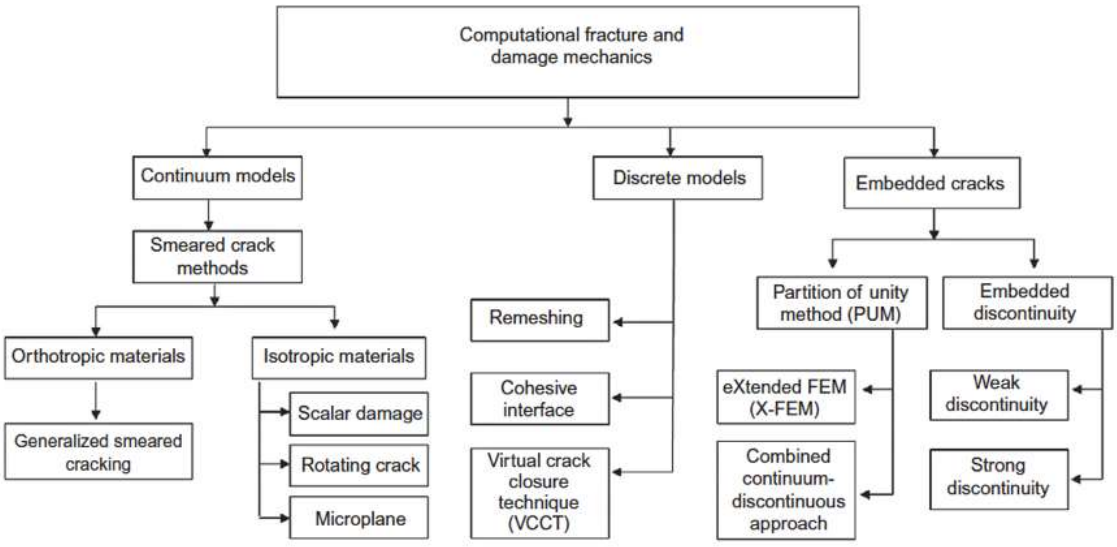

Figure 18 Classification of computational damage and fracture mechanics approaches [63]

Damage is defined as the progressive process and irreversible state by which materials lose their load-bearing abilities. Damage mechanics is the study of the mechanisms at play that lead to the deterioration of the material through irreversible nanoscopic or microscopic changes in the material state when subjected to loading, see Figure 19a. At the fine scale, stress concentrations stemming from impurities, imperfections, or heterogenous morphology are regions from which the local stress state is greater than the average stress state, these local concentrations act to prematurely break the bonds of either the homogenous material or heterogenous phases. The breakage of bonds leads to micro-cracks which then evolve and coalesce with neighboring cracks or voids as loading is progressed and eventually form into a macroscopic crack. The unstable propagation of the macroscopic crack is what leads to fracture or catastrophic failure. The tools developed for continuous media (i.e., continuum mechanics) at the mesoscale can be used to study and investigate damage mechanisms that exists at the microscopic level through means of a damage variable. Once a macroscopic crack has developed, continuum mechanics ceases to adequately represent the behavior of the media and the tools of fracture mechanics must then be employed to further investigate the crack propagation problem. Chaboche [66] provided a definition for the final state of continuous damage mechanics, he stated that "the final state corresponds generally to the macroscopic crack initiation, that is the presence of a material discontinuity, sufficiently large as to regards the microscopic heterogeneities (grains, subgrains…)," and provided a visual illustration of this conceptual definition shown in Figure 19b.

When continuum mechanics is used for studying damage mechanics, it is termed continuum damage mechanics. As mentioned by Lemaitre and Desmorat [67] and Jirásek [68], the phrase continuum damage mechanics was first introduced by Hult in 1972; however, the concept of a continuity field variable, ψ, related to damage had been introduced by Kachanov [69] in 1958 and it was applied to the creep rupture problem in metallic materials. Rabotnov [70] in 1969 extended this damage concept by introducing the effective stress concept. This concept was then extended in the 1970s by Hayhurst [71] and Leckie and Hayhurst [72] for multiaxial stress creep rupture problem in metals, Chaboche [73], [74] for high cycle fatigue and rate problems, Chrzanowski [75] for time-independent or time-dependent for creep-fatigue fracture, and Lemaitre and Chaboche [76] for the creep rupture problem. While these initial theories accounted for isotropic damage, anisotropic nature of damage could not be adequately represented. Vakulenko

and Kachanov [77] provided a more refined theory to take into account the anisotropic nature of damage by introducing a second-order damage tensor.

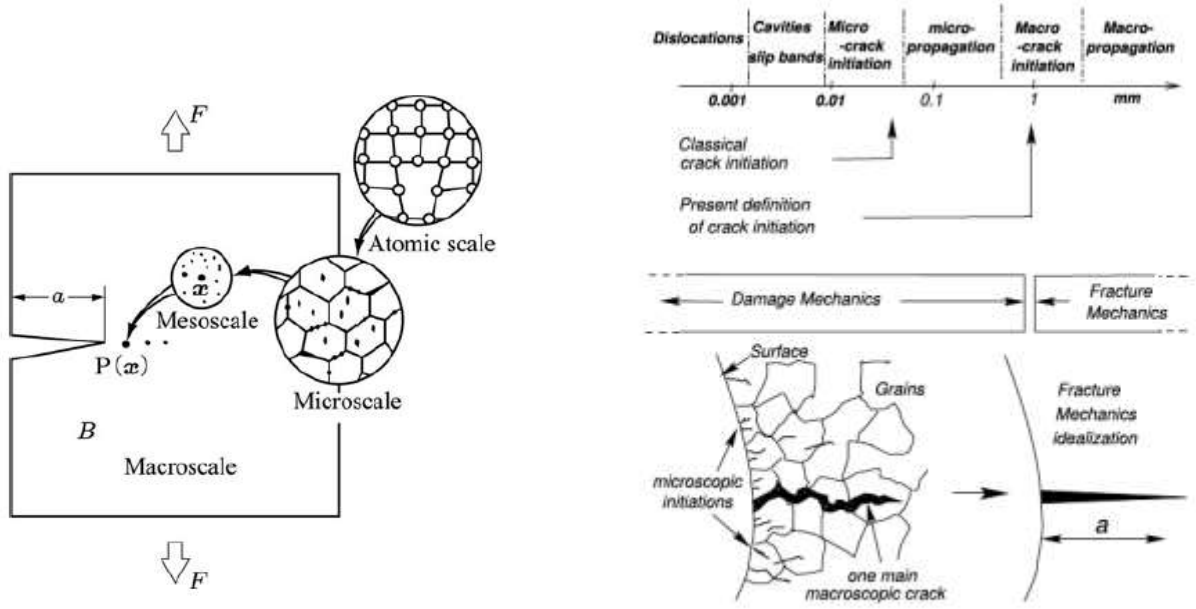

(a) (b)

Figure 19 (a) Different length scales of damage (Murakami, 2012 [78]), (b) Illustration of micro-macro damage initiation and mechanics domain (Chaboche, 1981 [66])

It was in the 1980s when continuum damage mechanics began to substantially grow with research ongoing in both the eastern and western hemispheres, it was around this decade that the theory was developed to include thermodynamic and micromechanic formalism by many researchers: Murakami and Ohno [79], Krajcinovic and Fonseka [80], Fonseka and Krajcinovic [81], Chaboche [66], [82], [83], Germain et al. [84], Murakami [85], Ladevèze [86], Lemaitre [87], Krajcinovic [88], Ortiz [89], Talreja [90], Mazars [91], Chow and Wang [92], Simo and Ju [93], Chow and Lu [94], and Ju [95]. Anisotropic damage theories were further extended with damage being represented in vectorial form [80], generalized fourth-order tensor [96]. Most of the anisotropic damage formulations were based on the equivalent strain concept [97] which has limitations on the transformation of the stress or strain tensor, Cordebois and Sidoroff [98] proposed the principle of energy equivalence to remedy the limitations of the equivalent strain principle. Hansen and Schreyer [99] provide a well written explanation of the differences between the equivalent strain and equivalent energy principles. From the 1990s and onward, a plethora of

literature and research on continuum damage mechanics can be found. Although not exhaustive, the anisotropic continuum damage mechanics formulations developed by of Zhu and Cescotto [100], Barbero [101]–[103], Lonetti and Barbero [104] were found useful for this work. For an in depth review on continuum damage mechanics, the motivated reader is recommended the following references [78], [105]–[109].

2.3.2 Local and Non-local Approach to Damage Analysis in Finite Element Method

In general, local approach to damage analysis involves the definition of discontinuous representation at the material point, this usually an integration point in finite element analysis. On the other hand, non-local approaches attempt to consider information about neighboring fields to evolve the localized discontinuity representation. Murakami [78] mentions that the local approach to damage analysis in the finite element method uses continuum damage mechanics to represent the damaged state of an element through degradation variables. The degradation variable represents the crack and its value ranges between zero and one, this variable characterizes the integrity of an element with a value of zero denoting full load-bearing capacity and a value of one signifying complete failure. Consequently, this approach produces material softening by degrading the element stiffness matrix which may cause the loss of uniqueness and cause numerical instability. The non-uniqueness of the solution causes instability and mesh-dependent results. The causes of mesh-sensitivity can be classified as (i) strain softening induced non-uniqueness and strain localization, (ii) damage localization, and (iii) stress singularity at the crack tip [78]. Strain softening leads to the onset of material instability which induces the loss of positive-definiteness of the tangent stiffness matrix at the material point; consequently, this leads to the loss of the ellipticity in the linear momentum balance partial differential equations (i.e., equilibrium equations). The material instability induced by strain softening causes bifurcation of deformation, this engenders an intense localization band of almost equal width to the mesh size. The bifurcation point in nonlinear uniaxial tensile analysis of brittle materials occurs at the peak stress, beyond this point, damage begins to localize. Bažant and Oh 1983 [110], Bažant 1990 [111] proposed a crack band model that imposes a lower bound on the size of the finite element meshes, this has been one popular approach to remedy the localization problem due to its ease in implementation in finite element analysis. Bilby et al. [112] proposed the cell method, this method allows mesh refinement within a cell; however, inner cell mechanical behavior is influenced by the cell-

averaged properties. Besides the crack band or cell methods, the method of mesh-dependent softening modulus also exists. Pietruszczak and Mroz [113] prescribed a shear band of a specified width in a finite element and derived a stiffness matrix that includes localized shear band deformation at some angle with respect to a horizontal axis. By the same token, Simo 1989 [114] included the micro-crack energy release into the internal dissipation of a finite element, and defined a modified strain-softening modulus dependent on mesh size and dissipated energy. Even though the mesh-dependent modulus approach can avert the localization intensity problem, it may provide unrealistic results and local states are still mesh-dependent.

Nonlocal damage theories can be categorized into four methods which are (i) method of nonlocal variable, (ii) gradient-dependent method (iii) the Cosserat continuum method, and (vi) the artificial viscosity method. The nonlocal variable method imposes that the evolution of damage at a material point is governed not only by the local state variable but also the neighboring fields. One issue with this approach is the integro-differential relation that arises in the consistency equations [115], this nonlocal approach does not lead to a simple algebraic expression in the implementation of a return-mapping algorithm. In the nonlocal approach, the damage variable takes the nonlocal form shown in Eq. (19), $\boldsymbol{V}_r(\boldsymbol{x})$ is the region of the body, Eq. (20), and $h(\boldsymbol{s}-\boldsymbol{x})$ denotes a nonlocal weighting function that monotonously decays with the distance $|\boldsymbol{s}-\boldsymbol{x}|$ and can be defined as shown in Eq. (21). It is noteworthy to mention that Pijaudier-Cabot and Bažant [116] and Bažant and Pijaudier-Cabot [117] made note that only the strain-softening variables are sufficient for specifying nonlocal behavior instead of all of the state variables involved in the finite element analysis. Moreover, the thermodynamic force, Eq. (22), conjugate to damage can also be defined nonlocally as well as the damage rate, Eq. (23) [117], [118].

$$\bar{\boldsymbol{D}}(\boldsymbol{x}) = \frac{1}{\boldsymbol{V}_r(\boldsymbol{x})}\int_V h(\boldsymbol{s}-\boldsymbol{x})\boldsymbol{D}(\boldsymbol{s})d\boldsymbol{V}(\boldsymbol{s}) \tag{19}$$

$$\boldsymbol{V}_r(\boldsymbol{x}) = \int_V h(\boldsymbol{s}-\boldsymbol{x})d\boldsymbol{V}(\boldsymbol{s}) \tag{20}$$

$$h(\boldsymbol{x}) = e^{-\frac{|\boldsymbol{x}|^2}{2l^2}} \tag{21}$$

$$\bar{\boldsymbol{Y}}(\boldsymbol{x}) = \frac{1}{\boldsymbol{V}_r(\boldsymbol{x})}\int_V h(\boldsymbol{s}-\boldsymbol{x})\boldsymbol{Y}(\boldsymbol{s})d\boldsymbol{V}(\boldsymbol{s}) \tag{22}$$

$$\bar{\dot{\boldsymbol{D}}}(\boldsymbol{x}) = \frac{1}{\boldsymbol{V}_r(\boldsymbol{x})}\int_V h(\boldsymbol{s}-\boldsymbol{x})\dot{\boldsymbol{D}}(\boldsymbol{s})d\boldsymbol{V}(\boldsymbol{s}) \tag{23}$$

The gradient-dependent method replaces the local variable, defined using the nonlocal approach, by the gradient-dependent variable $\bar{\boldsymbol{D}}(\boldsymbol{x}) = \boldsymbol{D}(\boldsymbol{x}) + c_1\nabla\boldsymbol{D}(\boldsymbol{x}) + c_2\nabla^2\boldsymbol{D}(\boldsymbol{x}) + \cdots$, where ∇ is the differential operator. The nonlocal gradient-dependent damage variable can be obtained as shown in Eq. (24) [78]. An example and application of gradient-dependent nonlocal approach applied to finite element method in Abaqus/Standard is given Abu Al-Rub, Darabi, and Masad [119]. Cosserat continuum approach requires additional static and kinematic quantities in the form of couple-stresses and micro-curvatures which includes a characteristic length scale, application of this approach, in commercial finite element software like Abaqus/Standard, requires coding the mathematical formulism into a user-defined element (UEL) subroutine. The artificial viscosity method introduces rate dependent terms into the constitutive relations to prevent loss of ellipticity in boundary-value problems, this approach is also referred to as viscous regularization. There are different methods of implementing an artificial viscosity scheme; for instance, Simo and Ju [120], [121] defined the viscous regularization of their proposed rate-independent strain-based model by introducing a damage fluidity coefficient, μ, into the damage evolution law. In a different approach, the Duvaut-Lions viscosity model [122] is modified to introduce an artificial viscous term into the damage rate variable, Maimí et al. [123] and Rose et al. [64] both use this approach to define the damage rate, $\dot{d}^v$, in terms of an artificial viscosity, ρ, stabilized damage variable, d^v, and the damage variable, d, as shown in Eq. (25). In numerical form, the updated stabilized damage variable can be defined as shown in Eq. (26) after algebraic manipulation of Eq. (25). While its ease of implementation is an advantage, care must be taken in choosing an appropriate viscosity.

$$\bar{\boldsymbol{D}}(\boldsymbol{x}) = \boldsymbol{D}(\boldsymbol{x}) + \frac{1}{2}l^2\nabla^2\boldsymbol{D}(\boldsymbol{x}) \tag{24}$$

$$\dot{d}^v = \frac{1}{\rho}(d - d^v) \tag{25}$$

$$d^v|_{t+\Delta t} = \frac{\Delta t}{\rho + \Delta t} d|_{t+\Delta t} + \frac{\rho}{\rho + \Delta t} d^v|_t \quad (26)$$

2.3.3 Multiscale, Micromechanical, and Phenomenological Modeling

Multiscale modeling, in the context of composites, is an attempt to predict material behavior at an arbitrary length or time scale based on information obtained at another length or time scale. Sullivan and Arnold [124] categorized multiscale modeling into three techniques, these are the (i) hierarchical or sequential technique, (ii) concurrent technique, and (iii) synergistic technique. Aboudi, Arnold and Bednarcyk [125] explain the techniques which are briefly summarized as follows:

- **Hierarchical/sequential technique**: Involves unilateral information passing between length scales in an either top-down or bottom-up fashion; for example, information about constitutive behavior at the micro-scale is passed to the macro-scale (i.e., at least two orders of magnitude greater than the micro-scale) in the bottom-up approach.
- **Concurrent technique**: this is a fully coupled method by which the length and time scales are considered at once and the models at different scales are solved are simultaneously solved.
- **Synergistic technique**: involves bilateral information passing between length and time scales. This approach is a hybrid between hierarchical and concurrent techniques, it handles field quantities either "*spatially sequentially and temporally concurrent or spatially concurrent and temporally sequentially"*

Micromechanics modeling is an approach that aims to capture micro-structural morphology to predict the effective mechanical or thermo-mechanical performance of a composite material. In short fiber composites, the micro-structural morphology plays an imperative role in stress transfer between fibers and matrix, this in turn governs the effective properties and ultimate load carrying characteristic of a composite. Analytical approaches which are based on evaluating the effective elastic properties of a unidirectional short fiber composite are the well-known Voigt and Reuss approximations, shear lag model, Eshelby inclusion approximation, self-consistent scheme, Mori-Tanaka scheme, and Halpin-Tsai model. Micromechanical analysis can be categorized into three main approaches; namely, the (i) modified rule of mixtures (ROM) approach, (ii) laminate analogy approach, and (iii) direct numerical analysis of an representative

volume element (RVE) of the composite micro-structure. The shear lag theory initially developed by Cox [126] and modified by Krenchel [127] captures the effective stiffness and strength of a composite by incorporating fiber length, and fiber orientation efficiency factors into the ROM equation. The Kelly and Tyson [58] model is another modified ROM approach which accounts for short fiber length distribution in an a composite with all fibers aligned in the loading direction. Halpin and Pagano [128], developed the laminate analogy approach which models a random or nearly random short fiber composite as a pseudo-laminate to predict the elastic properties of the composite. The pseudo-laminate model consists of unidirectional short fiber composites, with the fiber direction angle defined by the percentage of fibers at angle α in the composite material. The properties of unidirectional short fiber pseudo-lamina can be estimated using other theories [129], [130]. An example of application of laminate analogy is provided in the work of Fu and Lauke [131], the fiber orientation and length distribution is accounted for to estimate the composite modulus. The direct numerical approach is also referred to as RVE analysis and it is commonly performed using the finite element method. Unlike the analytical approaches, RVE analysis allows for an accurate representation of the microstructure by explicitly modeling the micro-phases and micro-morphology from which effective properties can be obtained using computational homogenization methods. Several authors [132]–[137] have used RVE analysis to predict progressive failure analysis in short fiber composite systems. When computational resources are available, RVE analysis offers high fidelity solutions to predict effective composite properties and micro-morphology induced progressive damage. Although computational RVE analysis is capable of modeling the heterogenous micro-morphology with relatively simple models (e.g., max stress criterion, traction-separation laws, etc.), the approach can become computationally taxing and often requires micro-constituent property inputs which are unavailable or difficult to experimentally characterize. For a review of multiscale and micromechanics, the following references are recommended [124], [138]–[142].

Phenomenological modeling is an approach that uses mathematical models designed to capture the experimentally-observed material behavior, this is sometimes referred to as the meso-scale approach. In this approach, the microstructural details or the heterogenous micro-phases that define the composite properties are replaced by an effective and fictitious homogenous equivalent; therefore, the heterogenous micro-fields induced by the microstructure is lost or perhaps smeared. As a result of this fact, the phenomenological approach requires sophisticated and complex

progressive damage models that is capable of capturing the anisotropic material behavior of the composite material. Evidently, the main advantage of the phenomenological approach is its computational efficiency relative to RVE analysis since the micro-phases are not explicitly modeled in realistic structural analyses. In EDAM process and performance analyses, computational efficiency is highly desirable, and implementation of phenomenological models is both feasible and viable.

3. THERMODYNAMIC-BASED THERMOVISCOELASTIC DAMAGE MECHANICS

3.1 Historical Background

Thermodynamic models are defined by the three laws of thermodynamics, these are formulations that describe the state of a system. The first law is essentially the conservation of energy principle and the second law establishes the concept of total, production and transfer of entropy which fundamentally governs the direction of spontaneous processes. Thermoviscoelastic damage models are described by internal state variables that define the energy function in a thermodynamically consistent way; moreover, the mathematical representations of the energy function or thermodynamic potentials are phenomenologically derived. Thermodynamic consistency is obtained by satisfying the Clausius-Duhem inequality, this inequality is an entropy expression derived from the first and second laws of thermodynamics. Furthermore, the inequality not only governs the thermodynamically allowable constitutive states, it also describes the nature of internal state variable evolution. It is noteworthy to mention, when internal state variables change, evolution equations are required, and dissipation potentials specified. Moreover, the inequality contains the products of generalized force vectors and their associated generalized flux vectors. The relation between the generalized force and flux vectors can be defined by the reciprocal relations developed by Onsager [143], [144] in 1931, it is a phenomenological relation that states the proportional matrix between the generalized force and flux vectors is both symmetric and positive semi-definite. The solution obtained using the reciprocal relations allows for the straightforward definition of internal state variable evolution, which is valid for materials that exhibit microscopic reversibility.

The thermodynamic framework was initially applied to viscoelastic materials by Staverman and Schwarzl [145] and Staverman [146], then extended by Meixner [147] in 1953. The theory linear irreversible thermodynamic process was then further developed by Biot [148] in 1954 for isothermal viscoelastic solids in a generalized form, it was also shown that the generalized Maxwell model or Prony series also can represent the thermodynamic system. Moreover, in a series of subsequent publications, Biot demonstrated the utility of the thermodynamic formulation to present a unified treatment of thermoelastic damping, study behavior of porous media, and deduce variational principles [149]–[151]. Schapery [152] in 1963 modified the thermodynamic

viscoelastic theory developed by Biot [148] to include an explicit temperature dependence and a thermodynamically consistent inclusion of the time-temperature superposition principle for treating media with temperature-dependent viscosity coefficients. Furthermore, he continue to develop the work on deformation, damage, and fracture of linear and nonlinear viscoelastic solids for monolithic and composite materials [153]–[161]. Following the work of Biot [148] and Schapery [152], [153], Weitsman [162] introduced the internal state variable γ_r $(r = 1, \dots, N)$ which represents the internal degrees of freedom within a glassy polymer to study the viscoelastic hygrothermal phenomenon in composites. The physical significance of the internal degree of freedom, γ_r, is based on polymer mechanics, this may be understood from the work of Rouse [40] where he explains that "a velocity gradient in a solution of a linear polymer continuously alters the distribution of configurations of the polymer molecules." In other words, a velocity gradient or strain rate disturbs the distribution of configurations of the polymer molecules away from its equilibrium form, storing free energy in the system. The coordinated thermal motions of the segments cause the configurations to drift toward their equilibrium distribution. In other words, a strain rate causes the equilibrium distribution of polymer molecular configurations to change and thus energy is momentarily stored. However, the coordinated thermal motions of the polymer molecules cause the already established configuration to drift toward a new equilibrated configuration. By the same token, Lubliner [163] states the following:

> "it is known that linearly viscoelastic amorphous polymers are described by relaxation spectra which are very smooth—which, in other words, do not correspond to a formalism of discrete internal variables (generalized Maxwell or Kelvin models) unless these are taken to be infinite in number. Physically this makes sense, since the irreversible mechanisms in polymers consist of coiling, bending, etc., of long chain molecules, and the relaxation time of each mechanism depends on the length and orientation of the molecule; the lengths and orientations are, however, randomly distributed, and the number of molecules is enormous; hence the internal variables are, in effect, infinite in number with a statistical distribution of relaxation times."

Abdel-Tawab and Weitsman [164] further developed the thermodynamic approach for viscoelastic materials by including the continuum damage mechanics framework to model the behavior of swirl-mat composites. In later years, they extended the formulation and proposed a strain-based formulation which coupled viscoelastic and damage behavior for creep problems [165]. The thermodynamic and continuum damage mechanics frameworks applied to linear viscoelastic

composites by Abdel-Tawab and Weitsman serve as the groundwork for the development of the linear thermoviscoelastic damage model applied to 3D printed short fiber composite systems.

3.2 Model Development

In this section, the formulation is described in two sections; namely, the first defines the viscoelastic constitutive behavior at fixed damage states and the second defines damage evolution of internal state variables. Thermodynamic consistency is enforced by satisfying the Clausius-Duhem inequality; moreover, the constitutive behavior is derived from a necessary condition in the inequality. Furthermore, the inequality is obtained via manipulation of the first and second laws of thermodynamics in general form, shown in Eq. (27) and Eq. (28), respectively. The first law of thermodynamics relates infinitesimal internal energy changes with variations in process variables such as heat, Q, mechanical work, W, and any other work, W' (e.g., chemical work). For simplicity, the last term on the right side of Eq. (27) can be disregarded since heat and mechanical work dominate the internal energy state of the material system in consideration. The second law states that the total entropy change of a system, ΔS_{sys}, is equivalent to the sum of entropy changes produced within a system, ΔS_p, and entropy transferred, ΔS_t, across the boundary during a process. Entropy production terms are always positive according to the second law of thermodynamics. For example, damage events in the form of micro-fractures or production of micro-cavities which act to decrease the material stiffness, is an entropy production term. For an ideal system, the thermodynamics of reversible processes relate the change in heat, δQ_{rev}, divided by absolute temperature, T, with the change in entropy, dS, as shown in Eq. (29). For irreversible and reversible processes, the general form of the infinitesimal change in entropy, Eq. (30), is an inequality which is known as the Clausius inequality [166].

$$dU = \delta Q + \delta W + \delta W' \tag{27}$$

$$\begin{gathered} \Delta S_{sys} = \Delta S_t + \Delta S_p \\ \Delta S_p \geq 0 \end{gathered} \tag{28}$$

$$\delta Q_{rev} = TdS \tag{29}$$

$$dS \geq \frac{\delta Q}{T} \tag{30}$$

The infinitesimal change in work, shown in Eq. (31), is written in its generalized form and it includes the work done on a body by tractions and body forces. Traction is defined as usual, $\boldsymbol{t} = t_i = \sigma_{ij} n_j$, with n_j denoting the outward normal surface vector, $\dot{\boldsymbol{u}}^{\boldsymbol{d}}$ denotes the displacement rate vector, $\boldsymbol{b}$ is the body force vector, ρ is the density, and $\boldsymbol{\sigma}$ the Cauchy stress tensor. The bolded notation signifies it is a tensor and the single or double dot signifies tensors being contracted once or twice, respectively. The divergence theorem (i.e., Gauss' theorem) is applied to obtain a single volumetric integral. The integral can be re-arranged as shown in Eq. (32) and the equilibrium equation can be applied to establish kinematically admissible displacement rates. For static equilibrium, linear momentum balance or the elasticity equilibrium equations must hold. In other words, we must have $\nabla \cdot \boldsymbol{\sigma} + \rho \boldsymbol{b} = \sigma_{ij,j} + \rho b_i = 0$ (except for this equilibrium expression, the comma notation does not signify differentiation in this work). Consequently, the infinitesimal change in work or the rate of work simplifies to Eq. (33).

$$\delta W = \int_{\partial V} (\dot{\boldsymbol{u}}^d \cdot \boldsymbol{t}) dS + \int_V (\dot{\boldsymbol{u}}^d \cdot \rho \boldsymbol{b}) dV = \int_{\partial V} \left(\dot{\boldsymbol{u}}^{\boldsymbol{d}} \cdot \boldsymbol{\sigma}\right) \cdot \boldsymbol{n}\, dS + \int_V (\dot{\boldsymbol{u}}^{\boldsymbol{d}} \cdot \rho \boldsymbol{b}) dV = \int_V \left(\nabla \cdot \left(\dot{\boldsymbol{u}}^{\boldsymbol{d}} \cdot \boldsymbol{\sigma}\right) + \dot{\boldsymbol{u}}^{\boldsymbol{d}} \cdot \rho \boldsymbol{b}\right) dV \tag{31}$$

$$\int_V \left(\dot{\boldsymbol{u}}^{\boldsymbol{d}} \nabla \cdot \boldsymbol{\sigma} + \nabla \dot{\mathbf{u}}^{\boldsymbol{d}} : \boldsymbol{\sigma} + \dot{\boldsymbol{u}}^{\boldsymbol{d}} \cdot \rho \boldsymbol{b}\right) dV = \int_V \left(\nabla \dot{\boldsymbol{u}}^{\boldsymbol{d}} : \boldsymbol{\sigma}\right) dV + \int_V \dot{\boldsymbol{u}}^{\boldsymbol{d}} \cdot (\nabla \cdot \boldsymbol{\sigma} + \rho \boldsymbol{b}) dV \tag{32}$$

$$\dot{W} = \delta W = \int_V \left(\nabla \dot{\boldsymbol{u}}^{\boldsymbol{d}} : \boldsymbol{\sigma}\right) dV = \int_V (\boldsymbol{\sigma} : \dot{\boldsymbol{\varepsilon}}) dV \tag{33}$$

The generalized heat balance differential equations for the heat rate, $\dot{Q}$, is provided in Eq. (34). The conservation equation implies that the total rate of accumulation of heat in the volume, V, must be equivalent to the total rate of inflow (i.e., heat flux) crossing the boundary surface plus the total rate of production of heat produced within the volume. The divergence theorem is applied to simplify the formulation.

$$\delta Q = \dot{Q} = \int_V \rho \delta q dV = -\int_{\partial V} (\boldsymbol{q} \cdot n) dS + \int_V (\rho \boldsymbol{r}) dV = \int_V (\rho \boldsymbol{r} - \nabla \cdot \boldsymbol{q}) dV \tag{34}$$

With the rate of work and heat shown in Eq. (33) and (34), we can express the first law of thermodynamics as shown below in Eq. (35). It is noteworthy to mention, extensive properties in the thermodynamic sense (i.e., properties of the bulk) are integrated localized material point values throughout the volumetric domain. Moreover, uppercase notation for thermodynamic state variable definitions are extensive properties and lowercase notation signify intensive properties. The integrands in Eq. (35) are combined, and simplified to yield the relationship shown in Eq. (36) since the expression in parenthesis must be null to satisfy the integral for any sub-volume.

$$\begin{gathered} \dot{U} = \dot{Q} + \dot{W} = \int_V (\rho \boldsymbol{r} - \nabla \cdot \boldsymbol{q}) dV + \int_V (\boldsymbol{\sigma} : \dot{\boldsymbol{\varepsilon}}) dV \rightarrow \\ \int_V \rho \dot{u} dV = \int_V (\boldsymbol{\sigma} : \dot{\boldsymbol{\varepsilon}} + \rho \boldsymbol{r} - \nabla \cdot \boldsymbol{q}) dV \rightarrow \\ \int_V (\rho \dot{u} - \boldsymbol{\sigma} : \dot{\boldsymbol{\varepsilon}} - \rho \boldsymbol{r} + \nabla \cdot \boldsymbol{q}) dV = 0 \rightarrow \\ \rho \dot{u} - \boldsymbol{\sigma} : \dot{\boldsymbol{\varepsilon}} - \rho \boldsymbol{r} + \nabla \cdot \boldsymbol{q} = 0 \end{gathered} \tag{35}$$

$$\rho \dot{u} = \boldsymbol{\sigma} : \dot{\boldsymbol{\varepsilon}} + \rho \boldsymbol{r} - \nabla \cdot \boldsymbol{q} \tag{36}$$

The relationship between the rate of entropy and heat for the reversible case is rewritten in Eq. (37) by substituting Eq. (34) into Eq. (29). Since we are concerned with the thermodynamics of irreversible processes, the entropy equality is replaced by the inequality according to the Clausius inequality, Eq. (30). With this in mind, the Clausius-Duhem inequality is presented in Eq. (38) since the expression in parenthesis must satisfy the inequality for any differential volume.

$$\begin{gathered} \dot{S} = \frac{\dot{Q}}{T} = \frac{1}{T}\left(-\int_{\partial V} (\boldsymbol{q} \cdot n) dS + \int_V (\rho \boldsymbol{r}) dV \right) \rightarrow \\ \int_V \rho \dot{s} dV = \int_V \left(\frac{\rho \boldsymbol{r}}{T} - \nabla \cdot \left(\frac{\boldsymbol{q}}{T} \right) \right) dV \end{gathered} \tag{37}$$

$$\begin{gathered} \int_V \left(\rho \dot{s} - \frac{\rho \boldsymbol{r}}{T} + \nabla \cdot \left(\frac{\boldsymbol{q}}{T} \right) \right) dV \geq 0 \\ \rho \dot{s} - \frac{\rho \boldsymbol{r}}{T} + \nabla \cdot \left(\frac{\boldsymbol{q}}{T} \right) = \rho \dot{s} - \frac{\rho \boldsymbol{r}}{T} + \frac{1}{\mathrm{T}} \nabla \cdot \mathbf{q} + \mathbf{q} \cdot \nabla T^{-1} \geq 0 \end{gathered} \tag{38}$$

The Helmholtz free energy function is adopted here, and it is a scalar function defined by internal state variables ε_{ij}, γ_i, D_{ij}, T, and δ denoting the infinitesimal strain tensor, viscoelastic state variables, the second-order symmetric damage tensor, temperature, and isotropic hardening, respectively. The free energy function, Eq. (39), is written in differential rate form as shown in Eq. (40). The entropy rate can be obtain by rearranging Eq. (40) and substituting Eq. (36).

$$\psi = \psi\left(\varepsilon_{ij}, \gamma_i, D_{ij}, T, \delta\right) = u - Ts \tag{39}$$

$$\dot{\psi} = \frac{\partial \psi}{\partial \varepsilon_{ij}}\dot{\varepsilon}_{ij} + \frac{\partial \psi}{\partial \gamma_i}\dot{\gamma}_i + \frac{\partial \psi}{\partial T}\dot{T} + \frac{\partial \psi}{\partial D_{ij}}\dot{D}_{ij} + \frac{\partial \psi}{\partial \delta}\dot{\delta} = \dot{u} - \dot{T}s - T\dot{s} \tag{40}$$

$$\dot{s} = \frac{1}{T}\left(\frac{1}{\rho}\boldsymbol{\sigma}\colon\dot{\boldsymbol{\varepsilon}} + \boldsymbol{r} - \frac{1}{\rho}\nabla\cdot\boldsymbol{q}\right) - \frac{1}{T}\left(\frac{\partial \psi}{\partial \boldsymbol{\varepsilon}}\dot{\boldsymbol{\varepsilon}} + \frac{\partial \psi}{\partial \boldsymbol{\gamma}}\dot{\boldsymbol{\gamma}} + \frac{\partial \psi}{\partial T}\dot{T} + \frac{\partial \psi}{\partial \boldsymbol{D}}\dot{\boldsymbol{D}} + \frac{\partial \psi}{\partial \delta}\dot{\delta}\right) - \frac{1}{T}s\dot{T} \tag{41}$$

The defined entropy rate enters the Clausius-Duhem inequality as shown in Eq. (42), then it is expanded in Eq. (43) and re-arranged to obtain Eq. (44). For independently varying strains and temperature rates (i.e., functional independence) [167], we obtain the necessary relations shown in Eq. (45).

$$\begin{aligned}\rho\left(\frac{1}{T}\left(\frac{1}{\rho}\boldsymbol{\sigma}\colon\dot{\boldsymbol{\varepsilon}} + \boldsymbol{r} - \frac{1}{\rho}\nabla\cdot\boldsymbol{q}\right) - \frac{1}{T}\left(\frac{\partial \psi}{\partial \boldsymbol{\varepsilon}}\dot{\boldsymbol{\varepsilon}} + \frac{\partial \psi}{\partial \boldsymbol{\gamma}}\dot{\boldsymbol{\gamma}} + \frac{\partial \psi}{\partial T}\dot{T} + \frac{\partial \psi}{\partial \boldsymbol{D}}\dot{\boldsymbol{D}} + \frac{\partial \psi}{\partial \delta}\dot{\delta}\right) - \frac{1}{T}s\dot{T}\right)\ldots \\ \ldots - \frac{\rho\boldsymbol{r}}{T} + \frac{1}{\mathrm{T}}\nabla\cdot\mathbf{q} + \mathbf{q}\cdot\nabla\left(\frac{1}{T}\right) \geq 0\end{aligned} \tag{42}$$

$$\begin{aligned}\frac{1}{T}\boldsymbol{\sigma}\colon\dot{\boldsymbol{\varepsilon}} + \frac{\rho\boldsymbol{r}}{T} - \frac{1}{T}\nabla\cdot\boldsymbol{q} - \frac{\rho}{T}\frac{\partial \psi}{\partial \boldsymbol{\varepsilon}}\dot{\boldsymbol{\varepsilon}} - \frac{\rho}{T}\frac{\partial \psi}{\partial \boldsymbol{\gamma}}\dot{\boldsymbol{\gamma}} \quad - \frac{\rho}{T}\frac{\partial \psi}{\partial T}\dot{T} - \frac{\rho}{T}\frac{\partial \psi}{\partial \boldsymbol{D}}\dot{\boldsymbol{D}} - \frac{\rho}{T}\frac{\partial \psi}{\partial \delta}\dot{\delta} - \frac{\rho}{T}s\dot{T} \\ - \frac{\rho\boldsymbol{r}}{T} + \cdots \\ \ldots\frac{1}{\mathrm{T}}\nabla\cdot\mathbf{q} + \mathbf{q}\cdot\nabla\left(\frac{1}{T}\right) \geq 0\end{aligned} \tag{43}$$

$$\frac{1}{T}\left(\boldsymbol{\sigma} - \rho\frac{\partial \psi}{\partial \boldsymbol{\varepsilon}}\right)\dot{\boldsymbol{\varepsilon}} - \frac{\rho}{T}\left(s + \frac{\partial \psi}{\partial T}\right)\dot{T} - \frac{\rho}{T}\frac{\partial \psi}{\partial \boldsymbol{D}}\dot{\boldsymbol{D}} - \frac{\rho}{T}\frac{\partial \psi}{\partial \delta}\dot{\delta} - \frac{\rho}{T}\frac{\partial \psi}{\partial \boldsymbol{\gamma}}\dot{\boldsymbol{\gamma}} + \mathbf{q}\cdot\nabla\left(\frac{1}{T}\right) \geq 0 \tag{44}$$

$$\sigma_{ij} = \rho \frac{\partial \psi}{\partial \varepsilon_{ij}}$$
$$s = -\frac{\partial \psi}{\partial T} \tag{45}$$

The Clausius-Duhem inequality simplifies to Eq. (46) which contains terms relevant to viscoelasticity, damage, and heat transfer. The thermodynamic forces, Y_{ij}, Π, and Γ_i, defined in Eq. (47), are conjugates to the damage state variables, D_{ij}, hardening variable, δ, and molecular motion state variable, γ_i, respectively. The inequality in Eq. (46) is rewritten compactly as shown in Eq. (48) by substituting the thermodynamic force definitions.

$$-\frac{\rho}{T}\frac{\partial \psi}{\partial \boldsymbol{D}}\dot{\boldsymbol{D}} - \frac{\rho}{T}\frac{\partial \psi}{\partial \delta}\dot{\delta} - \frac{\rho}{T}\frac{\partial \psi}{\partial \boldsymbol{\gamma}}\dot{\boldsymbol{\gamma}} + \mathbf{q}\cdot\nabla\left(\frac{1}{T}\right) \geq 0 \tag{46}$$

$$Y_{\mathrm{ij}} = -\frac{\partial \psi}{\partial D_{ij}}\,, \qquad \Gamma_i = -\frac{\partial \psi}{\partial \gamma_i}, \qquad \Pi = -\frac{\partial \psi}{\partial \delta} \tag{47}$$

$$Y_{ij}\dot{D}_{ij} + \Pi\dot{\delta} + \Gamma_i\dot{\gamma}_i - \frac{\mathrm{q_i}\cdot(\nabla T)_i}{\rho T} \geq 0 \tag{48}$$

Motivated by the work of Abdel-Tawab and Weitsman [165], the Helmholtz free energy function is defined by a Taylor series expansion, Eq. (50), about the equilibrium viscoelastic state variable, γ_i^e (i.e., fully relaxed state). Deformed viscoelastic solids, at fixed strains and damage states, are triggered by a thermodynamic process that drives the molecular motion internal state variables to an equilibrated quantity, which is denoted as γ_i^e in Eq. (49). The hypothesis of disparate length scales is adopted; viscoelastic behavior occurs at the molecular scale and damage at the micro-scale (i.e., matrix cracks, fiber/matrix debonding, fiber pull-out etc..). Under this assumption, arbitrary damage states will not alter the temporal stress relaxation or creep rate rather the effective magnitude of relaxation is changed. To derive the Helmholtz free energy function ψ, a Taylor series expansion, Eq. (50), is taken about the equilibrated variable, γ_i^e, . In the expansion, ψ_e refers to the value of the free energy function at equilibrium and ψ_{ij} as the twice differentiated quantity shown in Eq. (51), HOT refers to higher order terms of the Taylor expansion. Moreover, terms beyond second-order may be reasonably neglected since γ_i is a small enough quantity at the

scale of polymer chain displacement. It is noteworthy to mention, the free energy function is assumed continuous, sufficiently differentiable, a minimum, Eq. (52), and convex, Eq. (53), at the equilibrium point. The connection between the viscoelastic thermodynamic force and its conjugated state variable is made by employing the Onsager's theorem, which relates the equality of flows and forces for non-equilibrated thermodynamic systems through a symmetric positive semi-definite proportional matrix. With this consideration in mind, the Onsager's theorem, Eq. (54), states that the thermodynamic viscoelastic driving force, Γ_i, is proportional to the rate of the internal viscoelastic state variable, $\dot{\gamma}_i$, and the proportionality tensor, b_{ij}. When Eq. (54) is substituted into the entropy inequality, Eq. (48), for fixed damage and isothermal states, the inequality shown in Eq. (55) is obtained which shows that b_{ij} is positive semi-definite. Differentiation of Eq. (50) with respect to $\dot{\gamma}_i$ and substitution of Eq. (54) into the differential relation produces a system of first order differential equations, shown in Eq. (56). The system of differential equation can be diagonalized, where B_i and Ψ_i are diagonalized eigenvalue matrices to b_{ij} and ψ_{ij}, respectively, and $\hat{\gamma}_m$ are the transformed variables in Eq. (57); furthermore, the transformed internal state variables, $\hat{\gamma}_i$, can be solved for to obtain the general solution shown in Eq. (58). The relaxation times are defined as $\tau_i = B_i/\Psi_i$ (no sum on i), which depends on the diagonalized matrices obtained from the Taylor expansion and the Onsager's reciprocal relation. Furthermore, the relaxation times are positive semi-definite due to b_{ij} and ψ_{ij} already satisfying these conditions via the Clausius-Duhem inequality and convex condition at equilibrium.

$$\gamma_i^{\mathrm{e}} = \gamma_i^e(\varepsilon_{ij}, D_{ij}) \tag{49}$$

$$\psi\big(\varepsilon_{ij}, \gamma_i, D_{ij}, T, \delta\big) = \psi_e + \frac{1}{2}\psi_{ij}(\gamma_i - \gamma_i^e)\big(\gamma_j - \gamma_j^e\big) + HOT \tag{50}$$

$$\psi_e = \Big(\psi\big(\varepsilon_{ij}, D_{ij}, T, \delta\big)\Big)_e, \qquad \psi_{ij} = \left(\frac{\partial^2 \psi}{\partial \gamma_i \partial \gamma_j}\right)_e \tag{51}$$

$$\left(\frac{\partial \psi}{\partial \gamma_i}\right)_e = 0 \tag{52}$$

$$\psi_{ij}\delta\gamma_i\delta\gamma_j > 0 \tag{53}$$

$$\Gamma_i = b_{ij}\dot{\gamma}_j \tag{54}$$

$$b_{ij}\dot{\gamma}_i\dot{\gamma}_j \geq 0 \tag{55}$$

$$\begin{gathered} -\frac{\partial\psi}{\partial\gamma_i} = \Gamma_i = \frac{\partial}{\partial\gamma_i}\left(-\psi_e - \frac{1}{2}\psi_{ij}(\gamma_i - \gamma_i^e)(\gamma_j - \gamma_j^e)\right) \rightarrow \\ b_{ij}\dot{\gamma}_j = \frac{1}{2}\psi_{ij}(\gamma_j - \gamma_j^e) \rightarrow \\ 2b_{ij}\dot{\gamma}_j + \psi_{ij}\gamma_j = \psi_{ij}\gamma_j^e \end{gathered} \tag{56}$$

$$\begin{gathered} B_i\dot{\hat{\gamma}}_i + \Psi_i\hat{\gamma}_i = \Psi_i\hat{\gamma}_i^e \rightarrow \\ \dot{\hat{\gamma}}_i + \frac{\Psi_i}{B_i}\hat{\gamma}_i = \frac{\Psi_i}{B_i}\hat{\gamma}_i^e \rightarrow \\ \dot{\hat{\gamma}}_i + \frac{1}{\tau_i}\hat{\gamma}_i = \frac{1}{\tau_i}\hat{\gamma}_i^e, \qquad where\ \tau_i = \frac{B_i}{\Psi_i} \end{gathered} \tag{57}$$

$$\hat{\gamma}_i = \hat{\gamma}_i^e(1 - e^{-t/\tau_i}) \tag{58}$$

Schapery [168] derived the same linear equations of motion using the same process; additionally, the Taylor expansion was made with the generalized coordinates, q_i, and temperature, T. It was pointed out that the expansion of the free energy solely in terms of q_i can be made with an understanding that the matrices Ψ_i and B_i can be temperature-dependent and perhaps related through the polymer shift factor relation, a_T [152]. Following the Schapery [168] procedure, the connection between the proportionality tensor, b_{ij}, and the reduced time variable, a_T, is adopted. In essence, non-isothermal viscoelastic systems are represented by a reduced time expression which effectively transform b_{ij} and hence τ_i; moreover, this assumes the time-temperature superposition principle to be valid. The reduced time expression $\xi(t)$ used in this work is shown in Eq. (59). The transformation or shift factor, a_T, is commonly defined by the empirical William-Landel-Ferry (WLF) formula for thermorheologically simple polymers. However, the WLF relation is said to be valid above the polymer's glass transition temperature or at least near the glass transition point. Modified WLF expressions have been introduced in the literature [39] to account for temperatures below the glass transition. A piece-wise function, shown in Eq. (60), is adopted in this work to represent shift factors above and below the glass transition temperature.

$$\xi(t) = \int_0^t \frac{ds}{a_T(T(s))} \tag{59}$$

$$log_{10}\, a_T = \begin{cases} \dfrac{C_1\left(T_{ref} - T\right)^c}{C_2 + \left(T_{ref} - T\right)^c}, & T < T_{ref} \\ \dfrac{C_1(T_{ref} - T)}{C_2 + (T_{ref} - T)}, & T \geq T_{ref} \end{cases} \tag{60}$$

The Helmholtz free energy takes the form in Eq. (61) after substituting Eq. (58) into Eq. (50), this form contains an equilibrated and non-relaxed free energy contributions. With the free energy functions defined in terms of the viscoelastic internal state variables, the stresses are procured by substituting Eq. (61) into Eq. (45) while keeping all other variables constant and with $\rho = 1$ for simplicity. The stresses have two components that are associated with an equilibrated contribution and non-relaxed contributions. The variables, Λ_i, are a function of strains and damage because of $\hat{\gamma}_i^e$ and are obtained by a Taylor series expansion about the null strain state, up to the quadratic term considering infinitesimal strain theory. Linear terms correspond to a residual stress state, which are assumed zero at the reference strain state, and constant terms vanish since strain free states do not produce excite viscoelastic motion. The term left in the expansion is shown in Eq. (63), the twice differentiated transient Helmholtz energy terms must produce viscoelastic stiffnesses according to the law of elasticity [108]. Additionally, employing the principle of energy equivalence [99], [169], the transient stiffness tensor takes the form shown in Eq. (64), with P_{ijkl}^V denoting the fourth-order damage effect tensor corresponding to the viscoelastic stiffness tensors, $C_{ijkl,m}^V$.

$$\psi = \psi_e + \frac{1}{2}\sum_{i=1}^{I} \Psi_i\left(\hat{\gamma}_i^e e^{-t/\tau_i}\right)^2 \tag{61}$$

$$\begin{aligned} \sigma_{ij} &= \frac{\partial \psi_e}{\partial \varepsilon_{ij}} + \sum_{i=1}^{I} \frac{\partial \Lambda_i}{\partial \varepsilon_{ij}} e^{-t/\tau_i} \\ \Lambda_i &= \Lambda_i\left(\varepsilon_{ij}, D_{ij}\right) = \tfrac{1}{2}\Psi_i(\hat{\gamma}_i^e)^2 \ \text{(no sum over i)} \end{aligned} \tag{62}$$

$$\Lambda_m = \frac{1}{2}\left(\frac{\partial^2 \Lambda_m}{\partial \varepsilon_{ij} \partial \varepsilon_{kl}}\right)_0 \tilde{\varepsilon}_{ij} \tilde{\varepsilon}_{kl} \tag{63}$$

$$\Lambda_m = \frac{1}{2} P^V_{ijab} C^V_{abcd,m} P^V_{cdkl} \varepsilon_{ij} \varepsilon_{kl} \tag{64}$$

The transient viscoelastic stiffness is defined with the Prony series as shown in Eq. (65), it is similar to the well-known generalized Maxwell model. Since the generalized Maxwell model is derived from rheological elements, the relaxation time is defined in terms of the spring-dashpot constants; however, the thermodynamic approach defines the relaxation times based on the Ψ_i and B_i. The damage effect tensor acts to transform the viscoelastic stiffness tensors, $C^V_{abcd,m}$; however, the exponential is unaffected by the damage transformation. For the equilibrated portion of the energy function, ψ^e, a similar procedure is followed to obtain Eq. (66) with P^e_{ijkl} denoting the damage effect tensor corresponding to the equilibrated stiffness tensor, C^e_{ijkl}. With this in mind, the equilibrated stresses are the obtained as shown in Eq. (67). While the damage effect tensors, P^e_{ijkl} and P^V_{ijkl}, can be different, this work assumes damage is indistinguishable for both components and these tensors are then equivalent, demonstrated in Eq. (68). Therefore, the effective stiffness is defined in Eq. (69), it contains an equilibrated and non-equilibrated contribution. Boltzmann superposition is applicable for linear viscoelastic materials undergoing time-dependent strain inputs. Consequently, it follows that the stresses must take the form of Duhamel's integral, shown in Eq. (70); also, it is assumed the time-translation invariance hypothesis holds.

$$\mathrm{C}^{\mathrm{V}*}_{ijkl,m}(\xi(t)) = \sum_{m=1}^{M} P^V_{ijab} C^V_{abcd,m} P^V_{cdkl} e^{-\xi/\tau_m} \tag{65}$$

$$\psi_e = P^e_{ijab} C^e_{abcd} P^e_{cdkl} \varepsilon_{ij} \varepsilon_{kl} \tag{66}$$

$$\sigma^e_{ij} = \frac{\partial \psi_e}{\partial \varepsilon_{ij}} = P^e_{ijab} C^e_{abcd} P^e_{cdkl} \varepsilon_{kl} \tag{67}$$

$$P^V_{ijkl} = P^e_{ijkl} = P_{ijkl} \tag{68}$$

$$C^*_{ijkl}(\xi(t)) = P_{ijab}C^e_{abcd}P_{cdkl} + \sum_{m=1}^{M} P_{ijab}C^V_{abcd,m}P_{cdkl}e^{-\xi/\tau_m} \tag{69}$$

$$\sigma_{ij} = \int_0^t C^*_{ijkl}(\xi(t) - \xi(s))\frac{\partial \varepsilon_{kl}}{\partial s}ds \tag{70}$$

The fourth-order damage effect tensor is constructed from a dyad of symmetric second-order damage or integrity tensors, D_{mn} or Ω_{mn} [170], respectively, this is shown in Eq. (71). In the principal damage coordinate system, D_{mn} is a diagonal tensor with three principal values, D_1, D_2, and D_3. Analogous to the effective cross-sectional area concept, the damage variables quantify the ratio of damaged stiffness to the pristine stiffness. For example, a value of one denotes catastrophic failure or complete loss of load bearing capacity whereas a value of zero denotes a pristine material. Damage variables are homogenized representations of distributed microcracks within a material, for short fiber composites, damage variables homogenize micro-damage sites such as matrix cracks, fiber rupture, fiber pull-out, and fiber/matrix interface cracks into effective quantities. Damage in 3D printed short fiber composites can be dissociated into intra-bead and inter-bead damage. Intra-bead damage occurs within a bead and exhibit a combination of fiber, matrix, or fiber/matrix interface damage; on the other hand, inter-bead damage occurs in matrix-rich zones such as the interface between stacked beads and mostly comprise of matrix cracking. Two types of integrity tensors are considered, an intra-bead description with only two damage modes, Ω_{ij}, and inter-bead description with a single damage mode, Ω^I_{ij}, as shown in Eq. (72).

$$P_{ijkl} = \frac{1}{2}\left(\Omega_{ik}\Omega_{jl} + \Omega_{il}\Omega_{jk}\right), \qquad where\ \Omega_{ij} = \sqrt{\delta_{ij} - D_{ij}} \tag{71}$$

$$\Omega^I_{ij} = \begin{bmatrix} 1 & 0 & 0 \\ 0 & 1 & 0 \\ 0 & 0 & \sqrt{1-D_3} \end{bmatrix}, \qquad \Omega_{ij} = \begin{bmatrix} \sqrt{1-D_1} & 0 & 0 \\ 0 & \sqrt{1-D_2} & 0 \\ 0 & 0 & 1 \end{bmatrix} \tag{72}$$

Noteworthy to mention, other forms of the damage effect tensors have been proposed in the literature [171]–[176], which are an extension of the model proposed by Matzenmiller et al. [177]. The modified form introduces independent shear damage variables, D_4, D_5, and D_6 which allow for greater flexibility in modeling the nonlinear behavior in shear. In comparison to Eq. (71),

the shear reduction damage variables should be related to the principal damage variables, D_1, D_2, and D_3; for example, assuming the damage effect tensor form used in Chow and Wang [92], the shear damage variable associated with the 2-3 direction would be $D_4 = D_2 + D_3 - D_2 D_3$, in Voigt notation. For modeling shear damage, this approach can perhaps be more convenient.

$$P_{ijkl} = \begin{bmatrix} 1-D_1 & 0 & 0 & 0 & 0 & 0 \\ 0 & 1-D_2 & 0 & 0 & 0 & 0 \\ 0 & 0 & 1-D_3 & 0 & 0 & 0 \\ 0 & 0 & 0 & 1-D_4 & 0 & 0 \\ 0 & 0 & 0 & 0 & 1-D_5 & 0 \\ 0 & 0 & 0 & 0 & 0 & 1-D_6 \end{bmatrix} \tag{73}$$

The general forms of damage evolution equations can be sorted into three categories; namely, (i) purely-standard thermodynamic approach, (ii) quasi-standard formulation where separate potentials are used for both plastic and damage dissipations, and (iii) formulations not based on dissipation potentials [106]. In this work, the quasi-standard approach with a rate-independent formulation is adopted and no plastic potential is considered. Evolution equations require two functions; namely, a postulated damage surface, $g(\boldsymbol{Y}(\boldsymbol{D}), \kappa(\delta, T))$ defined in Eq. (74), and convex damage potential, $\hat{f}(\boldsymbol{Y}(\boldsymbol{D}), \kappa(\delta, T))$. An associated model, shown in Eq. (75), is adopted, and the norm of the damage thermodynamic force is used [92], [94], [98], [100], [178]; where $\boldsymbol{J}$ is a material-dependent damage interaction fourth-order tensor. A modified isotropic hardening/softening function, proposed by Barbero and Lonetti [103] and defined in Eq. (76), is used such that $\kappa_0(T)$ is the temperature dependent damage threshold, δ is the hardening variable, and both c_1 and $c_2(T)$ are material-dependent parameters. Since the damage potential is also a convex function, the following constraints, $c_1 > 0$, $c_2 < 0$ and $\kappa_0 > 0$ must hold.

$$g\big(\boldsymbol{Y}(\boldsymbol{D}), \kappa(\delta, T)\big) = \hat{g}\big(\boldsymbol{Y}(\mathbf{D})\big) - \big(\kappa(\delta, T) + \kappa_0(T)\big) \tag{74}$$

$$\hat{g}\big(\boldsymbol{Y}(\mathbf{D})\big) = \hat{f}\big(\boldsymbol{Y}(\mathbf{D})\big) = \sqrt{(\boldsymbol{Y} : \mathbf{J} : \boldsymbol{Y})/2} \tag{75}$$

$$\kappa(\delta, T) + \kappa_0(T) = c_1 \left(e^{\frac{\delta}{c_2(T)}} - 1 \right) + \kappa_0(T) \tag{76}$$

In the damage surface equality, Eq. (74), $g = 0$ corresponds to a point that lies on the damage surface and also signifies the point of damage onset. When damage onset is achieved, damage evolution follows and the kinetic equations, Eqs. (77) and (78), determine the change in damage and isotropic hardening of the damage surface. In the kinetic equations, the variable, $\dot{\lambda}$, is the Lagrangian multiplier (i.e., damage multiplier) and $\partial f/\partial \boldsymbol{Y}$ are the directions in the thermodynamic force space which are obtained from the normality rule [179]. The Lagrangian multiplier is assumed to affect the hardening rate in a similar manner except that the expansion is isotropic. The hardening function acts to increase the thermodynamically allowable space from which damage cannot evolve. To solve for the damage multiplier, the Kuhn-Tucker relations, Eq. (79), are needed for the unilateral constraint of g. The consistency conditions, provided in Eq. (80), are expanded as shown in Eq. (81) to determine the value of the damage multiplier defined in Eq. (82). Moreover, based on Eqs. (78) and (74), the hardening rate can be obtained as $\dot{\delta} = -\dot{\lambda}$. For the isothermal case, the change in damage simplifies to Eq. (83). The damage multiplier, damage variables, and hardening variable are numerically solved for using a standard return mapping algorithm [170].

$$\dot{\mathbf{D}} = \frac{\partial \boldsymbol{D}}{\partial \mathbf{X}} = \dot{\lambda}\frac{\partial f}{\partial \mathbf{X}} \tag{77}$$

$$\dot{\delta} = \dot{\lambda}\frac{\partial g}{\partial \kappa} \tag{78}$$

$$\dot{\lambda} \geq 0, \qquad g \leq 0, \qquad \dot{\lambda} g = 0 \tag{79}$$

$$\dot{g} = \frac{\partial g}{\partial \boldsymbol{Y}} : \dot{\boldsymbol{Y}} + \frac{\partial g}{\partial \kappa}\dot{\kappa} = 0, \qquad g = 0 \tag{80}$$

$$\begin{gathered} \dot{g} = \frac{\partial g}{\partial \boldsymbol{Y}} : \frac{\partial \boldsymbol{Y}}{\partial \boldsymbol{\varepsilon}} : \dot{\boldsymbol{\varepsilon}} + \frac{\partial g}{\partial \kappa}\frac{\partial \kappa}{\partial T}\dot{T} + \left(\frac{\partial g}{\partial \boldsymbol{Y}} : \frac{\partial \boldsymbol{Y}}{\partial \boldsymbol{D}} : \frac{\partial f}{\partial \boldsymbol{Y}} + \frac{\partial \kappa}{\partial \delta}\right)\dot{\lambda} = 0, \\ where\ \dot{\boldsymbol{Y}} = \frac{\partial \boldsymbol{Y}}{\partial \boldsymbol{\varepsilon}} : \dot{\boldsymbol{\varepsilon}} + \dot{\lambda}\frac{\partial \boldsymbol{Y}}{\partial \boldsymbol{D}} : \frac{\partial f}{\partial \boldsymbol{Y}} \text{ and } \dot{\kappa} = \frac{\partial \kappa}{\partial \delta}\dot{\lambda}\frac{\partial g}{\partial \kappa} + \frac{\partial g}{\partial \kappa}\frac{\partial \kappa}{\partial T}\dot{T} \end{gathered} \tag{81}$$

$$\dot{\lambda} = \begin{cases} L^d \boldsymbol{\phi} : \dot{\boldsymbol{\varepsilon}} + L^d \theta \dot{T}, & if\ g = 0 \\ 0, & if\ g < 0 \end{cases}$$

$$where\ L^d = -\frac{1}{\frac{\partial g}{\partial \boldsymbol{Y}} : \frac{\partial \boldsymbol{Y}}{\partial \boldsymbol{D}} : \frac{\partial f}{\partial \boldsymbol{Y}} + \frac{\partial \kappa}{\partial \delta}}, \qquad \boldsymbol{\phi} = \frac{\partial g}{\partial \boldsymbol{Y}} : \frac{\partial \boldsymbol{Y}}{\partial \boldsymbol{\varepsilon}}, \qquad \theta = \frac{\partial g}{\partial \kappa} : \frac{\partial \kappa}{\partial T} \tag{82}$$

$$\dot{\mathbf{D}} = \frac{\partial f}{\partial \boldsymbol{Y}} L^d \boldsymbol{\phi} \tag{83}$$

In finite element analyses, the tangent constitutive matrix, $\boldsymbol{C}^T$, is required and it is obtained from differentiating the stress tensor. The constitutive law is applied to Eq. (84) to simplify the relation as shown in Eq. (85) since the strains are independent of the damage variables. In the absence of damage evolution, the material tangent matrix is simply the differentiated stresses with respect to the strain; however, an additional contribution, provided in Eq. (86), must be added when damage is evolving.

$$\dot{\boldsymbol{\sigma}}(\boldsymbol{\varepsilon}, \mathbf{D}) = \frac{\partial \boldsymbol{\sigma}}{\partial \boldsymbol{\varepsilon}} : \dot{\boldsymbol{\varepsilon}} + \frac{\partial \boldsymbol{\sigma}}{\partial \boldsymbol{D}} : \dot{\boldsymbol{D}} = \frac{\partial (\boldsymbol{C}^T : \boldsymbol{\varepsilon})}{\partial \boldsymbol{\varepsilon}} : \dot{\boldsymbol{\varepsilon}} + \frac{\partial (\boldsymbol{C}^T : \boldsymbol{\varepsilon})}{\partial \boldsymbol{D}} : \dot{\boldsymbol{D}} \tag{84}$$

$$\dot{\boldsymbol{\sigma}}(\boldsymbol{\varepsilon}, \mathbf{D}) = \boldsymbol{C}^T : \dot{\boldsymbol{\varepsilon}} + \left(\frac{\partial \boldsymbol{C}^T}{\partial \boldsymbol{D}} : \boldsymbol{\varepsilon} \right) : \dot{\boldsymbol{D}} \tag{85}$$

$$\mathbf{C}^{\mathrm{T}} = \begin{cases} \boldsymbol{C}^T, & if\ \dot{\boldsymbol{D}} = 0 \\ \boldsymbol{C}^T + \left(\frac{\partial \boldsymbol{C}^T : \boldsymbol{\varepsilon}}{\partial \boldsymbol{D}} : \frac{\partial f}{\partial \mathbf{X}} \right) \boldsymbol{L}^d, & if\ \dot{\boldsymbol{D}} \geq 0 \end{cases} \tag{86}$$

3.3 Numerical Implementation for Implicit Finite Element Method

The outlined numerical formulations can be implemented in any implicit finite element solver that supports user-defined material subroutines. For this work, the numerical implementation is carried out in ABAQUS/Standard (Implicit). The Abaqus/Standard user material (UMAT) subroutine requires the specification of the stresses and the material tangent matrix (i.e., the Jacobian matrix) [18]. To compute the stresses, the integral in Eq. (87) needs to be numerically solved. A noteworthy point is that the solver provides the time and strain increments. The parameter, n, is the current

increment and $n+1$ denotes the updated increment, in other words, the beginning and end of the increment, respectively.

$$\sigma_{ij} = P_{ijab}\int_0^t C^*_{abcd}(\xi(t)-\xi(s))P_{cdkl}\frac{\partial \varepsilon_{kl}}{\partial s}ds = \\ P_{ijab}C^e_{abcd}P_{cdkl}\varepsilon_{kl} + \sum_{m=1}^{M} P_{ijab}C^V_{abcd,m}P_{cdkl}\int_0^t e^{-(\xi(t)-\xi(s))/\tau_m}\frac{\partial \varepsilon_{kl}}{\partial s}ds \tag{87}$$

Define the integral as,

$$I^*_{kl,m}(\xi(t)) = \int_0^t e^{-(\xi(t)-\xi(s))/\tau_m}\frac{\partial \varepsilon_{kl}}{\partial s}ds \tag{88}$$

In the updated incremental form, we have the following,

$$I^{(n+1)*}_{kl,m}(\xi_{n+1}) = \int_0^{\xi_{n+1}} e^{-\frac{(\xi_{n+1}-\xi(s))}{\tau_m}}\frac{\partial \varepsilon_{kl}}{\partial s}ds = \\ \int_0^{\xi_n} e^{-\frac{(\xi_{n+1}-\xi(s))}{\tau_m}}\frac{\partial \varepsilon_{kl}}{\partial s}ds + \int_{\xi_n}^{\xi_{n+1}} e^{-\frac{(\xi_{n+1}-\xi(s))}{\tau_m}}\frac{\Delta \varepsilon_{kl}}{\Delta s}ds = \\ \mathrm{a_T}\tau_m\frac{\Delta \varepsilon_{kl}}{\Delta \mathrm{t}}e^{-\frac{(\xi_{n+1}-\xi(s))}{\tau_m}}\Big|_{\xi_n}^{\xi_{n+1}} + \int_0^{\xi_n} e^{-\frac{(\xi_{n+1}-\xi(s))}{\tau_m}}\frac{\partial \varepsilon_{kl}}{\partial s}ds = \\ I^{(n+1)*}_{kl,m}(\xi_{n+1}) = \mathrm{a_T}\tau_m\frac{\Delta \varepsilon_{kl}}{\Delta \mathrm{t}}\left(1-e^{-\frac{\Delta t}{a_T\cdot\tau_m}}\right) + e^{-\frac{\Delta t}{a_T\cdot\tau_m}}\int_0^{t_n} e^{-\frac{(\xi_n-\xi(s))}{\tau_m}}\frac{\partial \varepsilon_{kl}}{\partial s}ds = \\ I^{(n+1)*}_{kl,m}(\xi_{n+1}) = \mathrm{a_T}\tau_m\frac{\Delta \varepsilon_{kl}}{\Delta \mathrm{t}}\left(1-e^{-\frac{\Delta t}{a_T\cdot\tau_m}}\right) + e^{-\frac{\Delta t}{a_T\cdot\tau_m}}\cdot I^{(n)*}_{kl,m}(\xi_n) \tag{89}$$

The updated stress tensor is computed as shown below,

$$\sigma^{(n+1)}_{ij} = P_{ijab}C^e_{abcd}P_{cdkl}\varepsilon^{(n+1)}_{kl} + \sum_{m=1}^{M} P_{ijab}C^V_{abcd,m}P_{cdkl}\,I^{(n+1)*}_{kl,m}(\xi_{n+1}) = \\ P_{ijab}C^e_{abcd}P_{cdkl}(\varepsilon^n_{kl}+\Delta\varepsilon_{kl}) + \\ \sum_{m=1}^{M} P_{ijab}C^V_{abcd,m}P_{cdkl}\left[\mathrm{a_T}\tau_m\frac{\Delta \varepsilon_{kl}}{\Delta \mathrm{t}}\left(1-e^{-\frac{\Delta t}{a_T\cdot\tau_m}}\right) + e^{-\frac{\Delta t}{a_T\cdot\tau_m}}\cdot I^{(n)*}_{kl,m}(\xi_n)\right] \tag{90}$$

The stress tensor at the current increment is then,

$$\sigma_{ij}^{(n)} = P_{ijab}C_{abcd}^{e}P_{cdkl}\varepsilon_{kl}^{(n)} + \sum_{m=1}^{M} P_{ijab}C_{abcd,m}^{V}P_{cdkl}\int_{0}^{\xi_n} e^{-(\xi_n-\xi(s))/\tau_m}\frac{\partial\varepsilon_{kl}}{\partial s}ds \rightarrow$$
$$\sigma_{ij}^{(n)} = P_{ijab}C_{abcd}^{e}P_{cdkl}\varepsilon_{kl}^{(n)} + \sum_{m=1}^{M} P_{ijab}C_{abcd,m}^{V}P_{cdkl}\, I_{kl,m}^{(n)*}(\xi_n) \tag{91}$$

Where the stress increment is defined as,

$$\Delta\sigma_{ij} = \sigma_{ij}^{(n+1)} - \sigma_{ij}^{(n)} =$$
$$P_{ijab}C_{abcd}^{e}P_{cdkl}\left(\varepsilon_{kl}^{(n)} + \Delta\varepsilon_{kl}\right) +$$
$$\sum_{m=1}^{M} P_{ijab}C_{abcd,m}^{V}P_{cdkl}\left[\mathrm{a_T}\tau_m\frac{\Delta\varepsilon_{kl}}{\Delta\mathrm{t}}\left(1 - e^{-\frac{\Delta t}{a_T\cdot\tau_m}}\right) + e^{-\frac{\Delta t}{a_T\cdot\tau_m}}\cdot I_{kl,m}^{(n)*}(\xi_n)\right] -$$
$$\left(P_{ijab}C_{abcd}^{e}P_{cdkl}\varepsilon_{kl}^{(n)} + \sum_{m=1}^{M} P_{ijab}C_{abcd,m}^{V}P_{cdkl}\, I_{kl,m}^{(n)*}(\xi_n)\right) = \tag{92}$$
$$\sum_{m=1}^{M}\left(e^{-\frac{\Delta t}{a_T\cdot\tau_m}} - 1\right)P_{ijab}C_{abcd,m}^{V}P_{cdkl}I_{kl,m}^{(n)*}(\xi_n) +$$
$$\left[P_{ijab}C_{abcd}^{e}P_{cdkl} + \sum_{m=1}^{M} P_{ijab}C_{abcd,m}^{V}P_{cdkl}\frac{\mathrm{a_T}\tau_m}{\Delta t}\left(1 - e^{-\frac{\Delta t}{a_T\cdot\tau_m}}\right)\right]\Delta\varepsilon_{kl}$$

Furthermore, the stress increment can be written compactly as shown below,

$$\sigma_{ij}^{*} = \sum_{m=1}^{M}\left(e^{-\frac{\Delta t}{a_T\cdot\tau_m}} - 1\right)P_{ijab}C_{abcd,m}^{V}P_{cdkl}I_{kl,m}^{(n)*}(\xi_n) \tag{93}$$

$$\Delta\sigma_{ij} = \sigma_{ij}^{*} + \left[P_{ijab}C_{abcd}^{e}P_{cdkl} + \sum_{m=1}^{M} P_{ijab}C_{abcd,m}^{V}P_{cdkl}\frac{\mathrm{a_T}\tau_m}{\Delta t}\left(1 - e^{-\frac{\Delta t}{a_T\cdot\tau_m}}\right)\right]\Delta\varepsilon_{kl} \tag{94}$$

Lastly, the Jacobian is computed as

$$\boldsymbol{C}^{T} = \frac{\partial\Delta\sigma_{ij}}{\partial\Delta\varepsilon_{kl}} = P_{ijab}C_{abcd}^{e}P_{cdkl} + \sum_{m=1}^{M} P_{ijab}C_{abcd,m}^{V}P_{cdkl}\frac{\mathrm{a_T}\tau_m}{\Delta t}\left(1 - e^{-\frac{\Delta t}{a_T\cdot\tau_m}}\right) \tag{95}$$

When damage is growing, the Jacobian must also account for the change with respect to the damage variable. Define the effective stiffness tensors as shown in Eqs. (96) and (97). The re-

written stresses, Eq. (98), facilitate demonstrating the damage contributing component to the Jacobian matrix. The additional damage contributing Jacobian component is defined as shown in Eq. (99).

$$\tilde{C}^{e}_{ijkl} = P_{ijab} C^{e}_{abcd} P_{cdkl} \tag{96}$$

$$\tilde{C}^{V}_{ijkl,m} = P_{ijab} C^{V}_{abcd,m} P_{cdkl} \tag{97}$$

$$\sigma_{ij} = \tilde{C}^{e}_{ijkl} \varepsilon_{kl} + \sum_{m=1}^{M} \tilde{C}^{V}_{ijkl} I^{*}_{kl,m}(\xi) \tag{98}$$

$$\frac{\partial \boldsymbol{C}^{T} : \boldsymbol{\varepsilon}}{\partial \boldsymbol{D}} = \frac{\partial \sigma_{rs}}{\partial D_{cd}} = \frac{\partial \tilde{C}^{e}_{rspq} \varepsilon_{pq}}{\partial D_{cd}} + \sum_{m=1}^{M} \frac{\partial \tilde{C}^{V}_{rspq,m} I^{*}_{pq,m}(\xi)}{\partial D_{cd}} \tag{99}$$

4. EXPERIMENTAL INVESTIGATION OF SHORT FIBER COMPOSITE PRODUCED VIA EDAM

4.1 Introduction

A 25% wt. short carbon fiber reinforced PESU processed via extrusion deposition additive manufacturing has been characterized for uniaxial tension and compression, and in-plane shear mechanical properties at room and elevated temperatures of 70°C, 130°C, and 190°C. Mechanical performance is examined by observing the effective stress versus the field-averaged Lagrange or engineering strain procured using the digital image correlation method. The mechanical tests were performed under displacement control, while monitoring the strain distribution. Based on the analyses, this material exhibited highly anisotropic behavior with the highest stiffness and strength along the print direction for both tension and compression. Compressive strengths were observed to be greater than tensile strengths at room and elevated temperatures. Degradation in strength with temperature is observed for all deformation modes, and tensile and compressive stiffness is found to generally decrease with temperature. Shear stiffness along the 1-2 plane is found to decrease with temperature; however, this trend is not observed for 2-3 and 1-3 in-plane shear stiffnesses. Averaged ultimate strains generally decrease with temperatures for tensile and compression loaded specimens along the 2 and 3 printing directions as well as average ultimate shear strains in the 2-3 and 1-3 plane. The behavior is not observed for samples loaded along the print direction in either tension, compression, or shear loaded specimens in the 1-2 plane.

Several authors have studied and reported mechanical properties of materials produced via FDM [4], [45], [188], [180]–[187], the types of mechanical properties reported are tensile stiffness, strength and failure strain, flexural stiffness, strength and failure strain, toughness, fatigue, torsional stiffness, yield strength, ductility, and interlaminar shear strength. Mechanical performance under tension and flexure for 3D printed short fiber composites are observed to be stiffer and stronger than their pure polymer counterparts; additionally, it is acknowledged that mechanical performance also depends on processing parameters and processing conditions [189]. In a review paper, Brenken [190] summarized a list of tensile strength and stiffness properties of FDM composite materials. It is noteworthy to mention that FDM or EDAM short fiber composite materials are not necessarily similar to those of compression molded or injection molded materials

since their microstructures contain different characteristics (e.g., differences in fiber orientation) [45], [187]. Therefore, injection or compression molded available data may not reflect the nature of EDAM or FDM materials. Fiber reinforced ABS, PPS, PEI, and PLA are the materials found in the literature; however, fiber reinforced PESU has not been reported. Relative to other thermoplastics, PESU has a greater glass transition temperature and this allows for temperature applications of at most 215°C without excessive deformation. Furthermore, performance of 3D printed short fiber composites at elevated temperatures are seldom reported which has proven a challenge to designers when attempting to model damage or failure of a large-scale printed structure. Talagani et al. [191] developed a 3D finite element analysis of a printed car chassis made from short fiber composite material to predict potential damaged regions as a result of significant residual stress build-up. The required thermo-mechanical input material properties were estimated using limited test data and micromechanical methods. Inter-bead shear stresses develop when incremental deposition of molten material onto cooler material occurs, which is a natural process in EDAM. Inter-bead shear stresses are influenced by long layer times as this allows for greater temperature gradients to exists between beads. Compton et al. [23] observed that long layer times resulted in significant warpage, substrate de-bonding, and inter-bead delamination in a 3D printed wall.

The scope of this study is to investigate mechanical performance data for 25% weight fraction of carbon fiber reinforced PESU to facilitate both an understanding of 3D printed material behavior and facilitate damage modeling efforts. The aim is to characterize stress versus strain behavior under tension, compression and shear at room and elevated temperature conditions while keeping processing variables constant within each set. The experimental work section contains details about the material identifier and form, EDAM process conditions, post-processing conditions, specimen preparation, standards used for specimen geometry, testing, and equipment used. The results and discussion provide the stress versus strain plots for temperatures under tension, compression and shear, and statistical information about the mechanical properties. Fracture surfaces of tensile coupons subjected to 25°C and 190°C are investigated for observable differences and similarities.

4.2 Mechanical Specimen Preparation

4.2.1 Experimental Design, EDAM Processing and Post-Processing Methodology

A standard set of geometries, shown in Figure 20, were designed for extracting specimens to characterize the material properties of the printed material, also these designs were chosen in an attempt to minimize time and cost of preparing specimens given the capabilities of the CAMRI system and available resources at CMSC. Panel A is a vertical printed wall that consists of three beads along the 2 direction, tension and compression specimens along the 1 and 3 directions can be extracted, also, shear specimens along the 1-3 or 3-1 direction. Block A consist of a simple cube with unidirectional infill, the block is designed to be sliced in order to extract shear coupons along the 2-3 or 3-2 direction. Panel B is a flat panel with the height dimension, H, much smaller than the in-plane dimensions, L or W, Panel B option 2, namely, *Panel_B2_1* and *Panel_B2_2* are smaller versions of Panel B. Tension and compression specimens along the 2 direction can be extracted from these panels as well as shear coupons along the 1-2 or 2-1 direction. Panel B option 2 is recommended if the larger panel significantly warps during or post-print, the subsequent machining steps require sufficiently flat panels. For the experimental campaign, 8 panel A, 21 panel B option 2 and one block A were printed. The dimensions of the geometries are provided in Table 2.

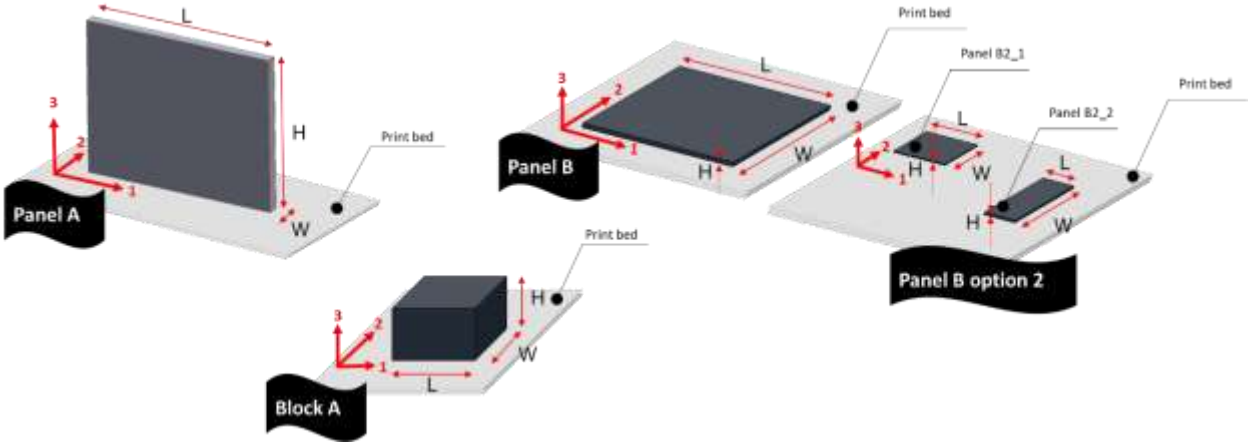

Figure 20 EDAM geometries used for extracting characterization specimens

Table 2 Dimensions of 3D printed geometries

Panel Type	**1 direction (X), L**	**2 direction (Y), W**	**3 direction (Z), H**
Panel A	320mm	18.45mm/3beads	321mm
Panel B	320mm	319.80mm	9mm
Panel B2-1	185.80mm	202.95mm	9mm
Panel B2-2	120mm	202.95mm	9mm
Block A	200mm	105mm	40mm

Simplify3D® was chosen as the slicing software for the geometries shown above. Figure 21a illustrates the infill structure for panel A, panel B and block A, although panel B option 2 is not shown, its print path follows that of panel B shown. The blue layers represent the outline and it is necessary to specify it as the designed dimensions will be smaller than specified otherwise. The purple layer is a print outline that surrounds the printed geometry, it does not come into contact with the part. A skirt layer is recommended to achieve a smooth print bead before the actual print of the geometry. An interesting observation are the transition regions, these are 90° turns which are clearly seen in panel B and block A. When extracting specimens from these printed geometries, care should be taken to avoid machining specimens too close to the transition region and a dimensional margin relative to the edges of the geometry should be considered. Another noteworthy observation is the commencement location at each new layer height for geometries of panel B type, this parameter is a fabrication choice made in the slicer software when selecting pre-specified or optimized start locations. Figure 21b illustrates this choice for panel B, the left hand side of the figure begins each new layer at the same location regardless of its previous spatial position whereas the right image shows the start location of a new layer at a different position relative to the commencement point at the current layer height. For geometries similar to panel B, it is wise to choose the same start point for each new layer height in order to reduce the likelihood of imposing a severe thermal gradient on the part. Moreover, a heated bed or print table is recommended for relatively large flat panels with the temperature preferably close to the glass transition temperature if possible and the layer time should be as quick as possible without inducing sagging effects. Overall, printing large flat panels is a challenge for certain materials such as reinforced polyphenylene sulfide (PPS) or PESU; however, certain materials like fiber reinforced polysulfone (PSU) may fare well when all of these considerations are accounted for.

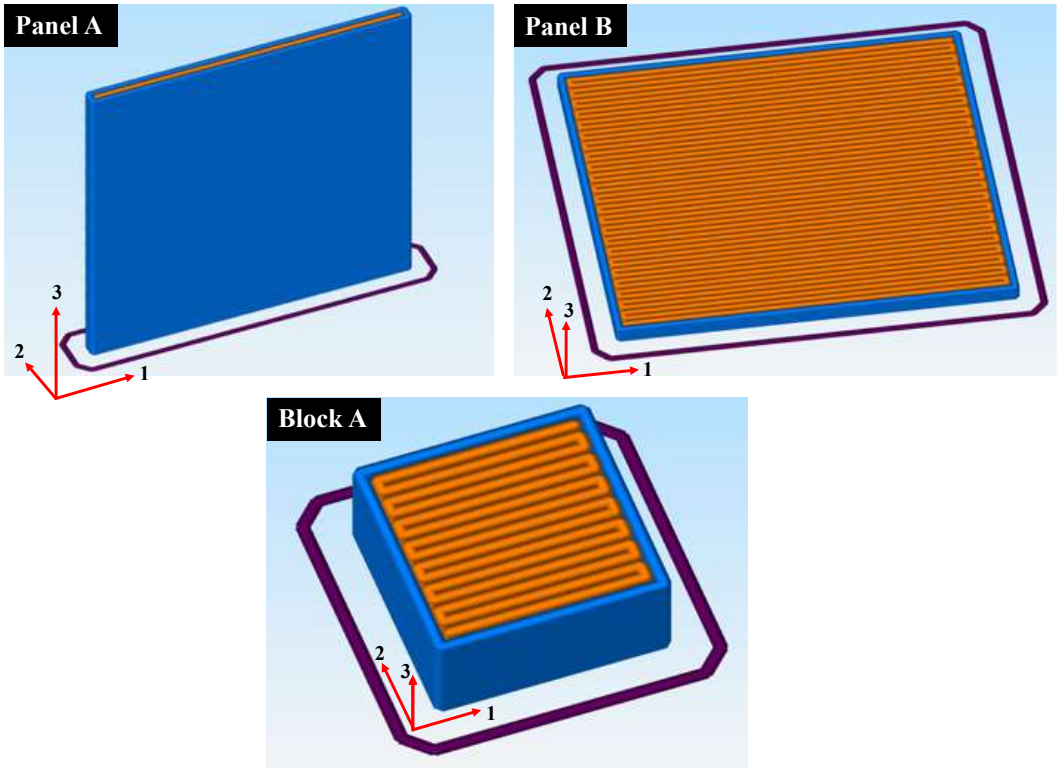

(a)

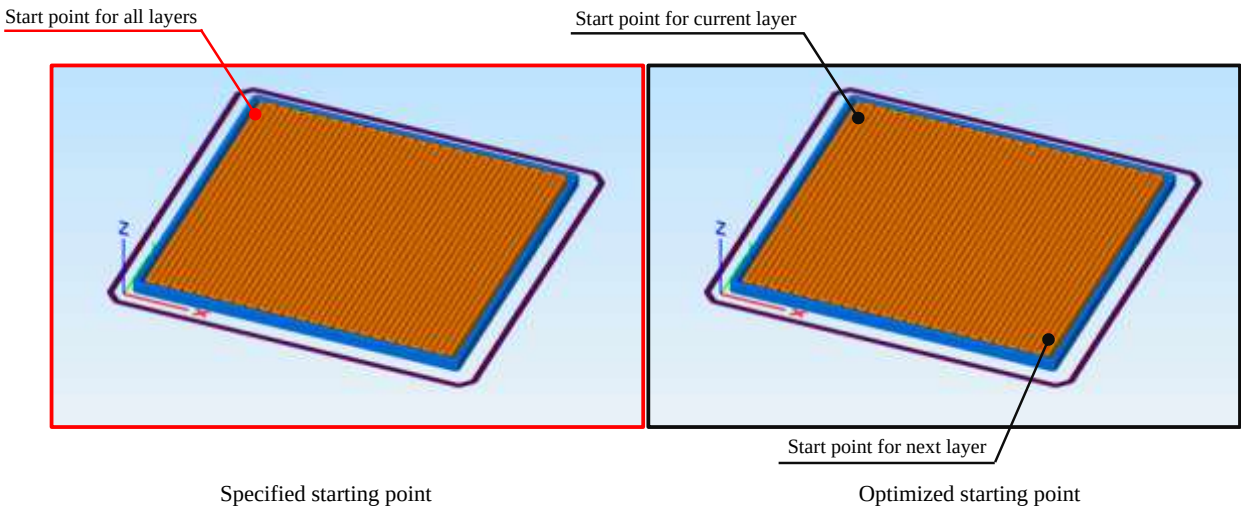

(b)

Figure 21 (a) Sliced geometries for characterization of material properties, (b) starting point specification for subsequent layer

The material feedstock used for this study is the 25% wt. carbon fiber reinforced PESU, this material is available in compounded pellet form as shown in Figure 22 and manufactured by Techmer PM. The feedstock identifier is *Electrafil® PESU 1810 3DP*. According to the

manufacturer's datasheet [192], the material is a specially formulated and compounded thermoplastic material designed for additive manufacturing of tooling for use in composite fabrication by autoclave curing; moreover, it can withstand cyclic temperatures in excess of 350°F (176.7°C). The compounded composite pellets are suggested to be dried in a desiccant dyer for up to four hours at 280°F (138°C) to obtain a recommended moisture content of 0.04% for printing. For this work, the composite feedstock were dried at 125°C for 4 hours before processing in the CAMRI system.

Figure 22 Compounded short carbon fiber reinforced thermoplastic feedstock for 3D printing

The EDAM processing conditions are specified in Simplify3D, it is encoded into a .gcode file then uploaded to the KMotionCNC program for execution. LabView alongside an external control panel are used for controlling temperature and other functions of the system (e.g., tamper). There are six temperature zones in the CAMRI system, the zones are illustrated in Figure 23 and they were set to 327°C, 343°C, 366°C, 365°C, 365°C, and 370°C, for zones 1 through 6, respectively. The temperature of the print bed was set to 120°C for panel A geometries, and 220°C for panel B and block A geometries. The print speed for panel A geometries was set to 3500mm/min, and 4000mm/min for panel B and block A geometries. A fan is turned on during the print session of panel A to prevent sagging, this fan is attached onto the CAMRI frame. However, a fan was not used for the other geometries. For all prints, a 4mm convergent zone nozzle diameter was used. The target bead width and height were 6.15mm and 1.5mm, respectively.

Lastly, an actively cooled mechanical tamper was used to compact the extrudate at a speed of 1500 rpm.

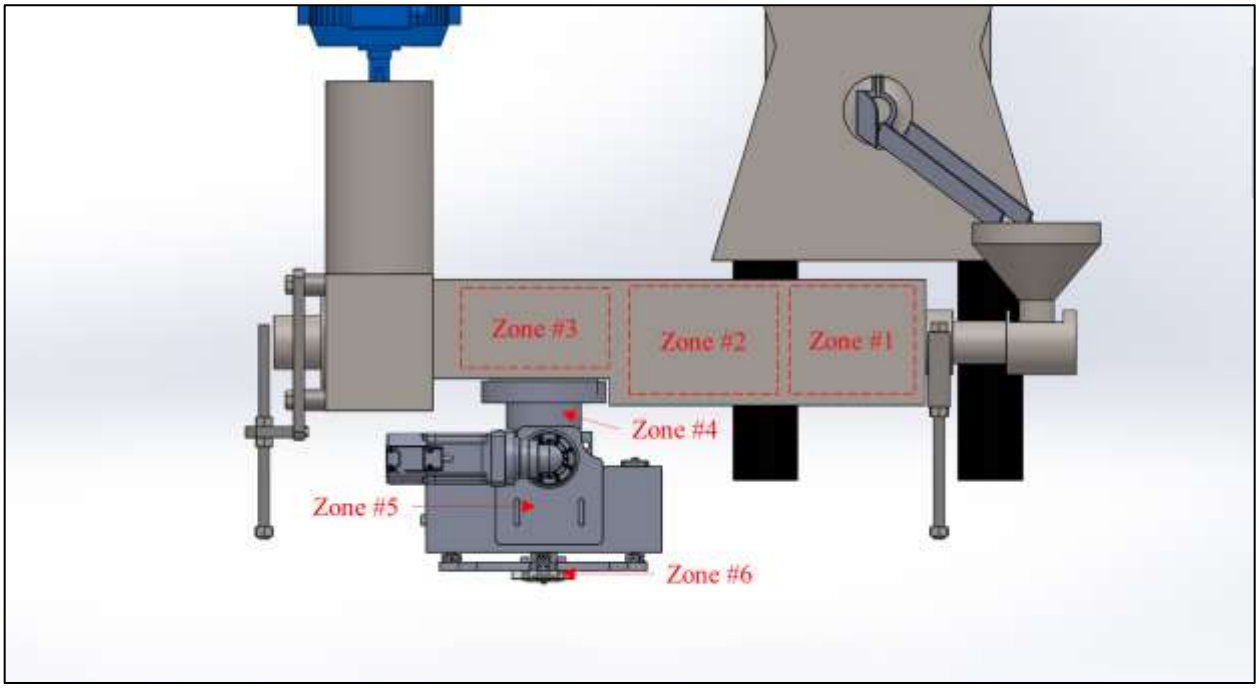

Figure 23 CAMRI extruder schematic with highlighted temperature zones

After the printing session, the geometries were thermally annealed for two hours at 190°C, this annealing process allows further polymer diffusion through the interface and alleviates some of the processing-induced residual stresses. A Grizzly helical cutterhead planer, model G1021x2 15 in. 3 HP, was used to machine away the two outer beads for panel A and the first two printed beads for panel B geometries, as depicted in Figure 24. For carbon fiber reinforced PESU, small increments of the surfaces were symmetrically machined away at a time; for example, the planer wheel handle moves the table height by 2mm for every revolution and approximately $1/16^{th}$ to $1/8^{th}$ of a revolution was made for each pass. One of the challenges encountered using a helical cutterhead planer is the fact that 3D printed vertical panels do not have a smooth flat surface and the ends are usually thicker than the center regions. A non-flat surface and thicker ends complicate the machining process since the first passes performed on a planer define the reference plane. The reference plane may not be parallel with the print direction and the entire operation will produce a panel with regions of the center bead machined away. As a result, the panel may warp, and this effect is shown in Figure 25 with the other end of the panel pinned to the table. While some of the

machined vertical panels warped, there were others that retained the center bead unmachined and did not warp. Despite this issue, there are benefits to using the panel such as reduced machining time, ease of use, and quality of machined surface. For characterization experiments that require critical dimensions and preservation of a single bead (i.e., assuming the geometries presented here are adopted), a computer numeric control (CNC) system is recommended; however, the use of a CNC does not guarantee the panels will not warp because of the internal stress re-equilibrium that inevitably occurs after material is removed. In general, machining process will induce warpage which can be avoided to some extent by symmetrically and incrementally machining both sides of a panel. To investigate the consequence of the machining outcome, tensile specimens were extracted from warped and non-warped panels and placed into a group. An analysis of variance (ANOVA) of the tensile stiffness and tensile strength were made to assess whether the hypothesis of sample properties is from the same population or not. Even though the sample size is relatively small, and the test is valid for normally distributed sets, the analysis can provide some insight into the samples exhibit different mean properties.

Block A had been sectioned into 24 rectangular ~4mm slices, along the 1 direction as displayed in Figure 24, using an evolution metal chop saw with a steel-rated cutting wheel. Due to the difficulty of precisely cutting the block, some variability in thickness is expected and was found to range between 3.5mm and 4.5mm. The top surface of panel B (i.e., non-machined side) and both sides of the block A slices were minimally grinded and polished using an orbital sander with 80-grit and 400-grit sandpaper, respectively. A more consistent cross-sectional dimension is found when grinding and polishing the surfaces of the 3D printed panels and block. A waterjet was used to cut the mechanical specimens from the panels and sliced sections of the block. To prevent the specimens from falling inside the waterjet, a small tab was added to the top of each specimen. For compression specimens that were tabbed, it is recommended to use a subsequent waterjetting step to remove the tabs to obtain a consistent flat surface which is a requirement for end-loaded compression samples. A belt sander or band saw can be used for removing the tabs from tensile and shear specimens since an irregular surface will not hinder experimental results. An example schematic for waterjetting the panels is provided in Figure 26a for reference. All mechanical coupons were dried in an oven for 2 hours at 115°C post-waterjet.

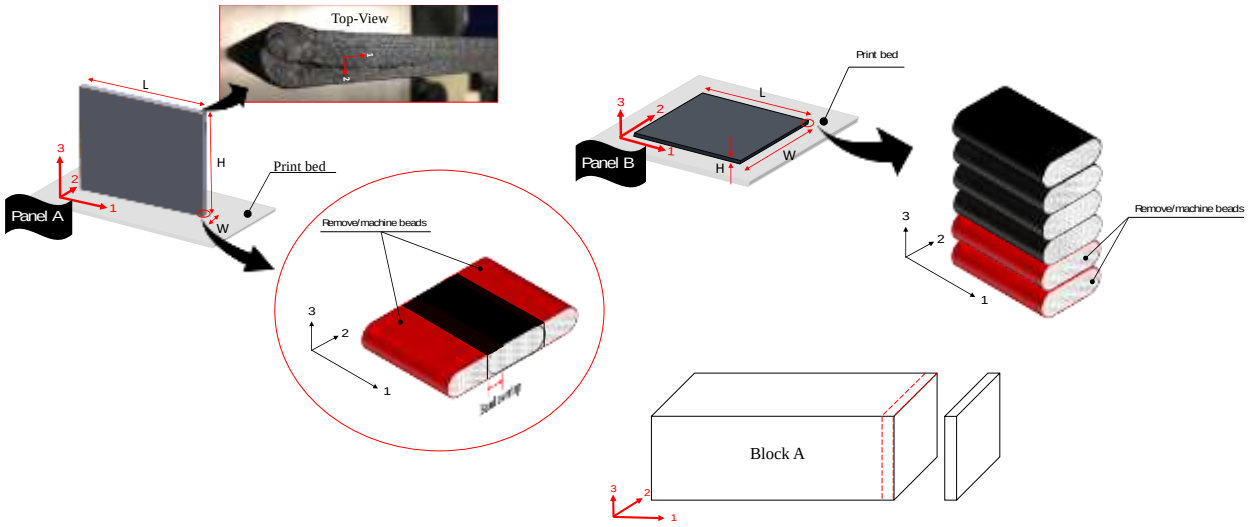

Figure 24 Machined regions of panel A, panel B and block A geometries

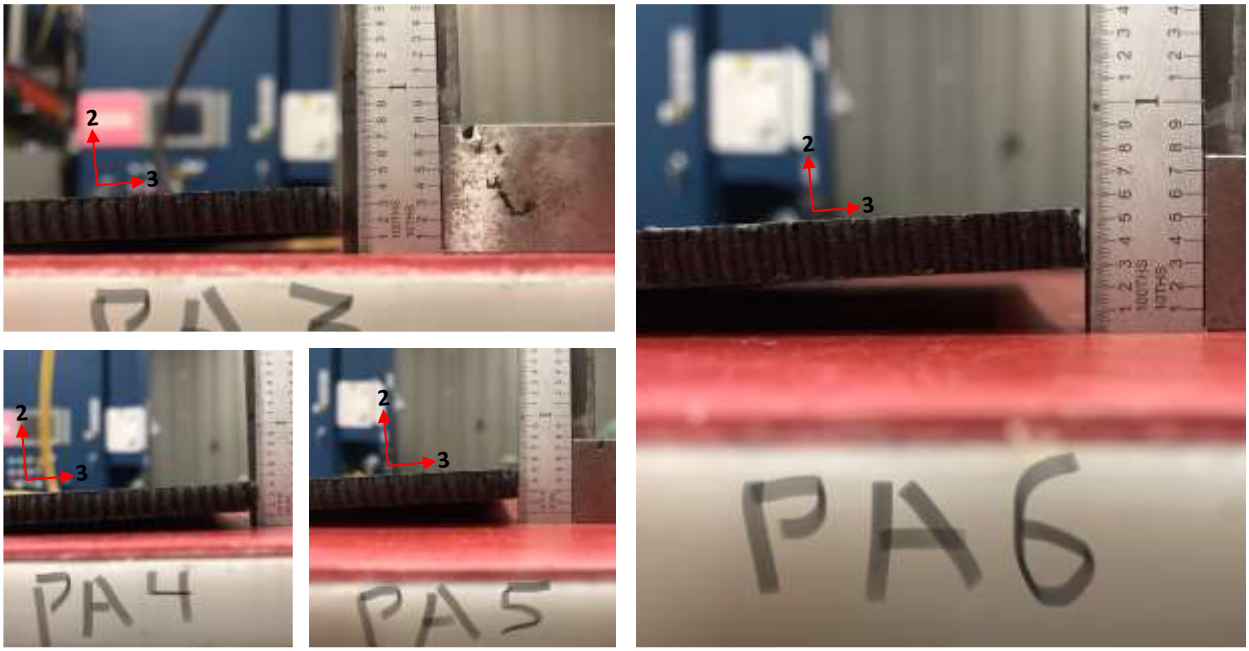

Figure 25 Warped panel A geometries (panels 3, 4, 5 and 6) after machining using helical planer

Tensile specimens were designed according to ASTM D638; however, different dimensions were used were used in an attempt to account for the printed bead's dimension. In other words, the gage section dimensions were designed to be an integer multiple of a bead width or height. Shear coupons were designed according to ASTM D5379; however, the width-to-notch ratio was kept at 2.0 and the notch-to-notch distance at 9mm. Dog-bone shaped compression designed based on the ASTM D695, no modifications were made to the geometry. Specimen

dimensions are illustrated and provided in Figure 26b. For convenience, Table 3 shows the elastic and strength properties that can be obtained for each printed geometry. The Poisson's ratio, ν_{23}, is challenging to obtain and it is estimated using micromechanical methods.

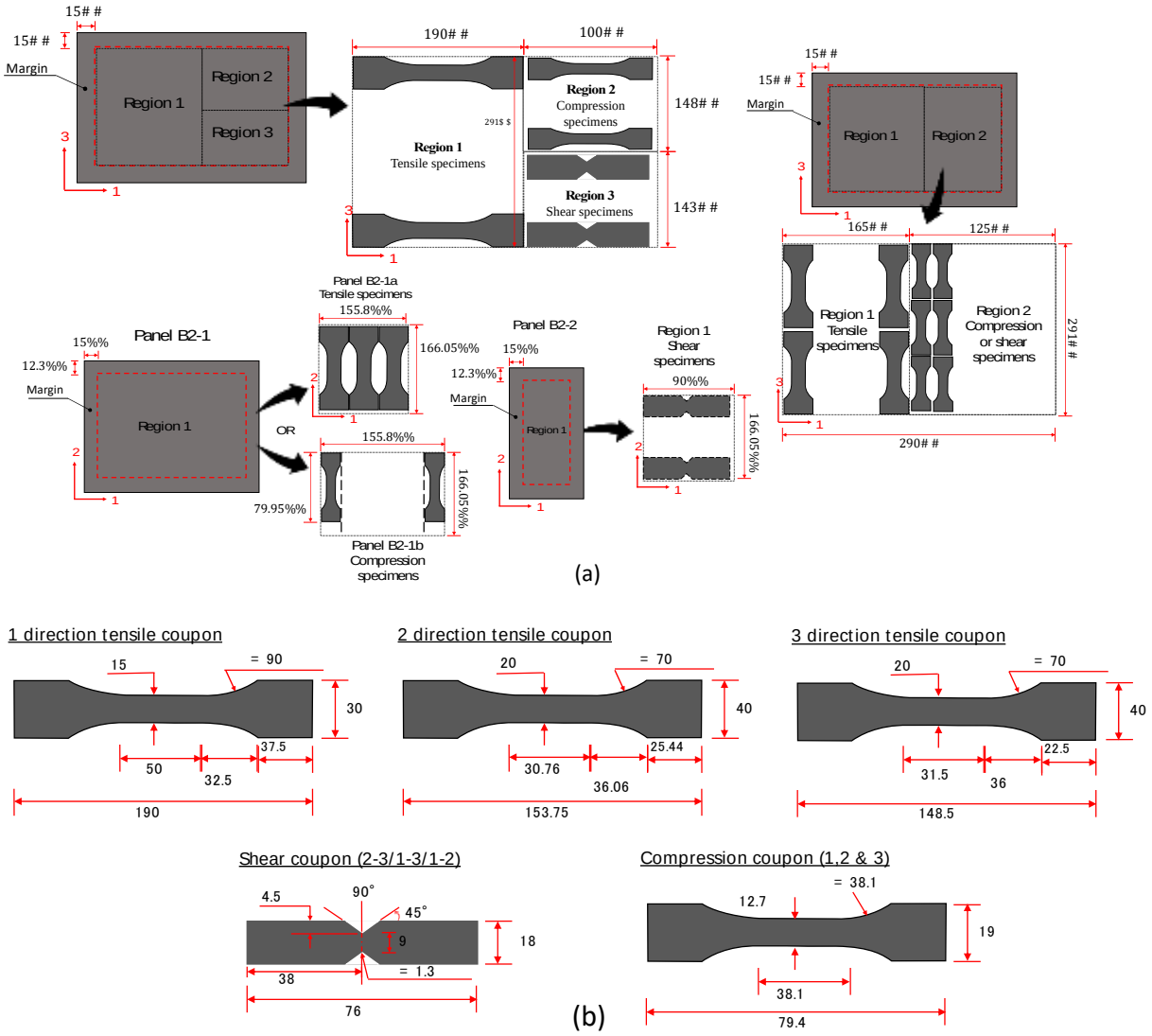

Figure 26 (a) Specimen outlines on panels, (b) specimen dimensions

Table 3 Extracted properties from printed geometry

Properties	*Panel A*	*Panel B*	*Block A*
$E_1/X_1^T/X_1^C$	X		
$E_2/X_2^T/X_2^C$		X	
$E_3/X_3^T/X_3^C$	X		
$G_{23}/G_{32}/S_4$			X
$G_{13}/G_{31}/S_5$	X		
$G_{12}/G_{21}/S_6$		X	
ν_{23}/ν_{32}			
ν_{13}/ν_{31}	X		
ν_{12}/ν_{21}		X	

4.2.2 Strain Acquisition, Mechanical Testing, and Post-Processing Methodology

The digital image correlation (DIC) technique was used for measuring the surface strain field of mechanical specimens, and an extensometer was installed in selected tensile experiments. To enable DIC measurement, the coupons were thinly coated with a Rust-Oleum high heat enamel white spray paint. Once dried, a random pattern of black speckle dots was imprinted onto the white surface. A dot size of 0.007" (0.178mm) was imprinted on compression and v-notch shear specimens, and a dot size of 0.013" (0.330mm) was used for tensile specimens. Cross-sectional dimensions were measured using a standard digital caliper for tension and compression specimens, and a micrometer for v-notch specimens. A servo-hydraulic MTS 810 with a 5-kip (22.24KN) load cell was used for all mechanical tests, and the MTS 651 environmental chamber was used for elevated temperature experiments. Mechanical wedge grips were used for all tensile specimens. Shear and compression specimens required the use of a fixture, an Iosipescu fixture was employed for shear deformation and the modified ASTM D695 test fixture (i.e., the associated fixture corresponding to the Boeing BSS 7260 standard) was utilized for compression experiments. The mechanical experiments were conducted in uniaxial displacement-controlled mode, and the effective elastic and strength properties were measured by applying uniaxial tension, compression and shear deformations.

Based on the glass transition temperature of the neat thermoplastic polymer, temperatures for mechanical tests were chosen within the glassy regime. The amorphous thermoplastic exhibits significant flow behavior at temperatures beyond the glass transition, it enters the rubbery phase and extensive creep, or relaxation behavior is observable. To determine the glass transition temperature of the PESU, a TA instruments dynamic mechanical analyze (DMA) Q800 was

utilized for performing a double cantilever beam experiment at a frequency of 1Hz. The glass transition temperature was deduced from the drop in storage modulus as defined in ASTM D7028, this was observed at 215°C.

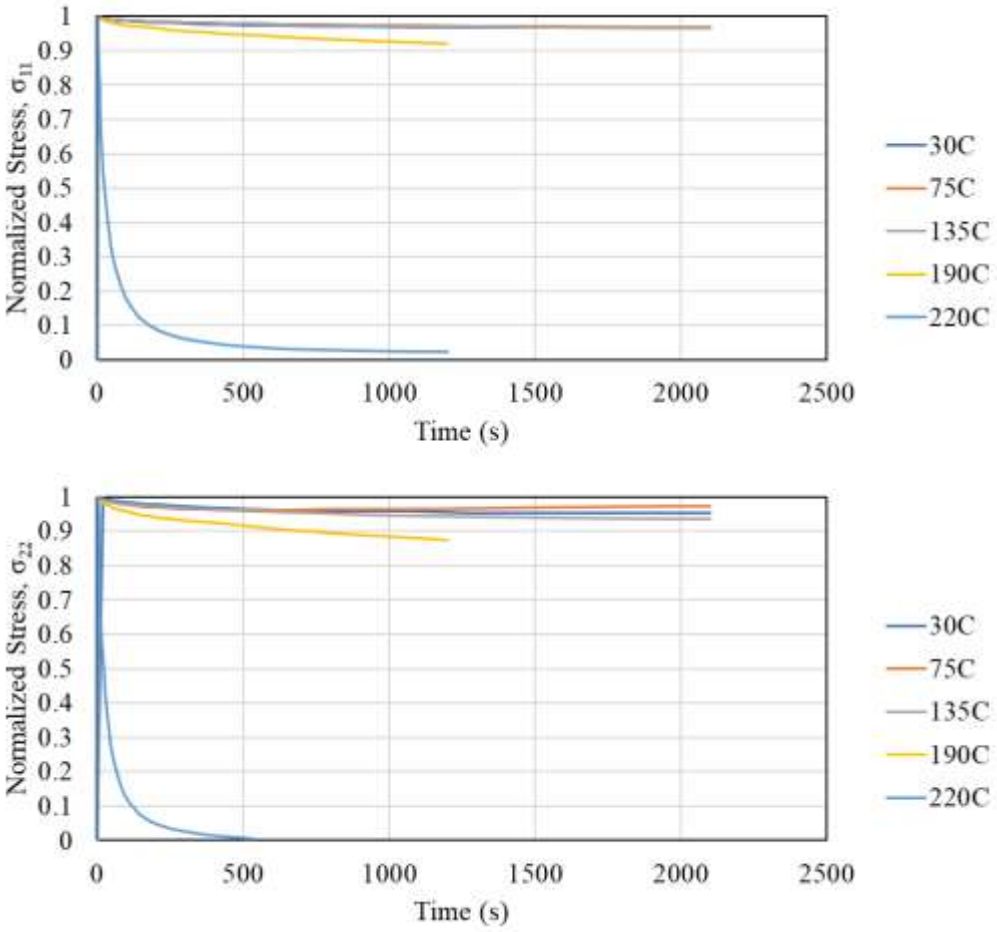

Figure 27 Stress relaxation along the print direction (top) and in-plane transverse direction (bottom)

Three temperatures above 25°C were chosen at approximately 30%, 60%, and 90% of the glass transition temperature (i.e., 70°C, 130°C, 190°C), these temperature values are somewhat arbitrary though the intention was to choose temperatures high enough to reflect the conditions in molding applications which are typically around 350°F (177°C) or below. In this work, room temperature is defined at 25°C, and it is used interchangeably in the subsequent sections. The nonlinear response stemming from stress relaxation is undesirable and needs to be minimized so that damage-induced nonlinearity can be properly investigated; therefore, stress relaxation

experiments were conducted to assess the extent of relaxation at the prescribed temperatures. The TA instruments Q800 DMA with the three-point bending fixture was used for uniaxially loading the composite beam at a constant strain value of 0.05% to investigate the stress relaxation phenomena. Noteworthy to mention, the stress relaxation experiments are also used for characterizing the Prony series of the composite along the 1 and 2 directions.

Figure 27 shows the normalized stress relaxation behavior near the chosen temperatures, two observations are evident; firstly, significant stress relaxation in a relatively short amount of time is observed past the glass transition temperature as expected, secondly, the chosen temperatures exhibit less than 5% relaxation before 300 seconds (5 minutes). Mechanical experiments performed on the MTS at elevated temperatures are typically done within 2 – 5 minutes. With this in mind, it is reasonable to assume that the nonlinear behavior associated with relaxation is minimal for experiments under 5 minutes. Although the strain rate affects the mechanical performance as discussed in Chapter 2, it is assumed negligible in order to minimize the total number of experiments. Since minimal relaxation is desired during the mechanical experiments, the cross-head displacement speed should be as quick as possible; however, a quasi-static condition must be induced so as to not induce inertial effects or dynamic motion. Room temperature tensile, compressive, and shear tests were performed with a crosshead displacement rate of 2mm/min, 1mm/min, and 2mm/min, respectively; furthermore, elevated temperature tensile, compressive, and shear tests were executed with a crosshead displacement rate of 1mm/min, 1.3mm/min, and 1mm/min, respectively.

The elevated temperature soak or dwell times for all geometries were determined through a finite element transient heat transfer analysis, the thermal material card is available in the Appendix section. The convective film coefficient of the environmental chamber is unknown and conservatively assumed as $50 W/m^2K$. Figure 29 illustrates the temperature contour for half of the print direction sample about the symmetric plane for 70°C and 190°C ambient temperature conditions. The analyses show that 5 minutes of dwell time was enough to achieve a uniform temperature distribution. Similarly, analyses were conducted for compression and shear coupons, and 5 minutes was also deemed sufficient. For all tensile coupons, a minimum dwell period of 5 minutes was adopted though some experiments were allowed to dwell for as long as 20 minutes in order to determine if there were noticeable differences in mechanical performance. No substantial difference in mechanical performance was found within a temperature set. To expedite the

experimental campaign, shear specimens that belonged to the tested temperature set remained inside the environmental chamber throughout the experiment and each specimen experienced a dwell period of at least 2 minutes with the exception of the first specimen which experienced a dwell period of at least 5 minutes during commencement. A similar procedure was followed for compression experiments at the elevated temperatures. For tension experiments conducted at elevated temperature, the wedge grips were tightened before closing the environmental chamber door and increasing the temperature. Thermal stresses are expected during the temperature ramp, to alleviate thermally induced stresses, the servo-hydraulic MTS was executed in force-control and the specimen was kept at a load level at zero or near zero until the dwell period ended. For additional details on the test methodology, the reader is referred to the ASTM D5379 and D695.

Figure 28 Experimental test configuration for a print direction coupon under tension within the environmental chamber

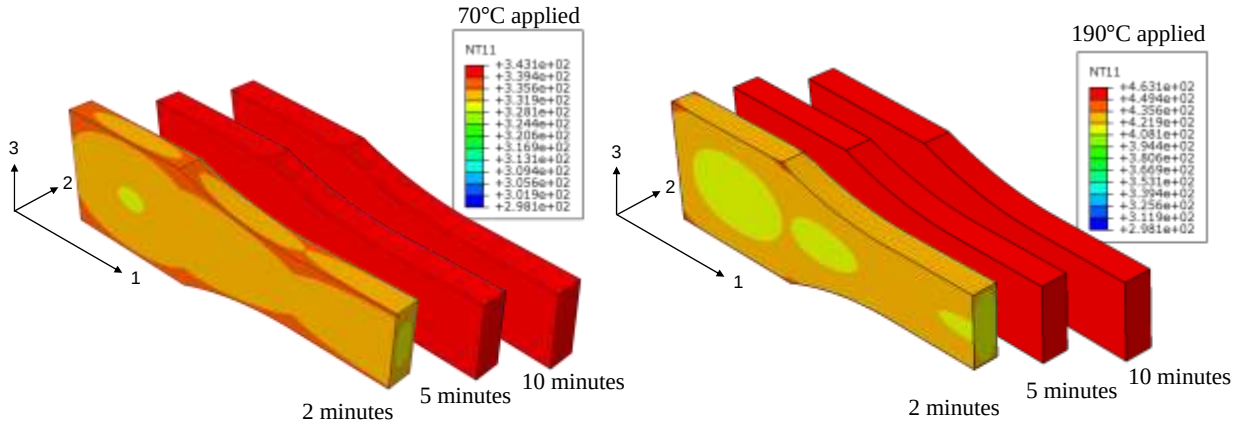

Figure 29 Finite element transient heat transfer analysis for print direction specimens

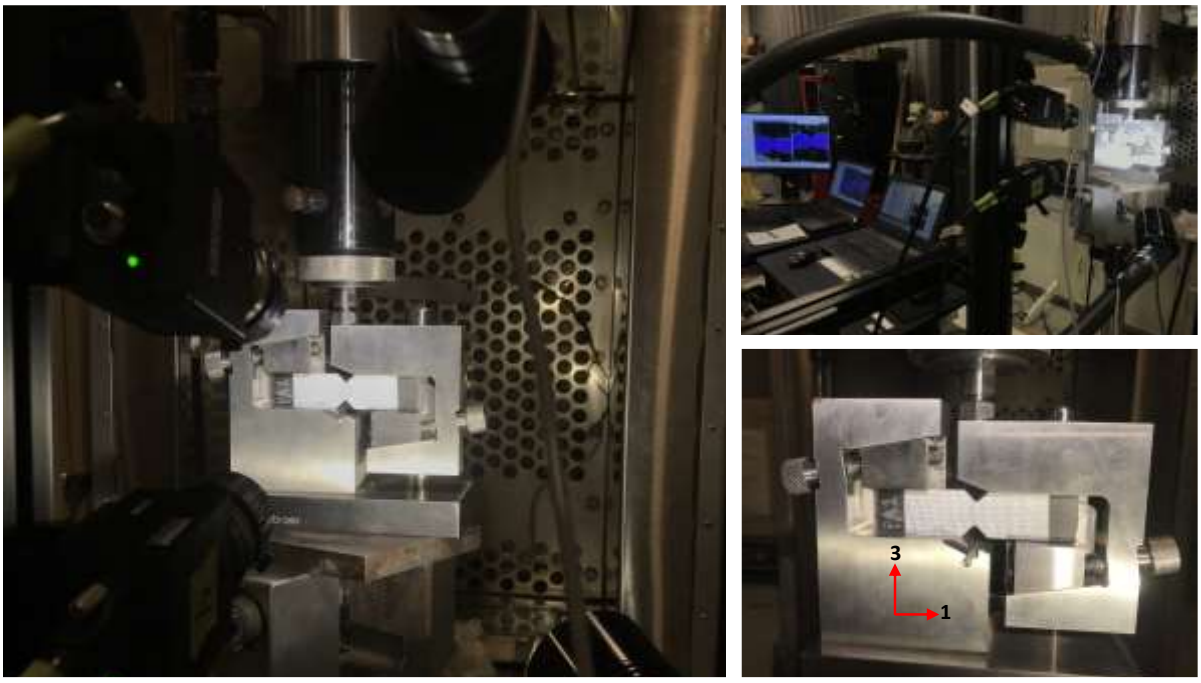

Figure 30 Experimental test configuration for Iosipescu shear test using two DIC cameras

For all room temperature mechanical tests and elevated temperature shear and compression tests, two 5-megapixel (MP) cameras with Correlated Solutions' VIC-SNAP software were used for 3D DIC. For elevated temperature tensile tests, a single 5MP camera with VIC-SNAP was used for 2D DIC. DIC-measured displacements were recorded to compute the surface full field Green-Lagrangian strain distribution for all room temperature tests, elevated shear and compression tests, and the 190°C tension tests, the engineering surface strain field for tensile coupons at 70°C and 130°C were computed and averaged to compare with the MTS 632.11B-20 extensometer of 1.0 in.

gage length. The average strain field, $\tilde{\varepsilon}_{ij}$, computed with DIC analysis was plotted against the effective stress, $\tilde{\sigma}_{ij}$, to characterize the meso-scale homogenized material response. The entire gage-section was chosen as a region of interest (ROI) to compute the global strain, $\varepsilon_{ij}(x_1, x_2)$ for tensile and compression coupons; however, global shear strains were computed from a narrow ROI between the notches. Effective stress, $\tilde{\sigma}_{ij}$, was calculated as the measured force from the load-cell divided by the tensile or compressive coupon's average width and thickness ($\tilde{w} \times \tilde{t}$) along the gage section or the notch width and thickness for shear specimens. The effective stiffness of a coupon was evaluated as the slope of $\tilde{\sigma}_{ij}$ versus $\tilde{\varepsilon}_{ij}$ curve within appropriate strain-ranges guided by the aforementioned ASTM standards. Compression and shear coupons generally have anomalous mechanical behavior during load introduction due to the fixture settling in place; in essence, this is observed as either an initial stiffening or softening effect. As a result, the strain ranges are chosen away from these anomalous regions. The ultimate strength of a coupon is reported as the maximum stress recorded or the stress corresponding to the intersection of the measured chord (i.e., stiffness) modulus at a 0.2% strain offset, from the true zero strain point, and the stress-strain data. The true zero strain point may not correspond to the measured zero strain due to anomalous material behavior at load-introduction, and it is defined as the intersection of the extended chord modulus line to the strain axis. A non-linear region is observed in all cases, and a non-linear onset value is computed from the stress-strain data. The non-linear onset value reported is computed as the 2% – 5% departure of chord linearity between the last strain value used in the computation of the chord modulus and the last strain data point. The ultimate strain is taken as the strain at rupture and the peak strain is taken as the strain corresponding to peak stress.

4.2.3 Optical and Scanning Electron Microscopy (SEM)

Knowledge of microstructural features is important to facilitate understanding of the meso-scale response. To obtain micrographs and microstructural information, small samples are extracted from a printed geometry. Samples used in microstructural investigations were extracted from panel A, three samples were considered for microscopy and one sample for fiber length distribution measurements. To remove the polymer from the composite, the sample is placed inside a furnace and exposed to a temperature of 700°C for at least two hours. During this process, the polymer degrades, carbonizes and essentially evaporates. Afterwards, fibers are collected using tweezers,

placed onto a glass slide, and dispersed using silicone oil as demonstrated in Figure 31. A matrix of images is captured using the Leica DMI 5000M optical microscope, the image set contains thousands of fibers and these images are stitched together to form a mosaic. ImagePro is utilized to measure the fiber lengths from end-to-end after calibrating the scale. The other samples are mounted and potted using epoxy, with the surface normal oriented along the three principal print directions. The potted sample is grinded and polished using the Struers© pads. The Leica optical microscope is also used for acquiring a mosaic of micrographs at 10x and 50x magnification. The mosaic is imported into the open source software imageJ, this software is used for obtaining the fiber volume fraction, void volume fraction, and void dimensions. The volume fraction of the constituents is measured using the particle thresholding technique, an example is illustrated in Figure 31. Fiber orientation requires cylindrical-shaped fibers and it was not measured because most fibers were observed to have a kidney-bean shape. The photographic method of measuring the fiber orientation based on the major and minor axes of a fitted ellipse cannot be performed on kidney-bead shaped fibers since this technique results in erroneous measurements [193].

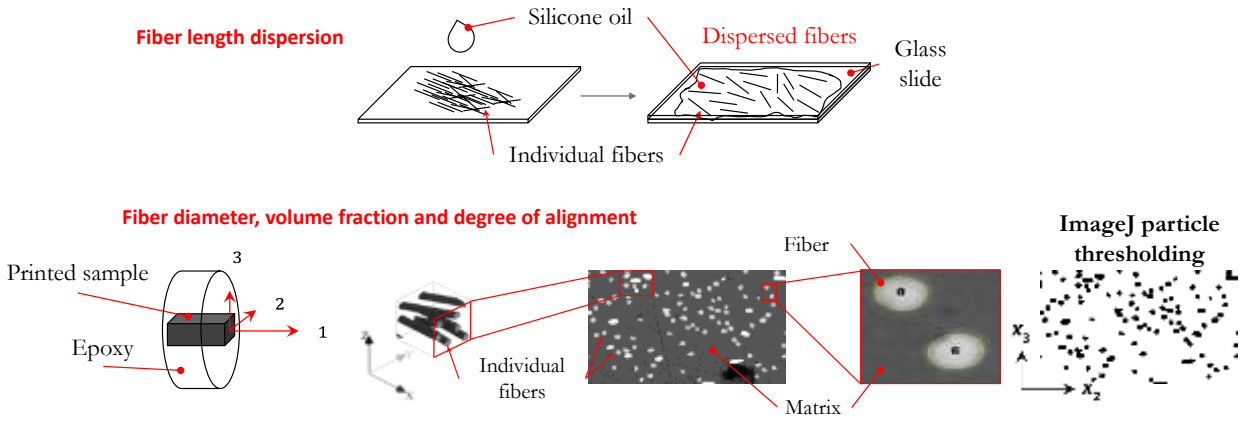

Figure 31 Fiber length dispersion illustrated for distribution measurements and depiction of prepared sample for micrograph observations using imageJ

Post-mortem fractography can provide insights into failure mechanisms and provide visual clues of the fiber orientation with respect to the fractured surface. Fractographic images were acquired via SEM to investigate features on the fracture surfaces. Specifically, the fracture surfaces of tensile specimens along the 1, 2, and 3 directions at 25°C and 190°C were investigated in addition to compression and shear specimens, compressive and shear images are provided in the

appendix section for completeness. A Quanta 650 FEG SEM was used for observing and acquiring the images. All samples were coated with a 3nm film of Platinum. The accelerating voltage was set to 15KV with a fixed working distance of 10mm.

4.3 Microstructural Observations

4.3.1 Microstructure along 1, 2, and 3 Direction via Optical Microscopy

Most fibers have a preferential orientation toward the print direction in material extrusion processes with convergent-zone nozzles. Tekinalp et al. [46] measured the fiber orientation state for an carbon fiber reinforced ABS processed using FDM and compression molding, the extrusion direction was labeled as a_{33}. In their study, the components of the second-order orientation state is reported and it is evident that most fibers are oriented preferentially along the extrusion or print direction since the measured a_{33} value was in the range of 0.87 and 0.92. In micrograph images, fibers are seen as the lighter phase, the matrix as a darker gray, and voids as nearly opaque. When fibers are preferentially oriented along the print direction, the micrograph appears to have white speckle dots contrasted with a gray background; On the other hand, fibers not oriented along the print direction appear as highly elliptical white regions. Figure 34a illustrates a micrograph of a polished surface of a section of a panel A geometry that is relatively close to the edge. Contrasting bands can be observed from the micrograph image, the darker regions correspond to sections of the cross-section with a greater amount of fiber collimation and lighter regions with less fiber collimation. From this micrograph, the bounds of a bead or at least the interfaces that encapsulates a bead is not clearly visible; however, there are regions of elongated voids which are suspect to lie at the interface. Two lines distances were measured, one between the dark and light region, and another offset vertically by one-half of the length of the dark region. The distances are observed to be approximately 1.6mm, which is close to the nominal bead height of 1.5mm. From these observations, a bi-orientation state exists within the span of a bead height or a core-shell morphology as commonly found in injection-molded samples. Figure 33b illustrates a closer look into the microstructure, with the core-shell section zoomed in. From this micrograph, it can be visually seen that lighter regions contain more fibers which are less collimated with respect to the print direction. Further micrographic investigated is required to verify this visual morphology and confirm it is not a flow-induced anomaly.

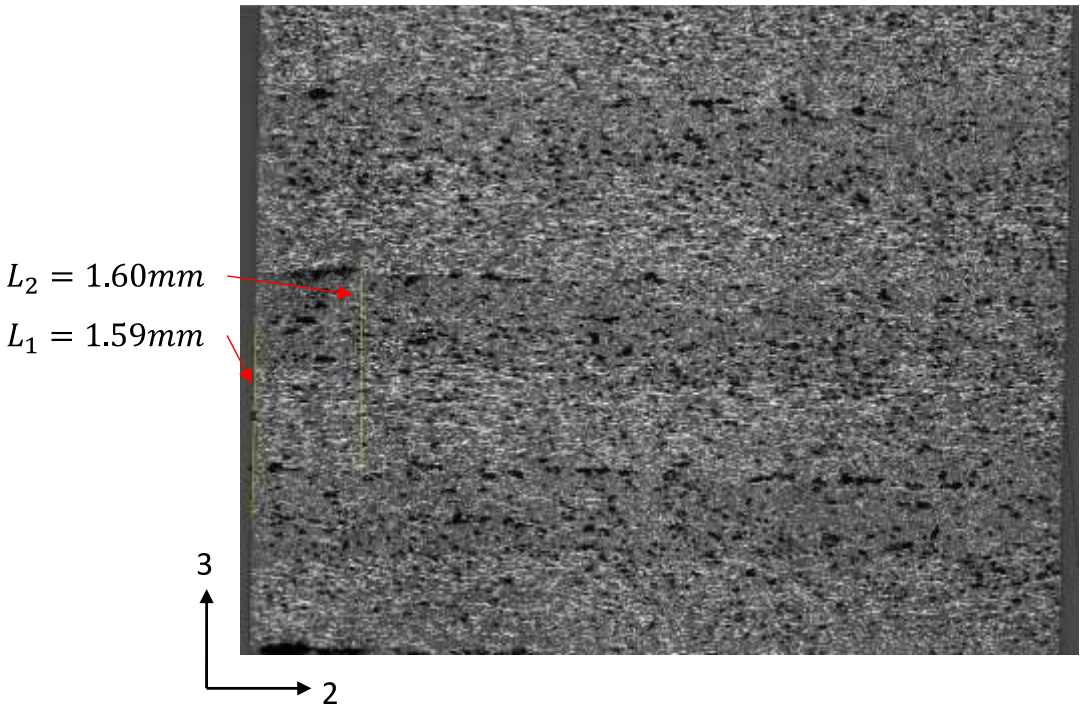

Figure 32 Micrograph along the print direction at 10x showing distinct high and low contrast bands

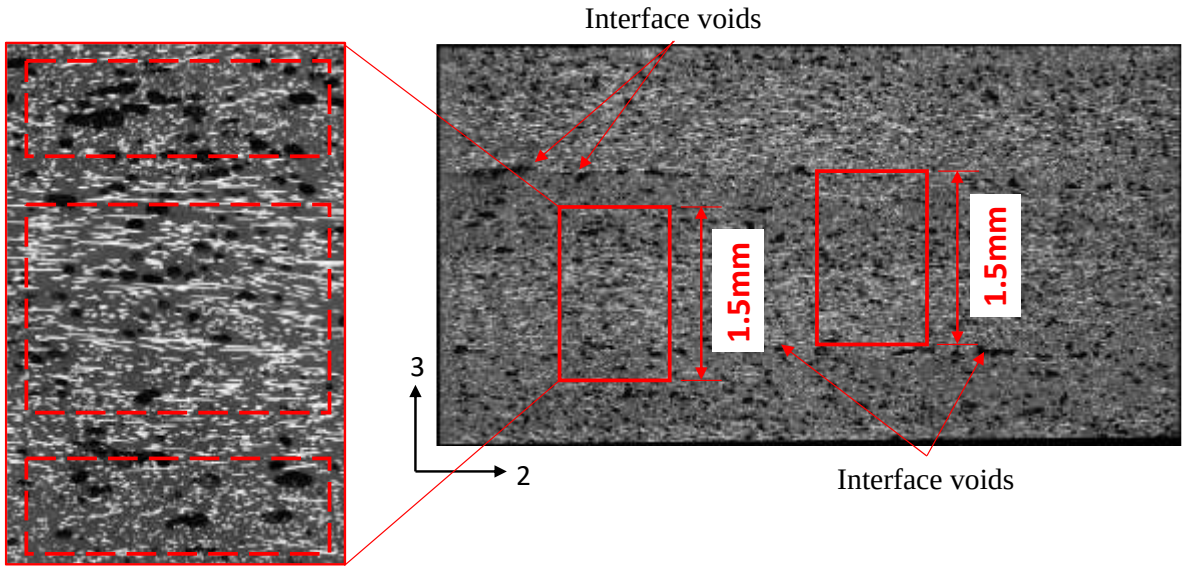

Figure 33 Micrographs along the print direction illustrating high contrast of misaligned fibers

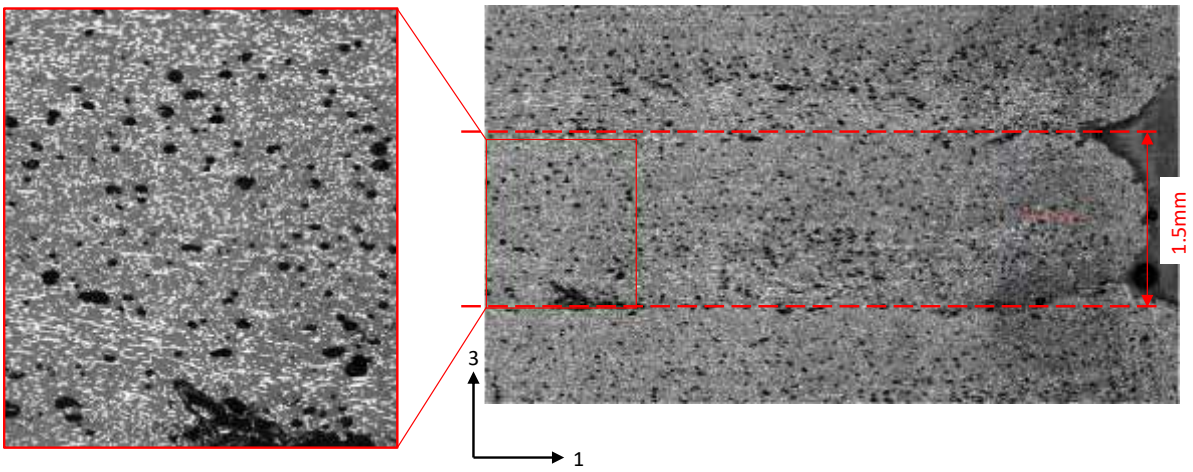

Figure 34 In-plane transverse (2) direction micrograph

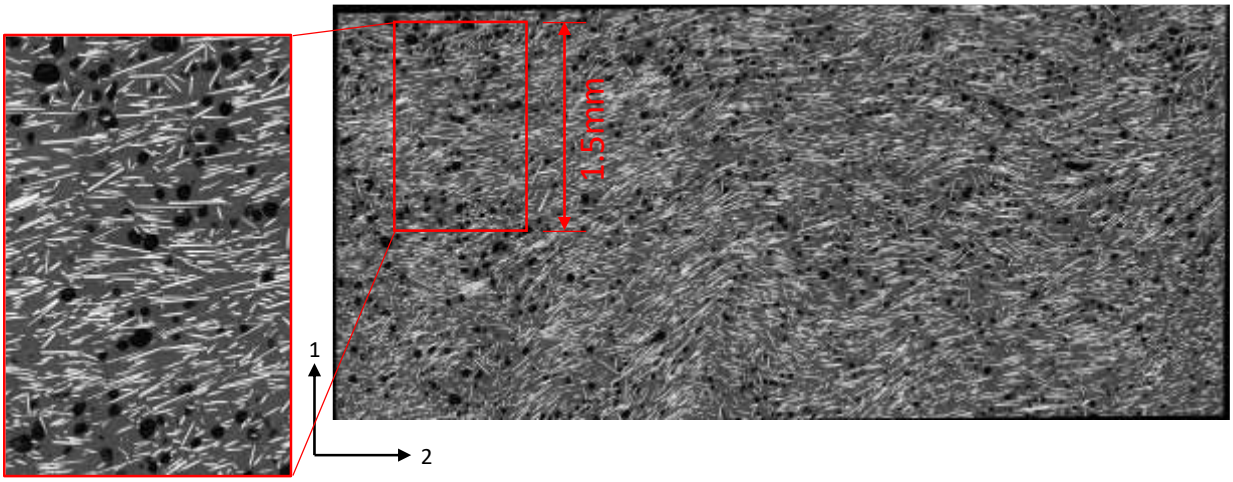

Figure 35 Stacking direction micrograph

4.3.2 Microstructural Measurements

The microstructural measurements made were the fiber volume fraction, fiber length, void volume fraction, and fitted ellipsoidal void size. The fiber orientation is not measured due to a majority of the fibers having a kidney-bean shape, this is seen in the micrograph shown in Figure 36. Moreover, a $100\mu m \times 100\mu m$ grid is superimposed onto the micrograph to measure the distribution of fiber volume fraction, the size of the grid is arbitrarily defined with the intention to assume a reasonable representative size; however, the overall average is not affected by the grid discretization. Likewise, a $500\mu m \times 500\mu m$ grid is used for measuring the distribution of void volume fraction. The voids can be reasonably assumed ellipsoidal as seen on the image at the right hand side of Figure 36,

ellipsoidal shaped voids have been observed within the bead and infrequently at the interface. Based on the displayed micrograph, the following observations are noticed: (i) the spatial configuration of the fibers are stochastic, (ii) voids are relatively large compared to the fiber-end size, (ii) a $100\mu m \times 100\mu m$ grid discretization can have a majority of fibers oriented along the print direction or misaligned.

The distribution plots are presented in Figure 37 below, most plots include the average and coefficient of variance values. The fiber length and void volume fraction distribution plots exhibit a skew distribution whereas the fiber volume fraction appears normally distributed. The fiber volume fraction distribution suggests that there are regions with high fiber clustering relative to other low-packed regions. Void distribution plot suggests a majority of the grid regions have a relatively low void presence; although, the mean void fraction stands at approximately 5%. It is should be noted that the volume fraction distributions are subject to the grid discretization and it will change if the grid size is altered. A total of 1000 fibers were measured; this distribution contains fibers between $18.5\mu m$ and $421\mu m$. While the arithmetic average is observed to be $90\mu m$, the fiber length weighted average, defined as $FL_w = \Sigma(n \cdot l^2)/\Sigma(n \cdot l)$, is computed as $119\mu m$. In the weighted average formula, n is the count of fibers associated with length l.

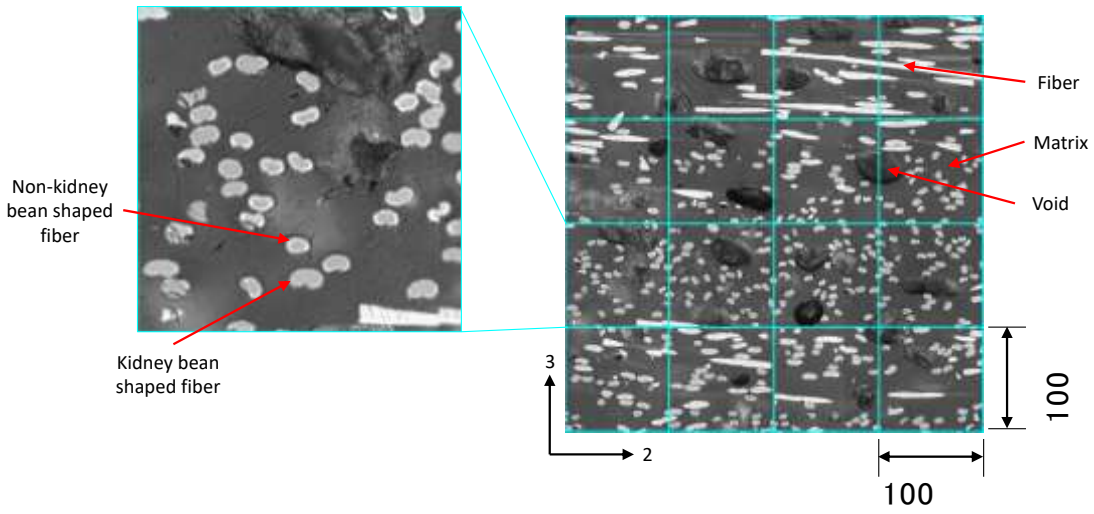

Figure 36 Print direction microstructure at 50x magnification

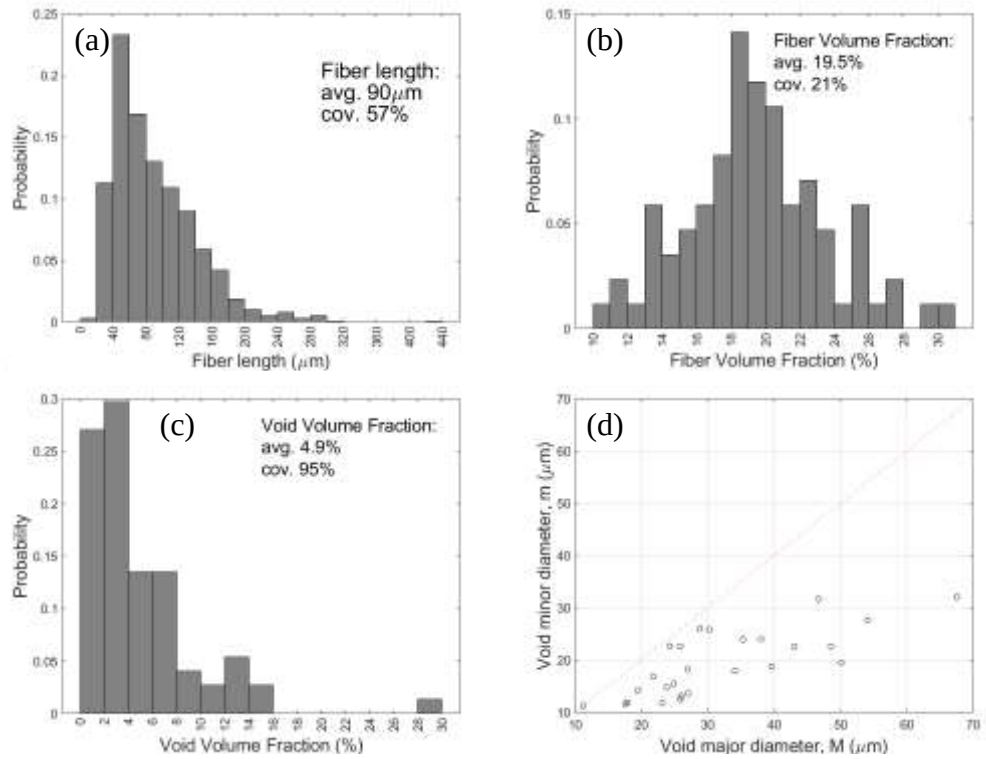

Figure 37 (a) Fiber length distribution, (b) fiber volume fraction distribution based on $100\mu m \times 100\mu m$ grid, (c) void volume fraction distributions based on $500\mu m \times 500\mu m$ grid, and (d) fitted ellipsoidal dimensions of voids

4.4 Tensile Performance of 25% Wt. Carbon Fiber Reinforced PESU

The DIC-computed surface strain field, stress versus strain plots for different temperatures, and bar plots illustrating the distribution of tensile mechanical properties with temperatures are provided in the sub-sections below. The effective tensile modulus and strength are observed to decrease with an increase in temperature along all directions. Specifically, the tensile modulus ratio between room temperature and 190°C for the 1, 2 and 3 directions are 1.35, 1.21, and 1.25, respectively; by the same token, the strengths are 2.03, 2.48, and 2.69, respectively. The average tensile modulus at room temperature along the 1 direction is observed to be 3.4x and 4.5x greater than the average tensile modulus along the 2 direction and 3 direction, respectively. Moreover, the tensile strength at room temperature along the 1 direction is 3.2x and 3.0x greater than the 2 direction and 3 direction, respectively.

The tensile properties along the print directions are evidently greater than the tensile properties along the 2 or 3 directions, this observation bolters the argument of significant fiber

collimation along the print direction. The room temperature tensile modulus along the 2 direction has been observed to be 1.3x greater than the room temperature modulus along the 3 direction; however, the strengths are observed similar. Based on the micrographs, the stacking direction has been observed with an insignificant amount of fiber collimation whereas some evidence of fiber collimation along the 2 direction is apparent. Therefore, the stiffness is expected to be greater and the strength is unlikely influenced. Stress concentrations arising from the presence of voids are hypothesized to adversely affect the strength properties, it produces intense localized stress regions by which micro-cracks initiate and evolve at low effective stress levels.

The nonlinear onset in stress versus strain plots denotes the point at which yielding occurs, the tangent stiffness begins to decrease beyond this point. A decrease in tangent stiffness accompanies a reduction in secant modulus, initiation and evolution of micro-crack increases the compliance and can be reasonably assumed to be directly responsible for the nonlinear behavior in brittle composites. Since temperature directly affects the polymer, it is expected to influence the nonlinear onset. For coupons loaded along the 1 direction, the nonlinear onset value does not follow a recognizable trend; however, a decreasing trend is noticeable for coupons loaded in either the 2 or 3 directions. Similarly, temperature is expected to impact the peak and rupture strains. While a pattern in peak and rupture strains was absent in tensile loaded specimens along the 1 direction, a discernable decreasing trend can be observed in the transverse directions with an increase in temperature.

4.4.1 Performance along 1 (Print) Direction

The surface strain-field distributions for tensile loaded specimens along the 1 direction at room temperature and 190°C are shown in Figure 38a and Figure 38b; in addition, the post-mortem images are also displayed. The strain distributions shown were taken at approximately the 0.2% average strain point. Strain-field images for tensile loaded specimens at different mean strain levels and temperatures are provided in the appendix. From the strain-field images, the magnitude of strain appears to change across the width. The reason for this varying strain contour across the width of the sample is due to load eccentricity, a bending moment is induced as a result of the load eccentricity. Although a bending moment is undesirable for uniaxial tensile tests, the severity of the bending moment can be estimated based on the difference in strains at equidistant points along the width [194]. The percent bending about the 2 direction can be computed using the following

formula, $B_2 = (2/3)(\varepsilon_2 - \varepsilon_2)/\varepsilon_{avg} \times 100$. The percentage of bending was found to be approximately 6% at the 0.2% strain level, however, a percentage of 25% can be obtained if the extreme strain values are used though bending percentage based on extreme values may not be accurate because of the inherent non-uniformity of the strain-field. The modulus of elasticity is not expected to be affected by the small amount of bending; however, the strength may be sensitive to the load eccentricity. Therefore, the true mean strength values are suspected to be slightly greater than the average strength values measured. The surface strain field at the elevated temperature are seen to have regions of high compliance and overall non-uniformity. The micrograph shown in Figure 34 illustrates irregular-shaped and elongated voids along the stacking direction interface, these are suspected to produce compliance along the print direction. Furthermore, consideration should also be given to the distribution of microstructural properties along the print direction; for example, local fiber volume fraction with fibers exhibiting greater collimation relative to the bulk fiber orientation state may also contribute to the observed non-uniformity in strain.

To assess whether the mean values of strength or stiffness are different between specimens extracted from warped and non-warped panels, an analysis of variance was conducted. The distribution between room temperature tensile coupons extracted from warped and non-warped panels is shown in Figure 39. The computed p-value for the strength distribution case was 0.0805, and 0.0308 for the stiffness case. Assuming the usual 5% confidence threshold, the null hypothesis is rejected for the mean stiffness and accepted for the mean strength; in other words, no difference is found in strength values and a difference in stiffness between both panels is suspected. However, the mean stiffness is similar in magnitude with a difference of 2.3%.

The failure modes for all coupons at room temperature were lateral and occurred at the start of the gage region, these are shown in Figure 40. A closer inspection of the fracture surface reveals the topographic roughness which is unlike the coupons tested along the 2 or 3 directions. Coupons tested at elevated temperatures were observed to fail within the gage section or at the start of the gage section with the overall fracture occurring laterally and a similar fracture topography to the room temperature case, the images are available in the appendix. Figure 41 illustrates the stress versus strain plots for all temperature data sets. The raw data set contains erroneous data points as a result of the noise inherent with high frequency acquisitions, the noisy data is mitigated using a MATLAB local regression smoothing function, called smooth. The observed undulations within the non-linear portion of the stress-strain plot are due to smoothing of stress-strain extreme data

kinks (e.g., reduction in stress and strain value as damage evolves). The stress-strain behavior has an initial linear portion followed by non-linear behavior, and the observed non-linear portion is pronounced at elevated temperatures. Within the glassy state of the polymer, the non-linear mechanical behavior observed is believed to be a dominated by competing damage mechanisms such as matrix cracking, fiber pull-out, and interfacial de-bonding. The distribution in tensile stiffness and strength properties for the different temperature sets are shown in Figure 42. Both strength and stiffness distributions at 190°C exhibit greater variability relative to the room temperature distribution. The increase in variability is suspected to arise from both a reduction in matrix shear transfer efficiency since the properties of the polymer degrade with an increase in temperature. Furthermore, the presence of voids are attributes that engender severe stress concentrations are perhaps exacerbated at elevated temperatures.

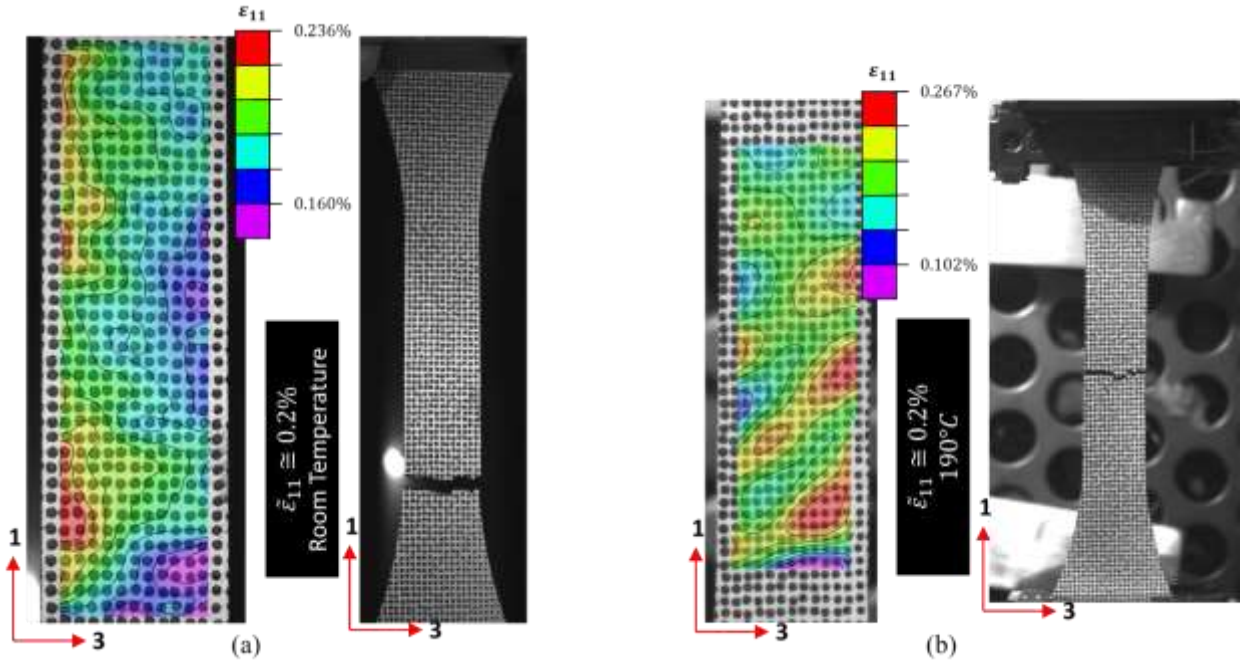

Figure 38 DIC-generated Lagrangian surface strain field at the 0.2% field-averaged value along the print direction (left) and post-mortem coupon (right) at (a) room temperature, and (b) 190°C

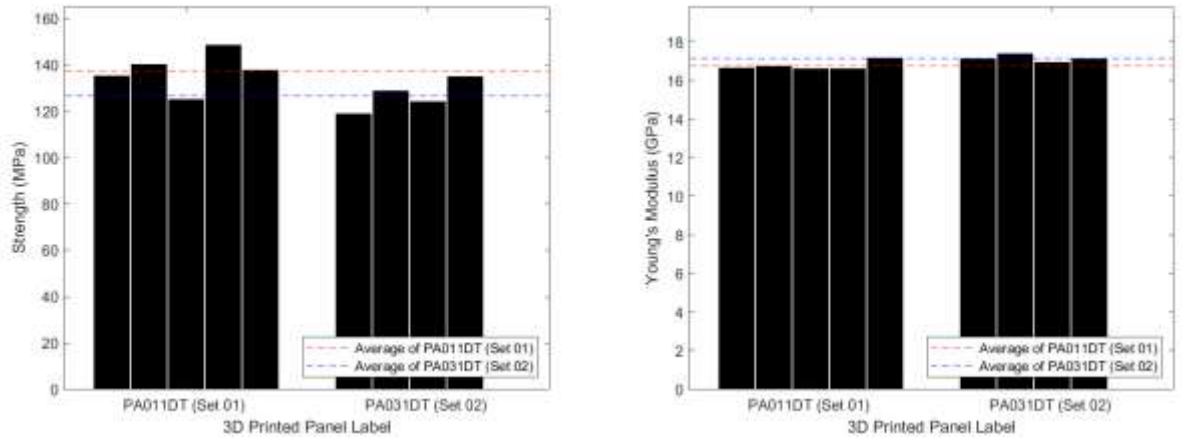

(a) (b)

Figure 39 Room temperature (a) strength distribution, and (b) stiffness distribution of specimens extracted from non-warped (PA011DT) and warped (PA031DT) panels

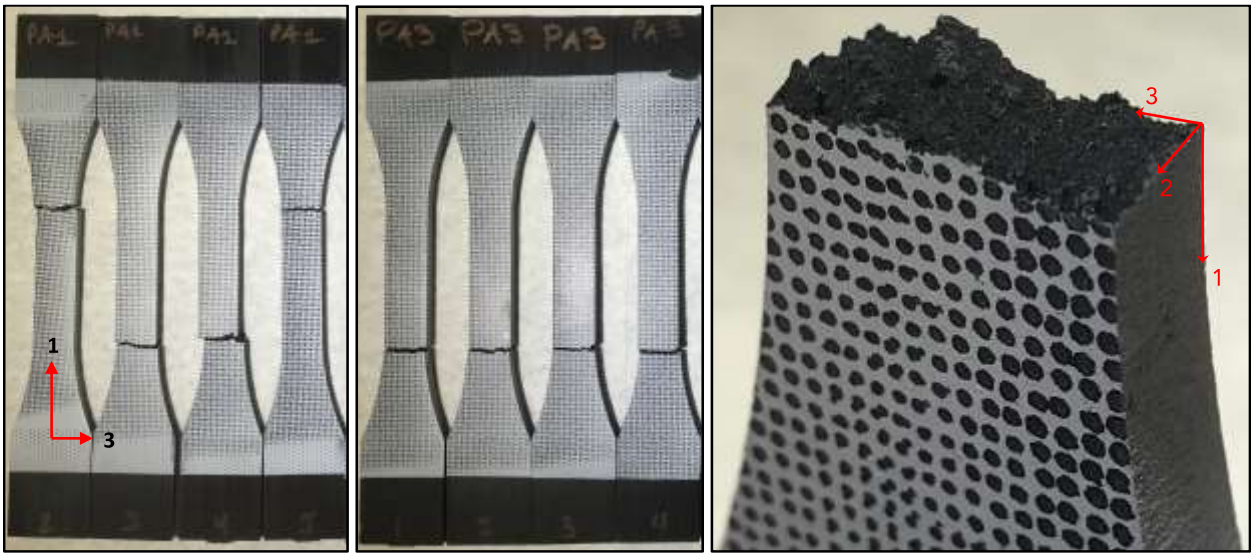

Figure 40 Fracture mode of tensile loaded coupon along the 1 direction at room temperature

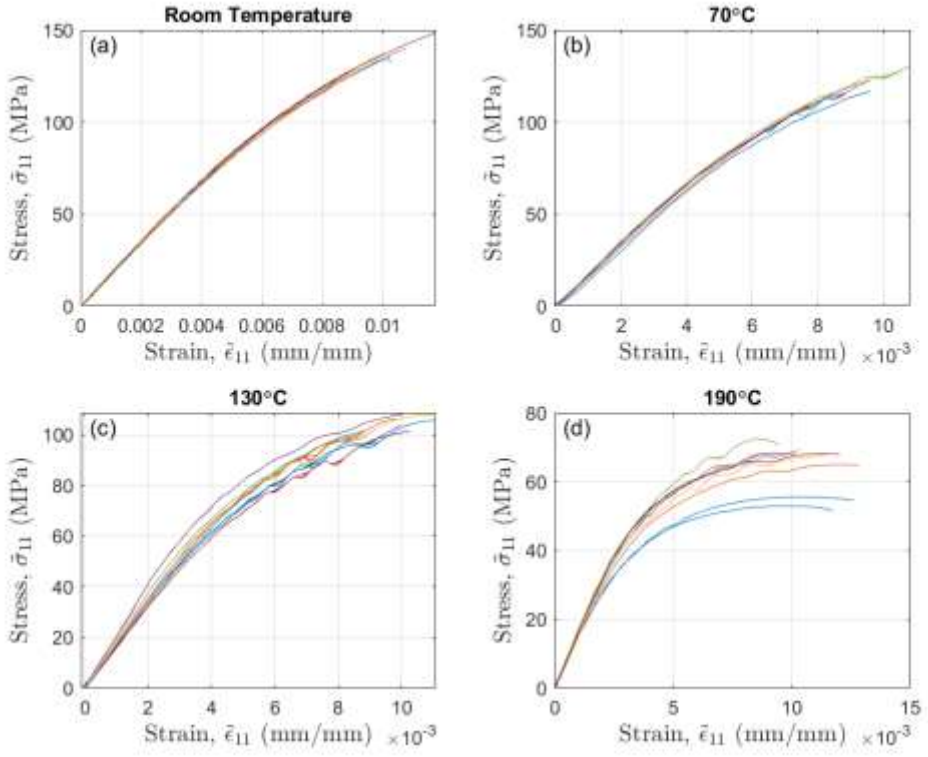

Figure 41 Effective stress versus field-averaged strain for tensile loaded specimens along the print direction at (a) room temperature (b) 70°C (c) 130°C (d) 190°C

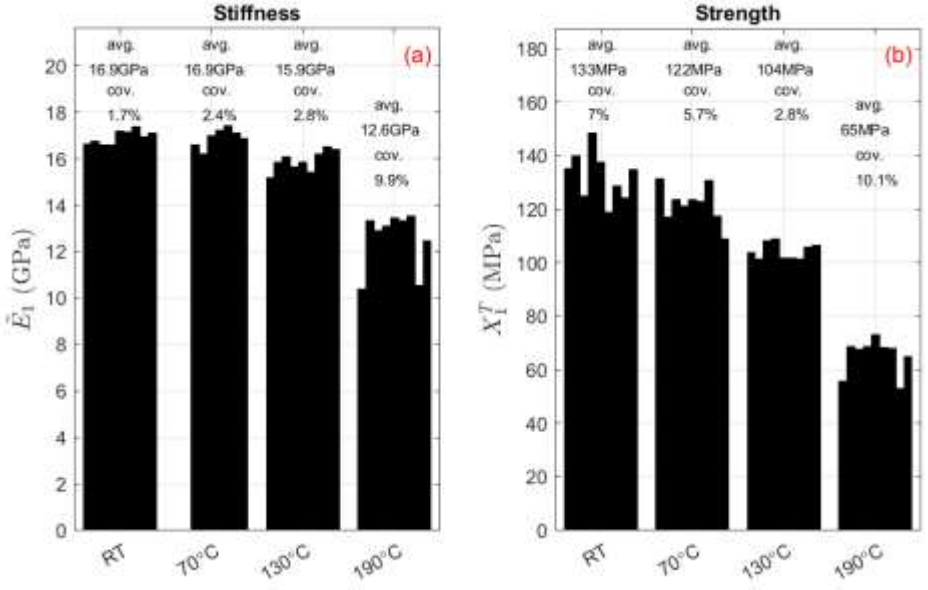

Figure 42 Distribution plot of effective tensile stiffness and effective tensile strength with temperature along the print direction

4.4.2 Performance along 2 (In-Plane Transverse) Direction & 3 (Stacking) Direction

The surface strain-field distributions for tensile loaded specimens along the 2 direction at room temperature and 190°C are shown in Figure 43a and Figure 43b, respectively, these distributions are snap-shots taken at approximately 0.2% average strain. The strain field distribution for these tensile loaded specimens at different average strain levels and temperatures are available in the appendix section. From these plots, a non-uniform strain distribution is observed, with a linearly-spaced contour range from 0.170% to 0.262% at room temperature and 0.127% to 0.270% at 190°C. In other words, certain regions on the surface of the tensile specimen are more compliant than others. From a micromechanical perspective, stiffness is influenced by fiber collimation, fiber volume fraction, strong fiber/matrix interface adhesion, and low void content. From a meso-scale point of view, bead-to-bead interfaces along the 2 direction are spaced approximately 6.15mm apart (i.e., the equivalent of a bead width), interfaces can be argued as exhibiting greater compliance than the regions within the bead itself since mechanical properties at the interface rely on polymer diffusion. The room temperature strain field plot does indeed contain compliant zones, the distance between two arbitrarily chosen compliant regions is approximately 6.15mm, although this coincidence does not necessarily imply with indubitable confidence that the interfaces lie in the compliant regions and a meticulous inspection is needed. At elevated temperatures, these compliant zones are still visible though a distinct spatial interval is not seen. The failure mode for these samples were all lateral, with the fracture plane located either in the gage section or within the width transition zone as shown in Figure 44. Evidently, the macroscopic crack is orthogonal to the loading direction and it is reasonable to assume the micro-cracks were oriented in a similar fashion. A closer look at the fracture surface of a sample is shown, four distinct dark narrow regions across the width is visible and these regions are the stacking direction interfaces. Despite the overall lateral fracture, the fracture surface appears to have local changes in depth. Upon visual inspection, the fracture surface appears to be located at the interface though some regions appear to transition into the bead. The stress versus strain plots are shown in Figure 45, from these plots the average rupture strains were observe to decrease with an increase in temperature; specifically, at 25°C, 70°C, 130°C, 190°C , these strains were 0.92%, 0.78%, 0.70%, and 0.52%, respectively. The distribution of tensile stiffness and strength is shown in Figure 46, it is clear that the mean values decrease with an increase in temperature.

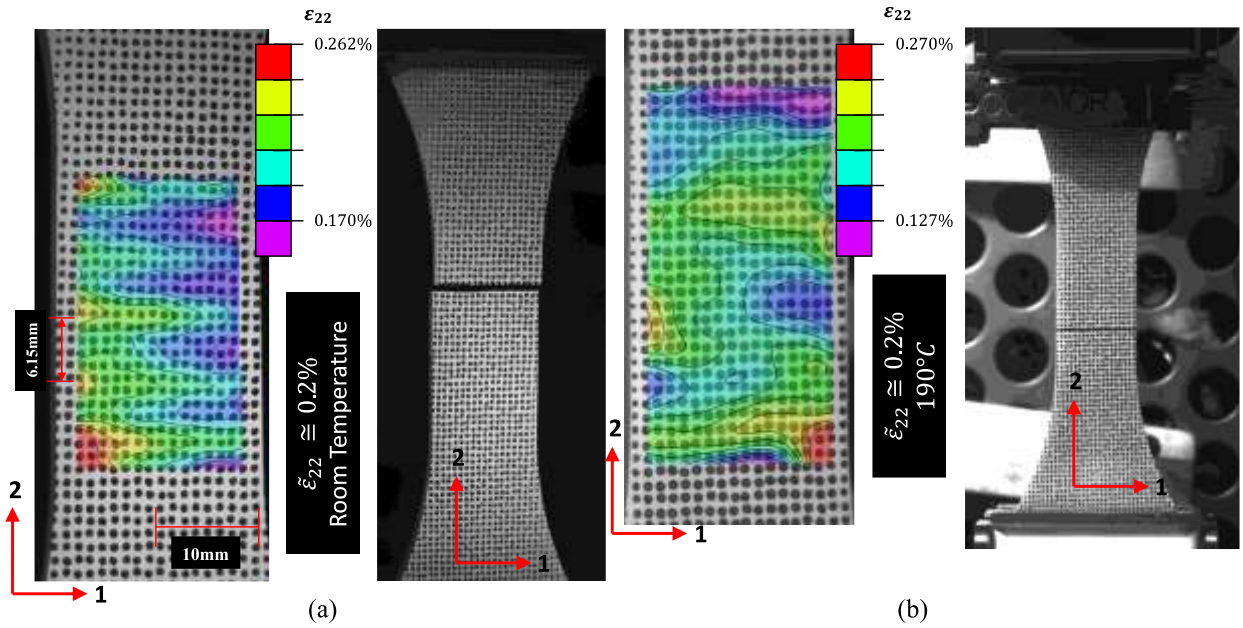

Figure 43 DIC-generated Lagrangian surface strain field at the 0.2% field-averaged value along the 2 direction (left) and post-mortem coupon (right) at (a) room temperature, and (b) 190°C

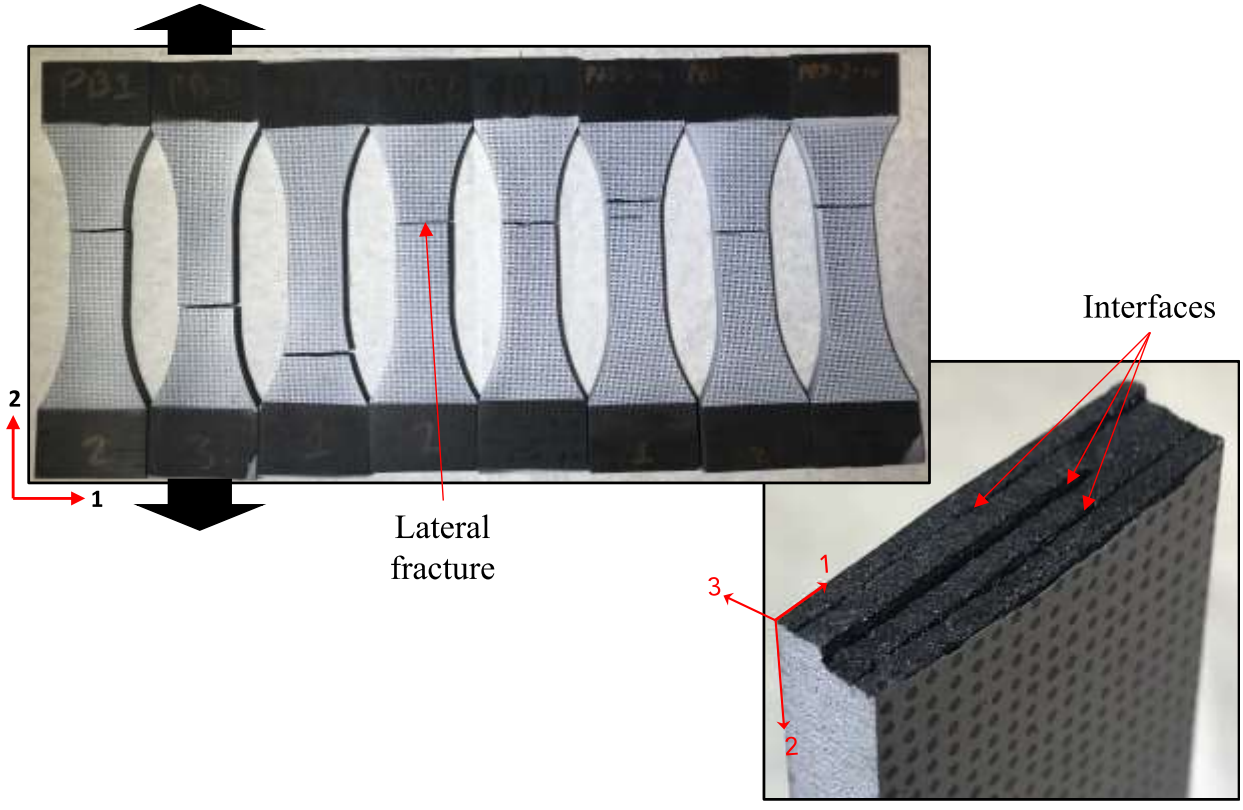

Figure 44 Fracture modes of tensile loaded specimens along the 2 direction at room temperature

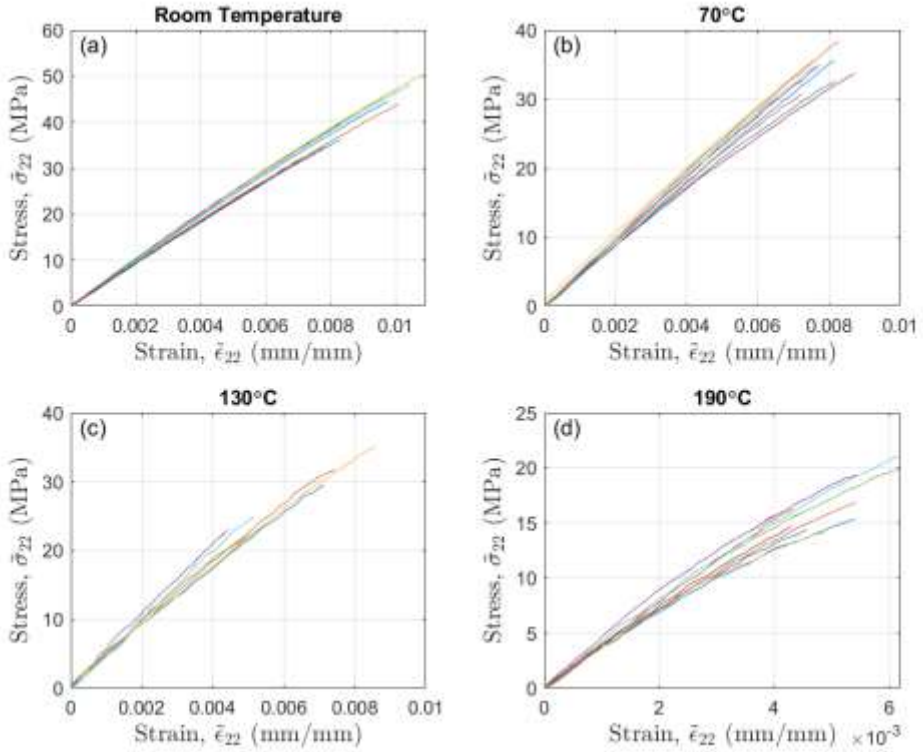

Figure 45 Effective stress versus field-averaged strain for tensile loaded specimens along the 2 direction at (a) room temperature (b) 70°C (c) 130°C (d) 190°C

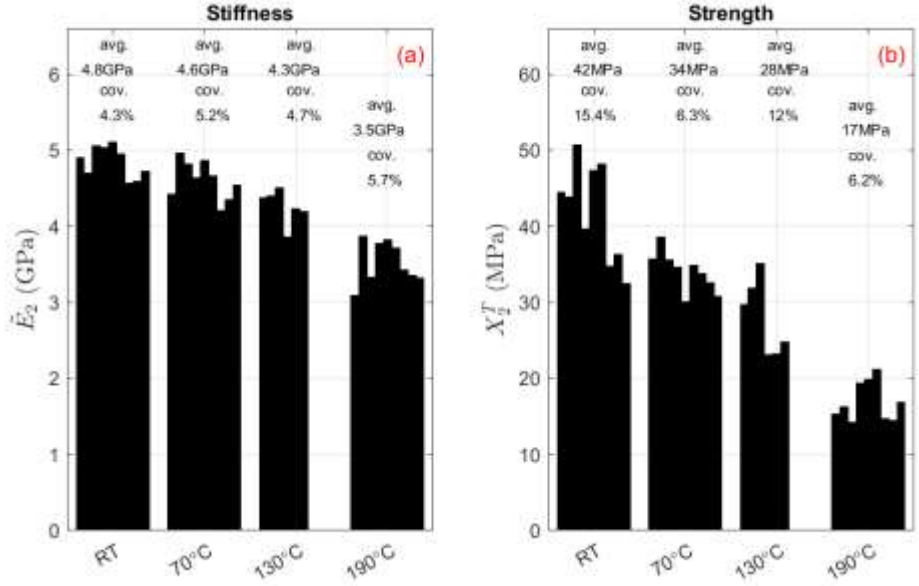

Figure 46 Distribution plot of effective tensile stiffness and effective tensile strength with temperature along the 2 direction

The surface strain-field distribution for tensile loaded specimens along the 3 direction at room temperature is shown in Figure 47. The distribution is taken at an effective strain level of 0.2% which lies within the linear elastic regime, and an effective strain level of 1.5% corresponding to the peak stress point at the moment before catastrophic failure. Within the linear elastic regime, the strain field is observed to vary between 0.178% and 0.230%. Bearing in mind the observations of Figure 34 and Figure 35, a low fiber collimation and interfacial voids render the strain state nonuniform albeit relatively mild relative to the 1 and 2 tensile specimens. At the mean strain level of 0.2%, a 15% strain concentration, computed as the percentage ratio between the largest strain value over the mean value, is observed in some regions. An interesting and noteworthy observation is the distinct strain concentration the moment before fracture, this concentration is a result of the macro-crack initiation which is seen as a narrow dark band splitting the speckle dots apart. In this concentrated region, a similar concentration factor, 15%, is observed. The crack does not rotate and a lateral fracture proceeds, this is observed for all samples shown in Figure 48. Unlike the fracture surfaces seen for specimens along the 1 and 2 directions, the fracture surface along the 3 direction is relatively flat.

The stress versus strain behavior along the 3 direction at various temperatures is shown in Figure 49. The behavior at all temperatures is brittle, with little extensive nonlinear behavior or plasticity. Similar to the behavior along the 2 direction, the strain at rupture decreases with an increase in temperature. Specifically, an average rupture strain of 1.3%, 0.94%, 0.73%, and 0.6% were observed at temperatures of 25°C, 70°C, 130°C, 190°, respectively. The distribution plots of stiffness and strength properties at different temperatures are provided in Figure 50. As expected, the modulus and strength properties decay with an increase in temperature. The variability in strengths at elevated temperatures, 130°C and 190°C are lower than the strengths observed at the lower temperatures. The consistency in strength values are also observed for loaded specimens along the 2 direction but not for specimens loaded along the 1 direction. One of the main differences between the print direction specimens and that of the transverse directions is the fiber collimation, it is reasonable to assume the matrix and fiber/matrix dominates the micro-damage modes for specimens loaded either along the 2 or 3 directions. At elevated temperatures, it is suspected than any load bearing capabilities the fiber/matrix interface had is substantially reduced and matrix micro-cracking is dominating the damage mode. Moreover, since nonlinear strain onset occurs at lower strain levels for higher temperatures, micro-damage to initiates and evolves sooner.

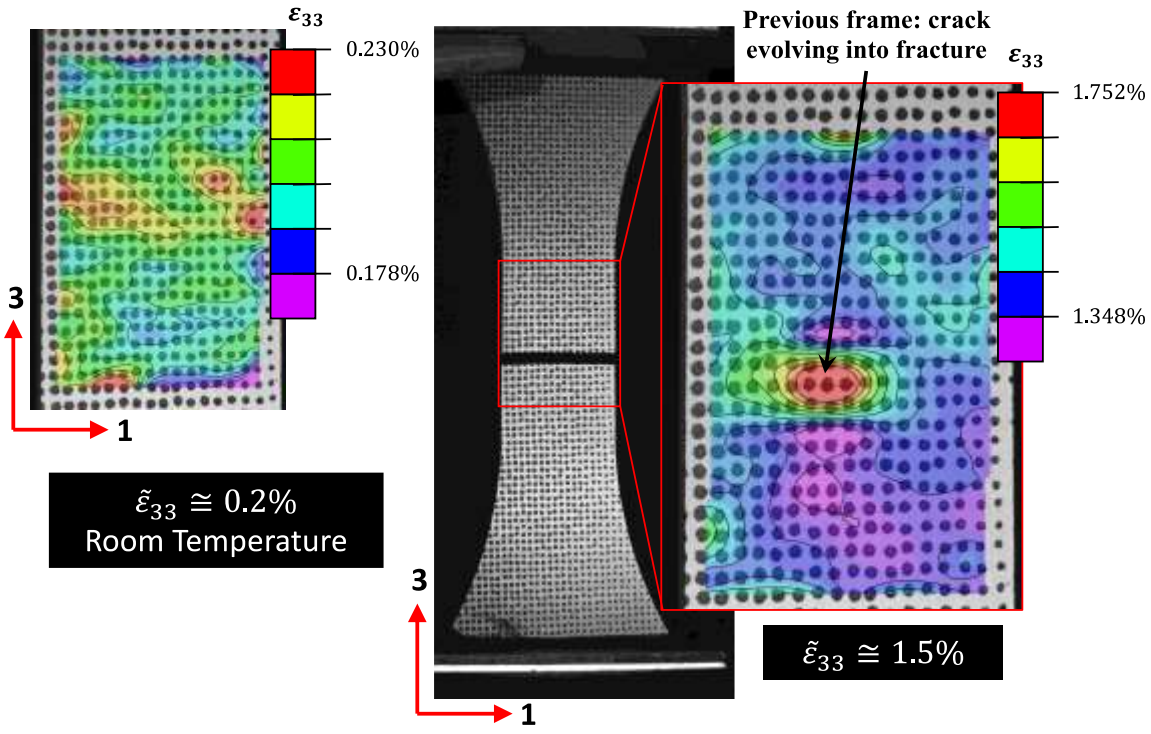

Figure 47 the DIC-generated Lagrangian surface strain field at the 0.2% field-averaged value along the stacking direction, the post-mortem coupon, and the strain concentration at the interface between stacked beads right before catastrophic failure at room temperature

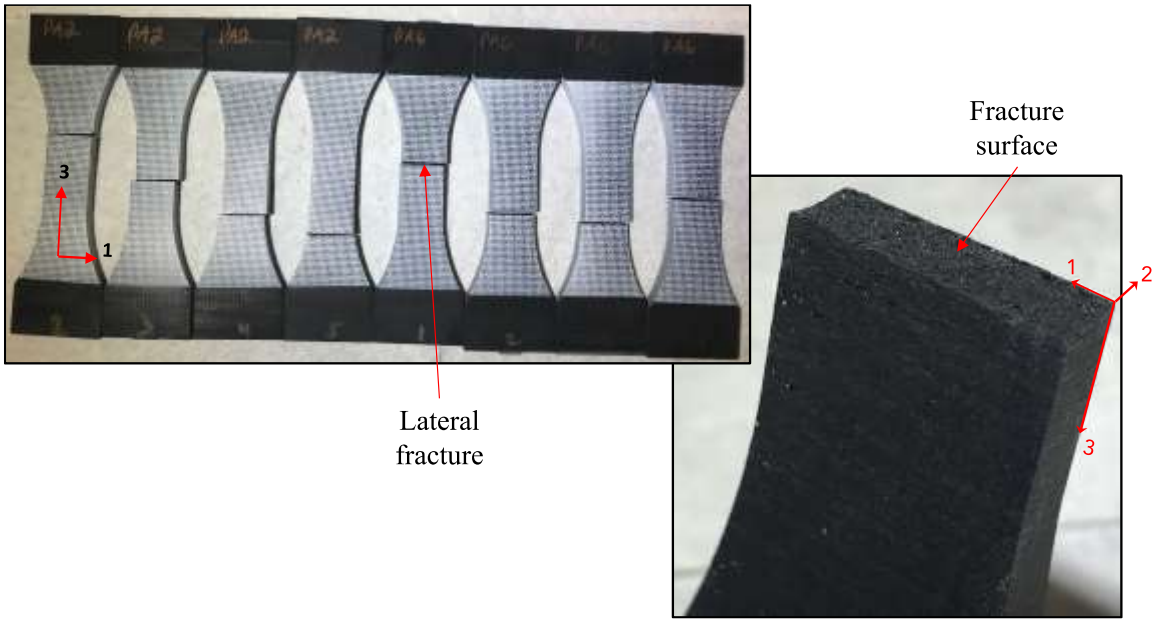

Figure 48 Fracture modes for tensile loaded coupons along the 3 direction at room temperature

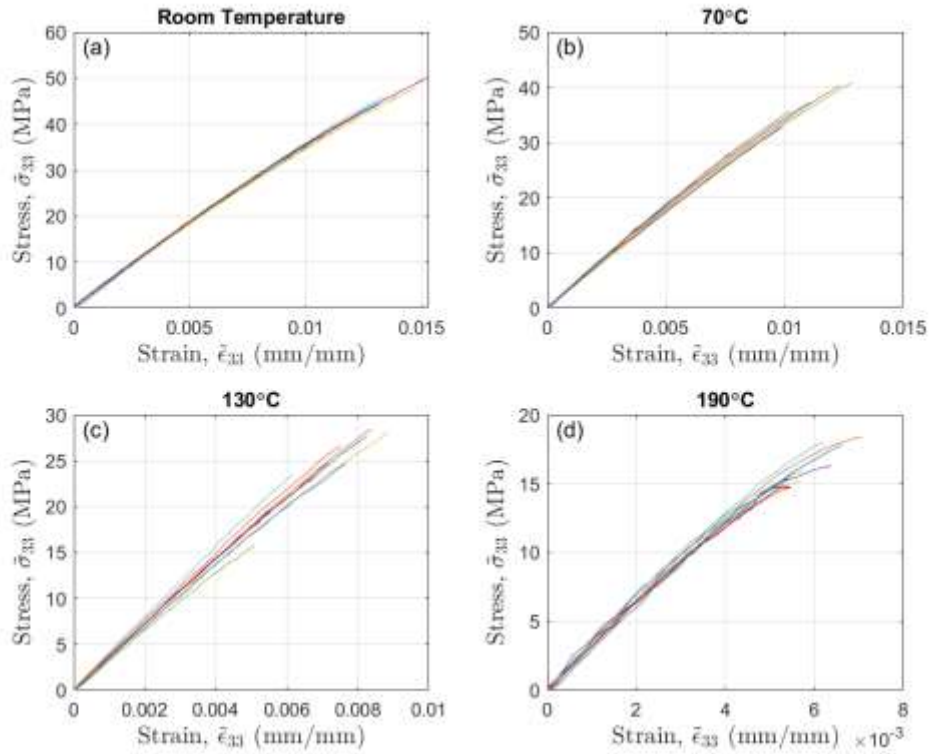

Figure 49 Effective stress versus field-averaged strain for tensile loaded specimens along the stacking direction at (a) room temperature (b) 70°C (c) 130°C (d) 190°C

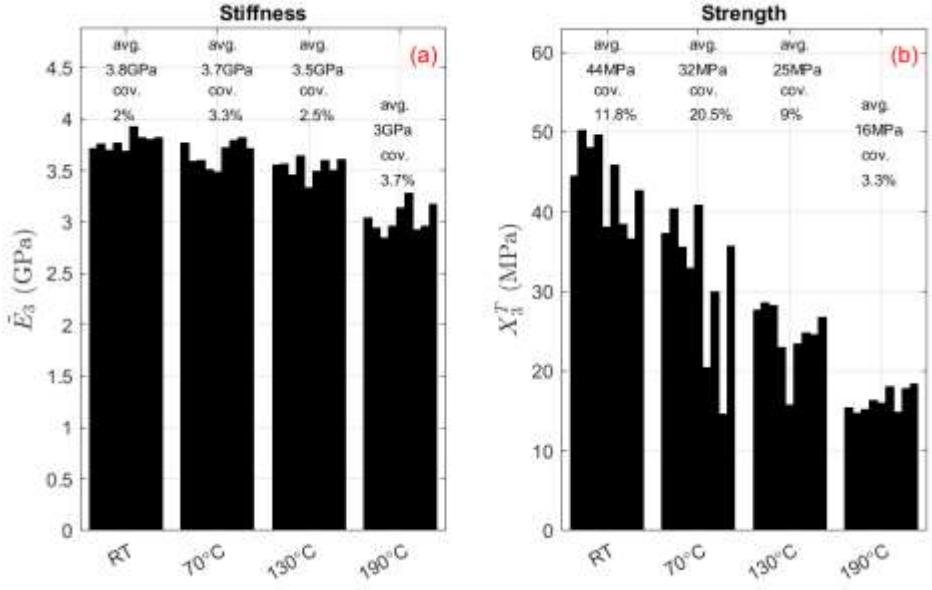

Figure 50 Distribution plot of effective tensile stiffness and effective tensile strength with temperature along the stacking direction

4.5 Compression Performance of 25% Wt. Carbon Fiber Reinforced PESU

The following sub-sections contain effective stress versus averaged strain plots, and bar plots depicting the distribution of compressive properties with temperatures. A diagonal/angled fracture path was observed for all 1 direction compression coupons. A single specimen at 190°C along the 1 direction was tested and its effective stress versus averaged mean strain is shown for reference, though no conclusion is made. Buckling with shear band formation was observed for coupons loaded in the 2 direction for all temperatures. Along the 3 direction loaded samples, buckling or a slight bulge at the gage section occurred after extensive deformation; however, some samples did not exhibit buckling failure or any discernable failure. Moreover, the non-softening response of the 3 direction loaded specimens made it difficult to unequivocally extract the compressive strength. As a result, two ultimate strengths are reported which are based on the peak stress value and the 0.2% offset strength commonly used for shear tests (e.g., ASTM D3518). While the peak strength is reported for reference, the 0.2% offset value is taken as the representative compressive strength along the 3 direction. However, the 0.2% offset strengths reported for the 1 and 2 directions are discretionary and the representative strengths for both of these directions are taken as the peak strength found in the effective stress versus averaged strain data. The compressive modulus along the 1 direction at room temperature is found to be similar to the tensile modulus at room temperature; however, the average compressive modulus at 130°C is observed lower than the tensile modulus at 130°C. Similar to tension behavior, the effective compressive stiffness along the 1 direction is greater than the 2 or 3 directions; specifically, the 1 direction modulus is 3.1x and 3.5x greater than the 2 and 3 direction modulus, respectively. The compression modulus along the 2 direction is found to be 1.2x greater than the 3 direction compressive modulus. Similarly, the 1 direction compressive strength is 1.2x and 2.6x (0.94x assuming ultimate 3 direction strength) greater than the 2 and 3 direction compressive strength, respectively, this assumes the strength at 0.2% offset for 3 direction specimens. Moreover, the 2 direction compressive strength is 1.8x greater (or 0.77x) than the 3 direction compressive strength. In comparison, the average compressive strengths along the 1, 2, and 3 directions at room temperature are 1.5x, 3.9x, and 1.8x (or 4.9x) greater than the 1, 2, and 3 direction average tensile strengths at room temperature, respectively. It has been observed that elevated temperature compressive strengths were higher than that of tensile strengths. Despite differences in processing methods, a similar trend is found

for short fiber composites knows as sheet molded compounds (SMC) [195], [196]. The average room temperature compressive strength along the 2, and 3 directions are 2.0x and 1.6x greater than their respective average 190°C strengths. Additionally, the 1 direction room temperature strength is 1.5x greater than its average 130°C strength. Based on these observations, a unilateral behavior is evident amongst all three directions; namely, the stress versus strain behavior in tension is different than in compression. The compressive non-linear onset strain values are on average larger than the tensile non-linear onset values for all three directions. The delayed nonlinear response is believed to be cause from a different microscopic damage mode since the macroscopic fracture modes are not identical. In a report by Hour [195], damage volumetric strains in short fiber composite SMC materials under compression is observed to initiate at a greater stress level relative to damage induced under tension. The nonlinear onset strain values between uniaxial tension and compression behavior may suggest damage initiation may be different or perhaps delayed.

4.5.1 Performance along 1 (Print) Direction & 2 (In-Plane Transverse) Direction

The stress versus strain plots for the uniaxial compression tests along the print direction are shown in Figure 51 below. The plots illustrate the nonlinear trend at room temperature, 130°C, and 190°C. Five specimens were tested at room temperature and 130°C, and a single specimen was tested at 190°C which is shown for reference. Since the modified Boeing fixture was utilized for the compression experiments, an initial stiffening zone at load introduction is apparent as clearly seen in Figure 51c. The initial stiffness is caused by the fixture settling in place during the commencement of load introduction. Evidently, the strain range used for extracting the modulus should not contain such material behavior as it will produce an erroneous modulus measurement. Therefore, the compressive modulus were extracted within the linear portion of the stress-strain curve at strain and regions beyond initial anomalous stiffening behavior. Similar to tension behavior, compression behavior exhibits linear and non-linear regions. Non-linearity is also pronounced at higher temperatures with the rupture strain more than double the tensile case. The strain field and fracture image taken from the DIC camera is shown in Figure 52. The fixture has an opening at the gage section which allows lateral movement as the load progressive on the right-hand side; however, the left-hand side of the fixture thwarts lateral movement. The low strain value seen on the lower left of the strain field map is believed to be caused by the fixture-induced displacement restriction. Although not shown, the supporting walls contain grooves which allows

for little Poisson expansion. Fracture has been observed to occur within the gage section or at least very close to the gage section.

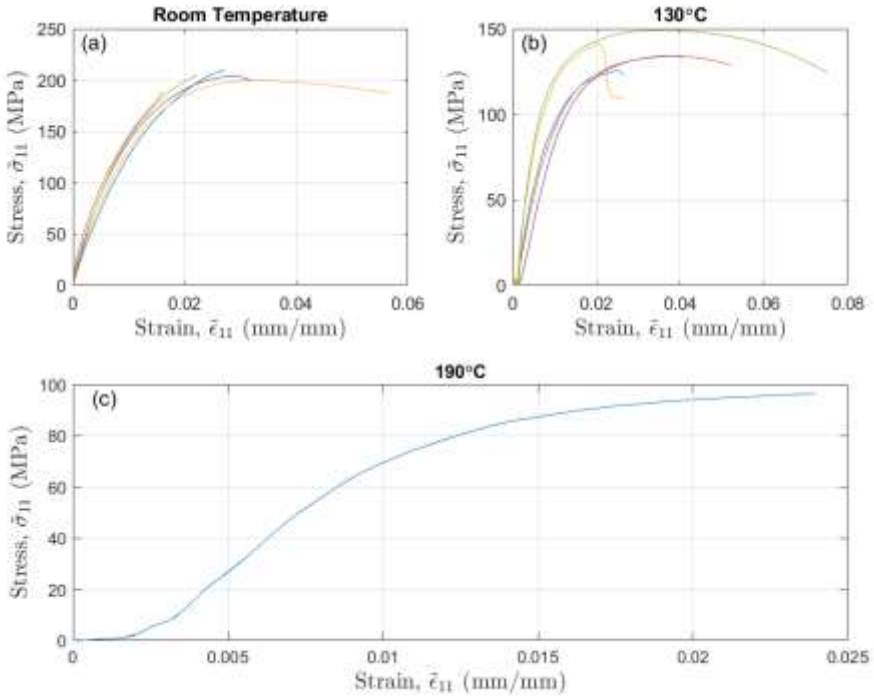

Figure 51 Effective stress versus field-averaged strain for compression loaded specimens along the print direction at (a) room temperature (b) 130°C (c) 190°C

The distribution of stiffness and strength properties along the print direction are provided in Figure 53. Compared to the tensile stiffness coefficient of variance, 1.7%, the variability of the stiffness measured in compression is 7x greater. Since the compression specimens have a smaller width than the tensile coupons, the differences in bulk microstructures between compression samples may be more significant than bulk microstructural variations in tensile specimens. Furthermore, errors from DIC-computed strain fields can also result in stiffness variability to some extent. Projection errors are expected to increase slightly due to the process of removing and adding specimens into the fixture; however, utmost care should be made to ensure minimal error and bias. Figure 54 shows the images of the fractured compression specimens for each temperature set, each sample exhibited a shattering fracture corresponding to a substantial load drop. A definite compression strength value, based on the peak or ultimate value, is deemed acceptable because of these experimental observations. Furthermore, it is interesting to note that the failure mode

consisted of an angled macro-crack with respect to the horizontal axis, fractures were located within or near the gage section.

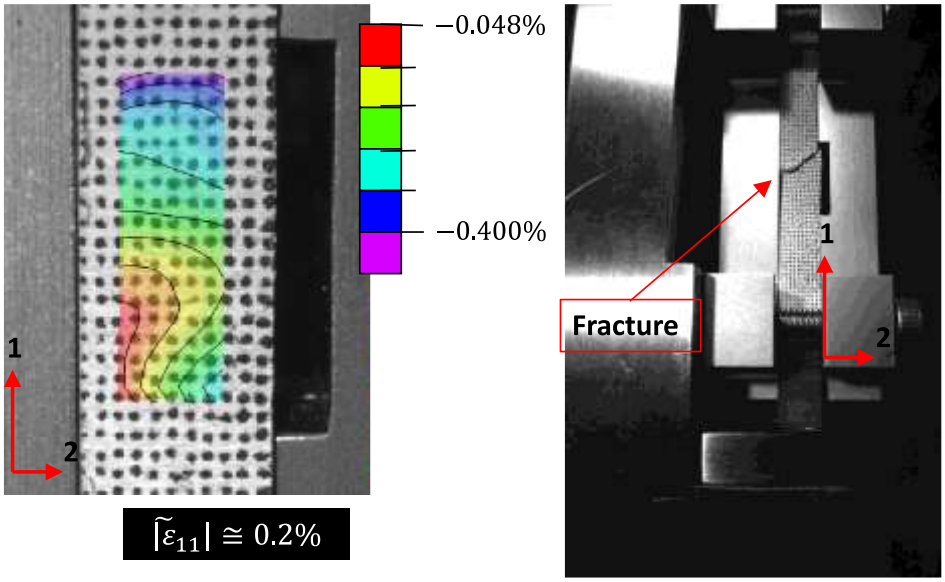

Figure 52 Strain-field map (left) of uniaxial compression specimen along the print direction at room temperature and post-mortem fracture image (right)

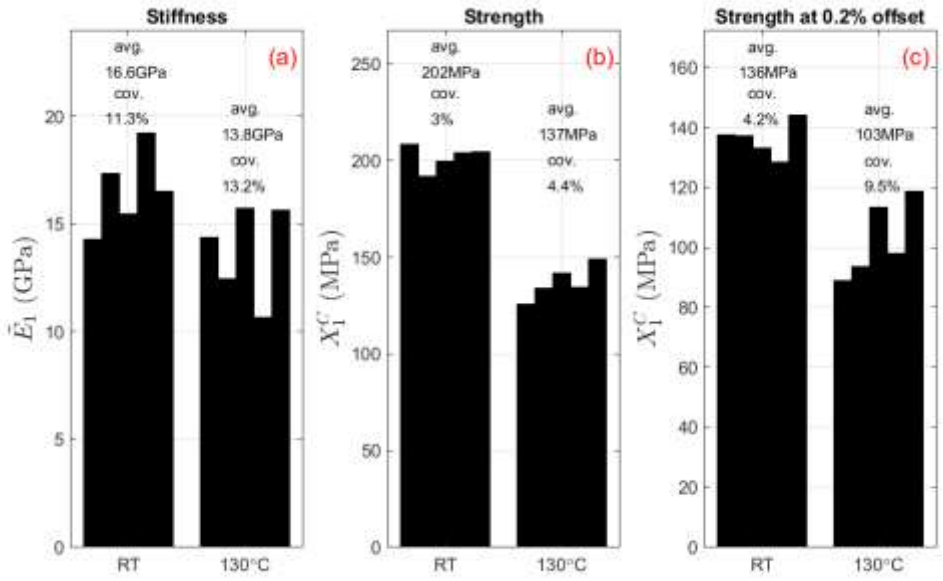

Figure 53 Distribution plot of effective compressive stiffness and effective compressive strength with temperature along the print direction

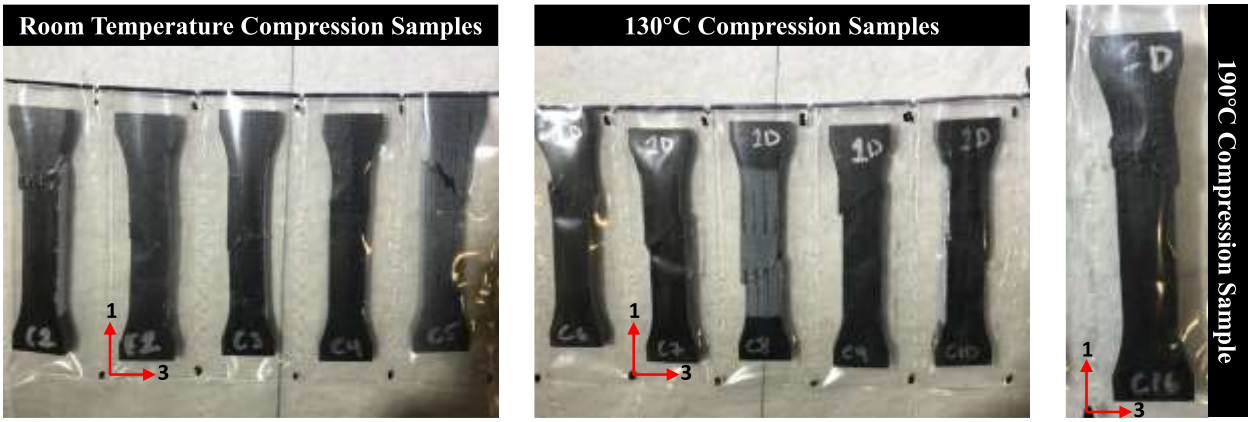

Figure 54 Fracture modes for uniaxial compression specimens along the print direction at (a) room temperature, (b) 130°C, and (c) 190°C

The compressive behavior along the 2 direction at 25°C, 130°C, and 190°C is shown Figure 55 below. Similar to the print direction response, the stress versus strain trend shows linear and nonlinear regions. In contrast to the tensile behavior, extensive deformation is observed for all temperatures. Under compression, a decrease in rupture strain is not observed, instead it appears to increase with temperature. Figure 56 illustrates the strain-field map for a compression loaded specimen along the 2 direction at room temperature, and its post-mortem failure image. Although buckling has been observed for most specimens, the nonlinear behavior is not entirely attributed to buckling as shown in Figure 57. A fairly uniform strain field is observed, though the corners appear to deviate from the 0.2% average strain value. The fracture image depicts two failure modes, the first is buckling failure and the second is the emergence of cracks which appear parallel to the specimen's longitudinal axis. Buckling was observed first followed by the cracks; therefore, the load-drop seen on the stress versus strain plots are believed to be associated with buckling. The compressive strength reported consist of two values, one based on the ultimate load which should be discretionally used and the second based on the 0.2% chord modulus offset method. Figure 58 shows the distribution of the stiffness and strength properties for each tested temperature set. The variability in stiffness is observed greater relative to tension modulus, this is also believed to be related to the sample dimensions and microstructural variability discussed earlier. The stiffness and strength properties degrade with an increase in temperature. Figure 59 illustrates the failed compressive coupons sets, each failed under buckling and some form of cracking which are less visible at the highest temperature.

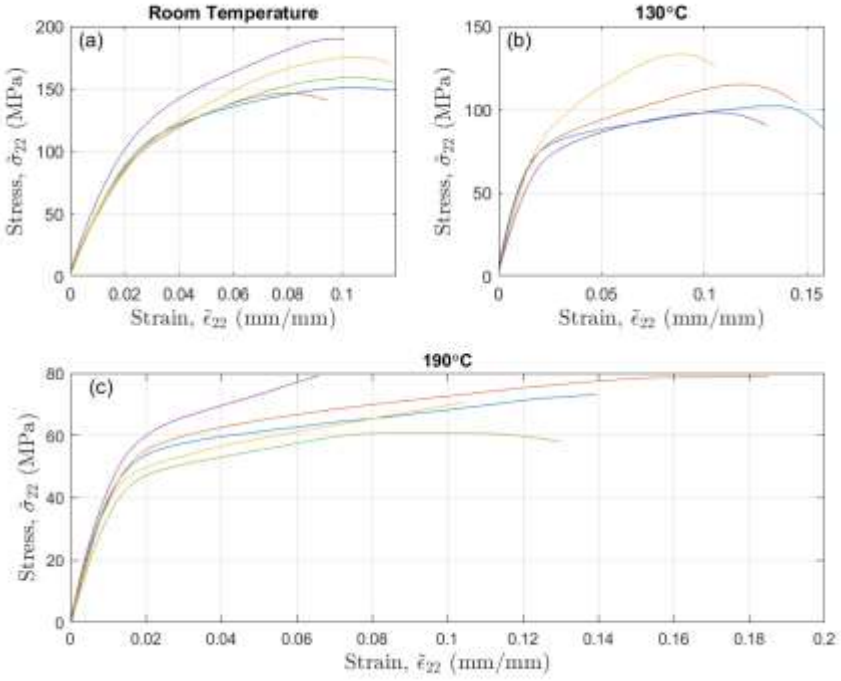

Figure 55 Effective stress versus field-averaged strain for compression loaded specimens along the 2 direction at (a) 25°C (b) 130°C (c) 190°C

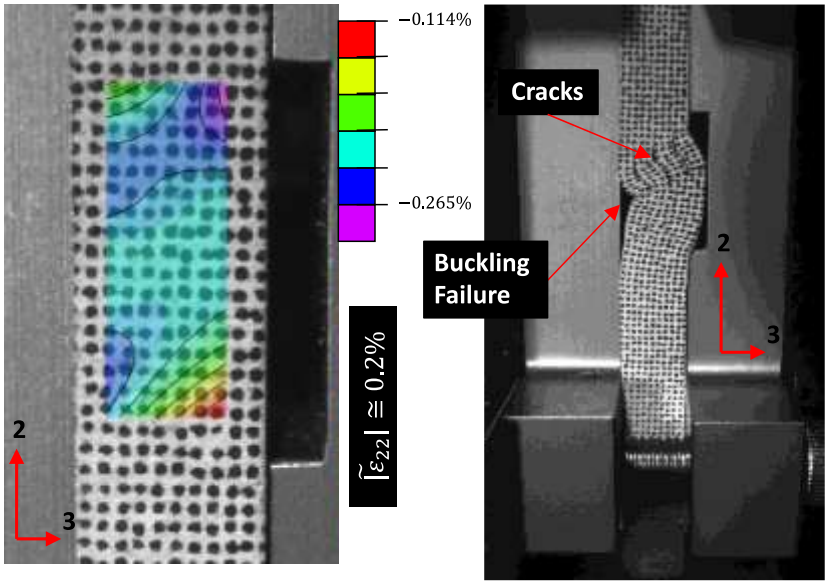

Figure 56 Strain-field map (left) of uniaxial compression specimen along the 2 direction at room temperature and post-mortem fracture image (right)

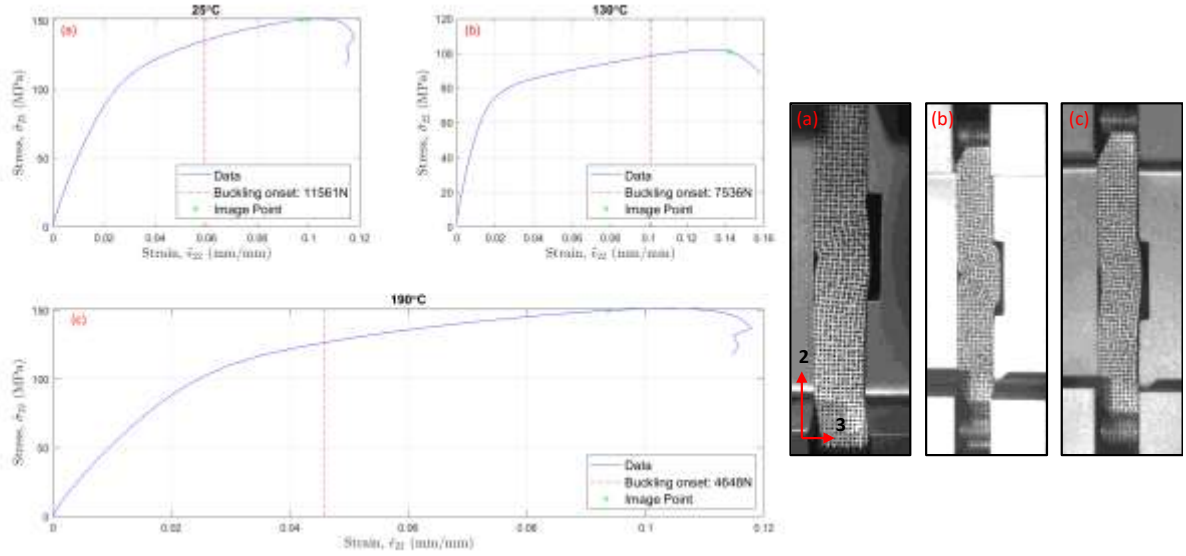

Figure 57 Compressive stress versus strain behavior along 2 direction for (a) 25°C (b) 130°C (c) 190°C

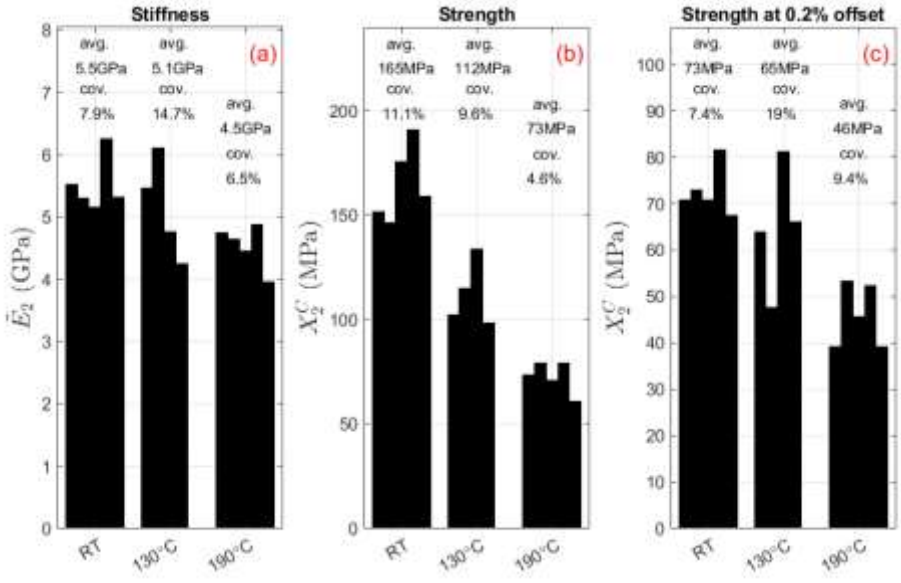

Figure 58 Distribution plot of effective compressive stiffness and effective compressive strength with temperature along the 2 direction

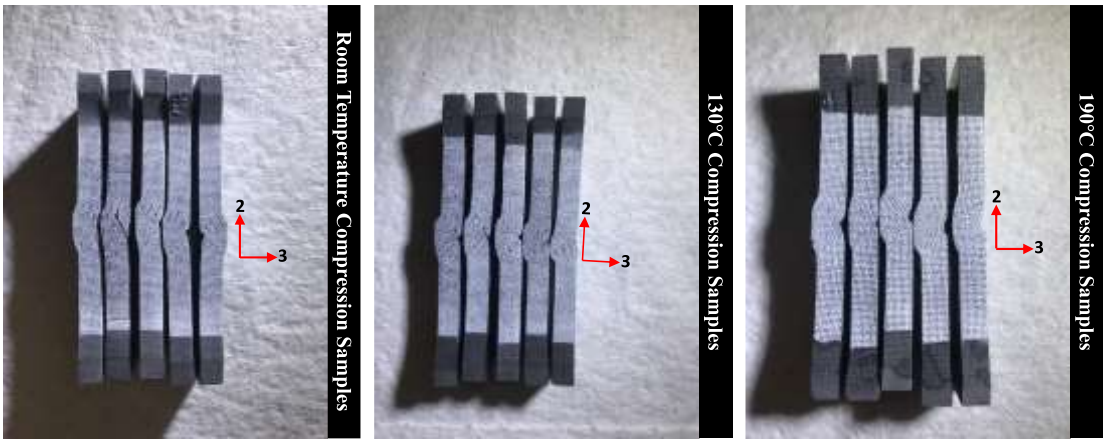

Figure 59 Fracture modes for uniaxial compression specimens along the 2 direction at (a) room temperature, (b) 130°C, and (c) 190°C

4.5.2 Performance along 3 (Stacking) Direction

The effective stress versus average strain along the stacking direction with temperature is shown in Figure 60. Similar to the compressive behavior along the 2 direction, extensive deformation can be observed with strains exceeding 10%. No distinct load-drop is observed for all temperature sets, and significant strain hardening is visible beyond the yield point. In many instances, displacement end reached the limits of the fixture and no further load could be applied. Some specimens experienced buckling without load-drop though no further load could be applied since the displacement end reached the limit of the fixture as well. Figure 61 illustrates the strain-field distribution and the buckling failure mode. Similar to the compressive loaded specimen along the 2 direction, buckling appears to be the likely failure mechanism for 3 direction loaded specimens under compression. The distribution plots are provided in Figure 61, a decrease in stiffness and strength is observed with an increase in temperature. It is noteworthy to mention that no well-defined fracture was observed during the test, this usually means that the nominal compressive strength is ambiguous. Furthermore, buckling failure does not represent true material failure since the loss of stiffness is primarily due to geometric instability. Nevertheless, for measured quantities are reported for reference yet the reader is cautioned not to directly assume the ultimate strength is representative of the compressive strength. Instead, a 0.2% offset compressive strength may be appropriate or the strength at yield. Figure 63 illustrates the post-test compression coupons, with some coupons not exhibiting any discernable failure mode.

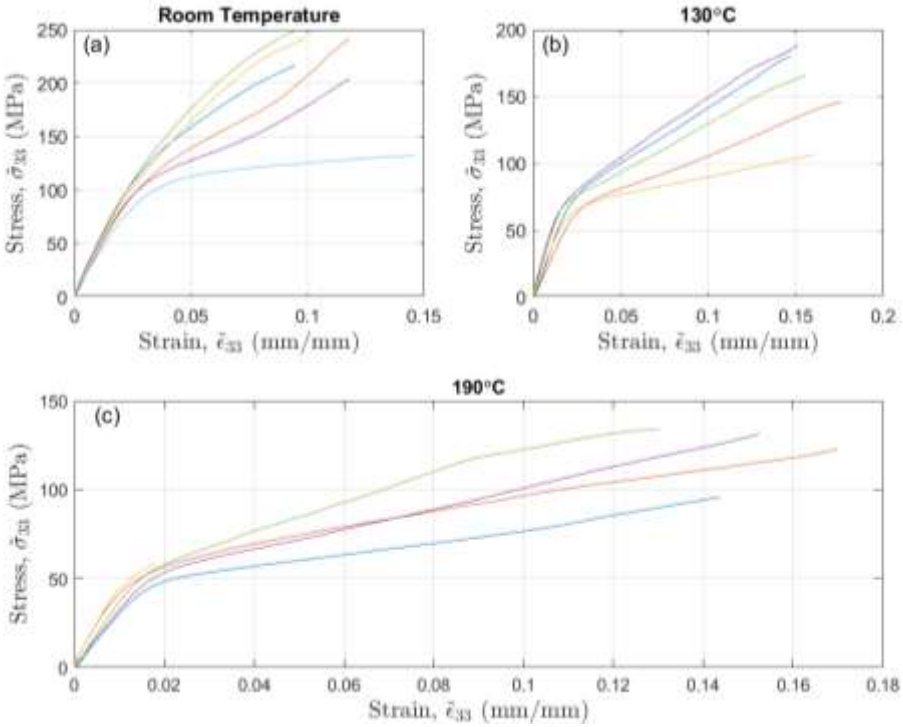

Figure 60 Effective stress versus field-averaged strain for compression loaded specimens along the stacking direction at (a) room temperature (b) 130°C (c) 190°C

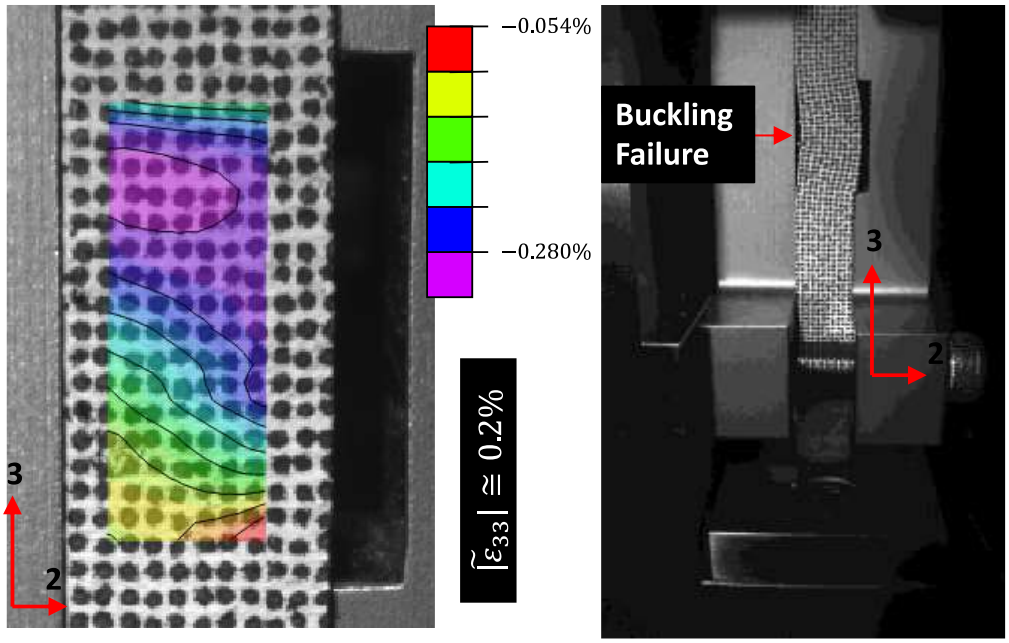

Figure 61 Strain-field map (left) of uniaxial compression specimen along the stacking direction at room temperature and post-mortem fracture image (right)

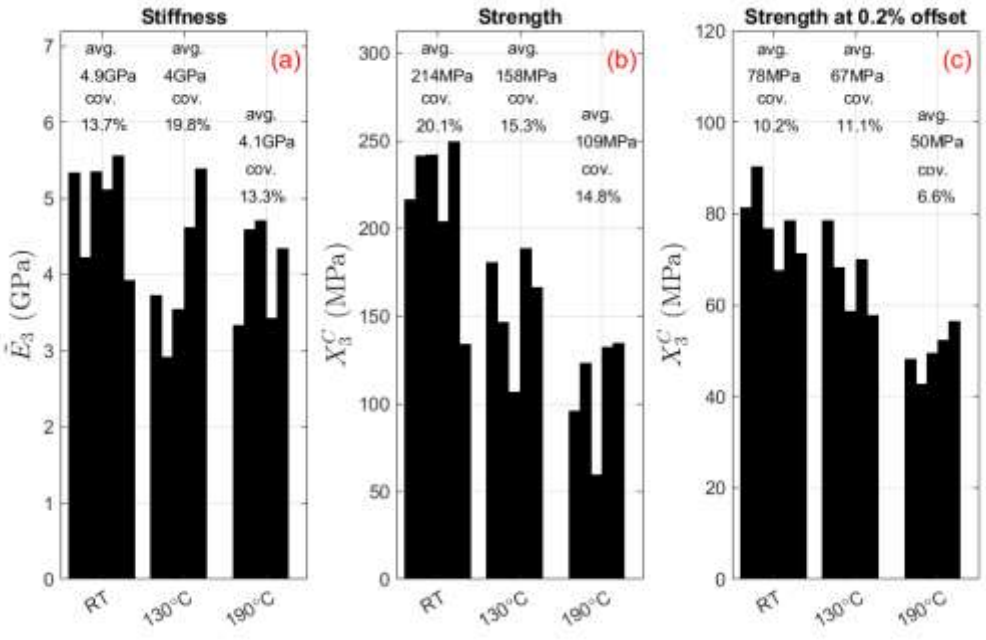

Figure 62 Distribution plot of effective compressive stiffness and effective compressive strength with temperature along the stacking direction

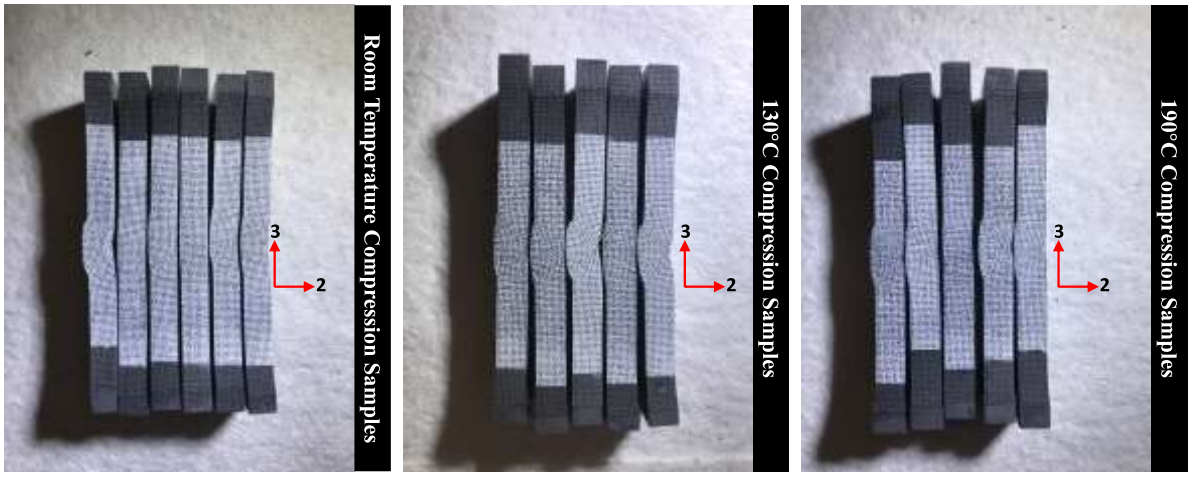

Figure 63 Fracture modes for uniaxial compression specimens along the stacking direction at (a) room temperature, (b) 130°C, and (c) 190°C

4.6 Shear Performance of 25% Wt. Carbon Fiber Reinforced PESU

The sub-sections below contain the effective shear stress versus engineering shear strain plots with temperature, the distribution of shear mechanical properties, and DIC-generated strain field and post-mortem images. The tested directions were along the 2-3, 1-3, and 1-2 planes. The naming

conventions and material orientations follow that of the ASTM D5379 standard. For example, v-notch specimens loaded in the 2-3 and 1-3 planes have the stacking direction along the width of the notch. For the 1-2 plane, the 2 direction is oriented along the width of the notch. The effective room temperature shear modulus along the 1-2 plane, $\tilde{G}_{12}$, is observed to be 2.5x and 2.6x greater than $\tilde{G}_{13}$ and $\tilde{G}_{23}$, respectively. However, no significant difference is observed between $\tilde{G}_{13}$ and $\tilde{G}_{23}$ and this similarity may be a result of the polymer dominating the shear behavior. Likewise, the ultimate shear strengths for S_6 (i.e., following Voigt convention) is 1.2x and 1.7x greater than S_5 and S_4, respectively; by the same token, the 0.2% offset shear strength for S_6 is 1.3x and 1.2x greater than S_5 and S_4, respectively. It is noteworthy to mention the 0.2% offset shear strengths of S_4 and S_5 are similar; however, the peak stress value of S_5 is 1.3x greater than S_4. The effective shear stiffness along the 1-2 plane is expected to be greater because of the greater fiber collimation relative to the other directions. The shear modulus, $\tilde{G}_{13}$ and $\tilde{G}_{23}$ are seen to not significantly change with temperature, and room temperature $\tilde{G}_{13}$ is observed to be slightly lower than the elevated temperature modulus.

4.6.1 Performance along 2-3 Direction & 1-3 Direction

Figure 64 illustrates the Lagrange strain distribution at the averaged value of approximately 0.275%, in essence, 0.55% for engineering shear strain. From the strain contour plots, it is evident that the shear strains are maximum between the notches. Furthermore, the maximum shear strain between the notches has been observed for the other temperature cases. The small region of interest visible between the notches has been averaged to compute the effective engineering shear strain between the notches. Figure 65 shows the effective shear stress versus engineering strain for the various temperatures cases along the 2-3 plane. From the shear stress versus shear strain plots, a general decrease in nonlinear onset shear strains with temperature has been observed, similar to tension and compression behavior along polymer dominated directions. Figure 66 provides the distribution of shear properties for the different temperatures. While the stiffness is not seen to vary significantly with temperature, the strength is seen to decrease on average with temperature for both the ultimate strength and the 0.2% strength definition.

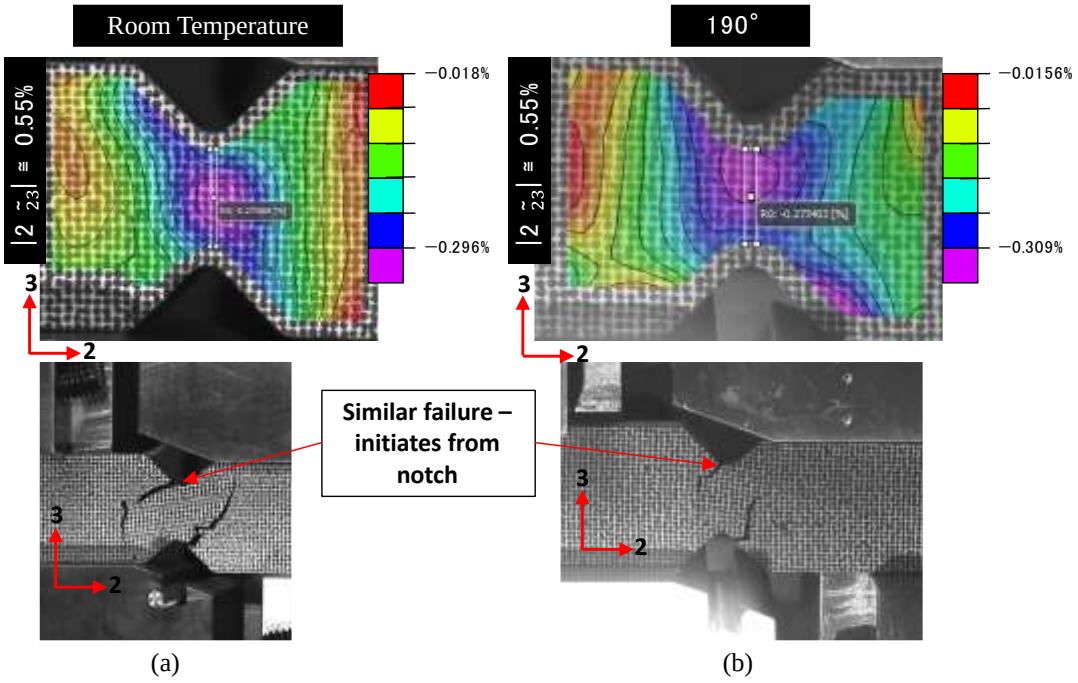

Figure 64 DIC-generated Lagrangian surface shear strain field at the 0.55% field-averaged engineering value along the 2-3 plane and the post-mortem coupon at (a) room temperature, and (b) 190°C

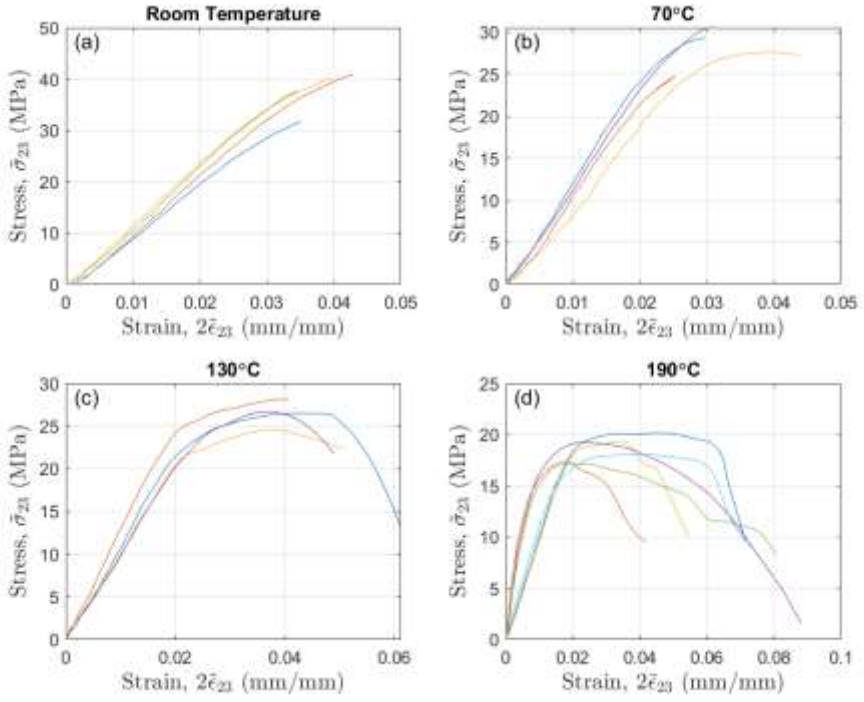

Figure 65 Effective shear stress versus field-averaged shear engineering loaded in the 2-3 plane at (a) room temperature (b) 70°C (c) 130°C (d) 190°C

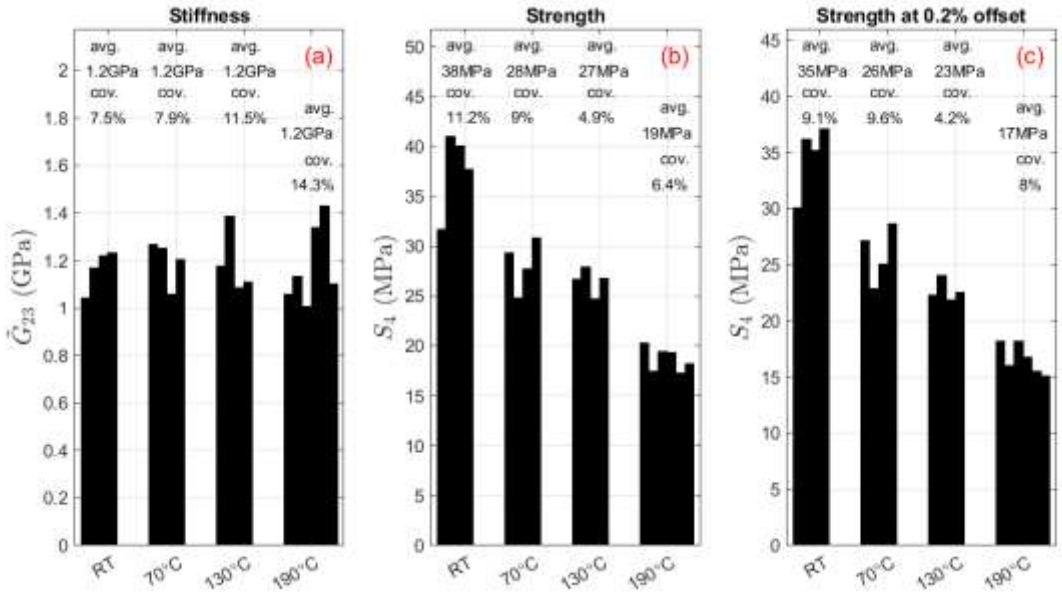

Figure 66 Distribution plot of effective shear stiffness and effective shear strengths with temperature along the 2-3 plane

The effective shear stress-shear strain behavior along the 1-3 plane for various temperatures is shown in Figure 67. The average ultimate strains have been observed to increase with an increase in temperature; specifically, at 25°C, 70°C, 130°C, and 190°C, these strains are 7.1%, 7.0%, 8.6%, and 18%, respectively. Relative to room temperature, extensive nonlinear behavior is observed for the specimen tests at 190°C. At the elevated temperature, a plateau region is observed, and its cause is not apparent. One possible explanation for the elongation observed is due to the associated polymer flow or plastic deformation. Similar to the shear specimens in the 2-3 plane, the nonlinear onset is also observed to decrease with temperature. Figure 68 illustrates the distribution in shear properties along the 1-3 plane. Similar to the 2-3 plane, an increase in temperature is observed to impact the shear strengths and not the shear stiffness.

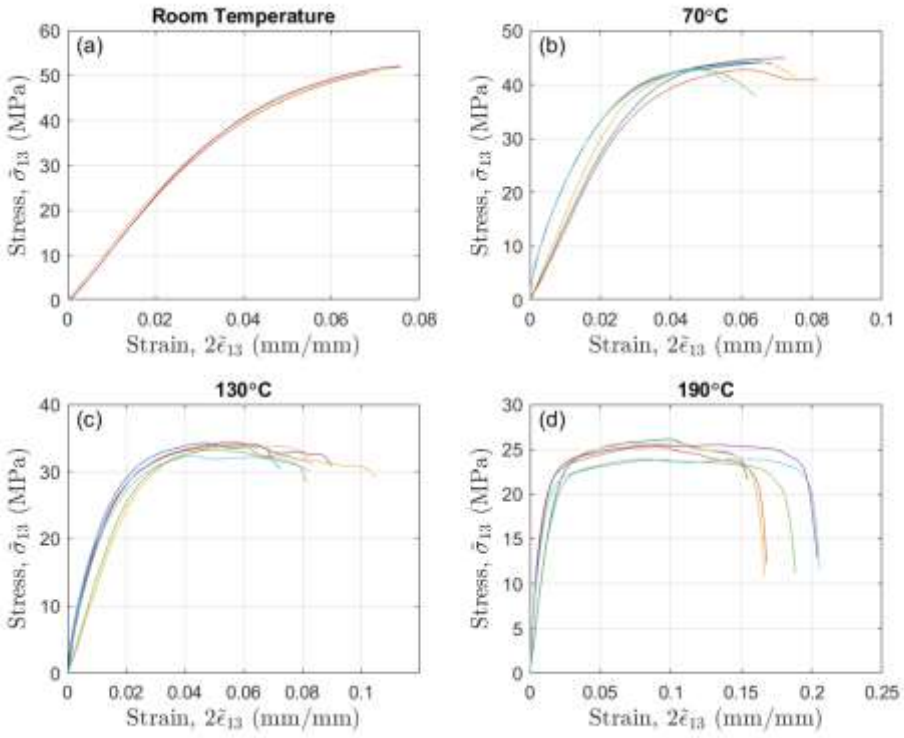

Figure 67 Effective shear stress versus field-averaged shear engineering loaded in the 1-3 plane at (a) room temperature (b) 70°C (c) 130°C (d) 190°C

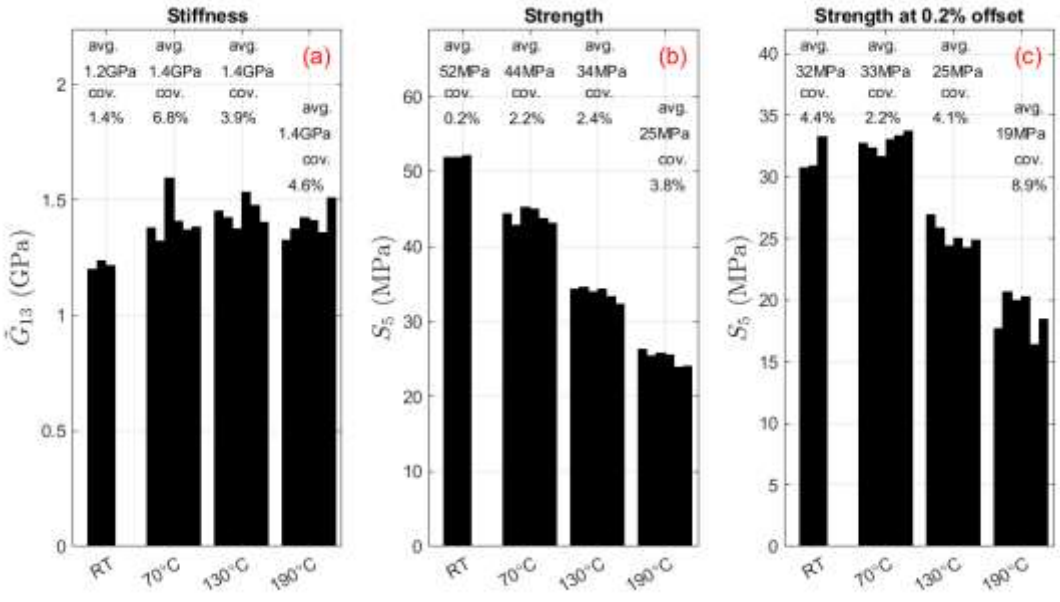

Figure 68 Distribution plot of effective shear stiffness and effective shear strengths with temperature along the 1-3 plane

4.6.2 Performance along the 1-2 Plane

The effective shear stress with shear strain along the 1-2 direction with temperature is shown in Figure 69. While the average ultimate strains are observed to increase with temperature, the nonlinear onset values do not appear to change significantly with temperature. Similar to compression behavior, erroneous mechanical behavior was observed at load introduction because of fixture settling. Consequently, linear elastic regions were defined between strain ranges which were beyond the anomalous regions. The ASTM D5379 recommends a strain range that commences anywhere between 1500 $\mu\epsilon$ – 2500$\mu\epsilon$ and extends over a 4000 $\mu\epsilon$ strain range for modulus extraction. At higher temperatures, the starting strain points were chosen slightly greater recommended values, this adjustment was determined necessary to capture the true linear shear response of the material. Figure 71 shows the distribution of mechanical performance for the various temperature cases. From the distribution plots, a decrease in both stiffness and strength is observed.

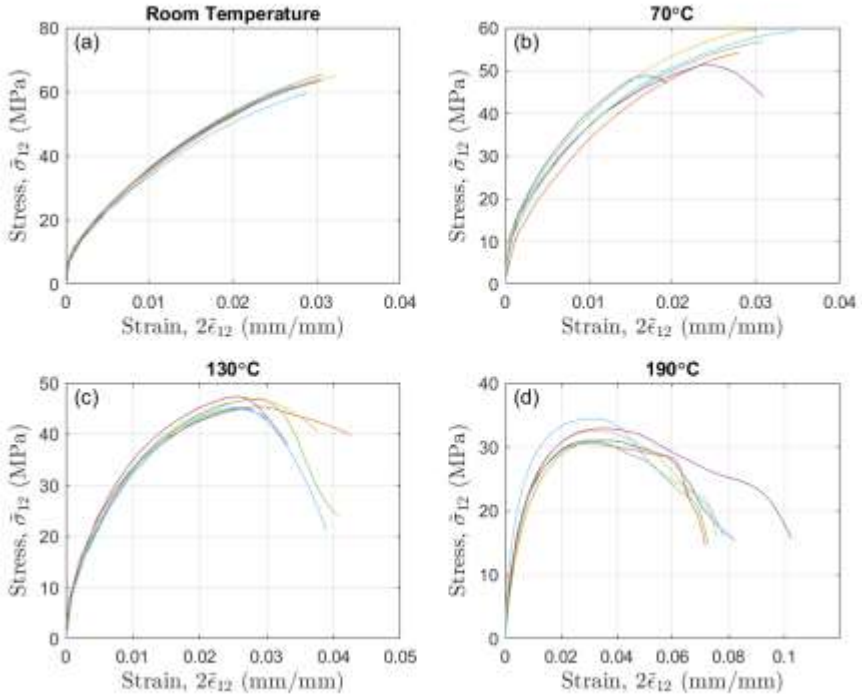

Figure 69 Effective shear stress versus field-averaged shear engineering loaded in the 1-2 plane at (a) room temperature (b) 70°C (c) 130°C (d) 190°C

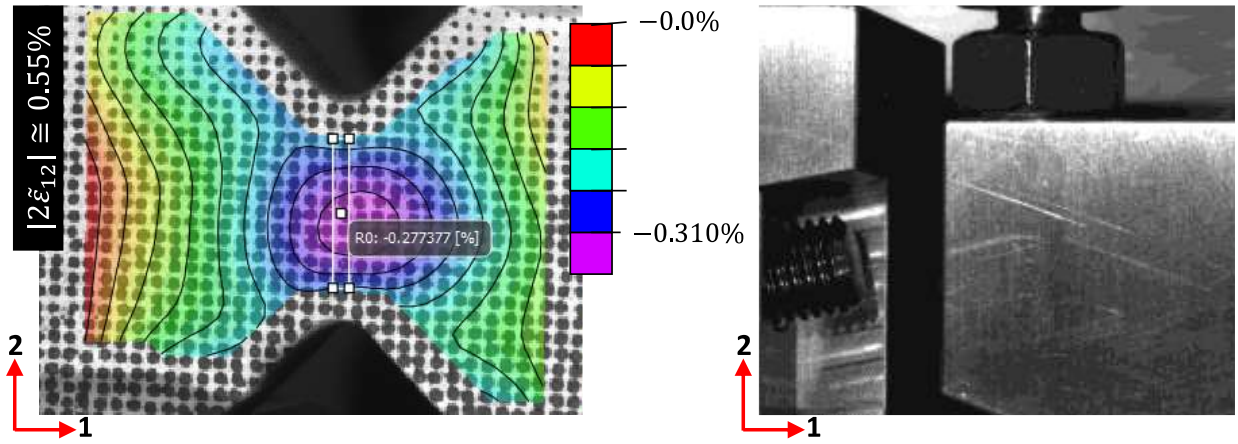

Figure 70 DIC-generated Lagrangian surface shear strain field at the 0.55% field-averaged engineering value along the 1-2 plane (left) and the post-mortem coupon (right) at room temperature

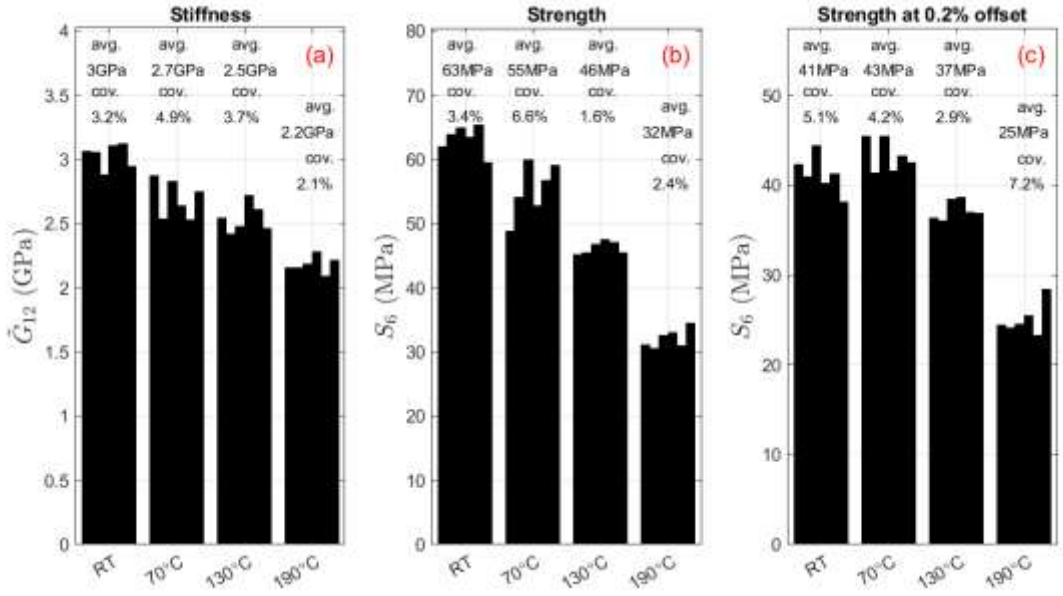

Figure 71 Distribution plot of effective shear stiffness and effective shear strengths with temperature along the 1-2 plane

4.7 Fracture Surface Investigation via SEM

4.7.1 Tensile Fracture Surface along 1 Direction for a Room Temperature and 190°C Specimen

Microscopic observations of the tensile fracture surfaces of the short carbon fiber reinforced PESU are shown in Figure 72. The top row contains images of specimens tested at room temperatures, while the bottom row contains images from the 190°C specimens. From these micrographs, the mode of failure is complex and appear dependent upon the fiber orientation. Figure 72(a) and Figure 72(d) show fibers extending above the fractured matrix, which is a possible sign of the fiber pull-out damage mechanism. Along the 2 and 3 directions, fibers are not observed to be collimated along the loaded direction and are seen to lie in the fracture plane. Voids are present and their size vary; however, they are large in comparison to the fiber imprints shown. Moreover, voids are common is EDAM processes and may arise from trapped air or polymer volatiles. Thin polymer fibrils are seen at the higher temperatures and are believed to be caused from the crazing mechanism.

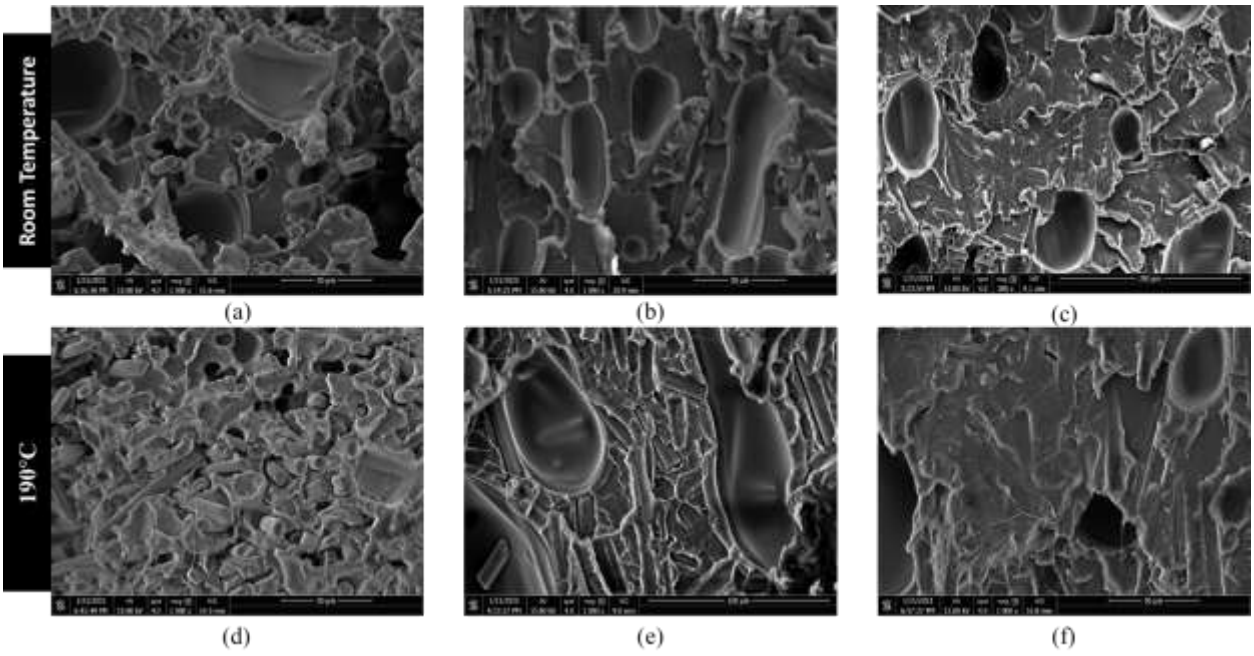

Figure 72 SEM of tensile loaded post-mortem specimens along (a) 1 direction (b) 2 direction (c) 3 direction at room temperature, and (d) 1 direction (e) 2 direction (f) 3 direction at 190°C

5. VISCOELASTIC DAMAGE MODEL SETUP

5.1 Introduction

Observations of additive manufactured short fiber composite mechanical performance at ambient and elevated temperatures reveal changes in nonlinear attributes, which plays an important part in the design of additive manufactured parts. Additive manufactured short fiber thermoplastics exhibit a reduction in nonlinear onset strain as the temperature increases in addition to a reduction in strength and stiffness. Moreover, the nonlinear trend changes as temperature rises. The 3D printed bead-to-bead interfaces as well as the polymer phase is an important factor in the mechanics of deformation, directions with polymer-rich zones or interfaces remain brittle even at elevated temperature when deformed under tension. Unlike tensile behavior, compression and shear deformations have extensive nonlinearity and greater strain-to-failure values. For the virtual design process, the important question is, can the proposed viscoelastic damage model predict these anisotropic and unilateral behavior? If so, then a procedure needs to be developed to calibrate the material model from either experiments or through parametric investigations. Here, the question is addressed by demonstrating the approach taken to tune the model and directly comparing experimental behavior to the predicted behavior. Limitations of the model are discussed and proposed mathematical changes is made to attempt providing a feasible solution to the issue. The ultimate goal is to develop a material model that can represent material behavior during the 3D printing process and in-service performance. In essence, this modeling capability can provide insights into (i) post-print part warpage, (ii) post-print accumulated residual stresses, (iii) knowledge of potential damaged zones, (iv) creep-damage from thermomechanical loading, and (v) intuition of undesirable 3D printed structural designs.

In the composition of 3D printed parts, there are beads, also denoted as layers or roads, and interfaces at the mesoscale, length scale of bead dimensions. Interfaces are regions where two beads come into contact; when a bead is deposited next to another in-plane or placed on top of each other. These interfaces bond to one another through polymer diffusion which is dependent on temperature and pressure. It is noteworthy to mention that a bead compactor (e.g., a vibrating plate known as a tamper or a roller) is often used in EDAM processes to compress the molten bead along its height which increases the contact area and facilitates the fusion process. Each deposited bead

has a heterogenous microstructure which includes discontinuous fibers, matrix, and voids. Most fibers are oriented along the print direction, denoted as the 1 direction, because of the flow conditions that exists in the extrusion-based processes [197]. Fiber volume content and degree of fiber collimation with the print direction determine the anisotropic properties. Squeeze flow from bead compaction drives some fiber collimation along the transverse print direction orthogonal to the stacking direction, denoted as the 2 direction. Moreover, virtually no fibers are collimated along the stacking direction, 3 direction. These directions, 1, 2, and 3, are understood as the principal directions. Carbon fibers, especially along its longitudinal axis, are much stiffer than the surrounding polymer matrix and they have a pronounce effect on the thermo-mechanical performance of the material; most importantly, the preferential alignment of fibers is responsible for the anisotropic material behavior. Viscous behavior originates from the isotropic polymer phase; however, the viscous behavior also experiences directional dependency because of the presence of fibers. The effective properties of the 3D printed material in the stacking direction are dominated entirely by the polymer matrix; therefore, the mechanical performance in the stacking direction is the lowest amongst all directions with viscous behavior being the most pronounced. On the other hand, the interface along the 2 direction is influenced, to some extent, by the fibers and this is why the mechanical performance along the 2 direction is not identical to the stacking direction. To describe the anisotropic behavior of the composite and account for the composition of 3D printed parts, distinction is made between properties of the interbead and intrabead. Noteworthy to mention, two intrabead damage variables and an independent intrabead damage variable are adopted, and these are the main damage variables under the assumption that the principal damage planes are coincident to the principal directions. Despite the shear properties being degraded by the principal damage variables, shear damage variables can be used for flexibility which are obtained by directly specifying the damage effect tensor.

In the past, a number of models to describe the viscoelastic behavior and/or nonlinear mechanical behavior associated with damage for a general anisotropic continuum have been proposed. Several approaches aimed at modeling the nonlinear behavior of short fiber reinforced polymers have been reported; namely, Dano et al. [198] adopted the continuum damage mechanics theory developed by Chow and Wang [92] to predict 2D damage in random short fiber glass reinforced composites with a damage evolution function linear with the thermodynamic force conjugate to damage. Oldenbo and Varna [199] used the same 2D continuum damage mechanics

theory but extended it to include linear viscoelastic properties of sheet molding compound, a quasi-elastic approach was used for linear viscoelastic stiffness definition and a similar damage evolution function was used. Varna and Oldenbo [200] implemented their 2D continuum damage formulation into the finite element solver Abaqus/Standard. In works [refs], the effect of time on damage evolution was ignored, which resulted significant deviation in predicted nonlinear response. Andriyana et al. used a different approach of modeling the nonlinear behavior of short fiber composites by extending the rheological work of Lion [201], [202], Huber and Tsakmakis [203] and Miehe and Keck [204], wherein the continuum mechanics approach is based on multiplicative decomposition of the deformation gradient into an elastic and inelastic parts. While their strain energy decomposition approach yielded good agreement between experiments and simulation, it required trial and error fitting of several material-dependent parameters based on off-axis tensile tests, x-ray tomography, relaxation tests, load-unload experiments. He et al. [205] used an internal state variable polymer model based on the work of Bouvard et al. [206], [207] and Francis et al. [208], and the model uses a second-order damage tensor decomposed into three micro-scale damage mechanisms, and does not account for viscoelasticity. In their work, characterization of the three micro-damage mechanisms required complex in-situ X-ray tomography experiments to track the evolution of the distinct micro-voids in an short fiber composite; moreover, this was done to investigate how these damage mechanisms evolve with the deformation of the composite at different stress levels and also to characterize some of the eleven material-dependent model parameters. To the best knowledge of the authors, there has been no linear viscoelastic damage model with temperature-dependent damage evolution behavior.

In the present treatise, a three-dimensional anisotropic thermoviscoelastic progressive damage model that is capable of modeling the nonlinear behavior of 3D printed short fiber composites at ambient and elevated temperature conditions is presented. The thermodynamic framework for linear viscoelastic solids initially proposed by Biot [148], then explored by Lublliner [163], and extended by Abdel-Tawab and Weitsman [165] is adopted in this work. Under the thermodynamic framework, the material model is subjected to the conservation of energy and thermodynamic consistency requirements which allows for admissible states for any given thermomechanical loading. The anisotropic damage theory initially proposed by Cordebois and Sidoroff [98] and Cordebois [209], then extended by Chow and Wang [92], Chow and Lu [94] and Zhu and Cescotto [100] is used. In the work of Barbero and Lonetti [103], a similar damage

anisotropic theory was used and further extended to include a simple isotropic hardening formulation, their isotropic hardening function has been adopted in this work. Simon et al. [175] used a three-dimensional extension of the work of Barbero [170], initially proposed by Bednarcyk et al. [174] for plain woven fabric, to model intralaminar and delamination damage in laminates. In the work of Simon et al. [175], a very useful methodology for obtaining the anisotropic damage model parameters is presented and followed in this work. For a comprehensive review of the theory of continuum damage mechanics, the reader is recommended the following references [78], [106], [108].

The scope of this chapter is to calibrate and exercise the thermoviscoelastic damage model to predict the nonlinear behavior of 25% wt. carbon fiber reinforced PESU for ambient and elevated temperature conditions. A temperature-dependent damage surface potential function has been proposed and calibrated from simple elevated temperature uniaxial tensile tests in addition to compression tests for the case of unilateral behavior. An energy-norm function with a material-dependent J-tensor is used for anisotropic damage description. The model is exercised in Abaqus/Standard (Implicit) with a user material subroutine. The aim of this study is to perform several load cases and assess its ability to predict the change in nonlinear behavior as observed from experimental results. Lastly, proposed changes to the model is made for shear deformation cases for situations where plastic deformations are not available.

5.2 Characterization of Thermoviscoelastic Material Model

The experimentally measured effective elastic properties of the composite for various temperatures are summarized in Table 1. The short fiber composite is assumed to behave in an orthotropic manner; hence, nine independent components of the stiffness tensor are required for its description. Moreover, the nine stiffness components are represented as a Prony series as shown in Eq. (100). The method used for characterizing the Prony series of the stiffness matrix is found in [14], it is a quasi-elastic method for estimating the effective thermoviscoelastic properties of the short fiber composite. The coefficients of the Prony series are summarized in Table 4. The method requires relaxation experiments performed on a dynamic mechanical analyzer using a three-point bending fixture to apply a constant strain for slender beams. Two samples are needed to estimate the thermoviscoelastic properties of the composites, a beam oriented along the print direction and another oriented in-plane or out-of-plane transverse to the print direction. The modulus versus log-

time for each temperature experiment is plotted, and the curves are shifted horizontally with respect to the reference curve at the glass transition temperature of the polymer. Vertical shifting of the modulus data below 180°C is done to ensure the relative instantaneous modulus is preserved. A normalized master curve is generated for both samples and the Prony series is fitted for each master curve. The print direction modulus is assumed to follow the trend of the print direction master curve; however, the remaining properties are assumed to follow the trend of the transverse direction master curve. Therefore, it is assumed the matrix controls the relaxation behavior of the remaining properties. Figure 74a illustrates the approximate relaxation behavior of the nine stiffness components based on the methodology adopted, and Figure 74b shows the fitted modified WLF piecewise equations for both sets of horizontal shift factors.

Table 4 Prony coefficients for thermoviscoelastic model

m	$C^V_{11,m}$	$C^V_{12,m}$	$C^V_{13,m}$	$C^V_{22,m}$	$C^V_{23,m}$	$C^V_{33,m}$	$C^V_{44,m}$	$C^V_{55,m}$	$C^V_{66,m}$	τ_m
1	1.210E-16	3.333E-13	2.382E-13	5.320E-13	2.027E-13	4.004E-13	1.101E-13	1.051E-13	2.402E-13	1.000E-18
2	1.706E+02	4.995E+01	3.569E+01	7.974E+01	3.038E+01	6.001E+01	1.650E+01	1.575E+01	3.600E+01	1.000E-17
3	2.362E+02	1.055E+02	7.539E+01	1.684E+02	6.417E+01	1.267E+02	3.485E+01	3.326E+01	7.603E+01	1.000E-16
4	2.401E+02	2.685E+01	1.919E+01	4.287E+01	1.633E+01	3.226E+01	8.870E+00	8.467E+00	1.935E+01	1.000E-15
5	2.788E+02	1.431E-07	1.022E-07	2.284E-07	8.701E-08	1.719E-07	4.726E-08	4.511E-08	1.031E-07	1.000E-14
6	2.401E+02	3.744E-06	2.676E-06	5.977E-06	2.277E-06	4.498E-06	1.237E-06	1.181E-06	2.699E-06	1.000E-13
7	1.520E+02	5.035E+01	3.598E+01	8.037E+01	3.062E+01	6.049E+01	1.663E+01	1.588E+01	3.629E+01	1.000E-12
8	3.814E+02	8.232E+01	5.882E+01	1.314E+02	5.007E+01	9.889E+01	2.719E+01	2.596E+01	5.933E+01	1.000E-11
9	4.646E+02	3.261E+00	2.330E+00	5.205E+00	1.983E+00	3.917E+00	1.077E+00	1.028E+00	2.350E+00	1.000E-10
10	2.149E-15	8.032E+01	5.740E+01	1.282E+02	4.885E+01	9.649E+01	2.653E+01	2.533E+01	5.789E+01	1.000E-09
11	7.105E+02	1.331E+02	9.509E+01	2.124E+02	8.094E+01	1.599E+02	4.396E+01	4.196E+01	9.590E+01	1.000E-08
12	6.873E+01	7.953E-10	5.683E-10	1.269E-09	4.837E-10	9.553E-10	2.627E-10	2.507E-10	5.731E-10	1.000E-07
13	3.775E+02	1.551E+02	1.108E+02	2.475E+02	9.431E+01	1.863E+02	5.122E+01	4.889E+01	1.117E+02	1.000E-06
14	3.756E+02	3.321E+01	2.373E+01	5.301E+01	2.020E+01	3.989E+01	1.097E+01	1.047E+01	2.393E+01	1.000E-05
15	2.943E+02	1.183E+02	8.452E+01	1.888E+02	7.194E+01	1.421E+02	3.907E+01	3.730E+01	8.525E+01	1.000E-04
16	3.427E+02	1.515E+02	1.082E+02	2.418E+02	9.212E+01	1.819E+02	5.003E+01	4.775E+01	1.092E+02	1.000E-03
17	4.337E+02	9.311E+01	6.653E+01	1.486E+02	5.663E+01	1.119E+02	3.076E+01	2.936E+01	6.710E+01	1.000E-02
18	2.033E+02	1.051E+02	7.510E+01	1.678E+02	6.392E+01	1.263E+02	3.472E+01	3.314E+01	7.574E+01	1.000E-01
19	4.298E+02	1.199E+02	8.567E+01	1.914E+02	7.292E+01	1.440E+02	3.960E+01	3.780E+01	8.640E+01	1.000E+00
20	5.673E+02	2.981E+02	2.130E+02	4.759E+02	1.813E+02	3.581E+02	9.847E+01	9.400E+01	2.148E+02	1.000E+01
21	4.976E+03	1.395E+03	9.966E+02	2.226E+03	8.483E+02	1.675E+03	4.607E+02	4.397E+02	1.005E+03	1.000E+02
22	7.647E+03	1.003E+03	7.167E+02	1.601E+03	6.101E+02	1.205E+03	3.313E+02	3.163E+02	7.229E+02	1.000E+03
23	3.678E+02	3.764E-11	2.690E-11	6.009E-11	2.290E-11	4.522E-11	1.243E-11	1.187E-11	2.713E-11	1.000E+04
24	3.730E+02	1.123E-09	8.024E-10	1.792E-09	6.830E-10	1.349E-09	3.709E-10	3.541E-10	8.093E-10	1.000E+05
25	6.331E-02	2.821E-08	2.016E-08	4.504E-08	1.716E-08	3.389E-08	9.319E-09	8.896E-09	2.033E-08	1.000E+06
C^e_{pq}	8.247E+01	1.471E-07	1.051E-07	2.347E-07	8.944E-08	1.767E-07	4.858E-08	4.637E-08	1.060E-07	

To verify the thermoviscoelastic behavior of the material model, the stress relaxation behavior was evaluated and compared to the experimental data. Figure 73 illustrates selected plots

for normalized stress along the print direction with respect to time in seconds. Three temperatures, (a) 30°C, (b) 75°C, and (c) 220°C, are chosen to show the normalized stress relaxation trend from the experiments and thermoviscoelastic model. An instantaneous uniaxial strain of 0.05% was applied for all simulations. The red curve represents the stress relaxation experimental data and the black curve represents the finite element thermoviscoelastic model. For each of the three plots, the model is found to have good agreement with the experimental results using the quasi-elastic approximation. Moreover, the model is found to be within 5% of the experimental results.

$$C^*_{mn}(\xi(t)) = \begin{bmatrix} C^*_{11}(\xi(t)) & C^*_{12}(\xi(t)) & C^*_{13}(\xi(t)) & 0 & 0 & 0 \\ C^*_{12}(\xi(t)) & C^*_{22}(\xi(t)) & C^*_{23}(\xi(t)) & 0 & 0 & 0 \\ C^*_{13}(\xi(t)) & C^*_{23}(\xi(t)) & C^*_{33}(\xi(t)) & 0 & 0 & 0 \\ 0 & 0 & 0 & C^*_{44}(\xi(t)) & 0 & 0 \\ 0 & 0 & 0 & 0 & C^*_{55}(\xi(t)) & 0 \\ 0 & 0 & 0 & 0 & 0 & C^*_{66}(\xi(t)) \end{bmatrix} \quad (100)$$

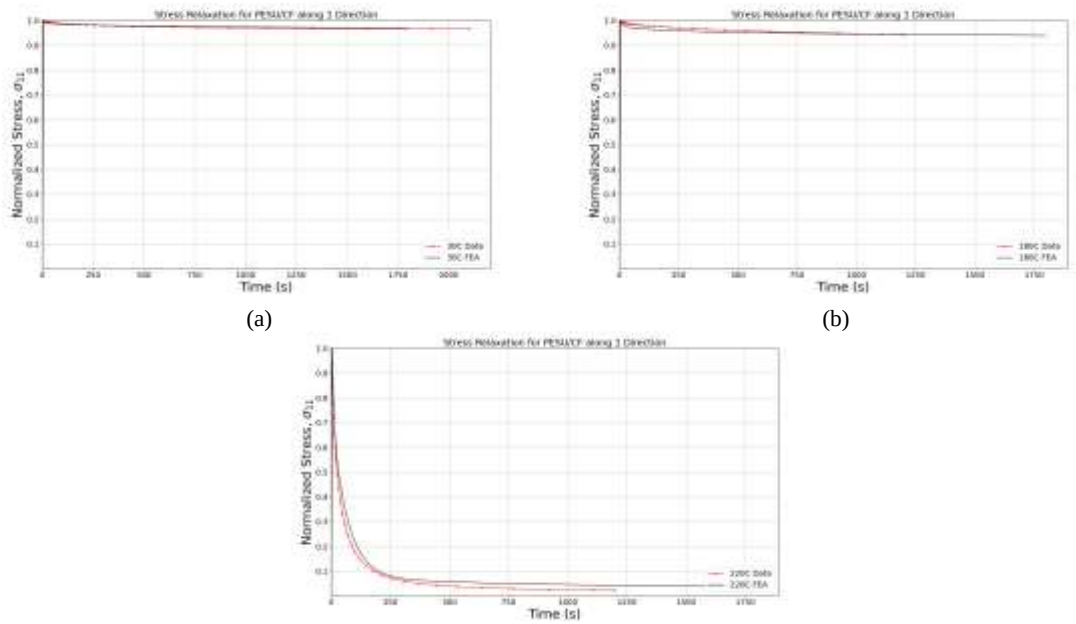

Figure 73 Selected normalized stress relaxation comparison between experiment and thermoviscoelastic model, strain along the print direction for (a) 30°C, (b) 75°C, and (c) 220°C

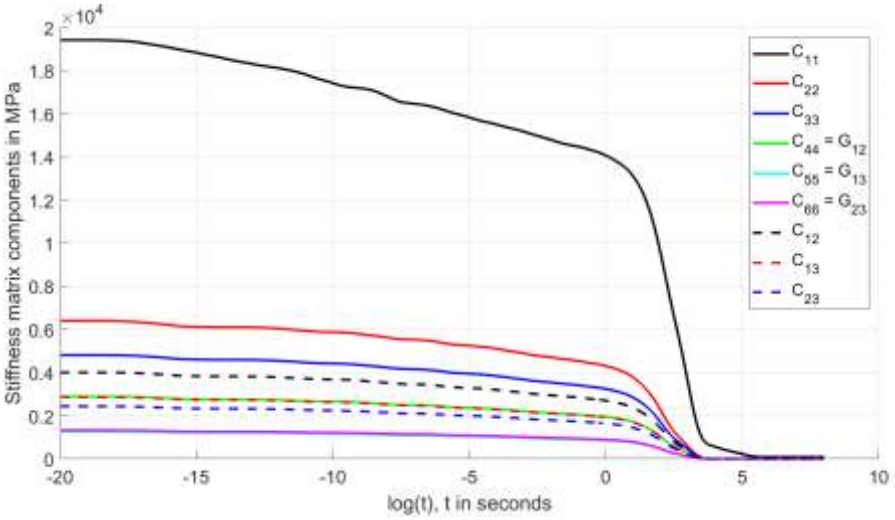

(a)

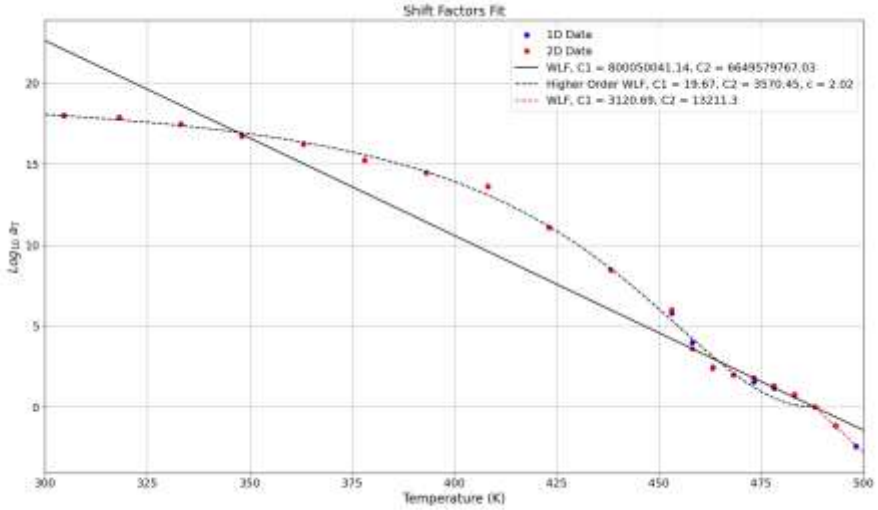

(b)

Figure 74 (a) Orthotropic stiffness matrix component relaxation behavior deduced from normalized master curves and mechanical properties of 25% wt. carbon fiber reinforced PESU, (b) Horizontal shift factors for print direction master curve (1D) and in-plane transverse direction (2D) alongside the piece-wise WLF trends

5.3 Calibration of Thermoviscoelastic Damage Parameters

The orthotropic continuum damage model for printed composites contains two damage descriptions: namely, the intrabead and interbead damage modes. Therefore, the following nine parameters, J_{11}, J_{22}, J_{33}^{I}, c_1, c_1^I, c_2, c_2^I, κ_0, and κ_0^I are required. Simon et al. [175] describe the procedure needed to characterize these parameters based on simple uniaxial tensile experiments. The uniaxial tension test along the print direction is used for characterizing c_1, c_2, and κ_0; on the other hand, the tension test along the stacking direction is used for characterizing c_1^I, c_2^I, and κ_0^I. For the assumed homogenous and uniaxial stress state, only one component of the damage thermodynamic force tensor is non-zero for either case (e.g., Y_{11} or Y_{33}). At damage onset, the hardening variable is zero and the damage surface equation reduces to Eq. (101), for example. The first value of the damage interaction tensor, J_{mn}, can be arbitrarily chosen since the same damage surface and evolution equations can be obtained for any other value; therefore, it is set to two. It is noteworthy to mention, only the ratios of the damage interaction parameters are relevant.

$$g = \sqrt{J_{11}/2}Y_{11} - \kappa_0 = 0 \rightarrow \kappa_0(T) = \sqrt{J_{11}/2}\left(C_{11}^{e} + \sum_{m=1}^{M} C_{11,m}^{V}\, e^{-\frac{\xi(t)}{\tau_m}}\right)(\varepsilon_1^0)^2 \qquad (101)$$

The two parameters in the hardening/softening function, c_1 and c_2, are determined by selecting two points on the stress versus strain plot from which damage is present. After damage onset, damage is approximated by using the secant modulus, this enables the use of the equation, $\sigma_1 = (1 - D_1)^2 E_1 \varepsilon_1$, to estimate the damage quantity relative to the pristine modulus, E_1^0. In other words, the two damage points, $D_1^{(I)}$ and $D_1^{(II)}$, are obtained as shown in Eq. (102) and are then used for estimating c_1 and c_2 by solving Eqs. (103) and (104) at the reference temperature T_0 (e.g., room temperature). Delamination material parameters are obtained in a similar fashion. To estimate the change in hardening softening behavior associated with temperature changes, Eq. (105) is recommended, this assumes c_1 remains constant with temperature. Additionally, $c_2(T > T_0)$ should be obtained for damage values above 0.01 to avoid anomalous values near $D = 0$ and preferably averaged over a small range after the values of $c_2(T > T_0)$ converge.

$$D_1^{(I)} = 1 - \sqrt{\frac{(\sigma_{11}^{(I)}/\varepsilon_{11}^{(I)})}{E_1^0}} \;\&\; D_1^{(II)} = 1 - \sqrt{\frac{(\sigma_{11}^{(II)}/\varepsilon_{11}^{(II)})}{E_1^0}} \tag{102}$$

$$\left[\left(1 - D_1^{(II)}\right)C_{11}^*(\xi)\left(\varepsilon_1^{(II)}\right)^2 - \kappa_0\right]\left(e^{-\frac{D_1^{(I)}}{c_2}} - 1\right)\ldots$$
$$-\left[\left(1 - D_1^{(I)}\right)C_{11}^*(\xi)\left(\varepsilon_1^{(I)}\right)^2 - \kappa_0\right]\left(e^{-\frac{D_1^{(II)}}{c_2}} - 1\right) = 0 \tag{103}$$

$$c_1 = \frac{\left(1 - D_1^{(I)}\right)C_{11}^*(\xi)\left(\varepsilon_1^{(I)}\right)^2 - \kappa_0(T_0)}{e^{-D_1^{(I)}/c_2} - 1} \tag{104}$$

$$c_2(T > T_0) = \frac{-D_1}{ln\left[\frac{(1 - D_1)C_{11}^*(\xi)(\varepsilon_1)^2 - \kappa_0(T)}{c_1} + 1\right]} \tag{105}$$

Table 5 Mechanical properties of 3D printed 25%wt. carbon fiber reinforced PESU

Properties	**Values**			
	RT	70°C	130°C	190°C
Avg. E_1 *(GPa)*	16.92	16.91	15.91	12.56
Std. E_1 *(GPa)*	0.29	0.41	0.61	1.24
Avg. E_2 *(GPa)*	4.83	4.59	4.26	3.52
Std. E_2 *(GPa)*	0.32	0.25	0.23	0.28
Avg. E_3 *(GPa)*	3.78	3.73	3.53	3.03
Std. E_3 *(GPa)*	0.08	0.14	0.18	0.14
Avg. G_{23} *(GPa)*	1.2	1.2	1.2	1.2
Std. G_{23} *(GPa)*	0.087	0.095	0.14	0.17
Avg. G_{13} *(GPa)*	1.44	1.41	1.43	1.40
Std. G_{13} *(GPa)*	0.017	0.095	0.057	0.065
Avg. G_{12} *(GPa)*	2.88	2.69	2.52	2.18
Std. G_{12} *(GPa)*	0.096	0.15	0.11	0.063
Avg. ν_{12} *at RT*	0.3441			
Avg. ν_{13} *at RT*	0.4978			
ν_{23} *at RT*	0.4367*			

*Estimated via micromechanics

The damage threshold value, $\kappa_0(T)$, is approximated using the nonlinear onset strain value, ε_1^0, found in the experimental tensile stress versus strain curve, an example is shown in Figure 75a, and the computed the stiffness matrix from the thermoelastic properties provided in Table 5.

Additionally, the nonlinear onset strain value is determined by extrapolating the fitted linear elastic curve, based on ASTM D3039 strain range, and computing the point at which nonlinear behavior commences (e.g., small percentage difference between the two curves). Eq. (103) is numerically solved to obtain $c_2(T_0)$; however, it is recommended to plot the equation, shown in Figure 75b, to clearly identify an initial value to avoid solving for an infinite value. The secant modulus, E_1^s, as a function of strain is illustrated in Figure 75c. The trend of the secant modulus is similar to the trend of the damage variable, which is illustrated in Figure 75d. The two points shown on this plot are used for computing $c_2(T_0)$, these are chosen near the fracture point and approximately 60% of ultimate fracture.

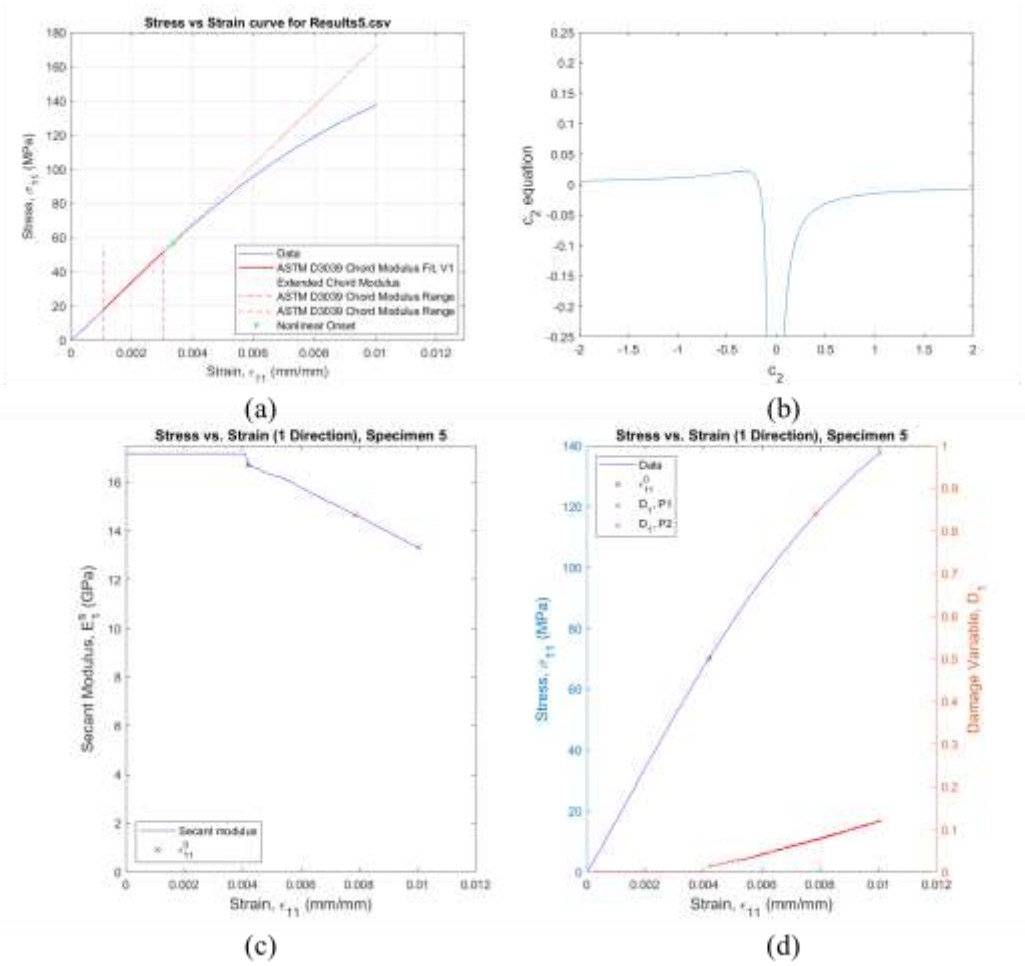

Figure 75 (a) Experimental stress versus strain along print direction (b) damage surface equation used for solving c_2 (c) secant modulus approximation based on experimental tensile test curve (d) damage variable trend and highlighted points, P1 and P2, for hardening characterization

The damage threshold value and the isotropic hardening parameter, $c_2(T)$, were plotted against temperature and a linear regression fit was made, this is shown in Figure 76a and Figure 76b. A temperature increase is observed to decrease the nonlinear onset strain value, this observation is especially pronounced for uniaxial tensile loaded specimens along the in-plane transverse and stacking direction. In other words, nonlinearity commences sooner at elevated temperatures. Figure 77a illustrates the stress versus strain response when κ_0 is varied, it shows that the nonlinear onset increases with an increase in κ_0. Thermoviscoelastic stress relaxation also contributes to the nonlinear behavior; however, the loading rate and time elapsed from beginning to failure has been determined to produce no more than a 3% relaxation effect for all temperatures. Therefore, nonlinear relaxation behavior is reasonably assumed to not significantly contribute to the nonlinearity observed in the stress versus strain behavior. Nevertheless, the reduction in nonlinear strain onset is expected to be a polymer effect. The reduction in $c_2(T)$ is due to the complex interaction between the damage variable, stiffness component and damage threshold value. Figure 78 illustrates the effect of a varying c_2 when c_1 and κ_0 are held constant, smaller values of c_2 lead to a faster evolution of the damage variable and a smaller strain hardening region. Damage critical values have been implemented in all analyses; these values are defined as the last value of the damage variable before fracture occurs. A critical value signifies the moment at which the damage variable rapidly evolves to a value of one to signify total loss of structural integrity. Critical damage variables are found to increase with temperature, and this trend is shown in Figure 76c. The maximum and average damage critical values are plotted with respect to temperature and a quadratic regression fit is made to model the change in the critical value with temperature. In this study, the maximum critical value is chosen since it reflects the data well. On the other hand, a constant room temperature damage critical value was chosen for the in-plane transverse, D_2^{cr}, and stacking, D_3^{cr}, directions to simplify the model.

The value of the second damage interaction component, J_{22}, is obtain by solving the damage surface relation at the point of damage onset for a uniaxially loaded tensile specimen along the in-plane transverse direction. Since the damage threshold value has been evaluated, the damage surface relation can be solved for J_{22} with knowledge of the nonlinear strain onset of a tensile loaded specimen along the in-plane transverse direction and stiffness matrix component, C_{22}^*. In Figure 77b, the stress versus strain plot for several different values of J_{11} is shown and this illustrates the changes in nonlinear material response. For the interface material damage

description, only J_{33}^I is present in the damage interaction tensor and its value is also set to two; furthermore, only c_1^I, $c_2^I(T)$, and $\kappa_0^I(T)$ require characterization. For the interface isotropic damage material parameter, c_2^I, a quadratic regression fit is made because of the observed trend shown in Figure 79a. It is noteworthy to mention, the nonlinear behavior is related to the nonlinear trend in the uniaxial tensile specimens loaded along the stacking direction. In other words, this suggests the strain hardening regime decays rapidly as temperature increases. A linear regression fit is made for the damage threshold parameter, κ_0^I, which is illustrated in Figure 79b. The damage model parameters are reported in Table 6.

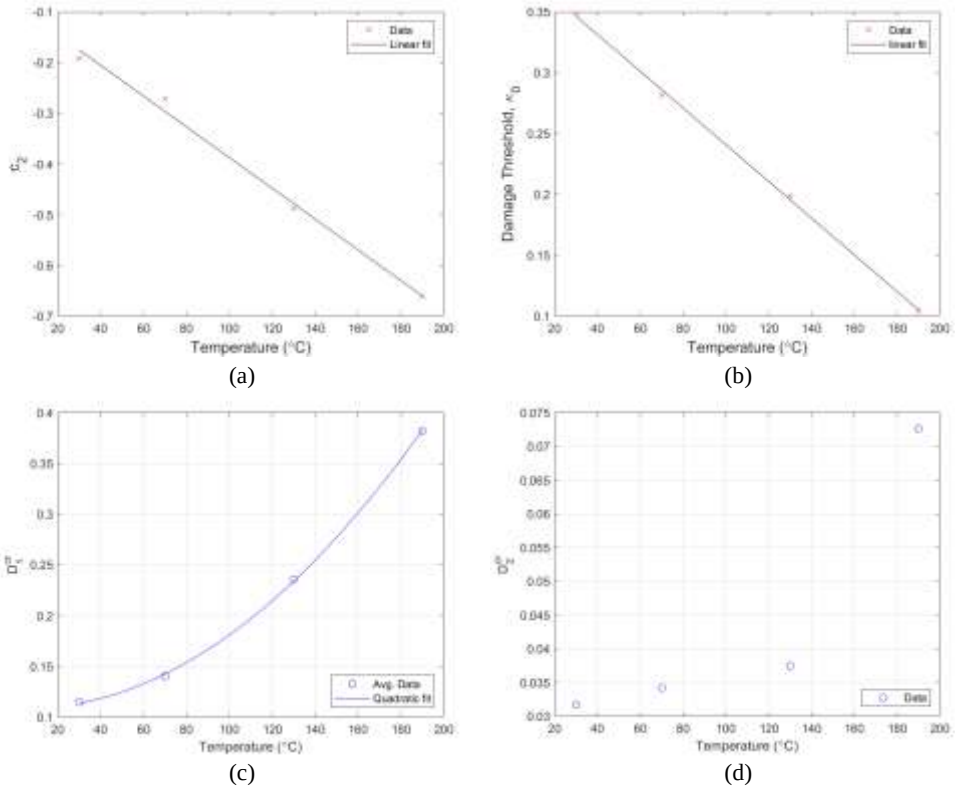

Figure 76 (a) Average isotropic hardening/softening parameter c_2 as a function of temperature, (b) average damage threshold, κ_0, as a function of temperature, (c) mean critical damage value as a function of temperature for print direction tensile coupons, and (d) mean critical damage values for in-plane transverse tensile coupons as a function of temperature

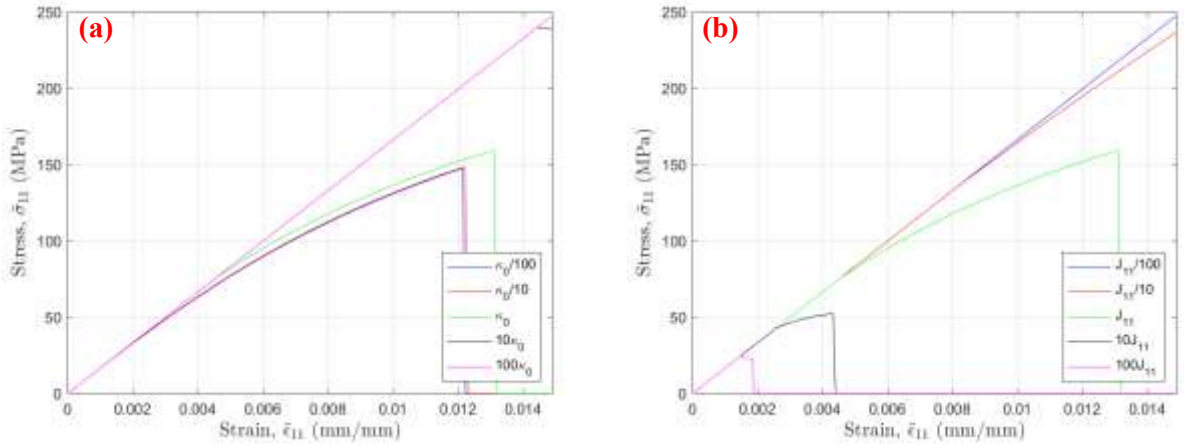

Figure 77 (a) Simulation of stress versus strain along print direction for different values of κ_0 while keeping all other model parameters constant, and (b) simulation of stress versus strain along print direction for different values of J_{11}

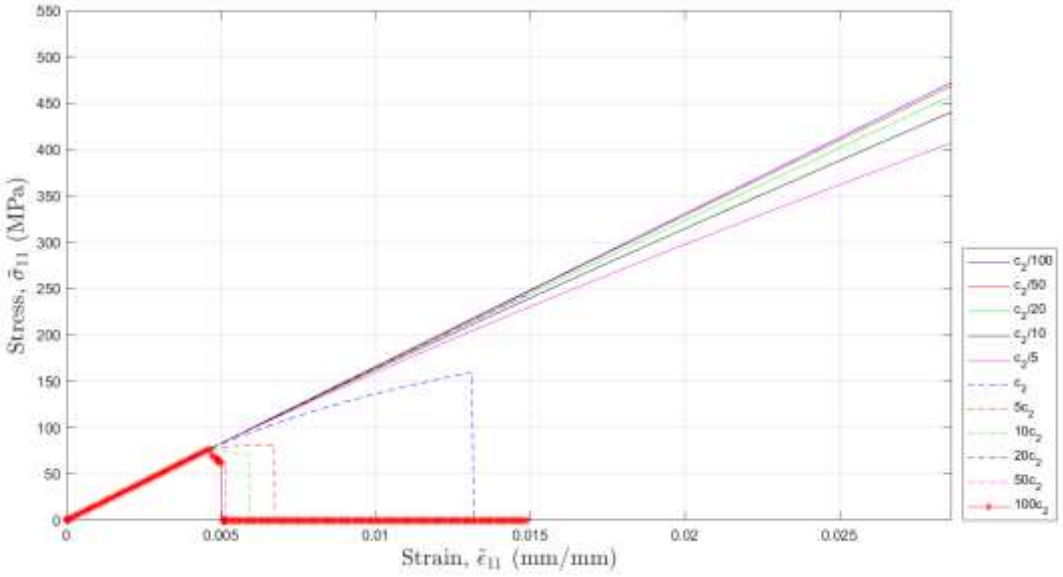

Figure 78 Simulation of stress versus strain along print direction at room temperature for different values of c_2 while keeping all other model parameters constant

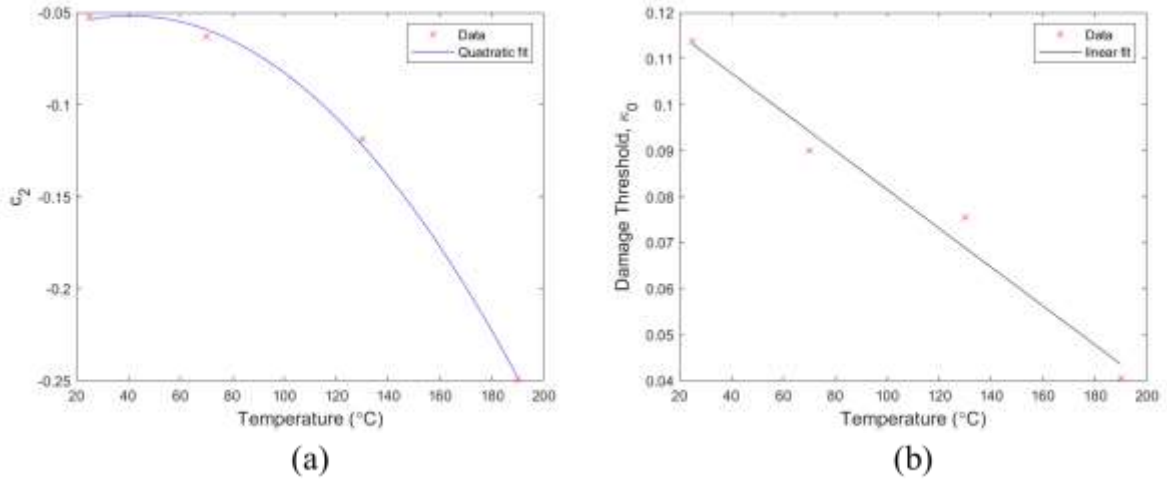

Figure 79 (a) Average interface isotropic hardening/softening parameter c_2 as a function of temperature and (b) average interface damage threshold as a function of temperature

Table 6 Damage model parameters obtained from uniaxial tensile tests

Property	**Value/Function**	**Purpose**
J_{11}	2.0	Intrabead
J_{22}	4.536	Intrabead
c_1	1.617	Intrabead
$c_2(T)$	$-0.003032T - 0.08433$	Intrabead
$\kappa_0(T)$	$-0.00147T + 0.3858$	Intrabead
$D_1^{cr}(T)$	$6.313 \cdot 10^{-6}T^2 + 0.000497T + 0.1234$	Intrabead
D_2^{cr}	0.0317	Intrabead
J_{33}^I	2.0	Interbead
c_1^I	0.335	Interbead
$c_2^I(T)$	$-8.835 \cdot 10^{-6}T^2 + 0.0007212T - 0.06633$	Interbead
$\kappa_0^I(T)$	$-0.0004214T + 0.1237$	Interbead
D_3^{cr}	0.0588	Interbead

Temperature-dependent damage evolution parameters are essential for properly capturing the observed nonlinear trends in experimental elevated temperature tensile tests. Not only does the strain hardening regime change, the ultimate strain and stress decay with an increase in temperature. Even though all three damage parameters, J_{mn}, c_2, κ_0, are capable of producing the change in material response, both c_2 and κ_0 should suffice in capturing the elevated temperature changes. Figure 80 depicts the uniaxial material response for three different cases, where (a) c_2 is kept constant, (b) κ_0 is maintained constant, and (c) both c_2 and κ_0 are constant. In Figure 80a, it is evident that keeping c_2 constant while allowing κ_0 to change with temperature does not produce a significant change in material response for RT, 70°C, 130°C temperatures. Additionally, the strain hardening response is similar for all temperature cases. Figure 80b illustrates the change in

nonlinear response produced when c_2 is not constant; however, the nonlinear onset is similar for all temperatures. By the same token, keeping both parameters constant with temperature does not significantly alter the material response as shown in Figure 80c, significant overlap is observed for the RT, 70°C, 130°C curves and a similar trend is followed by the 190°C behavior.

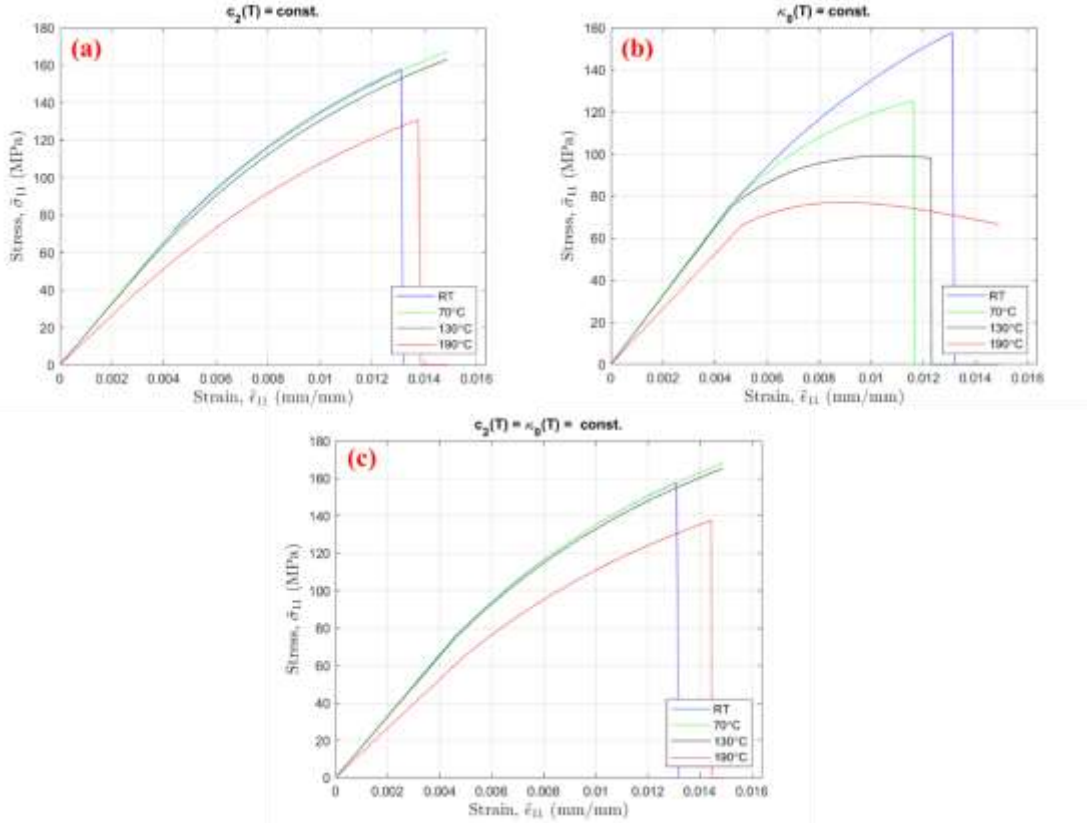

Figure 80 Simulation of stress versus strain at different temperatures while keeping (a) $c_2(T)$ constant, (b) $\kappa_0(T)$ constant, and (c) $c_2(T)$ and $\kappa_0(T)$ constant

5.4 Material Model Predictions

Comparison between experiment and simulation for uniaxial tensile loaded specimens along the print direction is made in Figure 81. The temperatures chosen were approximately 30%, 60% and 90% of the PESU glass transition temperature of 215°C, temperatures above the glass transition is expected to significantly contribute to the nonlinear response within the time scale of the tensile test. From plots shown, the nonlinearity observed for all experiments becomes more pronounced at higher temperatures. For all temperature cases, the blue crosses indicate the point at which abrupt failure or softening begin in the experimental specimens. The experimental data

is smoothed to reduce the noise output from the digital image correlation technique, and the undulations correspond to load drops during the test. The temperature-dependent model is shown to capture the trend observed in the experimental tests; namely, the reduction in nonlinear onset, nonlinear behavior, and decay in ultimate strength. The experimental average and model predicted values are summarized in Table 6. The abrupt failure in the model is produced by the critical damage parameter, $D_1^{cr}(T)$. For the present model formulation, the nonlinear response is solely due to damage accumulation. Therefore, permanent strain is not modeled; however, this is an assumption that is valid when little permanent strain is observed upon unloading of coupon.

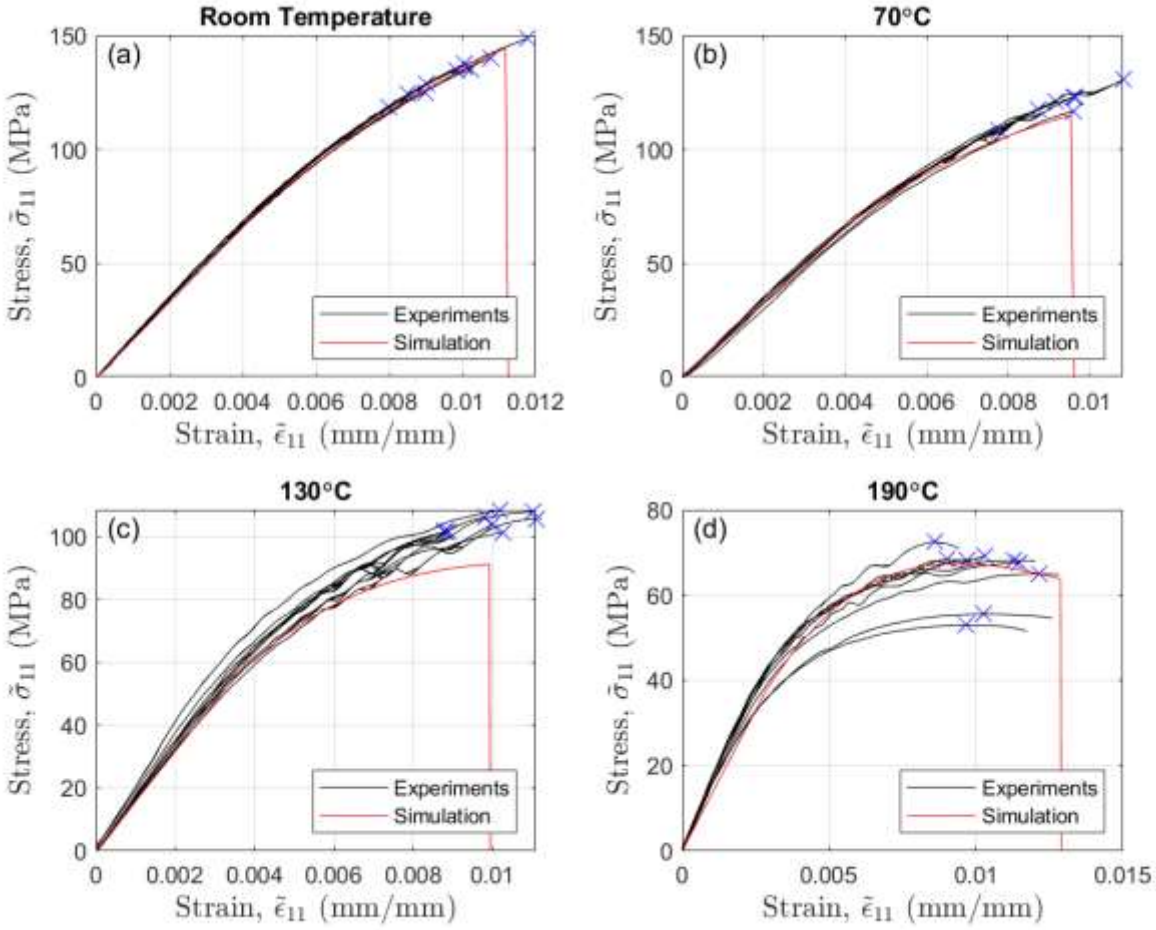

Figure 81 Comparison of stress versus strain behavior between simulation and experiments for different temperatures for uniaxial tensile loaded specimens along the print direction

Table 7 Summary of experimental average values and predicted values

	Experiment				*Simulation*			
	RT	70°C	130°C	190°C	RT	70°C	130°C	190°C
σ_{11}^{ult} *(MPa)*	133	122	104	65	144	115	91	67
σ_{22}^{ult} *(MPa)*	42	34	28	17	40	34	27	19
σ_{33}^{ult} *(MPa)*	44	32	25	16	50	45	28	18
ε_{11}^{ult} *(%)*	0.97	0.93	0.99	1.03	1.13	0.950	0.991	0.940
ε_{22}^{ult} *(%)*	0.92	0.78	0.63	0.52	0.89	0.76	0.64	0.53
ε_{33}^{ult} *(%)*	1.29	0.94	0.73	0.60	1.46	1.34	0.87	0.66
ε_{11}^{0} *(%)*	0.42	0.37	0.33	0.31	0.49	0.43	0.30	0.30
ε_{22}^{0} *(%)*	0.51	0.53	0.38	0.33	0.72	0.65	0.55	0.43
ε_{33}^{0} *(%)*	0.48	0.54	0.51	0.32	0.62	0.57	0.47	0.39
E_1 *(GPa)*	16.9	16.9	15.9	12.6	16.5	16.4	16.0	13.4
E_2 *(GPa)*	4.8	4.6	4.3	3.5	4.8	4.8	4.6	3.9
E_3 *(GPa)*	3.8	3.7	3.5	3.0	3.8	3.8	3.7	3.1

Figure 82 shows the comparison of experiments and simulation for uniaxial tensile loaded specimens along the in-plane transverse direction for different temperatures. Similar to the response along the print direction, the nonlinear response becomes pronounced at higher temperatures; however, the overall material response is brittle. The current formulation assumes the same isotropic damage surface growth as in the print direction. Consequently, the nonlinear trend beyond damage onset can be observed; however, both parameters, J_{22} and D_2^{cr}, act to abruptly fail the specimen as seen for all cases. The in-plane transverse contains bead-to-bead interfaces as well as some fiber collimation along this direction. The existence of the interface certainly influences the growth and evolution of the damage surface; however, the intrabead approximation is believed to be reasonable based on the predicted response.

The uniaxial tensile mechanical performance along the stacking direction is presented in Figure 83, all of the experiments were found to fail at the interbead interface. It is noteworthy to mention two attributes of printed short fiber composites loaded along the stacking direction; firstly, the interface mechanical performance is highly influenced by the polymer because of the insignificant fiber collimation. Secondly, large compacted voids along the interbead interface have been observed through micrographs and these voids are expected to engender stress concentrations that severely hinders the strength properties. Although variability in performance is not accounted for in the present model, the strength prediction is reasonably close to the experimental observations. Since the polymer dominates the tensile performance along the stacking direction, it is also believed that the nonlinear trend of the isotropic damage hardening parameter, $c_2^I(T)$, is caused by the polymer.

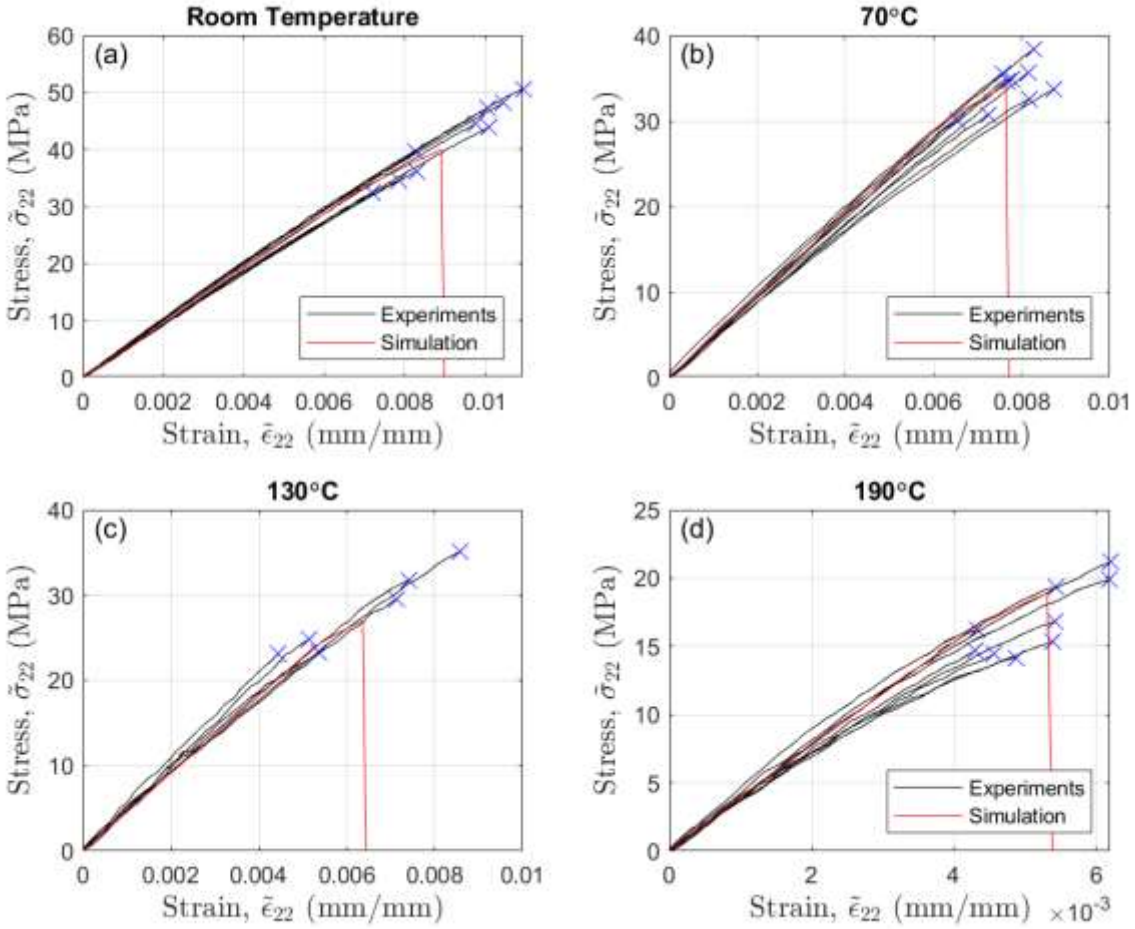

Figure 82 Comparison of stress versus strain behavior between simulation and experiments for different temperatures for uniaxial tensile loaded specimens along the in-plane transverse direction

The ultimate elongation strain at ultimate stress, ε^{ult}, reduction with an increase in temperature for specimens loaded along the in-plane transverse and stacking directions are believed to be a characteristic of the polymer blend phase. Along the print direction, this elongation strain reduction trend is not observed, and it may be reasonable to also assume the fibers are dominating the performance characteristics and inhibiting this trend along this direction. A similar trend for a comparable injection-molded thermoplastic composite can be observed in the work of Eftekhari and Fatemi [210]. In their work, they experimentally investigated temperature effects on the tensile behavior of multiple thermoplastic composites. One of the composite materials, a 20% wt. short glass fiber reinforced modified polyphenylene ether and polystyrene (i.e., Noryl), was tested along the transverse mold-flow direction at room and elevated temperatures. The transverse

to the mold flow direction was said to exhibit most of the fibers oriented orthogonal to the loading direction due to the core-shell morphology. The composite was tested at 23°C, 85°C , and 120°C, these temperatures were below the polymer's glass transition temperature of 135°C. For this composite system, the strain at ultimate strength, ultimate strength, 0.2% offset yield strength and elastic modulus all decreased with temperature. On the contrary, the strain at ultimate strength reduction with temperature was not observed for the other thermoplastic composites which did not contain a polymer alloy. Based on these observations, thermoplastic composites with polymer alloys tested in the glassy regime, this trend may be expected, and further investigation is needed to verify this behavior for other composite systems.

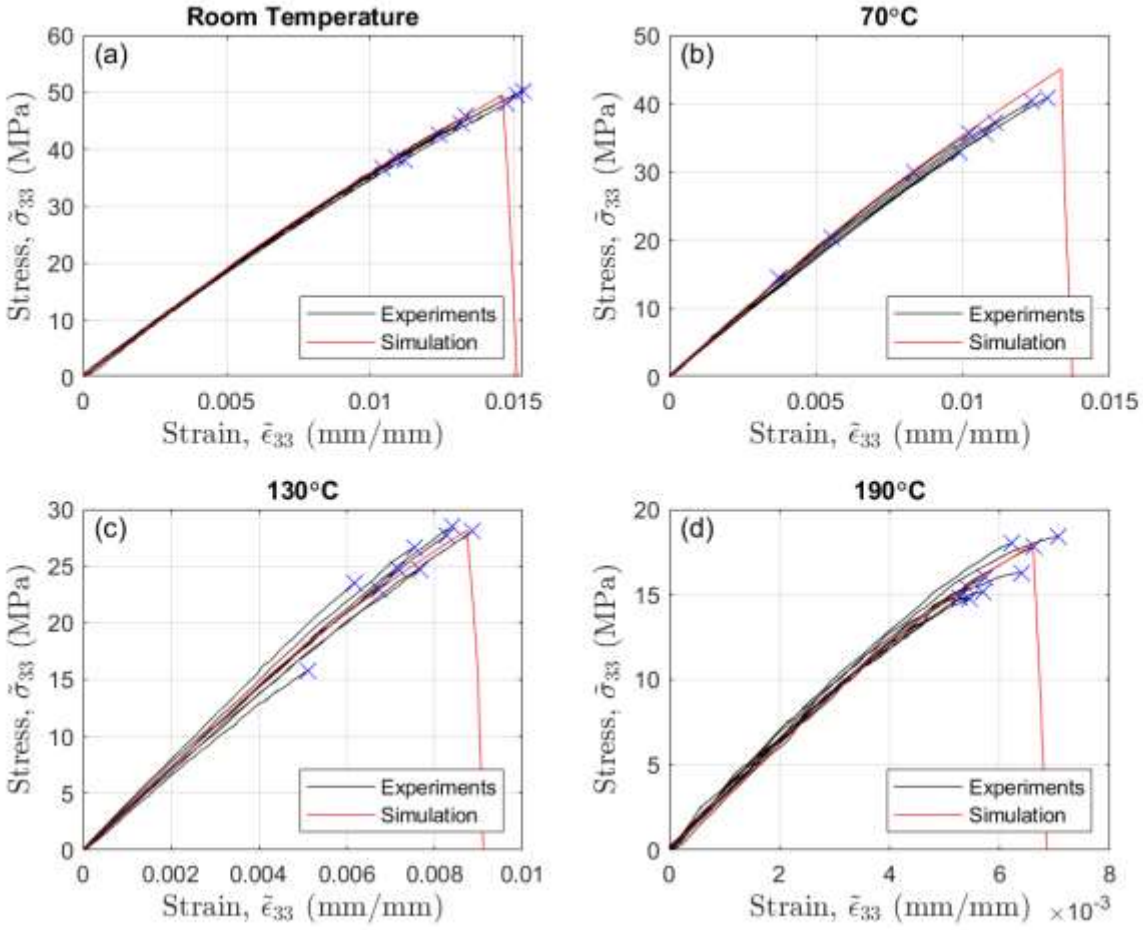

Figure 83 Comparison of stress versus strain behavior between simulation and experiments for different temperatures for uniaxial tensile loaded specimens along the stacking direction

The variability in the strain hardening behavior observed in Figure 81, Figure 82, and Figure 83 increases with temperature, this variability is pronounced for the behavior along the print direction and it is believed to be caused by the dominance of the matrix micro-damage mode. Since it is evident that the matrix softens with temperature and exhibits strain-to-failure brittleness at elevated temperature based on the performance along the in-plane transverse and stacking directions, it is reasonable to assume local compliant microscopic regions exhibits matrix-cracking and/or interfacial debonding at lower stress effective strain levels. The early micro-damage initiation combined with the spatial microstructural morphology produced by the EDAM process may lead to the observed strain hardening variability observed along the print direction. By the same token, the variability in thermo-mechanical properties are believed to be caused by the microstructural morphology, namely, differences in effective fiber orientation states and local spatial micro-constituent configurations between tensile specimens.

5.5 Single Element Creep-Damage Interaction

Since the material model is strain-based, the evolution of strain with time can initiate and progress damage. Creep occurs when a constant load is applied with time which causes strains to increase because of the time-dependent compliance. Viscoelastic induced strains also drive the evolution of thermodynamic forces. Time-dependent thermodynamic forces can create a material state that lies outside of the damage surface, eventually causing a non-allowable thermodynamic state that requires dissipation. To demonstrate the creep-damage behavior, Figure 84, Figure 85, and Figure 86 illustrate the evolution of the axial strain and damage with time for various temperatures at constant load. Figure 84 shows the creep response along the print direction at a constant stress of 60MPa, this stress value was chosen to accelerate damage evolution at higher temperatures and demonstrate the creep-damage behavior. The solid curves are the axial strain, $\tilde{\varepsilon}_{11}$, and the dashed curves represent the damage variable, D_1, along the print direction. A uniaxial stress is applied as a linear ramp from zero to one second, then it is held constant for 10 hours or until rupture occurs. Creep rupture happens when the strain increases substantially past the yield point and the damage variable reaches its critical value. For the 190°C case, the applied stress level is beyond the linear elastic regime and it is the reason why the damage variable is non-zero at the start. Likewise, the 130°C exhibits a small amount of damage at the start of the creep simulation because of the same reason. An interesting observation is the effect of damage on the strain evolution, damage acts to

further increase the strain magnitude. Moreover, damage continues to evolve after initiation and no plateau in damage evolution is observed. The moment before creep rupture, an accelerated damage and strain region is seen from the 190°C creep test and it is driven by the combined effect of the isotropic hardening variable, thermodynamic forces, critical damage variable, and creep compliance. After the critical damage value is reached, damage jumps to a value of one which causes the strain to substantially rise. The jump in damage variable at the critical value is merely an assumption based on experimental observation, and it is arguably a limitation of the model since a fracture energy based softening function is not considered to capture the rapid damage progression past the critical point. During the elapsed time, no deterioration is observed at low temperatures and this is because the creep compliance has not evolved enough to allow for thermodynamically unstable states. The creep compliance is expected to continuously increase with time, and this will cause strains to increase alongside the potential for damage dissipation.

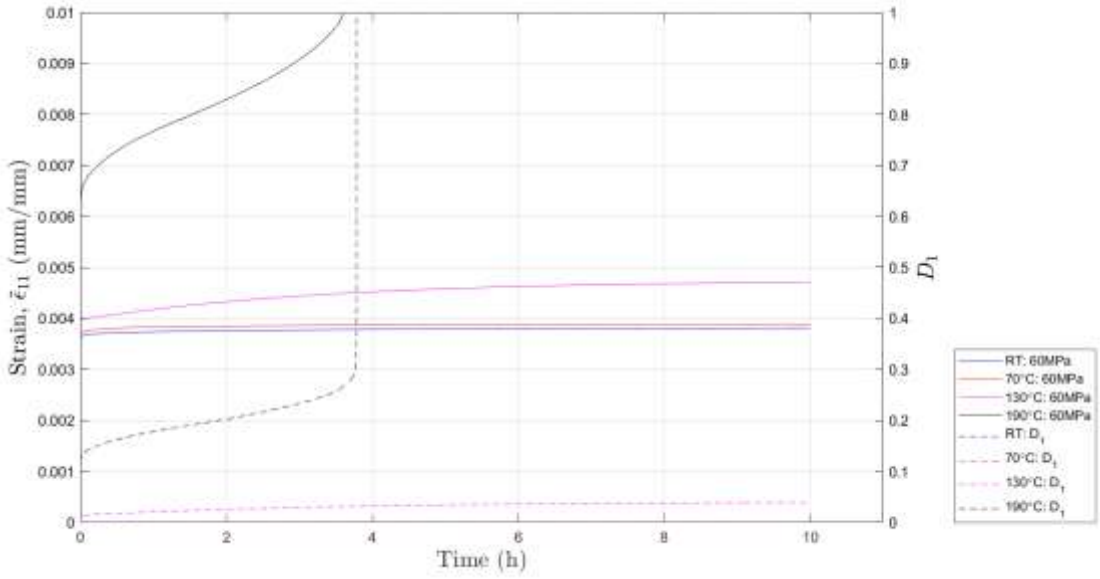

Figure 84 Single element creep-damage test along the print direction at various temperatures

Creep behavior along the 2 direction for various temperatures is shown in Figure 85 below. The strains, $\tilde{\varepsilon}_{22}$, are represented by solid curves and the damage variable, D_2, by the dashed curves. For each temperature case, a constant load, within the linear elastic regime, was applied. Therefore, no initial damage is observed at the start of the simulation. Amongst all temperature cases, the 190°C test experienced damage initiation, evolution and creep rupture with a sustained load of

15MPa. Simultaneously, the lower temperature tests did not experience any damage initiation. Creep rupture occurs at approximately 0.5% strain for the 190°C test, this value is similar to the rupture strain observed in uniaxial tensile tests. As seen from the room temperature and 70°C curves, the strain curves exceed the rupture strain of the 190°C test and this is expected since the damage threshold and hardening parameters change with temperature. Unlike the print direction creep test shown above, the creep rupture along the 2 direction is induced by the critical damage variable and it has the effect of steeply increasing both the strain and damage variable. The rapid change in these variables is due to the small amount of hardening experienced by the material, this means the damage surface experienced an insignificant amount of expansion which causes damage to rapidly evolve.

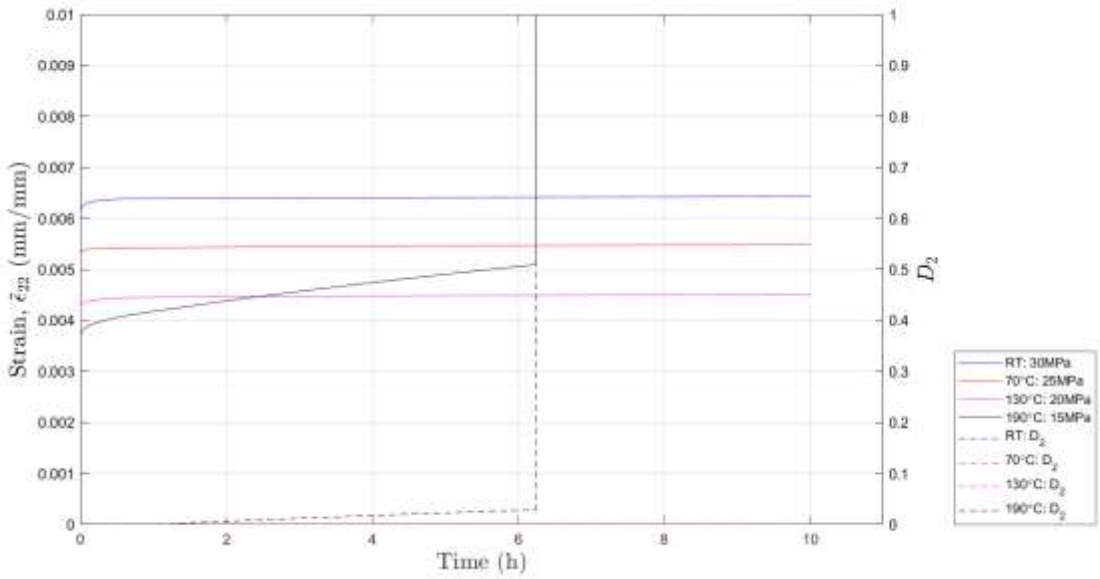

Figure 85 Single element creep-damage test along the 2 direction at various temperatures

Creep behavior along the stacking direction is shown in Figure 86. Similar to the creep plots shown above, a similar trend is found yet not creep rupture is observed. The plot shown below is provided for completeness. For all temperature cases except the 190°C test, an initial damage amount is observed which means that the applied loads were beyond the yield point of the material. Even though creep rupture is not observed within the elapsed time of the test and the applied loads, the strains and damage are continuously evolving. The instantaneous strain at 70°C is greater than the room temperature case because of the difference in instantaneous compliance.

Lastly, the creep strain evolution and an estimated creep rupture can be predicted using the continuum damage model. Creep experiments are needed to validate the model and confirm the trends predicted are representative of the material behavior.

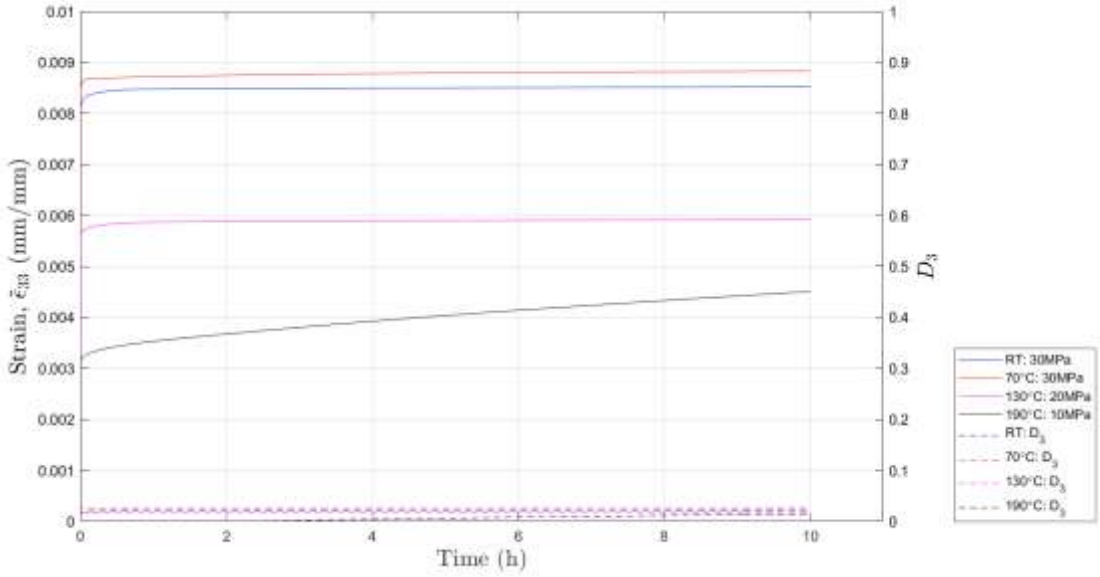

Figure 86 Single element creep-damage test along the stacking direction at various temperatures

5.6 Meso-Scale Tensile Coupon Exercise

Uniaxial tensile specimens, dog-bone shaped, were modeled in Abaqus/Standard to predict progressive damage with multiple elements. The dimensions of the dog-bone model were specified from the average measured values of the coupons used for tension experiments. Figure 87 illustrates the effective stress versus average strains for a tensile loaded bar along the print direction. The average strain was obtained by selecting and averaging the elements within the gage section at the surface. Additionally, the strain and damage contour plots are displayed at three points along the stress versus strain curve. The damage contour plots are displayed in white to black scale; essentially, the dark regions signify damaged zones. Along the print direction, the damage critical value at room temperature is approximately 0.14, and values beyond the critical amount will fracture. Therefore, black regions represent zones of fracture. Point A lies within the linear elastic region, we can observe no damage has occurred based on the damage plot. Due to the anisotropy of the material and specimen geometry, the strains at the gage section are not strictly

uniform; however, the strain state is uniform for practical purposes since the difference between the strains is approximately 0.02%. Past the yield point, point B, damage has initiated, and it is distributed at the center of the gage section and slightly concentrated at the fillet-gage transition zone. Moreover, the strain field is observed to also have a concertation on the same regions. At the width transition zone, a small amount of shear strain, ε_{13}, exist and it contributes to both the thermodynamic force, Y_{11}, driving the damage variable, D_1. Despite the presence of shear strains, the expected solution for a uniaxial and homogeneous state of stress does not appear to be affected since the stress vs strain response between the single element test and the meso-scale coupon are nearly identical. Point C corresponds to the peak stress, damage has localized at the strain concentration points and the likelihood of fracture at room temperature is predicted at the fillet-gage transition. In comparison to the tensile experiments at room temperature, the failure sites are similar.

While damage softening is an important aspect of progressive damage theories, it is not explicitly addressed in the presented models because of the implementation of the damage critical value. Figure 88 illustrates the prediction of the room temperature uniaxial tensile test for three different mesh densities; specifically, with 40K, 196K, and 300K elements. The linear and nonlinear response is nearly identical for all three cases, though upon closer inspection the predictions do not technically overlap. Nevertheless, significant differences between mesh densities have not been observed and the need for softening methods can be reasonably circumvented. However, for explicit softening behavior, at least one of the methodologies discussed in Chapter 2 should be implemented to mitigate convergence issues and mesh-dependent results.

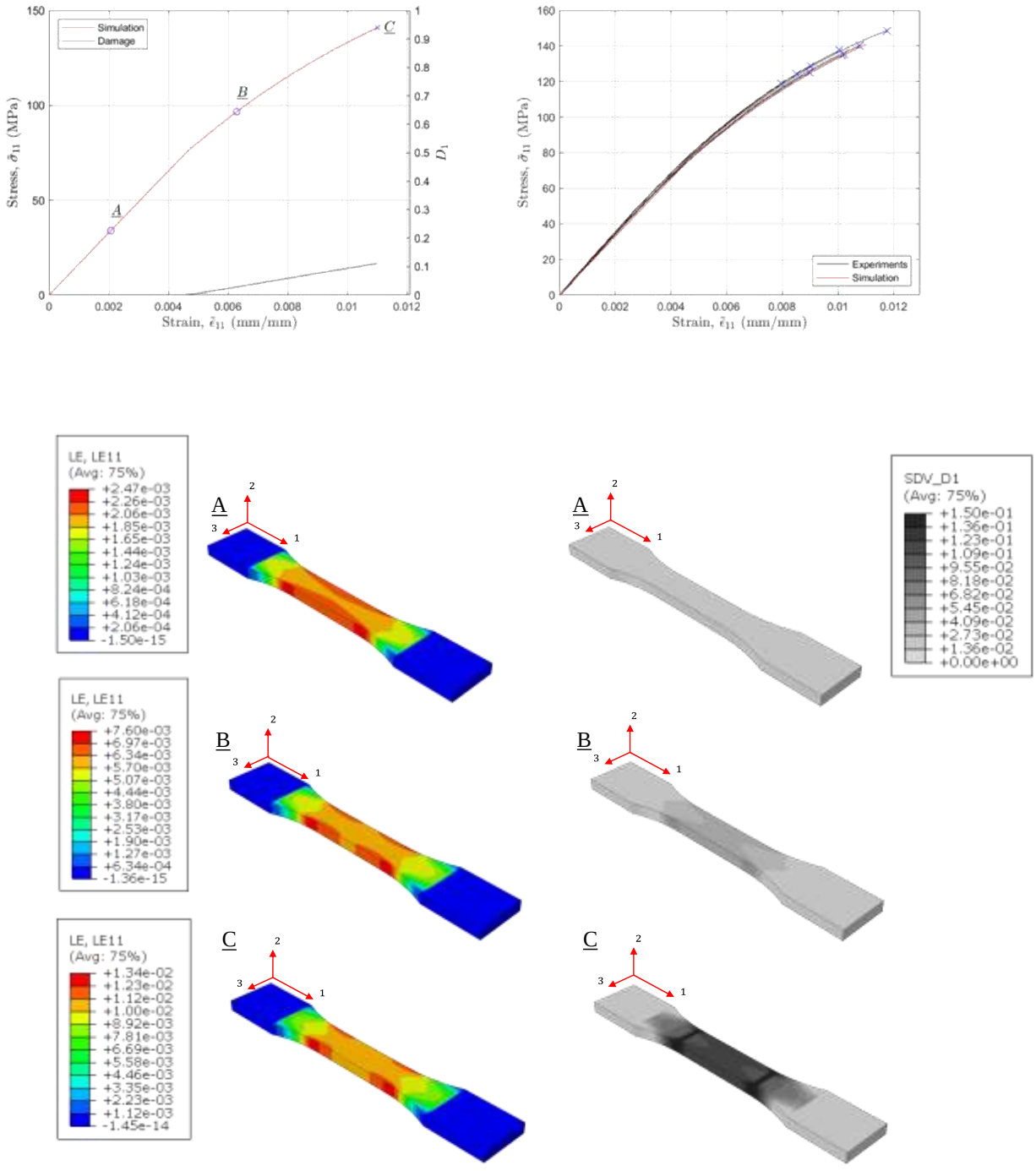

Figure 87 Stress versus strain and damage evolution along the print (1) direction at room temperature

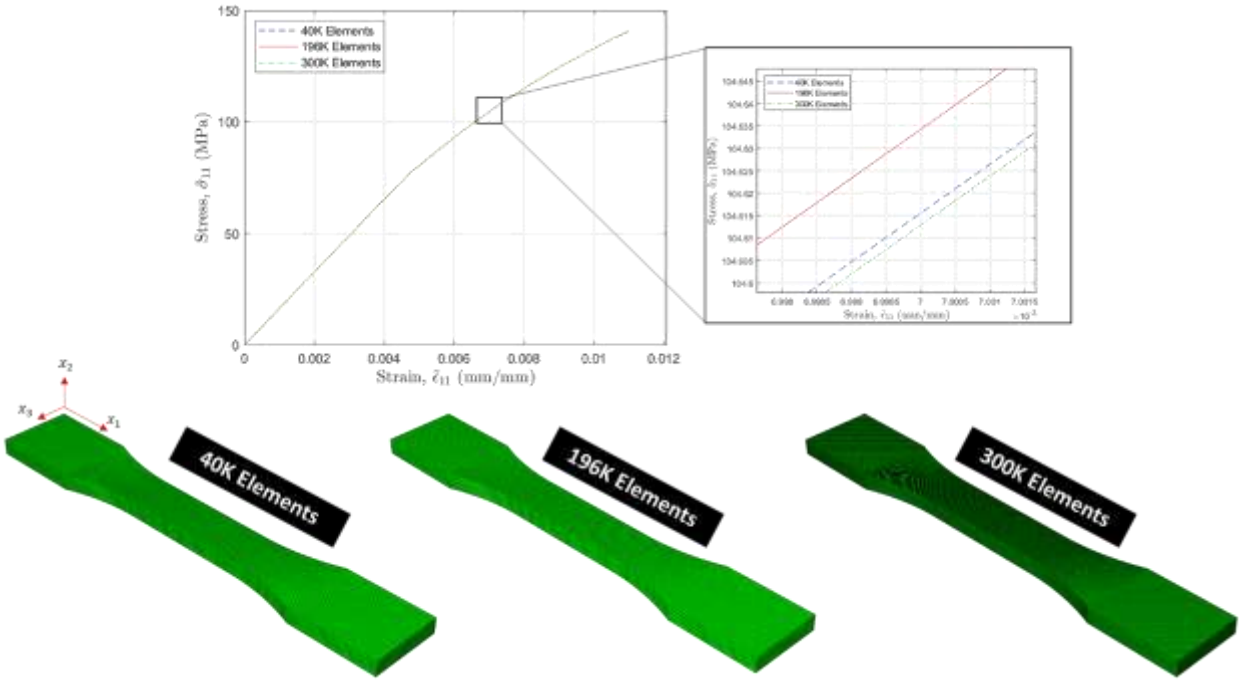

Figure 88 Mesh sensitivity for 1 direction room temperature coupon, using C3D8 elements

A load eccentricity was applied to the tensile bar modeled at room temperature to understand the implications of a bending moment on the solution, the results are presented in Figure 89 below. The displacement at a reference node is tied to all of the displacements of the nodes within the loaded tab regions, this reference node only displaces along the length of the specimen, U_1, under uniaxial deformation. The bending moment is applied by specifying a lateral displacement, U_3. Two lateral displacements were specified, these were 0.2mm and 0.8mm. At the 0.2% mean strain value, the strain contours for all three cases are shown in Figure 89. Eccentric loaded specimens experience a uniaxial strain and bending strain which are superimposed, this produces the effect shown in the strain contour plot. Specifically, the effect of having a greater strained region on one end of the specimen relative to the other. A greater bending moment magnifies the difference strains between the two regions. Figure 90 illustrates the damage contour plots for all three cases, it is interesting to observe the symmetric and non-symmetric damage distributions. For the case of no lateral displacement, $U_3 = 0$, damage is symmetric about the x_3 plane. On the other hand, the load-eccentric cases exhibit greater damage quantities on the regions with greater tensile strains, this is most apparent for the case of $U_3 = 0.8$. Above all, the strength between the case of $U_3 = 0$ and $U_3 = 0.2$ were alike (140.861MPa); on the flip side, the case for

$U_3 = 0.8$ had a slightly lower strength, 138.461MPa. While the strength appears to decrease with an induced bending moment, the overall trend appears unaffected.

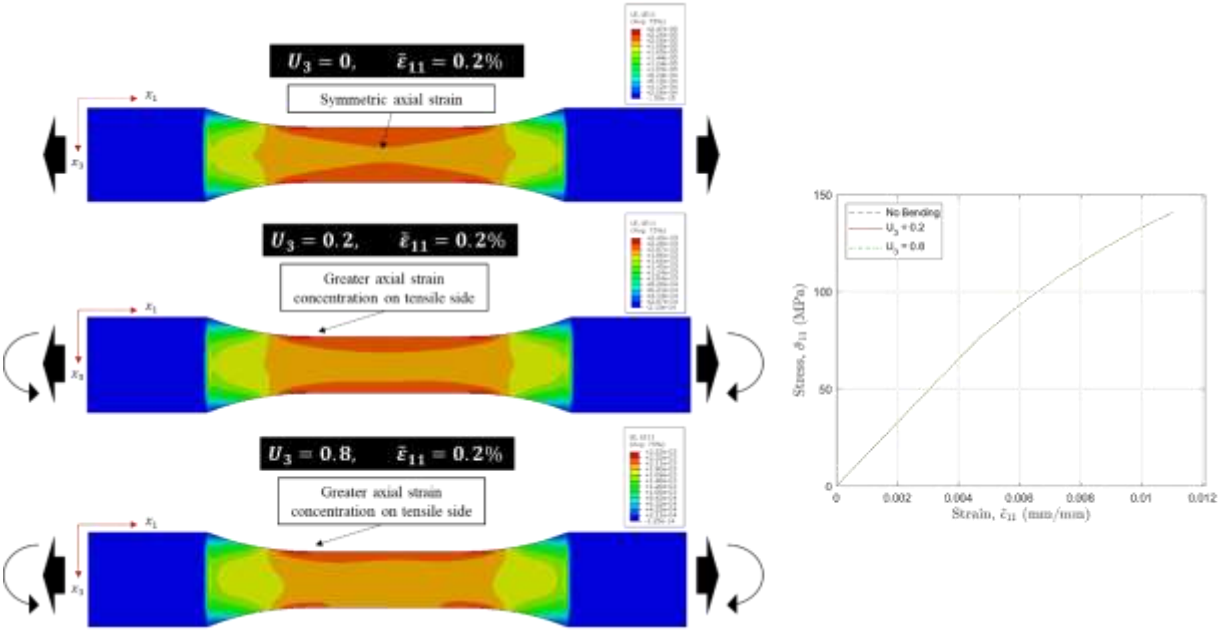

Figure 89 Comparison of eccentrically loaded coupon strain field and stress vs. strain behavior at room temperature along 1 direction

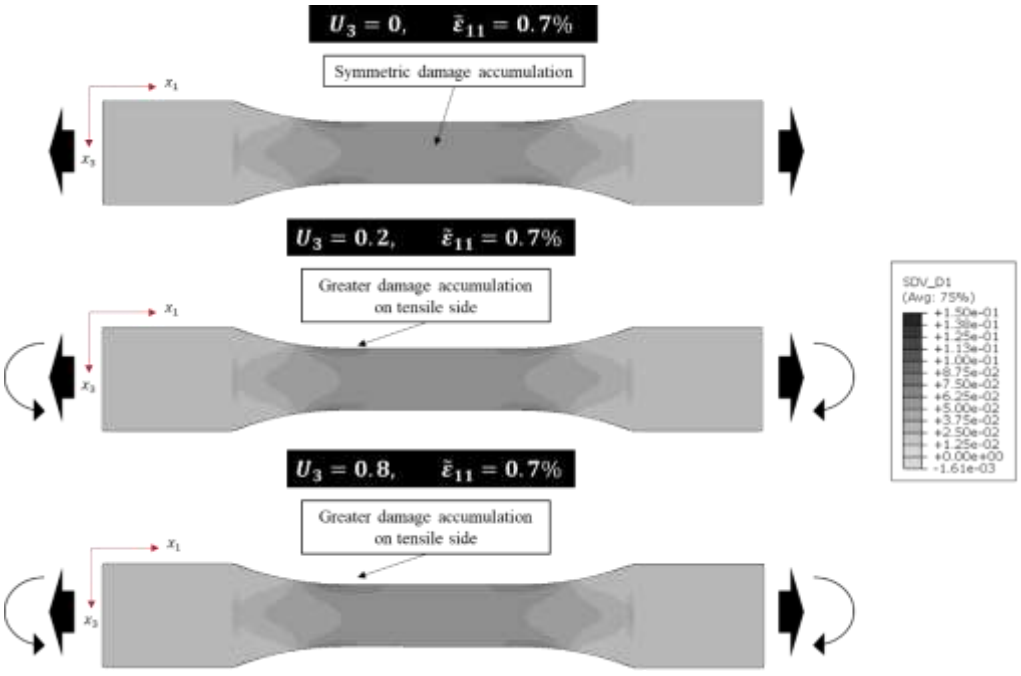

Figure 90 Damage accumulation with load eccentricity for 1 direction room temperature coupon

While modeling efforts are facilitated via the use of an isotropic damage function, it has limitations since anisotropic hardening behavior is not captured unless a separate damage surface function is defined for the damage mode of interest. The intra-bead damage assumption inherently adopts the same hardening equations which produce similar intra-bead nonlinear trends. Due to the significant brittle response along the 2 direction relative to the print direction tensile response, it is evident that an anisotropic damage function is more suitable; however, the implementation of a damage critical value with the isotropic damage hardening function calibration with print direction tensile behavior is reasonable since the experimental trends are captured. Figure 91 illustrates the difference stress versus strain behavior for the case of no damage critical value and one with the critical value implemented. The trends are identical and the critical value acts to curtail the monotonous growth of the damage variable thus prematurely terminating load progression. Figure 92 displays the strain, ε_{22}, and damage variable, D_2, contours, these contours are indistinguishable and verifies that no change in mechanical response is made when the critical damage variable is implemented. It is interesting to point out that a unilateral effect can be potentially modeled if the damage interaction tensor, J_{ijkl} and the damage variable, D_{mn}, are dissociated into tensile and compressive parts (i.e., J^{+}_{ijkl}, J^{-}_{ijkl}, D^{+}_{mn}, and D^{-}_{mn}). It has been shown that a reduction in J will delay the onset of damage and the removal of D^{cr} will allow the monotonous evolution of the damage variable, these are the trends observed in compression and can be a useful engineering approach for capturing the unilateral behavior.

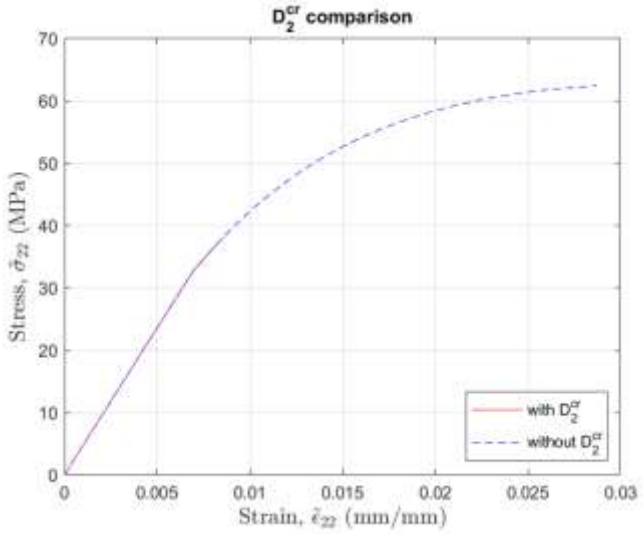

Figure 91 Simulation with and without D_2^{cr} implemented

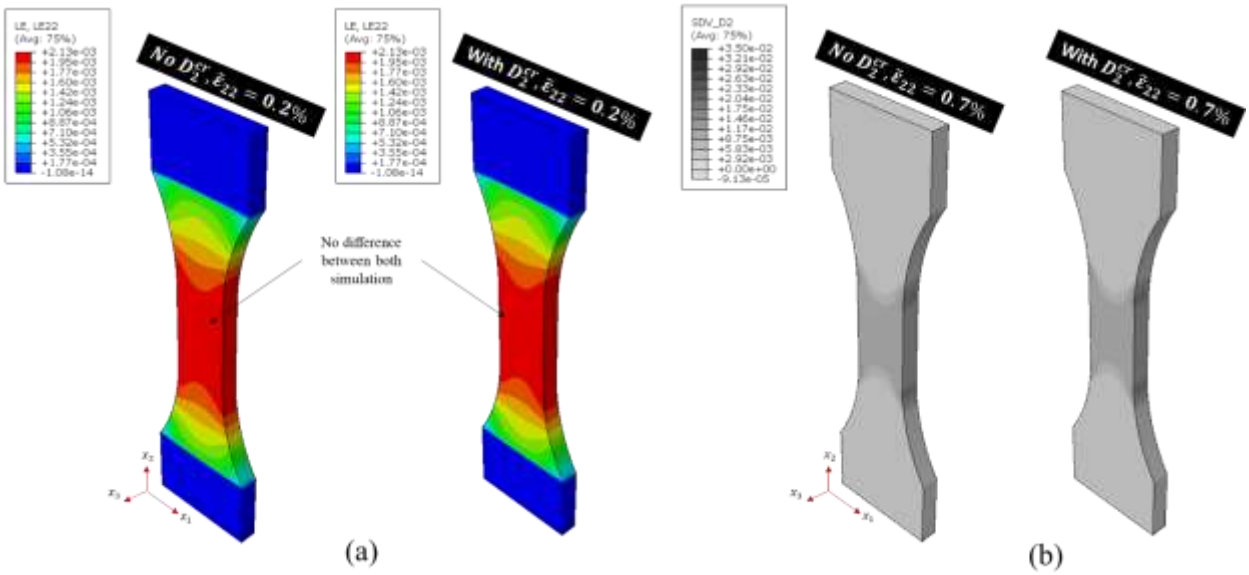

Figure 92 (a) Axial strain along 2 direction between simulation with and without D_2^{cr} (b) damage field with and without D_2^{cr}

Since tensile failure along the stacking direction occurs mainly at the interface between stacked beads, a separate damage surface relation is defined to properly capture the nonlinear behavior. The approach requires specification of elements that can undergo interfacial damage, the elements are then classified as either having an intra-bead damage description or all-mode damage behavior. Analysis of 3D printed structures, either process-based or performance-based, are typically meshed with an integer multiple of the bead height (e.g., 1, 2, 3 …, N elements per bead height) along the Z-axis. With this in mind, the proposed approach defines the inter-bead damage mode inside the element previous to the start of a new bead, this is illustrated in Figure 93. Although the damage is dissociated into two parts, a single damage effect tensor (i.e., a hybrid of damage variables consisting of D_1, D_2, and D_3^I) is used and the Jacobian has damage evolution contributions from both the intra-bead and inter-bead damage modes. To demonstrate the viability of this approach, three dog-bone shape according to the dimensions of the experimental coupons were generated, each with different mesh densities across a bead height, 1.5mm. Mesh 1 is the case with a single element across the bead height, mesh 2 and 3 contain two and three elements across the bead height. From Figure 94, this approach agrees reasonably well with the experimental observations. Mesh 2 and mesh 3 slightly differ from mesh 1 because of the increased intra-bead resistance from the non-interface damageable elements.

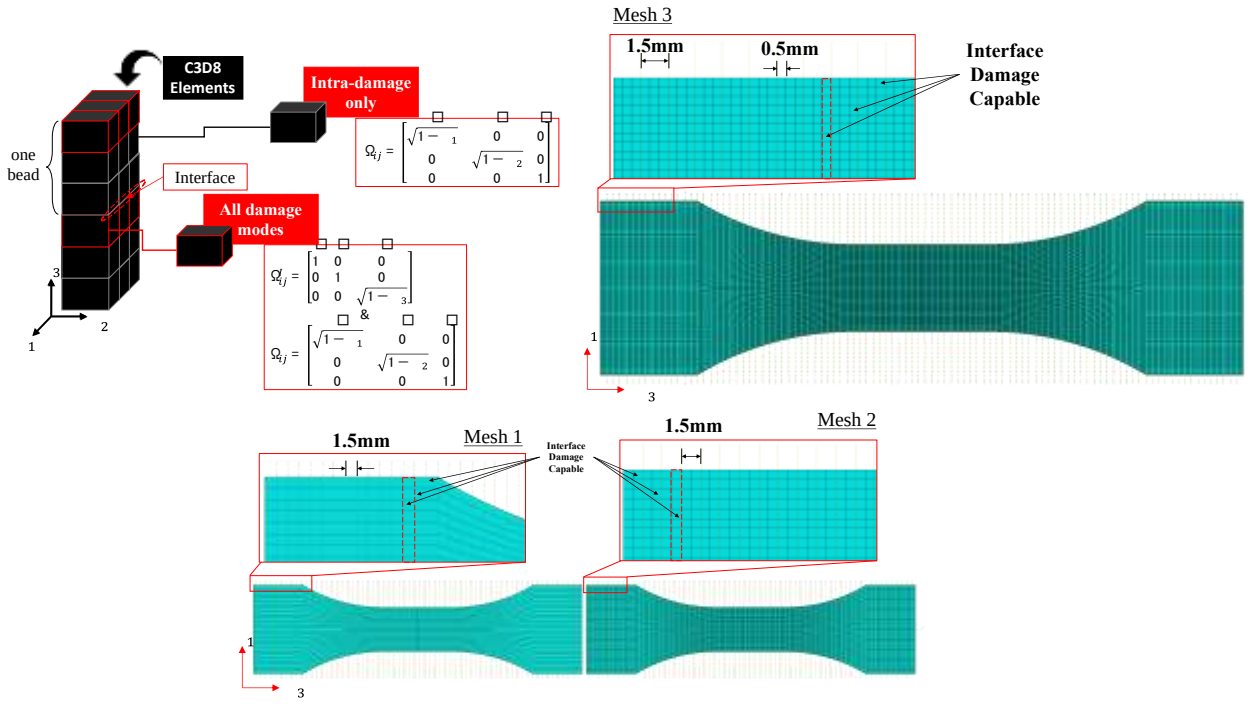

Figure 93 Illustration of elements with and without interfacial damage

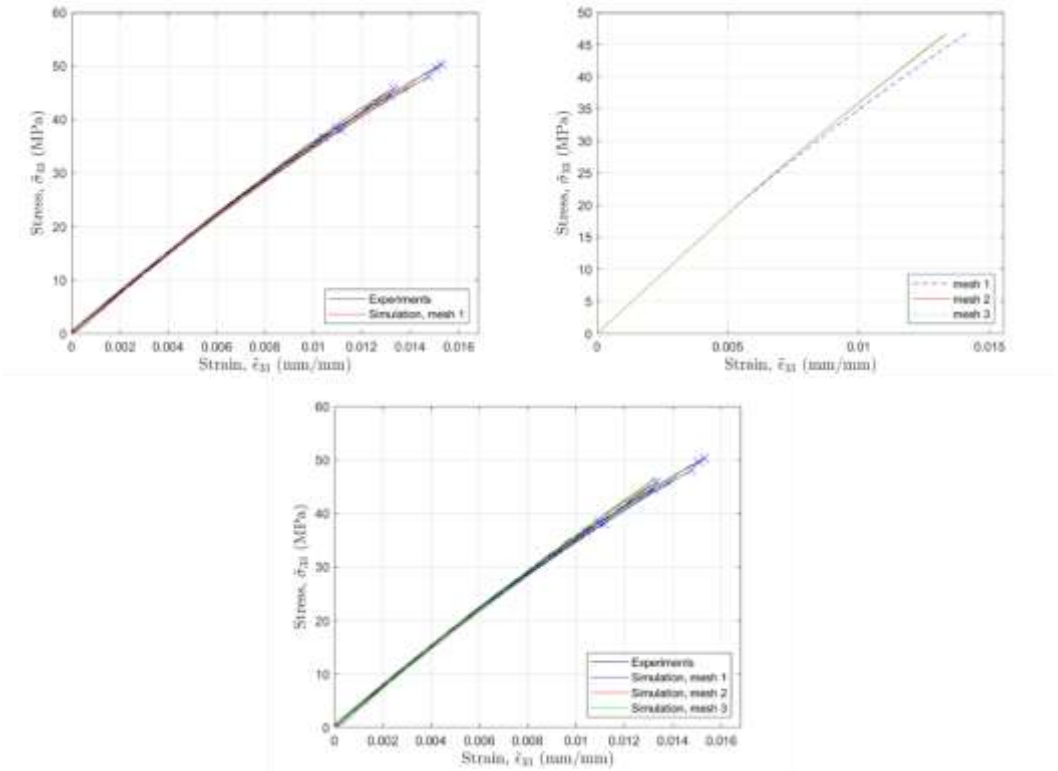

Figure 94 Experimental and simulation comparison for 3 direction tensile performance

5.7 Unilateral Tension-Compression Behavior and Modeling

Experimental evidence demonstrates the disparate material behavior when subjected to tension or compression loads, differences are observed in peak stress, ultimate and rupture strains. Moreover, angled macro-cracks are seen for compression loaded specimen regardless of temperature; in contrast, tensile specimens fail with the macro-crack approximately orthogonal to the loading direction. Materials that behave differently in tension and compression are classified as unilateral. Currently, the model implemented and exercised in section 5.4 does not include any unilateral effects or parameters; therefore, it does not properly capture the compression behavior well, this is evident for 2 and 3 direction loaded modes. From a phenomenological perspective, the micro-cracks open or close depending if the subjected load is tensile or compressive, respectively, crack closure is often referred to as damage deactivation and several theories have been developed to address this phenomenon [106]. Damage activation or deactivation is governed by the dissipative potential laws, which can be loading-mode dependent. In this approach, the damage variable is dissociated into tension and compression parts activated via the sign of the normal strains, shown in Eq. (106). The damage variable associated with tensile strains are D_{ij}^{+} and for compressive strains, D_{ij}^{-}, the Heaviside function is denoted by $H(\varepsilon_{ij})$ and it equals to one if the normal strain is positive and zero otherwise. The damage variable dissociation approach allows for the change in stiffness upon load reversal if dissipation has occurred during tensile or compressive loading. Similarly, the normal components of the damage material tensor, J_{ijkl}, are decomposed into tensile and compressive parts, e.g., $J_{11}(T) = H(\varepsilon_{11}) \cdot J_{11}^{+}(T) + [1 - H(\varepsilon_{11})] \cdot J_{11}^{-}(T)$. Experimental strain onset values in compression, ε_{ij}^{0-}, and the temperature-dependent damage onset parameter, $\kappa_0^{+}(T)$ or $\kappa_0^{I+}(T)$, calibrated using tensile experiments are used for obtaining the normal components of the damage material tensor under compression. The trends with temperature are fitted using a least-square approach, the coefficient and plot are provided in Figure 95. Most notably, the trends are downward which correlates with decrease dissipation as demonstrated in Figure 77b, this is expected since compressive nonlinear behavior is extensive and compressive strengths are greater.

$$D_{ij} = H\left(\varepsilon_{ij}\right)D_{ij}^{+} + \left[1 - H\left(\varepsilon_{ij}\right)\right]D_{ij}^{-} \text{ for } i = j \tag{106}$$

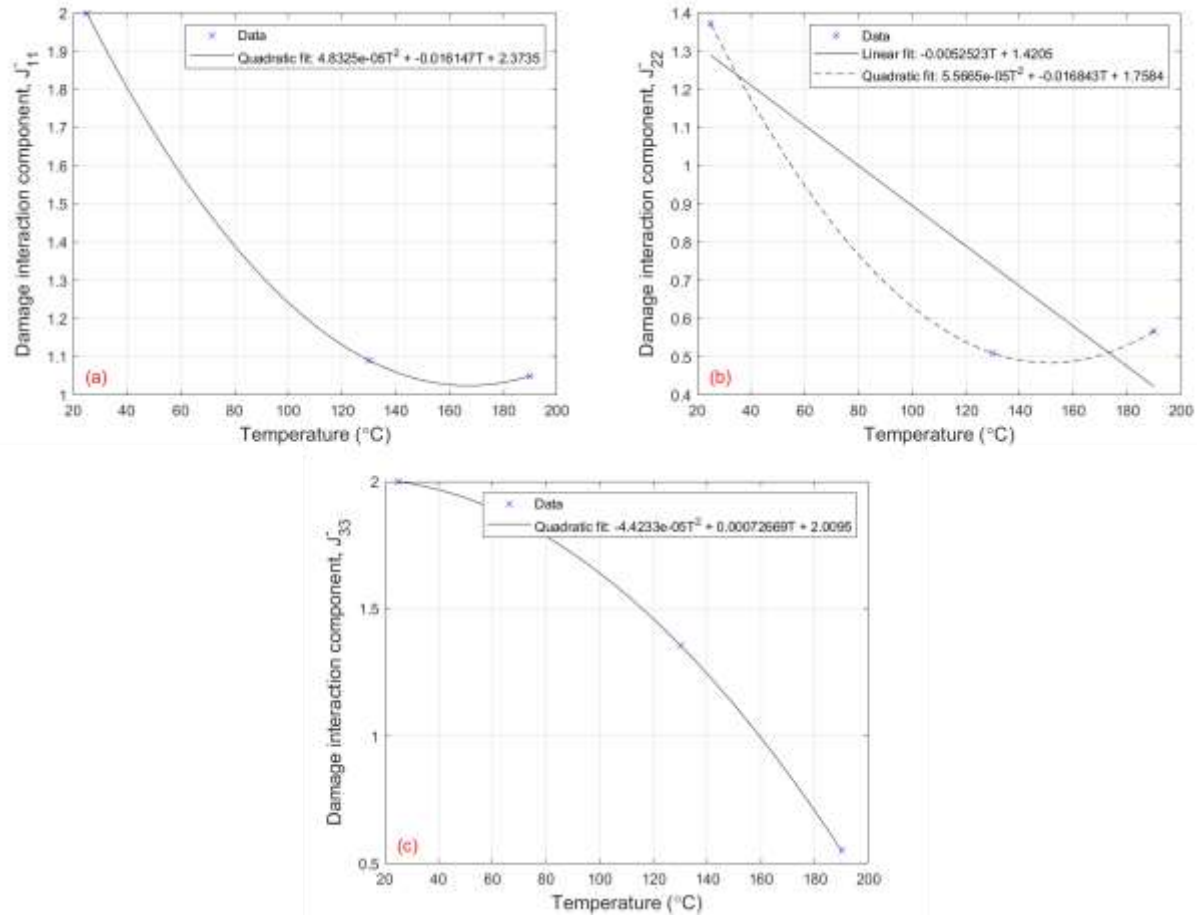

Figure 95 Compression damage component versus temperature (a) along print direction, J_{11}^{-}, (b) along 2 direction, J_{22}^{-}, and (c) along stacking direction, J_{33}^{-}

The expansion of the damage surface appears to significantly halt as load progresses past the peak stress, this results in significant strain softening behavior in specimens loaded in either tension or compression. The rate of hardening or softening is dictated by Lagrange damage multiplier, $\dot{\lambda}$, and the isotropic hardening material parameters c_1 and $c_2(T)$. Experimental evidence suggests the rate of hardening changes beyond the peak stress. Although fracture mechanics theories can be adopted to better capture the softening regime, a simple approximation to the softening behavior is adopted by inhibiting further hardening past the peak stress point, as shown in Eq. (107). Since the model is strain-based, the ultimate strains corresponding to peak stresses are considered and plotted with respect to temperature in Figure 96. The strains at each temperature are the averaged values of that set and the overall average across the temperature are used for providing the threshold for which no additional hardening occurs; however, the decreasing

trend observed for 2 and 3 direction tensile modes are captured with a linear or quadratic least-squares fit.

$$\dot{\delta} = \dot{\lambda} \cdot \left[1 - H\left(\varepsilon_{ij}^{ult}\right)\right] \tag{107}$$

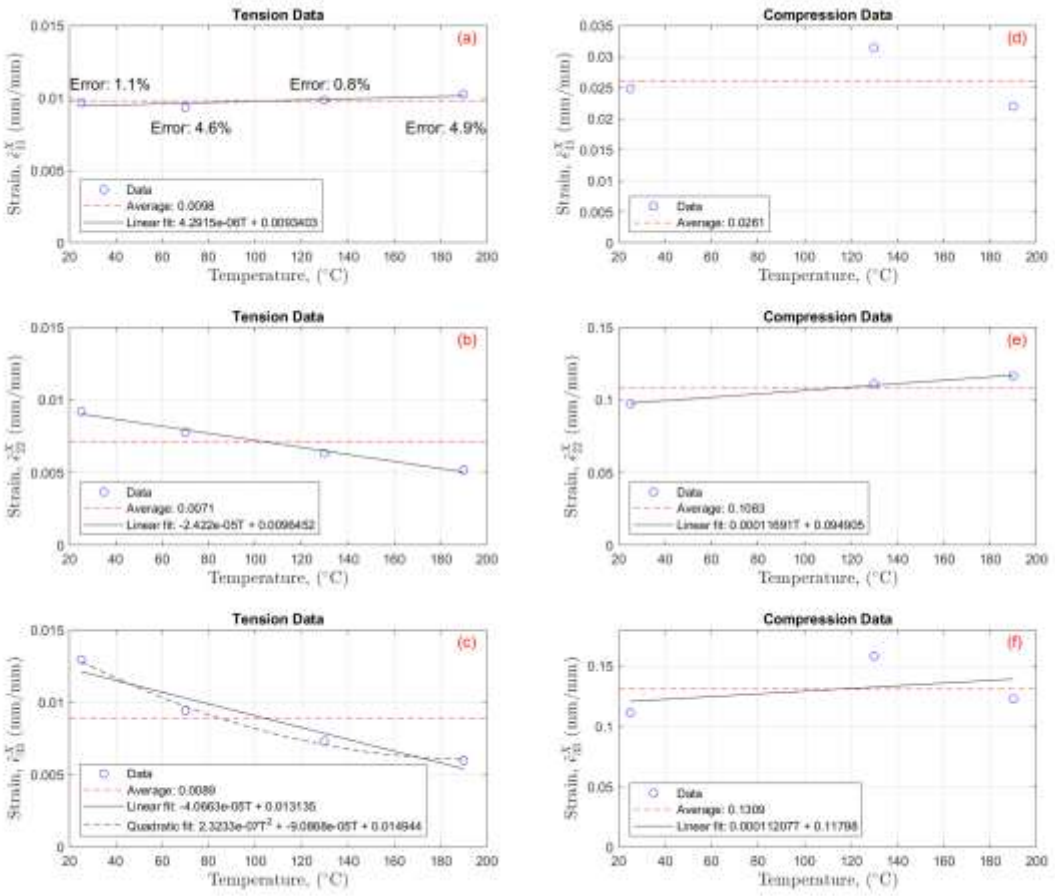

Figure 96 Average of ultimate strains corresponding to peak stress with respect to temperature

The stress versus strain plots for tension and compression along the print direction are shown in Figure 97 and Figure 98, respectively. The room temperature J_{11}^{+} and J_{11}^{-} values are equivalent; therefore, the difference in behavior is attributed to the ultimate strain hardening cut-off. The room temperature value of the damage tensor component, J_{11}^{-}, was chosen similar to J_{11}^{+} since the nonlinear trend in compression was observed to be similar to the tension case. A constant J_{11}^{-} with temperature does not represent the observed nonlinear behavior at elevated temperatures,

which warrants the need to include its change with respect to temperature at higher temperatures. The reason J_{11}^{-} decreases with temperature is to compensate for the increase in the rate of damage progression with temperature. Even though J_{11}^{+} is constant with temperature, it was observed to be a reasonable assumption based on the model correlation with the data. However, the accuracy of the model can be improved by including the temperature dependency of J_{11}^{+} at elevated temperatures. For example, the nonlinear strain onset value is found to be between 0.33% and 0.34% at 130°C, this is obtained by using a 1% deviation in chord modulus estimate. From these nonlinear onset values, the J_{11}^{+} can be computed, and it is found to be within the range of 1.3 and 1.8. It is noteworthy to mention that the values of J_{11} at elevated temperatures are estimated using experimental values of stiffness and nonlinear onset strain and these contain experimental error which needs to be carefully considered when computing the J_{ijlk} values. The mean experimental values were observed to provide reasonable estimates to the J_{ijkl} damage parameters; however, an iterative approach to find representative values is recommended for experiments with significant variability in properties. Furthermore, since the values related to damage initiation and damage surface limits depend on the microstructure, micrographic scans or micromechanical approaches aimed at analyzing micro-damage initiation with respect to strain-levels should be considered whenever possible to obtain a more representative estimate of J_{ijkl}. Sine damage is assumed to initiate at nonlinear strain onset, the components of J_{ijkl} are sensitive to the C_{11}^{*} and ε_{11}^{0+} experimental values. These values do contain experimental error resulting from the Young's or shear modulus fit, chord modulus deviation, force and DIC-computed strain errors. Despite measurement uncertainties, the average values of model parameters yield simulated behavior that correlates well for both tension and compression data.

Figure 99 and Figure 100 illustrate the stress versus strain behavior along the 2 direction for tension and compression deformation modes, respectively. The simulated behavior in tension, Figure 99, is similar to the predicted results shown in Figure 82, and the difference is observed after the peak stress corresponding to the ultimate strain threshold. The deactivation of the hardening rate, $\dot{\delta}$, produces the increase in damage progression, this deactivation of the hardening rate is seen to cause the rapid evolution of the damage variable, D_2^{+}, and softening response. The accelerated damage progression is expected when the hardening rate goes to zero since no further expansion of the damage surface is allowed and greater unloading is required to bring the material back into the allowable thermodynamic force space. The brittle behavior of the short fiber

composite is reasonably modeled by the deactivation of the hardening rate and implementation of either a damage critical value or deactivation of hardening is a viable approach for capturing the extensive softening or brittle fracture beyond the peak stress. Unlike the brittle behavior in tension, compression behavior is more ductile, and the model reflects this trend well as seen in Figure 100. The compressive material behavior shows two main differences relative to the tensile case, the extent of nonlinear deformation is greater, and the peak stress and strain is also greater regardless of the tested temperature. It is noteworthy to mention that the isotropic hardening function remains unmodified and calibrated via tensile behavior; therefore, the increase in deformation and peak stress is caused by the implementation of the J_{22}^{-} parameter which was determined using the 2 direction's experimental compressive properties. Moreover, the model exhibits two softening mechanisms at 130°C and 190°C, it is caused by the change in the isotropic hardening rate parameter, $c_2(T)$, and the deactivation of the hardening rate, $\dot{\delta}$. At lower temperatures, the deactivation of the hardening rate dominates the softening behavior, on the other hand, the reduced c_2 allows for a reduced strain hardening effect and earlier softening at elevated temperatures. It is noteworthy to mention that the strain hardening behavior observed at high temperature and large strains are partly due to buckling and fixture support as the deformed material comes into contact with the fixture. Overall, good agreement between experiments and simulation are found with this considered approach.

The predicted stress versus strain behavior along the stacking direction is shown in Figure 101 and Figure 102 for tensile and compressive deformation modes, respectively. Similar to the tensile predictions along the 2 direction, the deactivation of the hardening rate produces the extensive softening beyond the ultimate strain observed in Figure 101. The compressive behavior is governed by the temperature-dependent isotropic hardening response which had been calibrated using the stacking direction tensile performance, it is seen to represent the compressive nonlinear trend well alongside the implementation of J_{33}^{I-}. Since the nonlinear trends in tension and compression at room temperature are observed to be relatively similar, the damage components J_{33}^{I+} and J_{33}^{I-} are set to the same reference value of two. The nonlinear onset strain range was observed to be between 0.4% and 0.66% for the specimens subjected to 130°C, these were used to obtain the average J_{33}^{I-} parameter of 1.36. By the same token, the strain range for specimens tested at 190°C were between 0.4% and 0.54%, which resulted in an average J_{33}^{I-} value of 0.55. The strain hardening regime is reasonably predicted utilizing this approach.

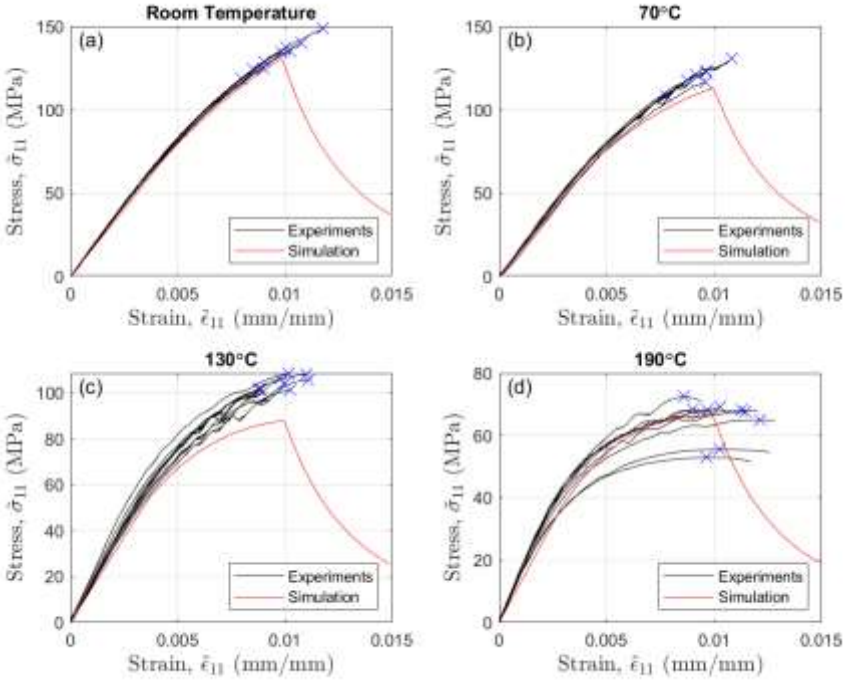

Figure 97 Tensile experimental and simulation comparison along print direction for (a) 25°C, (b) 70°C, (c) 130°C, and (d) 190°C

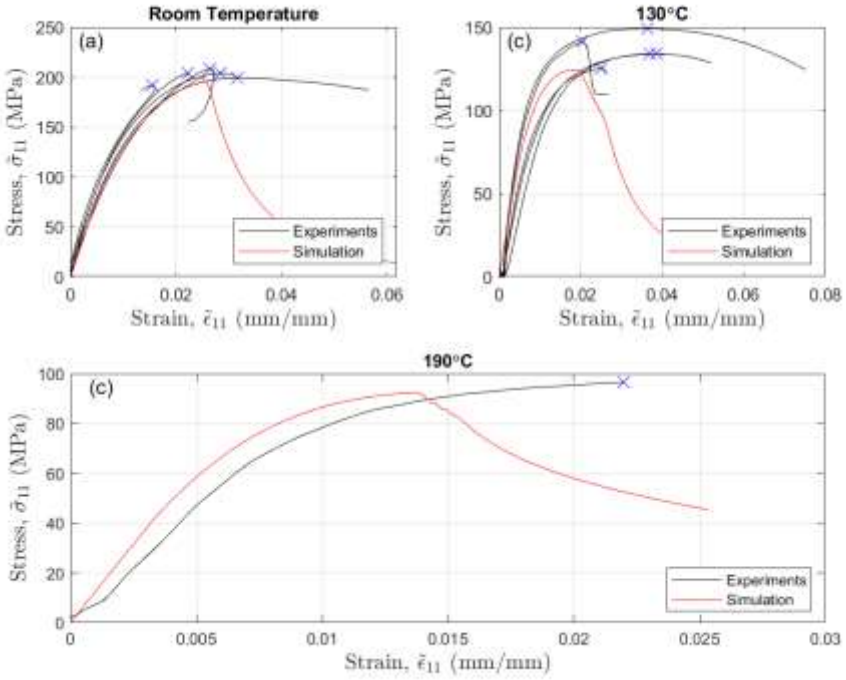

Figure 98 Compression experimental and simulation comparison along print direction for (a) 25°C, (b) 70°C, (c) 130°C, and (d) 190°C

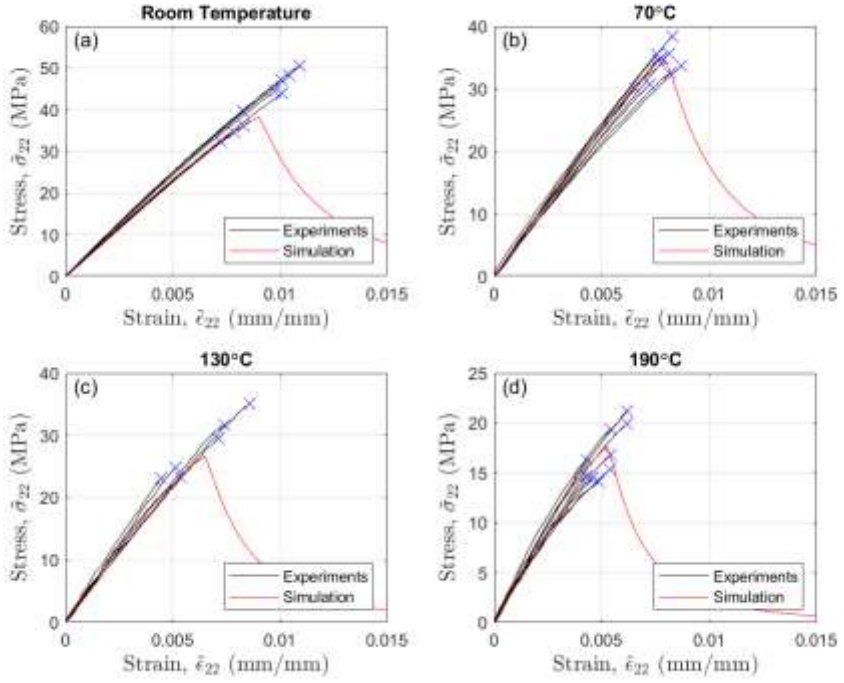

Figure 99 Tensile experimental and simulation comparison along 2 direction for (a) 25°C, (b) 70°C, (c) 130°C, and (d) 190°C

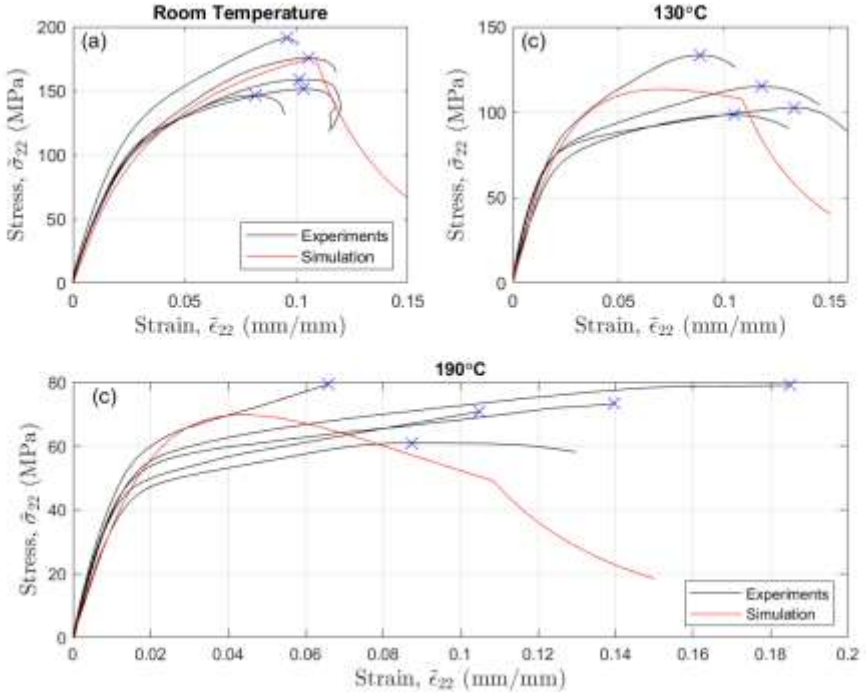

Figure 100 Compression experimental and simulation comparison along 2 direction for (a) 25°C, (b) 70°C, (c) 130°C, and (d) 190°C

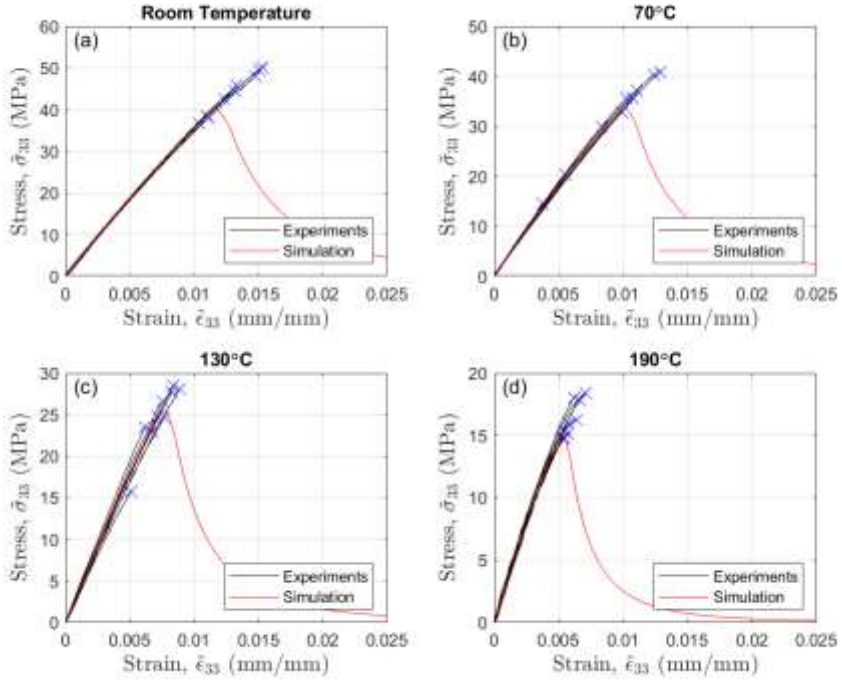

Figure 101 Tensile experimental and simulation comparison along stacking direction for (a) 25°C, (b) 70°C, (c) 130°C, and (d) 190°C

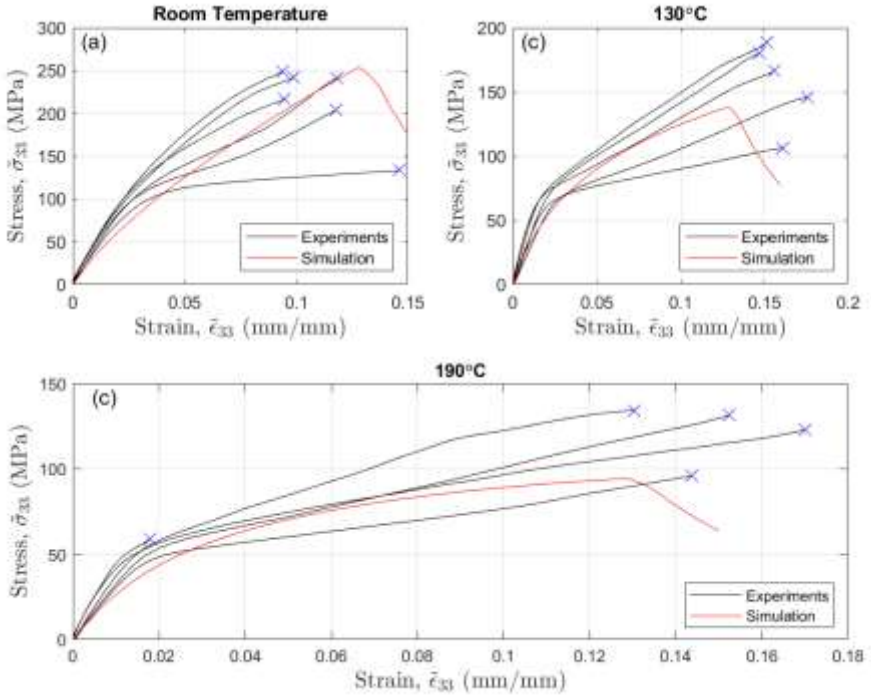

Figure 102 Compression experimental and simulation comparison along stacking direction for (a) 25°C, (b) 70°C, (c) 130°C, and (d) 190°C

5.8 Shear Behavior Calibration

5.8.1 Shear Behavior with Independent Damage Variables

The comparison between simulation and experiments for shear deformations along the 2-3, 1-3 and 1-2 directions are shown in Figure 103, Figure 104, and Figure 105, respectively. Independent shear damage variables were used to allow for more flexibility in capturing the shear trend, inclusion of the three shear damage variables D_4, D_5, and D_6 require specification of the corresponding shear damage components J_{44}, J_{55}, and J_{66}. The shear damage components were assumed and adjusted to obtain reasonable correlation to the experimental results. The kink found in the model occurs at the point of damage initiation, this kink is a result of the coarse time incrementation. A finer time incrementation will reduce the severe change in slope after damage initiation. At room temperature, the predicted nonlinear behavior is in good agreement with the experimental results; however, there is a departure in model and experiments at elevated temperatures. The shear deformation at elevated temperatures, specifically the 130°C and 190°C cases along the 2-3 and 1-3 directions, exhibit a plateau region. The plateau region is believed to arise from inelastic strain mechanisms stemming from the polymer phase, this inelastic mechanism differs from damage and acts to irreversibly elongate the specimen instead of softening it. Although the inelastic strains are not captured in the model, the model is capable of representing the nonlinear behavior in shear. With this in mind, the model will have limitations if shear stresses dominate the stress state and the body is at relatively high temperatures as the irreversible elongation is not properly captured. The hardening rate is deactivated beyond the ultimate strain threshold, which causes the rapid softening past the ultimate strain. The deactivation of the hardening rate is observed to capture the decrease in stress well. The average ultimate strain values provided in Figure 106, Figure 107, and Figure 108 were used for specifying the onset on hardening deactivation; furthermore, the assumed values of $J_{44}(T)$, $J_{55}(T)$, and $J_{66}(T)$ are provided in the plots. For compression and shear, a decrease in J is required to properly reflect the trend observed for 3D printed short fiber composites if the hardening is calibrated using tensile behavior.

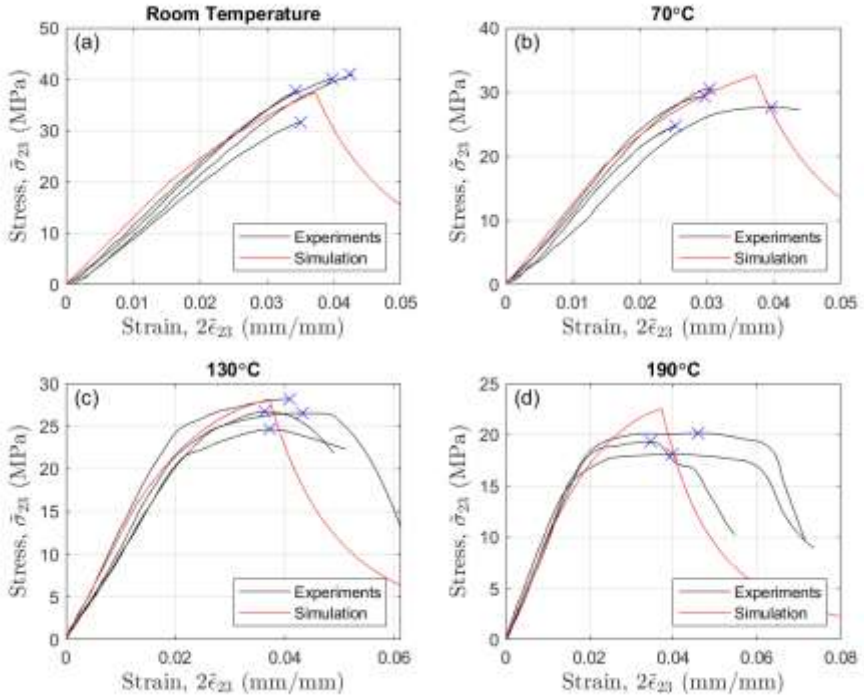

Figure 103 Experimental and simulation comparison of shear behavior along 2-3 direction for (a) 25°C, (b) 70°C, (c) 130°C, and (d) 190°C

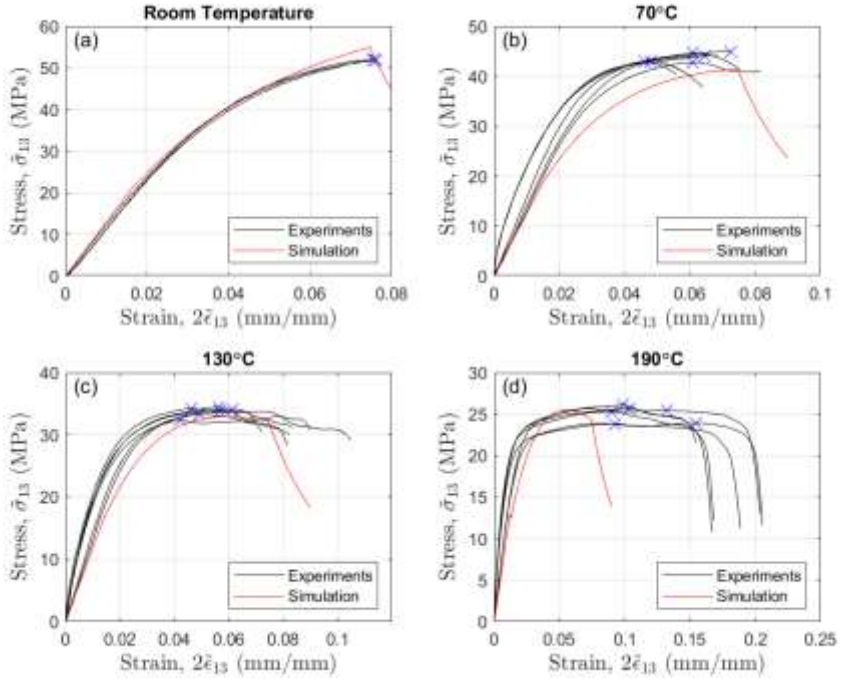

Figure 104 Experimental and simulation comparison of shear behavior along 1-3 direction for (a) 25°C, (b) 70°C, (c) 130°C, and (d) 190°C

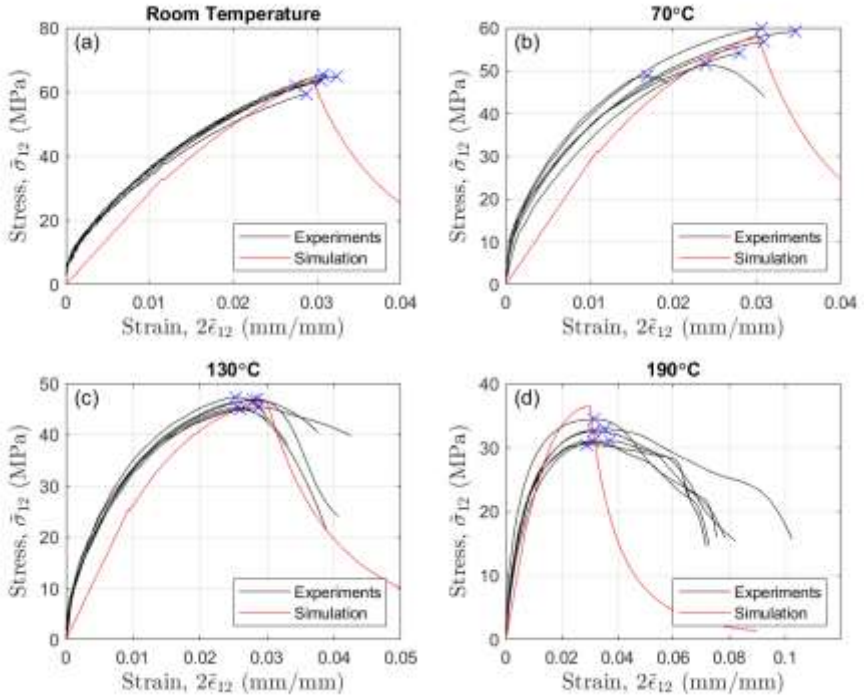

Figure 105 Experimental and simulation comparison of shear behavior along 1-2 direction for (a) 25°C, (b) 70°C, (c) 130°C, and (d) 190°C

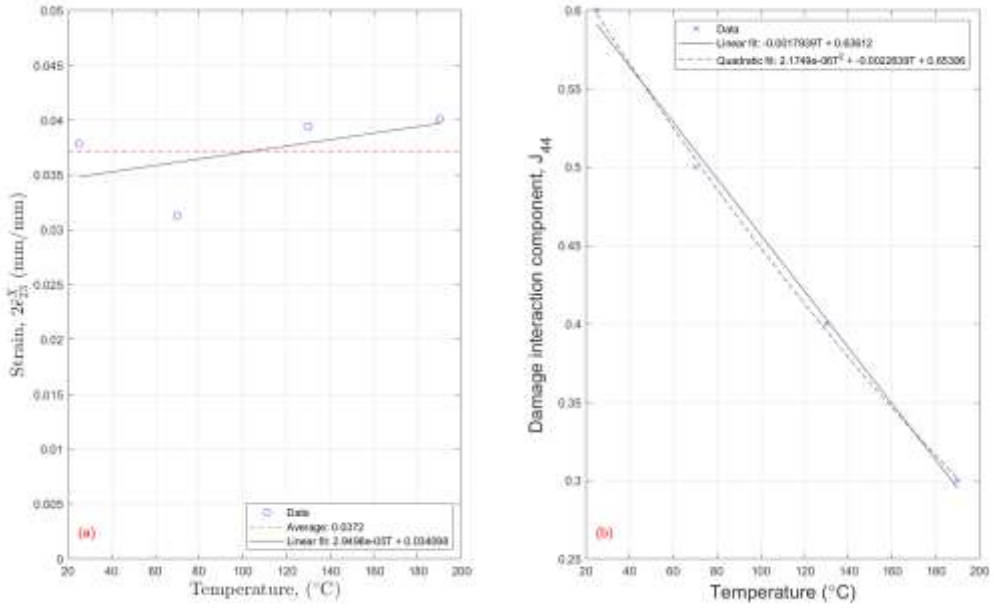

Figure 106 (a) Ultimate effective shear strain, $2\tilde{\varepsilon}_{23}$, corresponding to peak shear stress, and (b) damage component J_{44} versus temperature

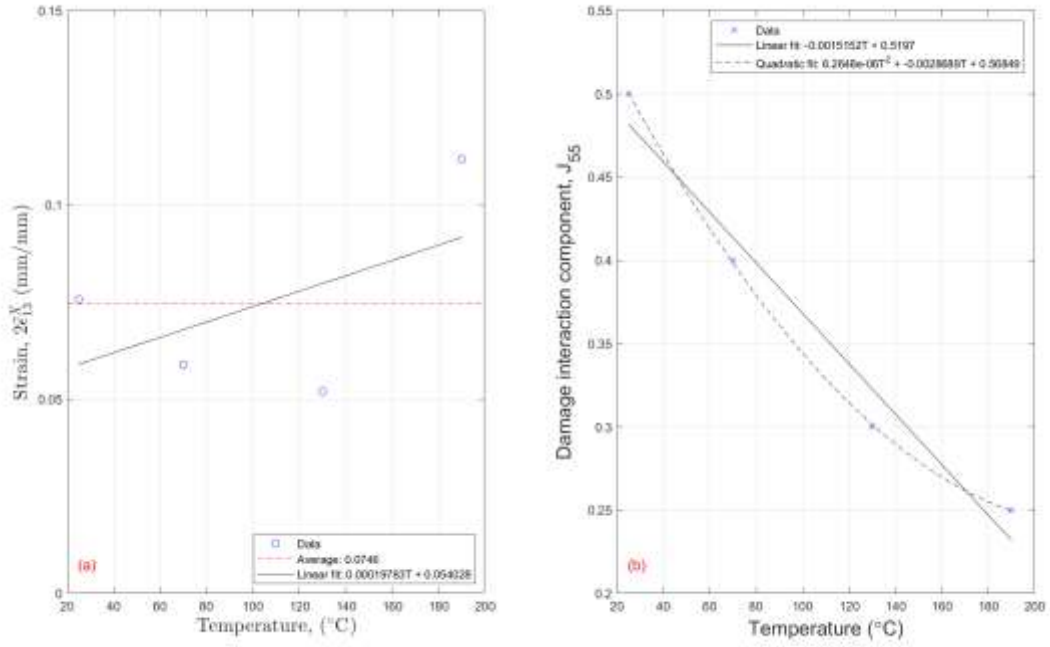

Figure 107 (a) Ultimate effective shear strain, $2\tilde{\varepsilon}_{13}$, corresponding to peak shear stress, and (b) damage component J_{55} versus temperature

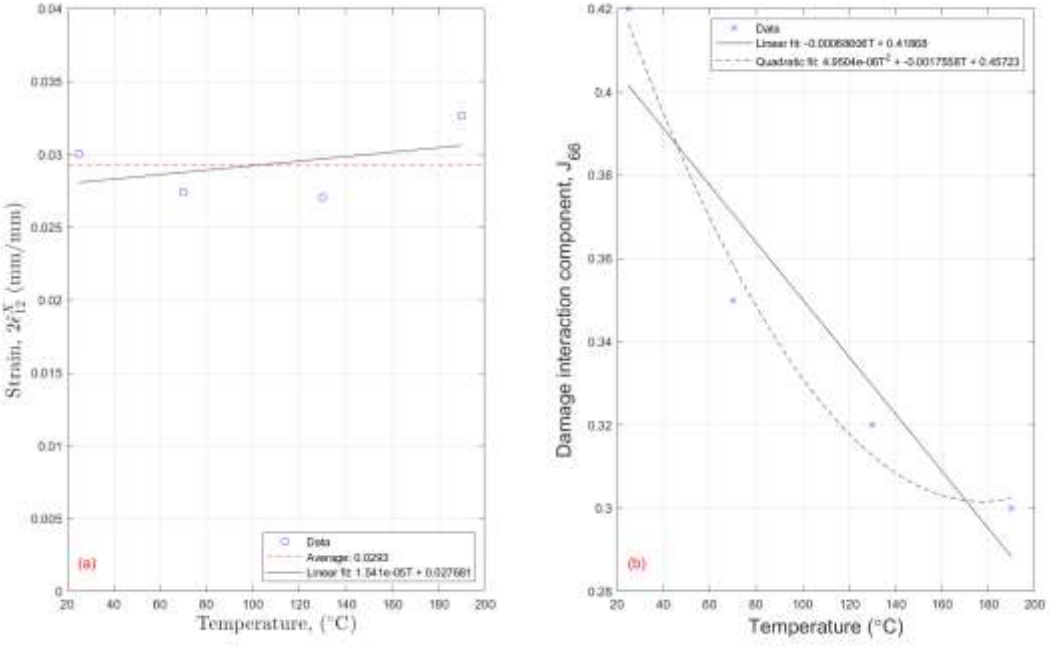

Figure 108 (a) Ultimate effective shear strain, $2\tilde{\varepsilon}_{12}$, corresponding to peak shear stress, and (b) damage component J_{66} versus temperature

5.8.2 Modification of Hardening Rate by Shifting

The nonlinear shear response can be described in three parts, the first part is the gradual softening that occurs after damage onset, the second is the somewhat stress plateau region for which damage progression begins to accelerate, and the last is the softening zone. The strain yield point, ε_{ij}^{y} marks the transition from a gradual failure process to one in which the stress remains failure constant for continued deformation. An empirical parameter is proposed, $h(T)$, which is activated past the yield point using the Heaviside function as shown in Eq. (108), this empirical parameter acts to shift the c_2 function to reflect the change in strain hardening associated with damage. An example of the predicted shear behavior along the 2-3 direction using this approach is presented in Figure 109. Although not a standard approach, it demonstrates the viability of capturing the different regimes in stress versus strain behavior.

$$\dot{\delta} = \dot{\lambda}\left[H(\varepsilon_{mn} = 0) - H\left(\varepsilon_{ij}^{y}\right)\right] + \dot{\lambda}\left[H\left(\varepsilon_{ij}^{y}\right) \cdot h(T)\right], \qquad i \neq j \tag{108}$$

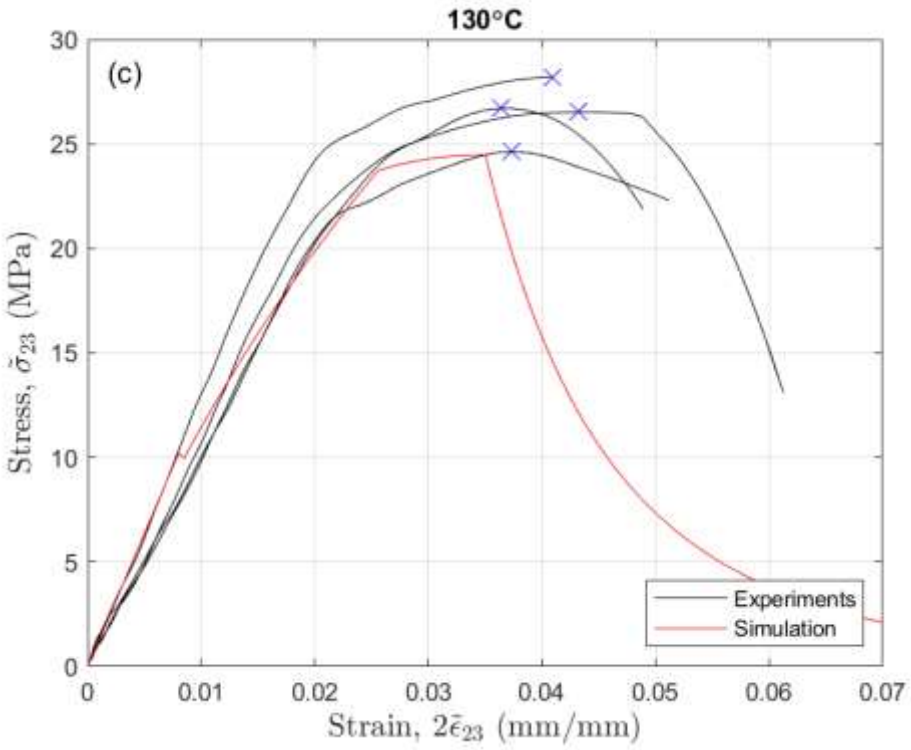

Figure 109 Example of shifted hardening function effect

6. ANALYSIS OF AN ADDITIVE MANUFACTURED MOLD WITH PROGRESSIVE DAMAGE

6.1 Integration of Thermoviscoelastic Damage into Additive3D

The modified additive3D framework is illustrated in Figure 110, it depicts the elements of the framework and the highlighted modification for process and performance analyses. For the implementation of viscoelastic damage, most of the elements of the framework remain unchanged except for the UMAT. Within the UMAT, the equations of viscoelasticity must be altered to include both the damage effect tensor. Moreover, the damage evolution equations must also be integrated. The Prony series equations used for modeling the viscoelastic phenomena is preserved. The Fortran code used for defining the UMAT is provided in the appendix section of this work.

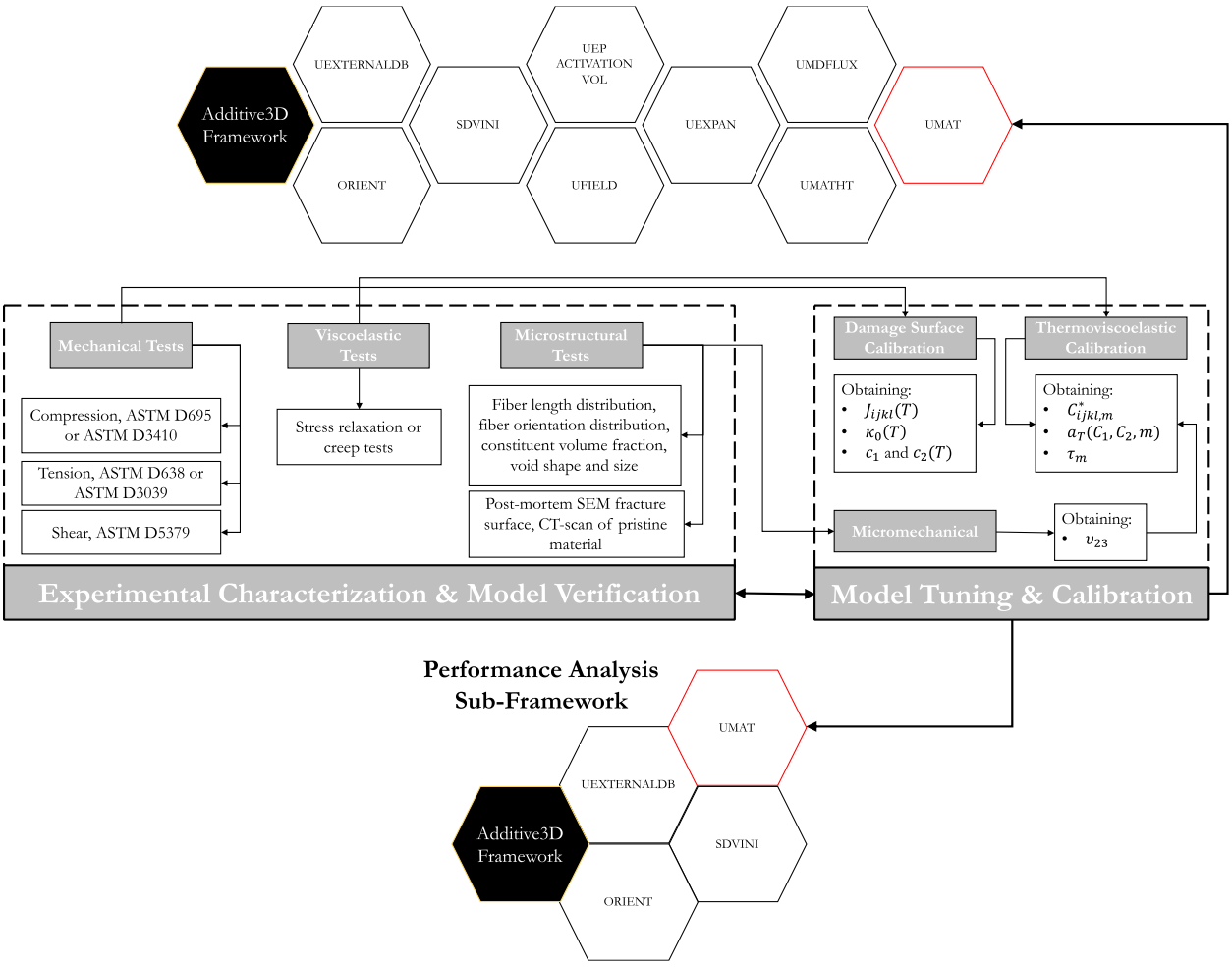

Figure 110 Thermoviscoelastic damage integration into the Additive3D framework

The illustration above has two essential open-boundary sub-modules which are essential in the integration of the viscoelastic damage model into the Additive3D framework. The first sub-module is labeled experimental characterization and model verification, in this sub-module, experiments were conducted to obtain information about the fundamental deformation properties of the short fiber composite. Next, this information is passed into the model tuning and calibration sub-module. Noteworthy to mention, fundamental effective properties of the short fiber composite can be obtained using the ASTM methodology; however, a multitude of methods can be adopted for damage analysis and quantification. For example, loading and unloading experiments appear to be the most straightforward method to obtain damage evolution parameters. Although, for certain low strain-to-failure materials, the monotonic stress versus strain behavior can be used to estimate damage evolution parameters as shown in this work. The damage mechanics calibration process utilizes the effective elastic, damage, and failure properties to compute the parameters of the viscoelastic damage model, these are the components of the J_{ijkl} tensor, hardening parameters, c_1 and c_2, and damage threshold, κ_0. While experimentally-obtained or calibration model parameters are ideal, an iterative and optimization approach can still be used to obtain an estimate to the damage model parameters if experimental results are not available or limited. After the model tuning process is complete, a verification step is performed by comparing the experimental stress versus strain behavior to the predicted nonlinear results at various temperatures.

6.1.1 Model Limitations

Several assumptions were made in an attempt to simplify the problem of predicting progressive damage accumulation in the short fiber composite. While the chosen assumptions were shown to provide good agreement between experiments and simulations, caution in interpretation of model results should be made. One of the assumptions is based on the definition of intrabead damage, which encompasses damage behavior of bead-to-bead interfaces along the 2 direction. Interfaces are not explicitly modeled with cohesive laws as doing so will produce a computationally expensive model; moreover, cohesive elements are not compatible with the progressive activation routine and cannot be justifiably used in additive manufacturing process simulations at the present time. Nevertheless, interfacial behavior, either along the 2 or 3 directions, is accounted for in the continuum sense such that the equations governing interfacial damage accumulation is embedded into the material model. The option of using only the integration points that lie within a delimiting

space surrounding the expected location of the interface is possible; however, it is feasible to adopt this approach for the stacking direction but it requires a sophisticated searching algorithm for interfaces along the 2 direction. Another assumption is the quantification of damage, it relies on the absence of any irreversible strains or plasticity so that any unloading and reloading will pass through the peak value and continue its nonlinear path as it otherwise would have. For brittle glassy thermoplastic composites, neglecting plastic deformation under tensile load at low temperatures appears reasonable given that the damage quantity, computed from the degraded stiffness, outputs material parameters capable of describing the nonlinear behavior. The calibration of the model to predict tensile and compressive behaviors were strictly deduced from experimentally characterized properties and not arbitrarily tuned to fit the experimental results, this point is emphasized and an important consideration. Another assumption is on the choice of damage initiation and evolution, the damage surface relation which includes the hardening function was chosen based on the fact that (i) it has the capability of predicting anisotropic damage, (ii) it requires only simple uniaxial tensile, compression, and shear data, (iii) kinematic hardening and softening is easily modeled, (iv) implementation of temperature-dependent parameters is straight-forward, and (v) it has compatibility with the Additive3D simulation framework. Indeed, different damage initiation functions or criterions can be used based upon modeling needs. The fracture energies of the material were not experimentally characterized nor available in the literature; therefore, the softening regime of the material model is somewhat questionable. Two types of approaches were taken to reflect the softening part of the stress versus strain behavior; firstly, a damage critical value was implemented, and this produces the fracture behavior observed in the response of the material by instantaneously evolving the damage value to one. Secondly, no further hardening was allowed past the ultimate stress point, this caused the rapid evolution of the damage variable observed. Although obvious, the material model is not meant for problems which require fracture mechanics capabilities, for instance, to assess damage tolerance. Another assumption is the regularization approach, the artificial viscosity method was adopted for its simplicity in implementation which does not add to the computational expense of the model unlike the other approaches. Nevertheless, the choice of the viscosity parameter is difficult to determine since it requires awareness of its impact on the solution; in other words, it cannot be chosen arbitrarily and requires multiple analyses to understand its effect on the solution.

6.2 Design of a Short Fiber Composite U-Shaped Mold

A short fiber composite mold, inspired by the LSAM printed tool shown earlier in Figure 2, is re-designed at a smaller scale with supports. The dimensions of the tool are provided in Figure 111, the spline geometry, used for defining the complex u-shape, can be replicated using the coordinates of the event series provided in the appendix section. Compression molding is the intended application; therefore, a corresponding pressing surface (i.e., plunger) is needed. The assembly of the compression tool is shown in Figure 112 which illustrates the composite mold in dark-grey, prepreg charge, and aluminum plunger. Noteworthy to mention, the shape of the mold, provided in Figure 111, is an idealized version of the 3D printed mold. Moreover, the dimensions correspond to the nominal size of the tool. Although optional, it is customary to design the outer dimensions of the mold approximately half a bead width larger than the nominal dimensions, a subsequent machining step to obtain a smooth surface then follows to obtain the desired nominal outer dimensions.

One of the challenges with t additive manufactured designs of this size is the deviation of the sliced geometry to the idealized CAD model. Figure 113 illustrates the CAD model and its sliced representation. The oversized model is sliced using the commercial software Simplify3D©. In the sliced model, there are gaps present in regions where print segments meet, an example of the region is enlarged in the figure. While the flow rate and compaction depth can be modified to attempt closing the gaps, the bead dimensions will be altered which can make it more difficult to control the overall size of the geometry. The gaps and sharp turn radii are generally not captured in both process and performance simulations, and the idealized model is often used for approximating the printed and machined geometry. The relevant slicing parameters used for creating the sliced model are provided in Table 8. External and internal thin wall type were found to be essential for obtaining a non-distorted sliced model. The end-point extension distance is specified at half of a bead width, this ensures the infill region does not have gaps at the z-transition zones.

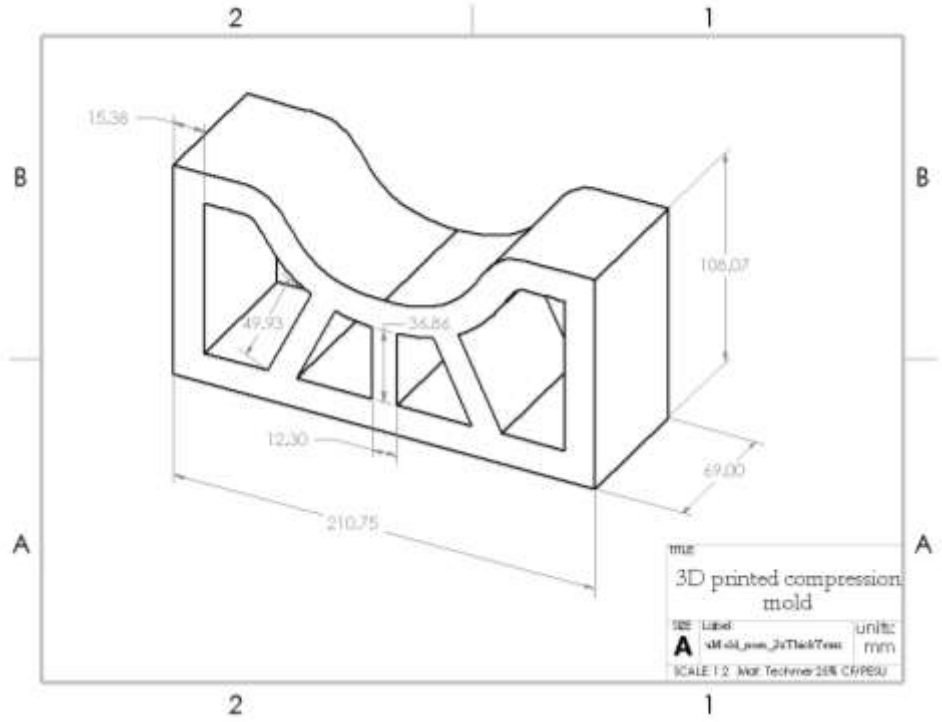

Figure 111 Nominal dimensions of designed u-shaped mold

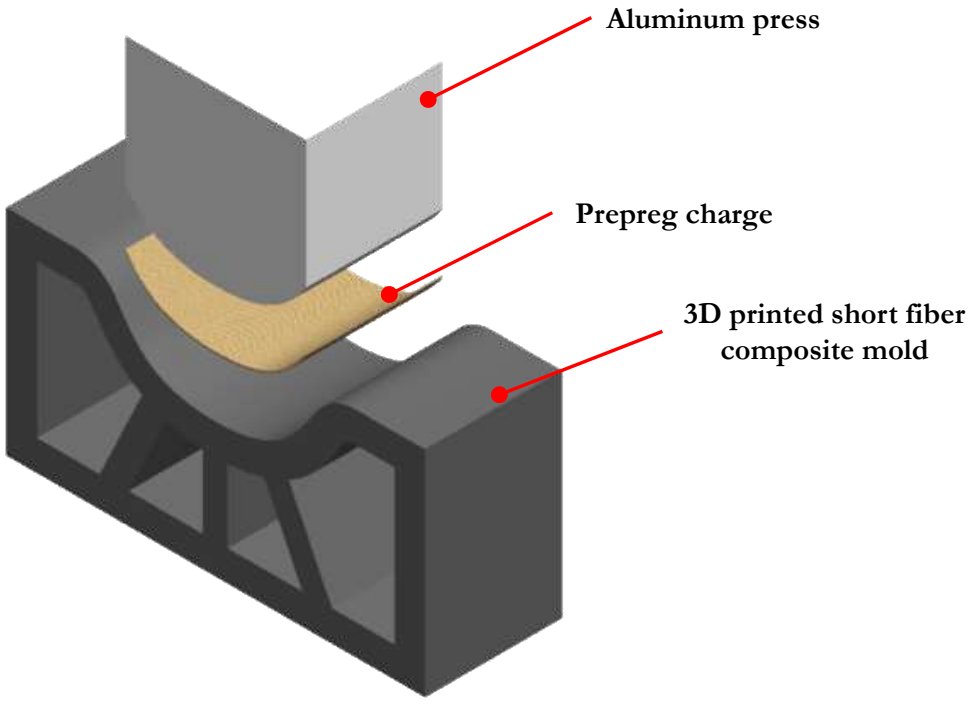

Figure 112 Schematic of compression molding assembly with 3D printed short fiber composite mold

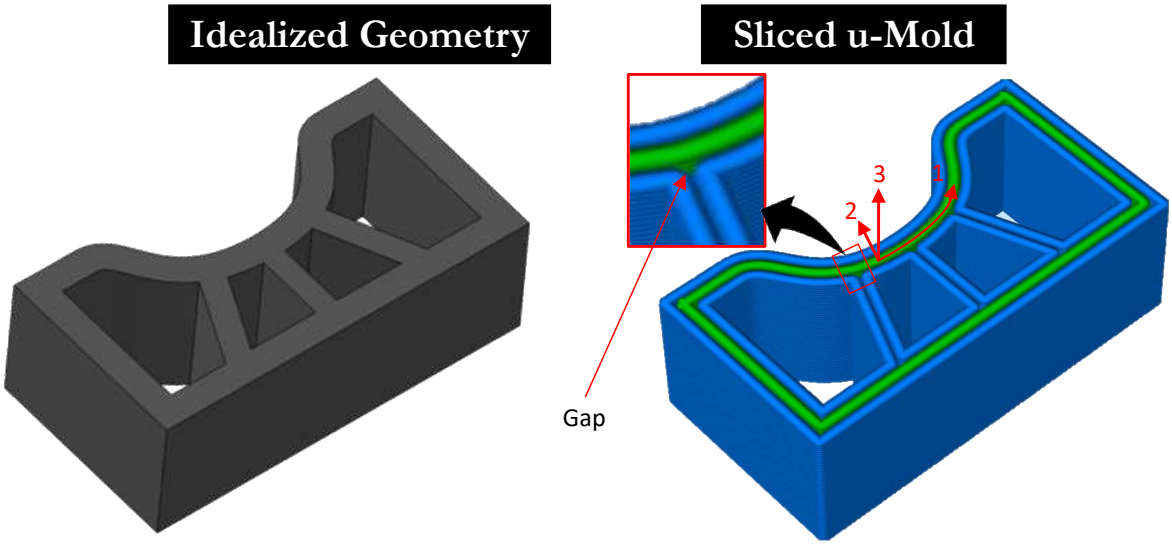

Figure 113 Idealized u-Mold geometry and Simplify3D© sliced model

Table 8 Relevant Simplify3D© parameters

Parameter	**Specification**
Nozzle diameter	4mm
Top solid layers	0
Bottom solid layers	0
Outer/Perimeter Shells	2
Outline overlap	5%
Speed (mm/min)	4000mm/min
External thin wall type	Allow single extrusion walls
Internal thin wall type	Allow single extrusion fill
Allow perimeter overlap	5%
Minimum extrusion length	50mm
Endpoint extension distance	3.075mm
Avoid crossing outline for travel movements	Enabled
Maximum allowed detour factor	4.0
Non-manifold segments	Heal

6.3 Process Simulation of a Mold

Severe thermal gradients and relatively high stresses are not desirable during and after printing, the purpose of conducting process simulations is to predict the temperature and stress distributions throughout the history of the manufacturing process. The stress and temperature distributions will help determine if the chosen process conditions are appropriate; therefore, the goal is to change the process conditions if stresses or temperature gradients are significant. The temperature profile of the u-shaped mold is shown in Figure 114, the contour plots are taken at the end of the 12th,

23rd, and 35th layers, these are within the deposition step. During the deposition stage, the build plate is set to 120°C (398.15K) and it acts as a heat sink. In addition, the temperature at the base of the part, which is in contact with the build plate, exhibits the coldest temperatures throughout the deposition history. Heat losses through conduction plays a significant role in the cool down of the part for layers close to the build plate. Heat losses through convection and radiation dominate the cool down of the molten material after it has been deposited within the layer time. For reference, the layer time is approximately 33s for the chosen process conditions, this layer time is computed from the event series by taking the difference in time at the beginning and end of the layer. Figure 115 illustrates the temperature contour after printing at approximately 26 minutes after deposition and after 10 minutes of cool down. After deposition, conduction heat losses are still significant relative to heat losses from radiation or convection. During the cool down steps, the temperature boundary condition specified at the base of the part is removed. Consequently, convection and radiation occur at all of the exposed free surfaces, this causes the temperature at the free surfaces to decrease faster than the bulk regions.

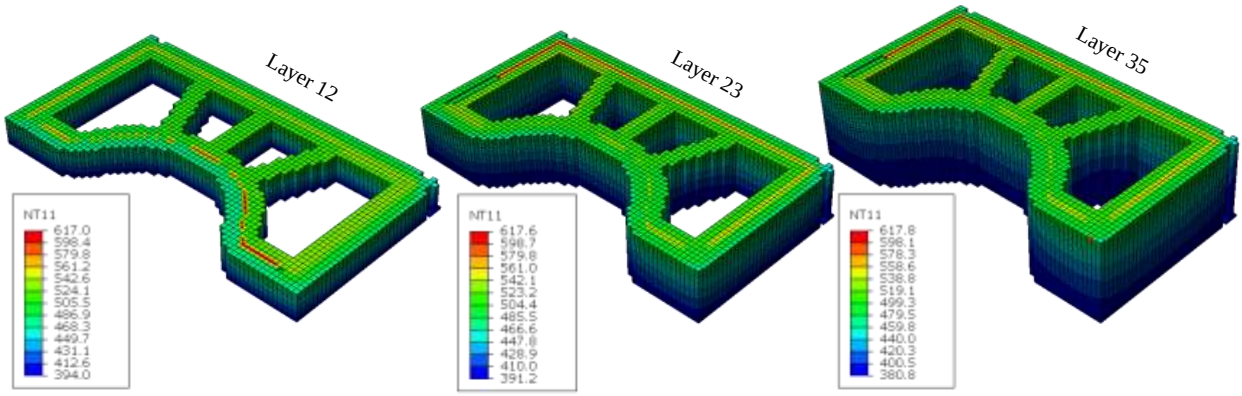

Figure 114 Temperature distribution during the deposition stage at three different times

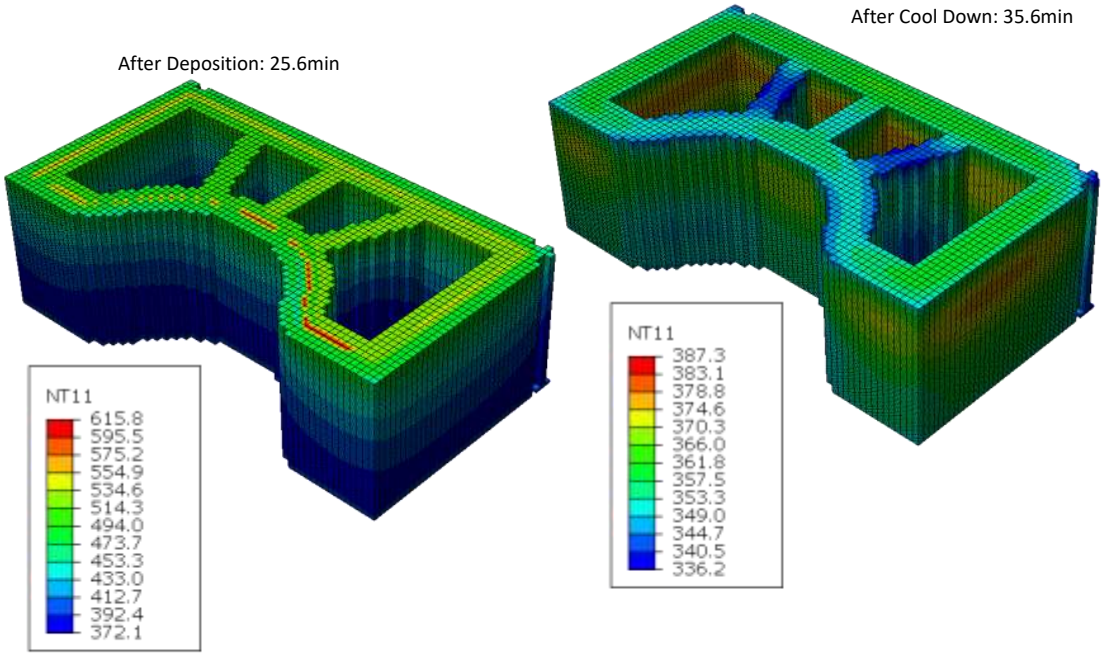

Figure 115 Temperature distribution after deposition and after 10 minutes of cool down

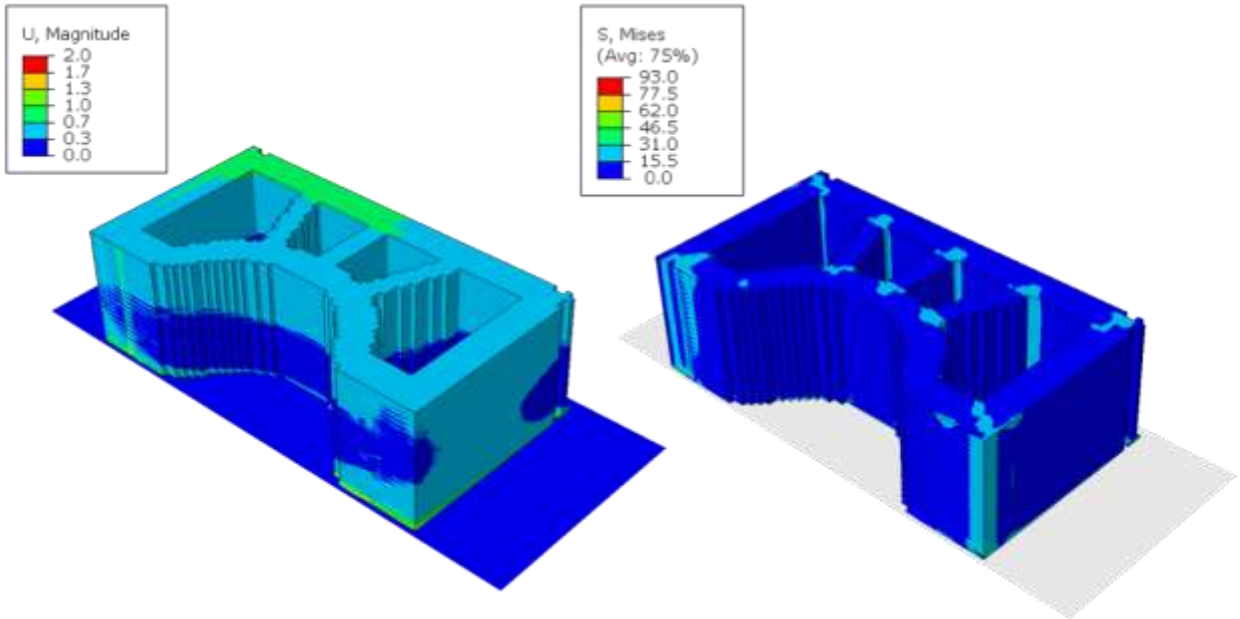

Figure 116 Displacement magnitude and mises stress distributions after 10 minutes of cool down

The displacement magnitude and von mises equivalent stress of the printed part after cool are shown above in Figure 116. A displacement magnitude of approximately 0.6mm is observed throughout the part, with 0.7mm seen at the top-left region of the displayed part. Large displacement magnitudes were found at the base of the part where contact is made with the build

plate. The rapid cooling of the first layer as a result of the imposed temperature boundary conditions causes this region to experience significant deformation relative to subsequent layers. The mises stresses are approximately 5MPa in the dark blue regions, and around 40MPa in the lighter regions, these lighter regions are located at the ends of the supports and at the four outer corners of the part. Similarly, the high mises stress is found at the base of the part.

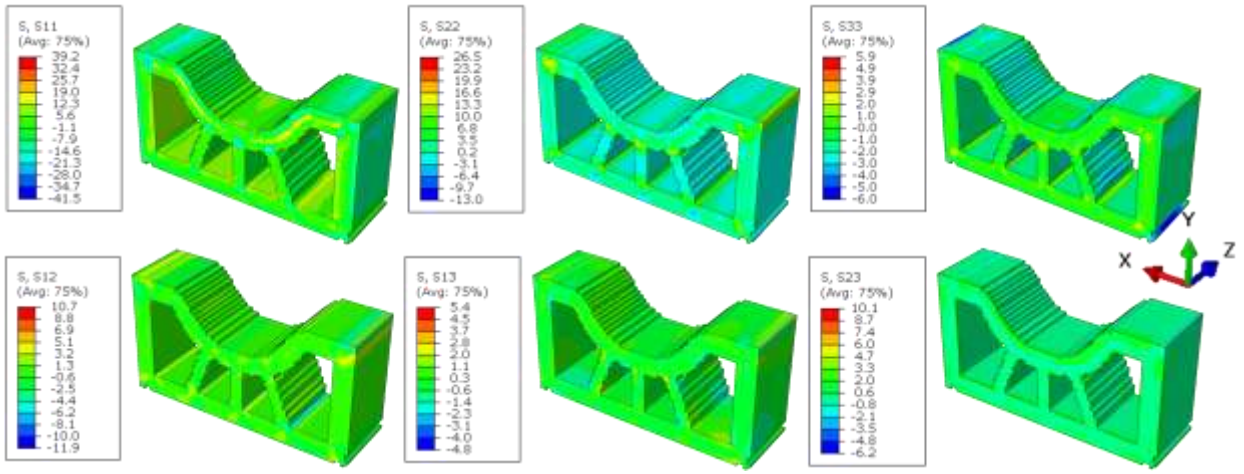

Figure 117 Displayed stresses for cross-sectional cuts taken 6mm above the print bed

Three process-based analyses were conducted to observe the differences in displacement and von mises magnitudes after the part has been printed and cooled down. Table 9 provides a summary of the process parameters modified, the convective heat transfer equations can be found in [8], the external wall feature type was used. For completeness, the polynomial function coefficients describing the air kinematic viscosity of zero, first, and second degrees are -8.96868D-06, 6.36467D-08, and 6.21664D-11, respectively. Likewise, the polynomial coefficients of air thermal conductivity for the zero, first, second, and third order are 3.49201D-04, 9.89608D-05, -4.57695D-08, and 1.39744D-11, respectively. The Prandtl number for air is 0.702, the first correlation coefficient for an external wall is -1.0169549D-03, the second correlation coefficient is 0.10586658, the n exponent is equal to 0.3665147, and the m exponent is equal to 0.2. The plots and figures shown earlier were for the process01 case. Only the build plate temperature, print speed, and base constraining method were changed. Process02 has similar process parameters as process01 except for the print speed, the lower print speed relates to a longer layer time which was approximately 44 seconds. Process03 was specified with the same print speed as process02 except that the build plate was set to room temperature and the base of the part fixed throughout the

deposition stage. Figure 118 illustrates the displacement magnitudes for each of the process conditions for the top three illustrations, and the mises stress distributions for the bottom-most plots. Like the first case, the displacement magnitudes were found to be greatest at the base of the part. A node at the top-center region of the curved part is chosen for extracting the displacement magnitude. The displacement magnitudes are similar for all three conditions at the chosen location, and were generally within 10% in most regions. However, the mises stress magnitudes were observed to be different for all three cases. Process03 exhibited the greatest stress in the base region, this is attributed to the imposed room temperature boundary condition and the fixed condition at the base. Since the mises stress distribution and the displacement magnitudes were not significant for most of the part when using when conditions in process01, it is chosen for the physical print.

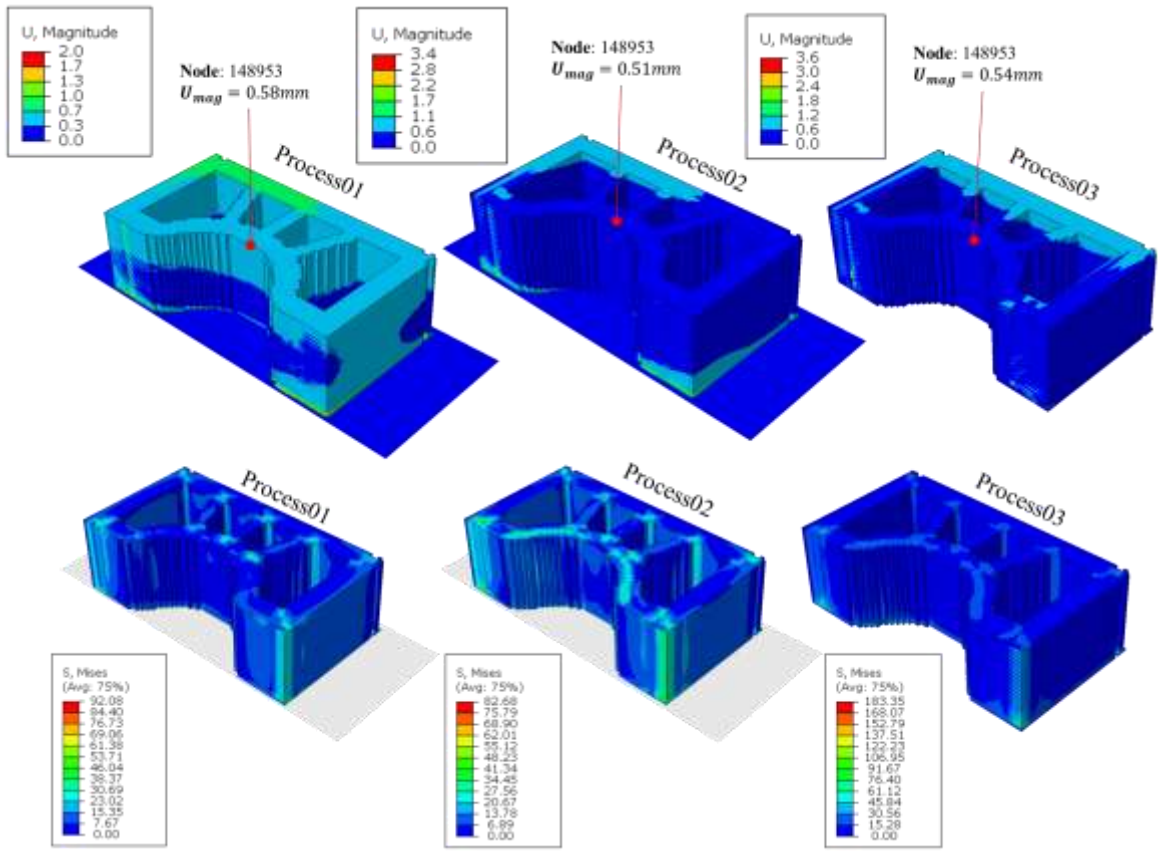

Figure 118 Comparison of displacement magnitudes for three different processing conditions

Table 9 Values of simulated process condition parameters

Parameters	***Process01***	***Process02***	***Process03***
Build plate temperature	393.15K	393.15K	298.15K
Speed	4000mm/min	3000mm/min	3000mm/min
Base constraint	Cohesive	Cohesive	Encastre
Elements per bead width		2	
Elements per bead height		2	
Total elements		124,662	
On bed cooling duration		300s	
Off bed cooling duration		300s	
Deposition time increment		1s	
Cooling time increment		5s	
Ambient temperature		298.15K	
Material extrusion temperature		638.15K	
Emissivity		0.96	

6.3.1 Temporal Plot of Temperature between Physical Print and Simulation

Figure 119 illustrates the temporal plot of the temperature at three locations along the backwall of the printed geometry, the temperature profile of the backwall, on the flat side, is shown below. The goal here is to provide a comparison of the temperature evolution during the deposition stage. Three curves are taken at layer heights 12, 23, and 35, and these are approximately located at center region of the flat region. Experimental values were extracted from a similar location on the physical mold, and the data was obtained using a thermal camera at a fixed distance from the print bed. The predicted temperature evolution were shifted in time to overlap with the experimental value to facilitate comparison, this shift is required since the event series used for simulations were generated using a python script which reads data from the *gcode* file and it does not account for changes in acceleration/deceleration during turns and transitions. From the plot shown below, the temperature evolution between the simulated and experimental results are in mostly good agreement during the deposition stage which lasts about 1500 seconds, some deviation is observed as the part is allowed to cool-down toward room temperature. A decrease and subsequent increase in temperature at approximately 100, 400, and 800 seconds occurs since the layer commences at the melt, cools down, and slightly re-heats when the layer directly above is deposited. The important point here is that the heat transfer material model captures the expected trend from heat losses in conduction, convection and radiation, this verifies the model works as expected. The heat transfer material model is utilized to conduct a sequentially-coupled thermal-stress analysis with

an approximate convective coefficient specified at the exposed surface during compression molding of the heated tool.

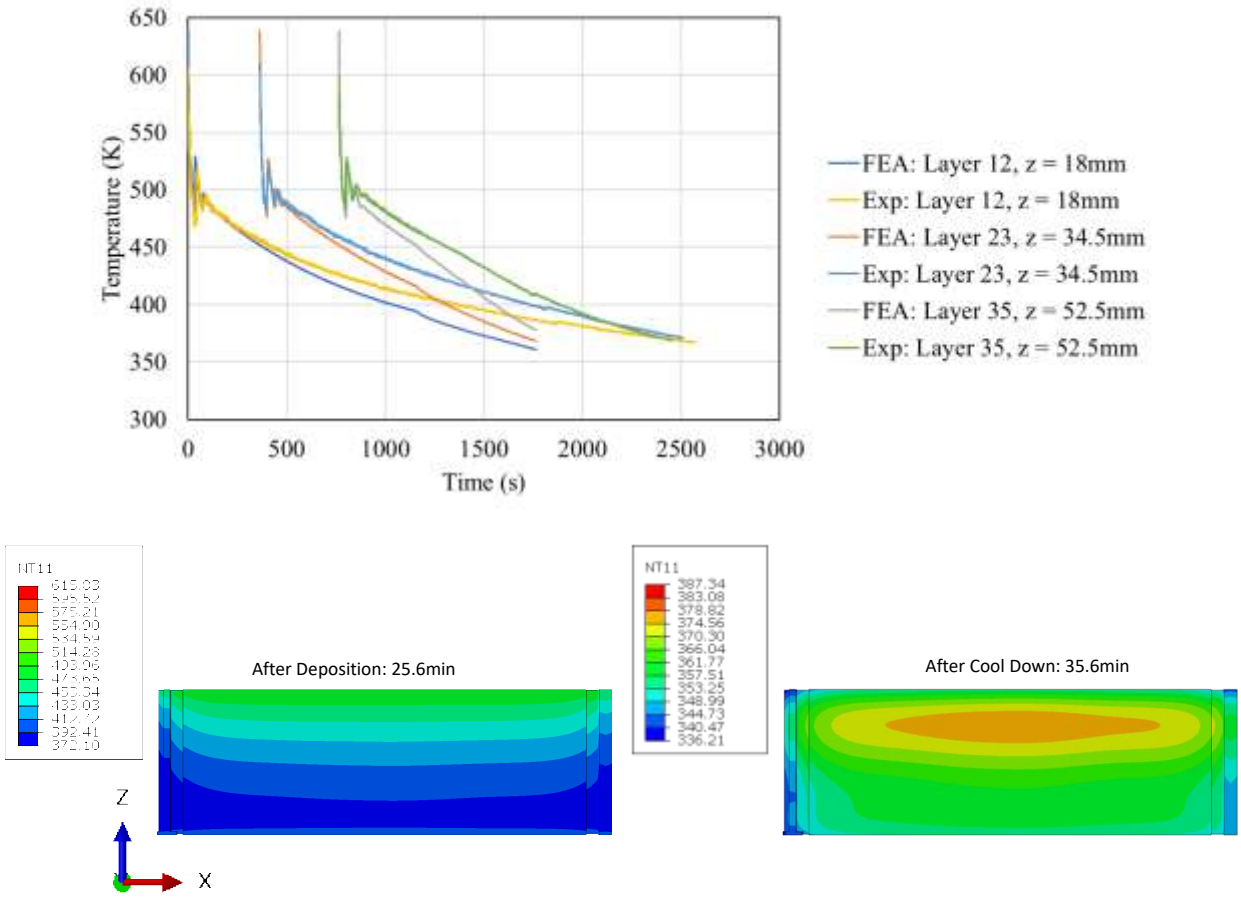

Figure 119 Temporal temperature plot for three different layers heights (top), and backwall temperature profile after deposition and cool-down (bottom)

6.4 Performance Simulation of a Mold

Figure 120 illustrates the load versus deflection, print direction stress state, and print direction compression damaged zones. The model has 131,560 C3D8 elements, with one element per bead height. No stress-mapping was performed in order to reduce the computational burden; however, it is possible to map the voxelized model stresses onto the conformal mesh. A uniform temperature of 150°C is applied at all of the nodes. A displacement boundary condition is specified at the surface nodes which are meant to be in contact with the plunger, this type of boundary condition was chosen for simplicity. The bottom flat surface is fixed. A ramp rate with an amplitude of zero

at commencement and one at 120 seconds is specified, the total time increment is 120 seconds. The specified displacement was 3mm downward to induce compression in the supporting regions, this produces a displacement rate of 1.5mm/min. The nonlinear geometry option, nlgeom, was used alongside an unsymmetric matrix storage. Automatic stabilization was enabled with the default dissipated energy fraction of 0.0002 and an adaptive stabilization with maximum ratio of stabilization to strain energy specified at 0.05. The initial, minimum and maximum time increments were set to 0.5, 1e-15, and 0.5 seconds, respectively. Solution controls were modified from the default settings, the following parameters were set to $C_n^{\alpha} = 100$, $I_0 = 8$, $I_R = 10$, and $I_A = 50$, these can be found under the field equations and time incrementation tabs. The subsequent analyses have similar parameters with the exception of the minimum time increment, which in some cases were specified as low as 1e-50 in an attempt to achieve convergence. All finite element models were solved using the Halstead cluster that is available at Purdue University.

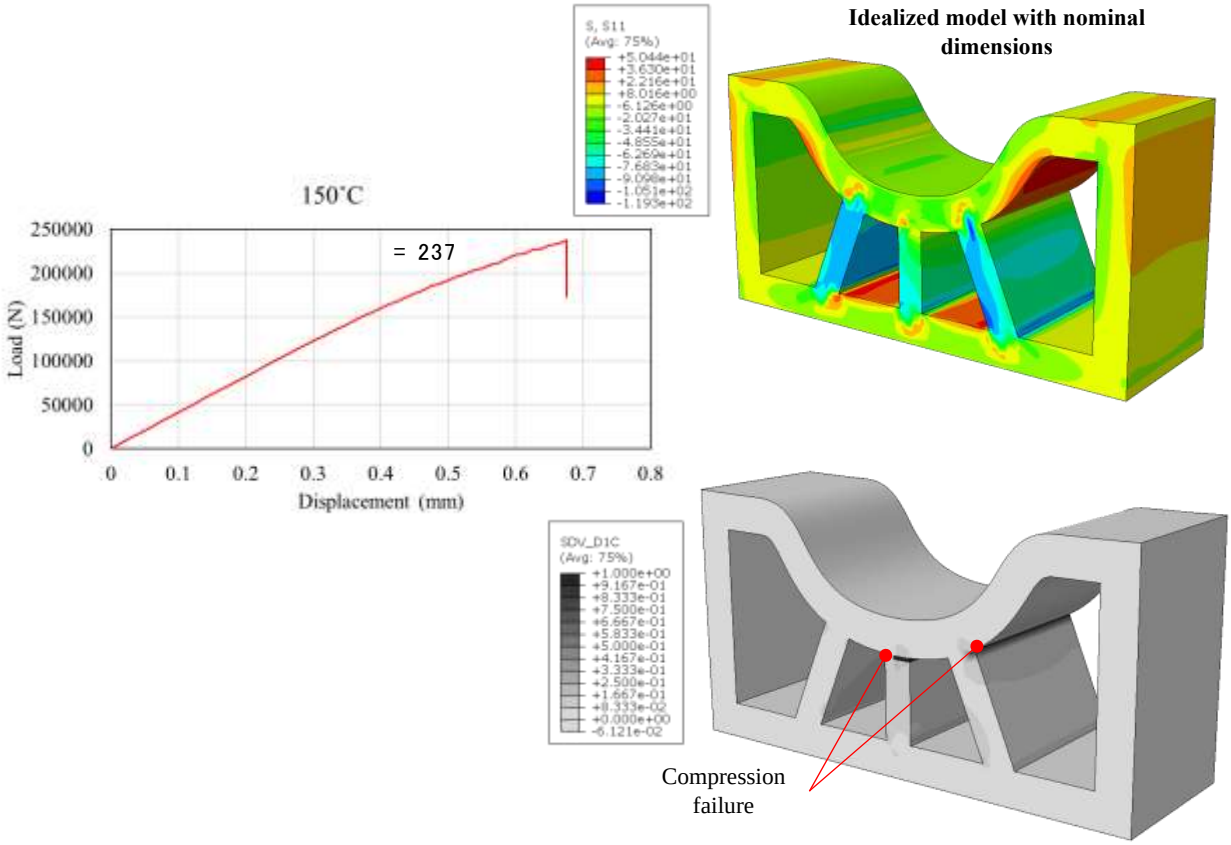

Figure 120 Idealized u-shaped mold with nominal and original dimensions

For all analyses conducted here, the material model that takes into account unilateral behavior without hardening past the peak load is used. In the idealized model, an ultimate failure load is predicted at 237KN since the load is seen to significantly drop. The nonlinear behavior that is seen is mostly a result of accumulated tensile, compressive, and shear damage. In the plot shown above, a linear regime is observed though it does not signify the absence of damage since the print direction compression damage variable begins to evolve at approximately 67KN at the supports. After 0.6mm of displacement, the material's tangent stiffness is visibly different, and this happens when damage localizes as shown in the black and white damage contour plot. The dark zones represent regions of damage, and when the damage variable reaches a state of one, it implies that the element can no longer support any load since its stiffness has fully degraded. Further, this contour plot illustrates the localized damage zones which happens at the sharp corners of the supporting regions, this is expected since load concentrations are expected in regions where a disruption to load transfer occur. The print direction stress contour at the peak load is shown, this illustrates how the load is redistributed after damage and before failure.

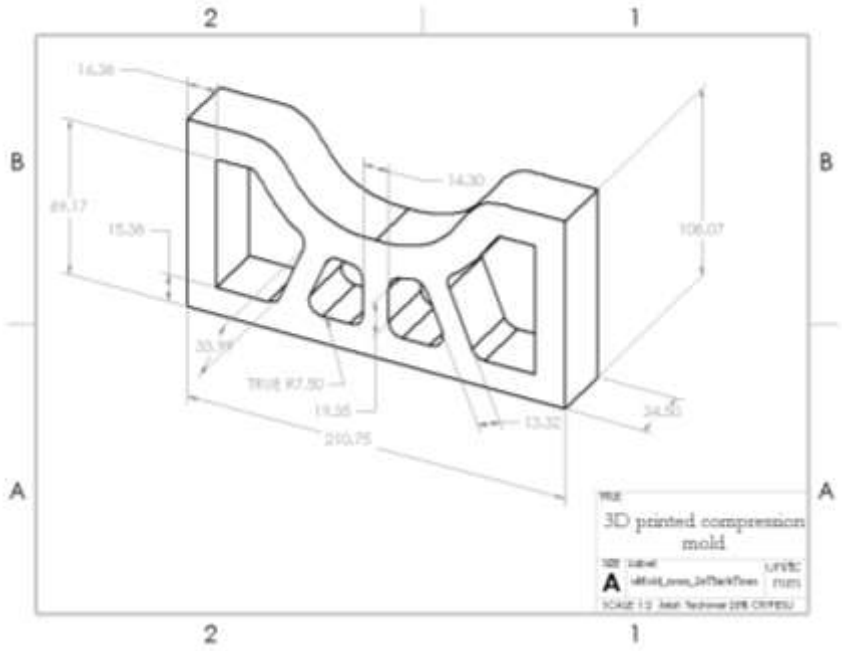

Figure 121 Representative dimensions of 3D printed and machined u-shaped mold

Figure 121 is a re-scaled u-shaped mold, the z-direction height was reduced by half and several fillet regions each with a 7.5mm radius was included. The mold is re-designed to ensure it will fail within the load capacity of the 55-kip (245KN) MTS, the idealized model previously

shown does not include these fillet regions and the slightly thicker inner walls that result from the 3D printing process. In the model shown above, thickness deviations are accounted for and the sharp corners are removed to better reflect the actual printed mold.

Figure 122 shows the load versus displacement plot for the re-designed u-shaped mold illustrated in the figure above. The same boundary conditions were applied as in the idealized case except for the loading mechanism which is explicitly modeled. An aluminum plunger with C3D6 elements within the curved region is used, and C3D8R elements in the rectangular regions. The stiffness of the aluminum is specified as 68900MPa with a Poisson's ratio of 0.31. A reference point is tied to the nodes at the top of the aluminum plunger, this reference point is fixed in all directions except the vertical for which a downward displacement condition is specified with a magnitude of 3mm. A uniform room temperature field is prescribed at the initial step, no initial residual stress state is mapped onto the mold for computational ease. At this temperature, damage is likely to occur at the curved region under tensile loads and on the angled supports from shear damage. No peak load is reported since the analysis was not fully completed in the allotted time given, significant time-increment cut-backs were observed. It is assumed the model can withstand more load since full fracture or damage evolution has not been observed yet.

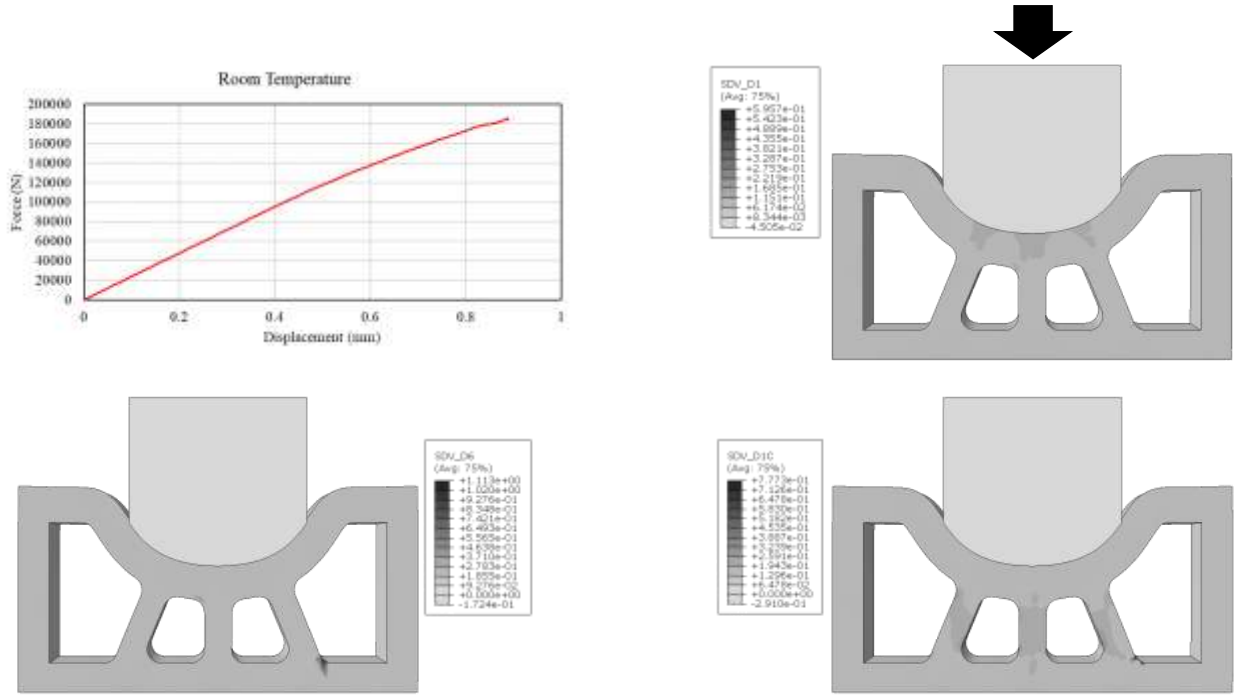

Figure 122 Performance of u-shape mold under compression at room temperature

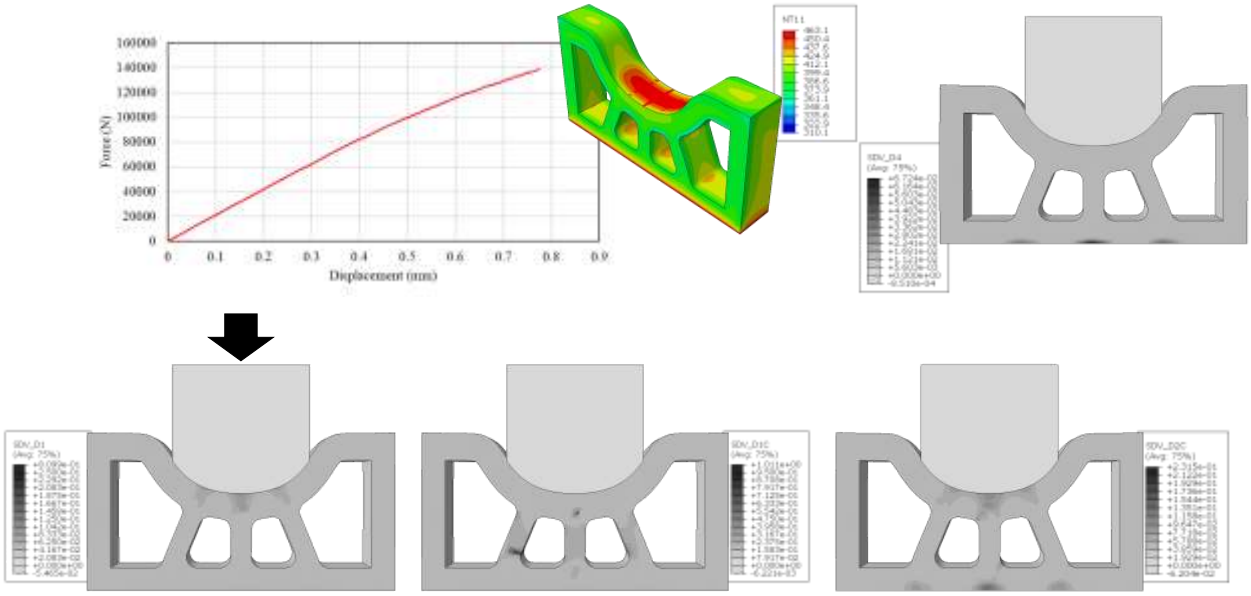

Figure 123 Sequentially coupled thermal-stress analysis of short u-shape mold with a film coefficient, $h = 25mW/mm^2K$, at the exposed surfaces, with 298.15K sink temperature

Similar to the load case in Figure 122, the short u-shaped mold is modeled with the same mechanical boundary conditions except with a non-uniform temperature distribution. A sequentially coupled thermal-stress analysis is conducted. In the thermal analysis, the same material model is used as in section 0. The tool initially begins with a uniform temperature of 190°C applied at the nodes, then all free surfaces are subjected to convection heat loses with the film coefficient specified as $25W/m^2K$. In a subsequent step in the thermal analysis, the bottom flat surface is specified with a constant temperature condition of 190°C for two minutes. Moreover, the plunger is specified with a constant temperature at the top face. These conditions reasonably reflect the experimental setup used for the trial run, though it is noteworthy to mention that the actual conditions are more complex than assumed here. Figure 123 illustrates a snapshot of the temperature distribution at the end of the thermal analysis, this temperature distribution is then mapped onto the structural model. In the figure below, the load versus displacement is shown alongside the damage contours for the print direction tensile and compressive damage variables, the 2 direction compressive damage variable, and the 2-3 shear damage variable. These damage variables were observed to be the most pronounced at the peak load value. The load versus displacement curve exhibits nonlinear behavior, similar to the load case of the idealized model shown earlier, this nonlinearity results mostly from the accumulated damage. Supporting regions

are predicted to likely fracture under compression in addition to the base under shear and the curved side under tension.

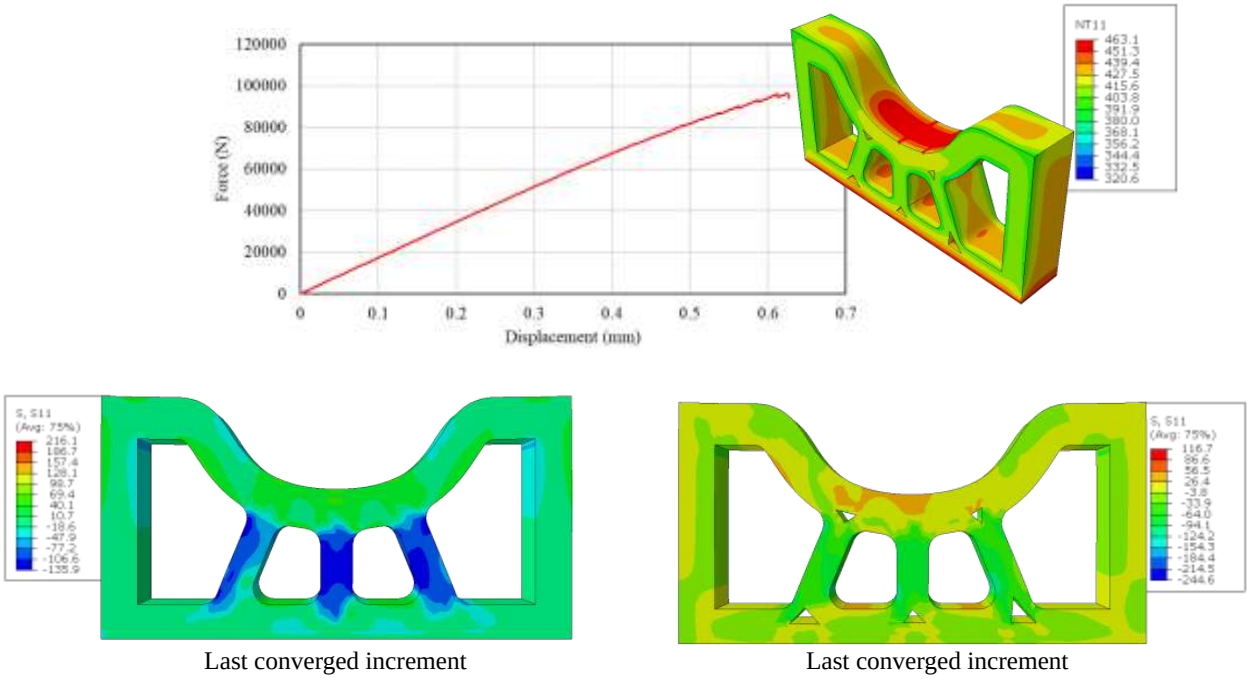

Figure 124 Sequentially coupled thermal-stress analysis of imperfect short u-shape mold with a film coefficient, $h = 15mW/mm^2K$, at the exposed surfaces, with 298.15K sink temperature

The gaps shown earlier in Figure 113 for the sliced geometry will impact the stress distribution in the mold, these empty regions are not straightforward to model and an attempt to include these discontinuous regions is made as shown in Figure 124. The size and shape of the discontinuous regions have some form of curvature since these regions are produced when the printer makes a turn or loop. In the model shown above, these regions are approximated by triangles with varying sizes which are representative of the stochastic nature of the print quality. A similar sequential thermal-stress analysis is performed as in the previous case illustrated in Figure 123, the film coefficient is specified to be $15W/m^2K$ as an assumption. The temperature distribution is shown above, and it is also mapped onto the structural model. The load versus displacement curve is presented above, and similar to the previous case, compression print direction damage is observed to also commence within the linear region. The load at which damage begins is approximately 37KN. The stress distribution along the print direction is also shown at the last converged time increment for the models with and without the discontinuities. These

discontinuous regions have an amplifying effect on the compressive stresses at the three supports relative to the non-discontinuous model.

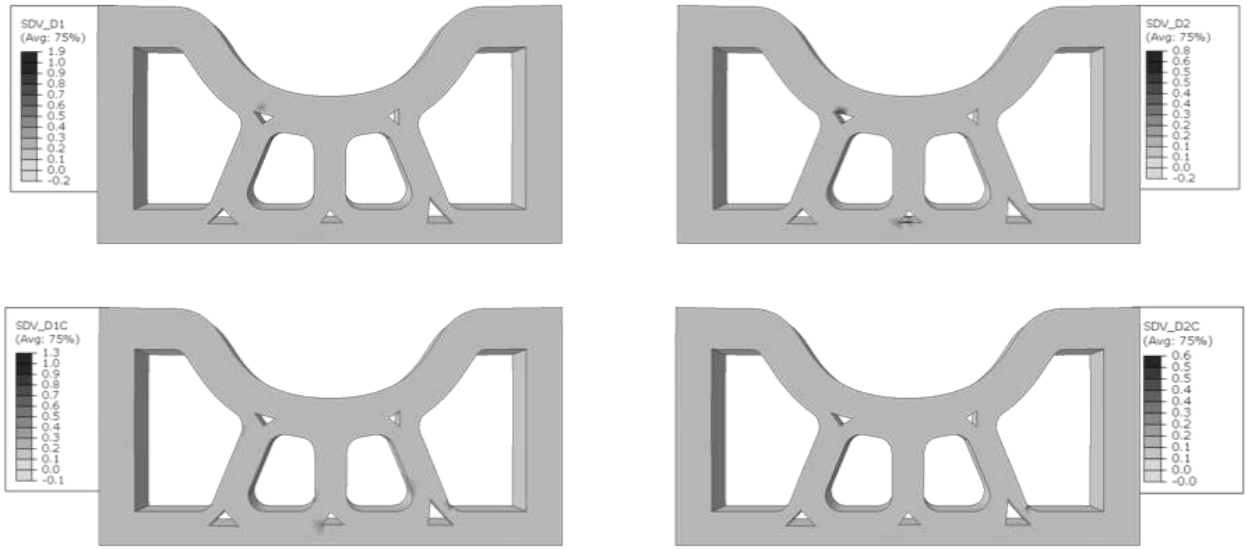

Figure 125 Tension and compression damage along 1 and 2 directions for imperfect u-shape mold

Figure 125 illustrates the print direction tensile and compression damage variables on the left hand side, and the 2 direction tensile and compressive damage variables on the right hand side for the same model shown above. These damage plots were obtained at the last converged time increment. Dark regions are representations of damaged zones as mentioned previously, and the darker regions are seen to be within some proximity to the discontinuous regions. For instance, print direction compressive damage is observed at the bottom center in addition to 2 direction tensile damage. Keeping in mind the temperature distribution, the temperature is near the applied boundary temperature of 190°C, which directly implies that the strengths of the material is lower in this region; therefore, it is reasonable to expect some fracture at this location. It may be noteworthy to highlight that damage is not seen to localized or accumulate in one region for all damage modes, rather it occurs at different locations yet within some proximity to the discontinuity.

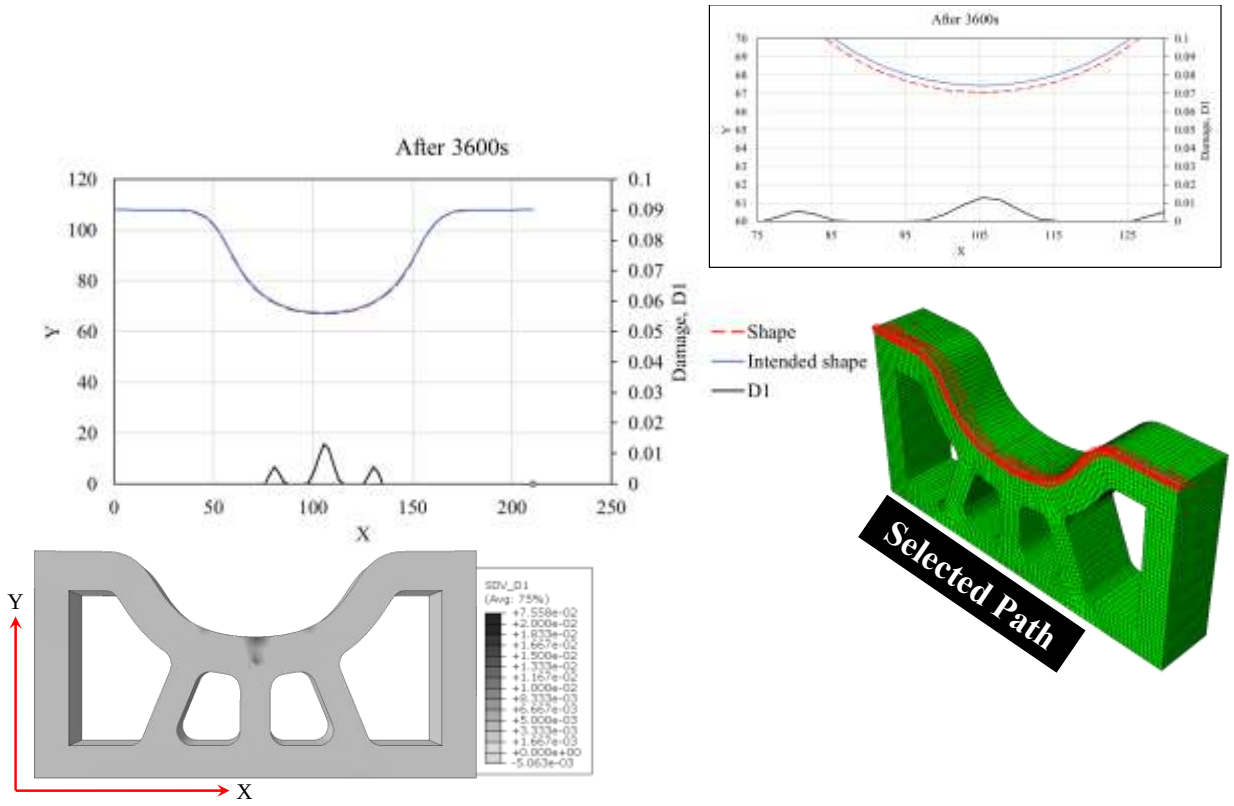

Figure 126 Short u-shape mold with a constant applied pressure of 10MPa, shape deviation as a result of creep-damage interaction

A mold without discontinuities is analyzed under a constant applied load of 10MPa and a uniformly distributed temperature of 190°C. Although not displayed, the aluminum plunger is present, its top surface is prescribed with a uniformly distributed pressure. The constant pressure conditions induce creep behavior since the compliance of the material increases with time for constantly sustained loads. A loading rate of 5MPa/min is applied, and the applied pressure was sustained for at least one hour (3600s) to monitor the evolution of the shape and damage variable. The plot shown in Figure 126 contains the shape outline of the tool after an hour at the sustained pressure, the selected path used for extracting the X-Y coordinates of the mold shape is highlighted in red. In the same plot, the print direction damage variable is also plotted with respect to the X-coordinate. Damage was observed after the load was applied, with a maximum magnitude of 1.16%. After an hour, this magnitude slightly increases to 1.3% and to 1.4% after 1.7 hours. The location of the damage is in the curved region of the mold, directly below the plunger. This signifies that there is a likelihood that material softening will occur in this region; consequently, the shape of the mold may be adversely affected by this softening.

6.5 Experimental Investigation

The mold presented in section 6.1 was 3D printed using the CAMRI system, it is made from the 25% wt. carbon fiber reinforced PESU which had been characterized in Chapter 1. The pellets were dried at 125°C for four hours prior to processing. In the CAMRI system, the temperatures in zones 1 through 6, as illustrated in Figure 23, were set to 327°C, 343°C, 366°C, 365°C, 365°C, and 370°C, respectively. Moreover, the build plate temperature was maintained at 120°C and a thin layer of Weldwood® contact cement was deposited onto the build plate to ensure the initially deposited beads remained fixed during the deposition stage. A bead compactor, i.e., a tamper, was used to flatten the deposited layers, the vibrating plate's speed was set to 1500rpm. The processing conditions labeled "process01" discussed in section 6.3 was used. After the mold was 3D printed and cooled down to room temperature, it was placed inside an oven for the thermal annealing process. The mold was subjected to a temperature of 190°C for at least two hours to alleviate residual stresses; also, since polymer diffusion is driven by temperature, it is assumed the interbead bonding is also improved during the annealing process.

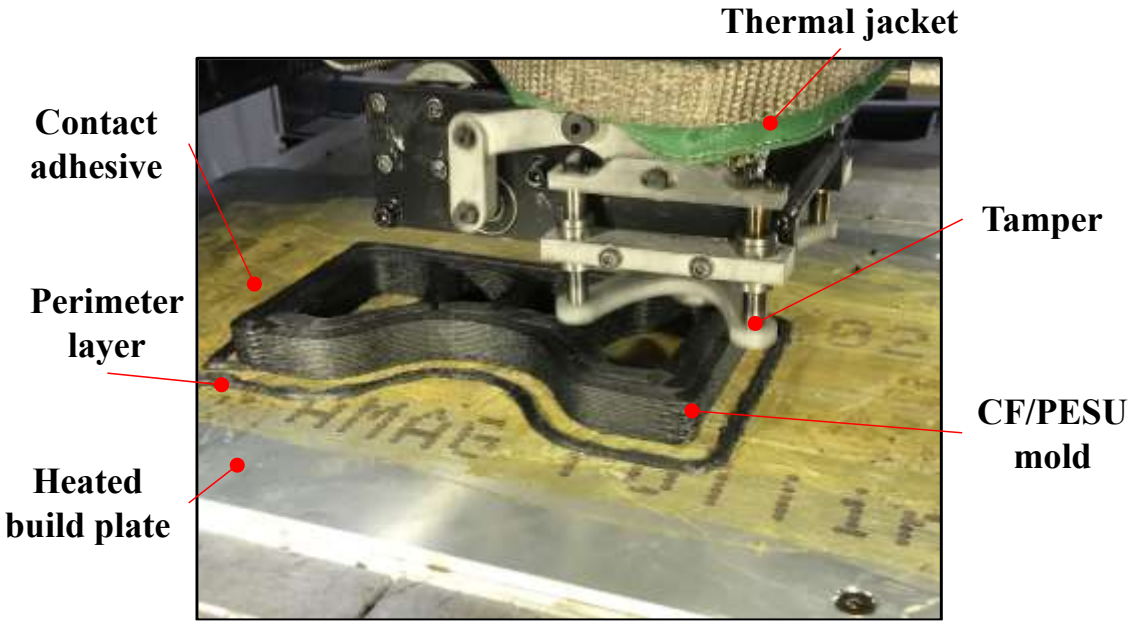

Figure 127 3D printing process of u-shaped mold using the CAMRI system

After the annealing process was completed, the outer perimeters of the mold were machined using a computer numerical control (CNC) system. Half of a bead's width was removed during the machining process. A servo-hydraulic MTS 810 with a 55-kip (245 KN) load cell was used for the compression test. An in-house built press with temperature-controlled platens was installed onto the 55-kip MTS frame, the bottom platen was controlled in displacement mode by the movable piston and the top platen was in contact with the load cell. An actively cooled plate was placed between the load cell and the top platen. For the experimental procedure, a 120 grit medium drywall sanding screen was placed onto the top and bottom platens and secured using high temperature tacky tape, the screen was used for increasing the friction between the platens and the compression assembly. The platens were pre-heated to approximately 190 ° C before the compression test. An oven was placed near the MTS setup to minimize the time to transfer the heated mold onto the press. The short fiber composite mold and aluminum press was heated to a temperature of 190°C inside the oven, a thermocouple was placed at the inner wall of the mold to monitor the surface temperature of the mold. Figure 129 illustrates a transient heat transfer analysis conducted on the mold design shown in section 1.1, the film coefficient specified at the free surfaces was set to $50 W/m^2K$ with a sink temperature of 463.15K. Further, the time to a uniform temperature of 190°C is estimated to be approximately 26 minutes, this serves as a conservative estimate for the time required to reach the desired temperature once the ambient reaches 190°C.

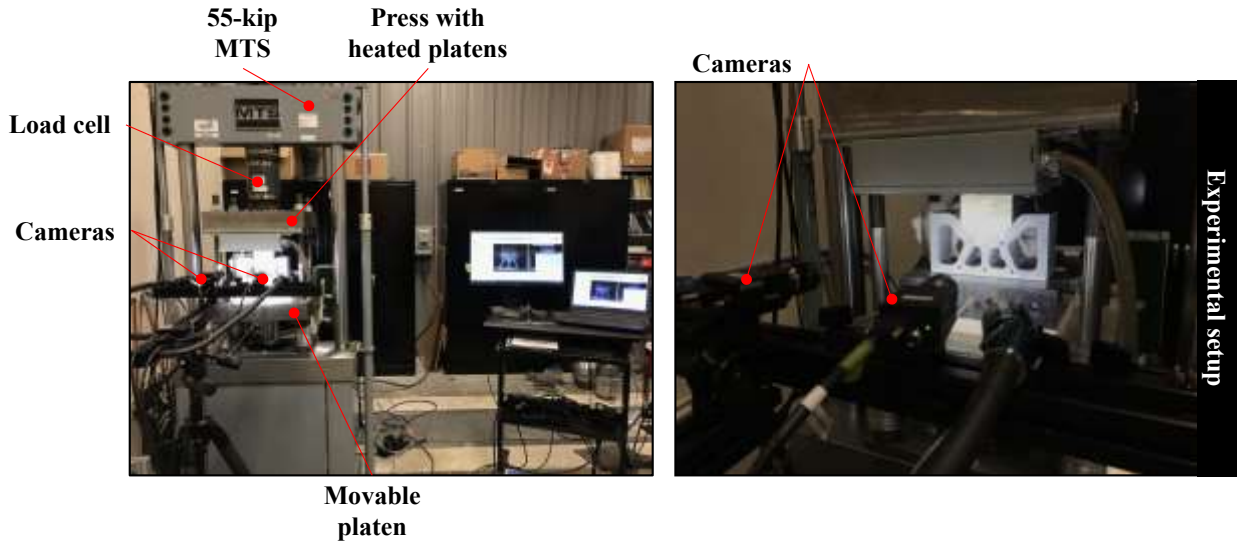

Figure 128 Experimental setup of short fiber composite mold for compression testing

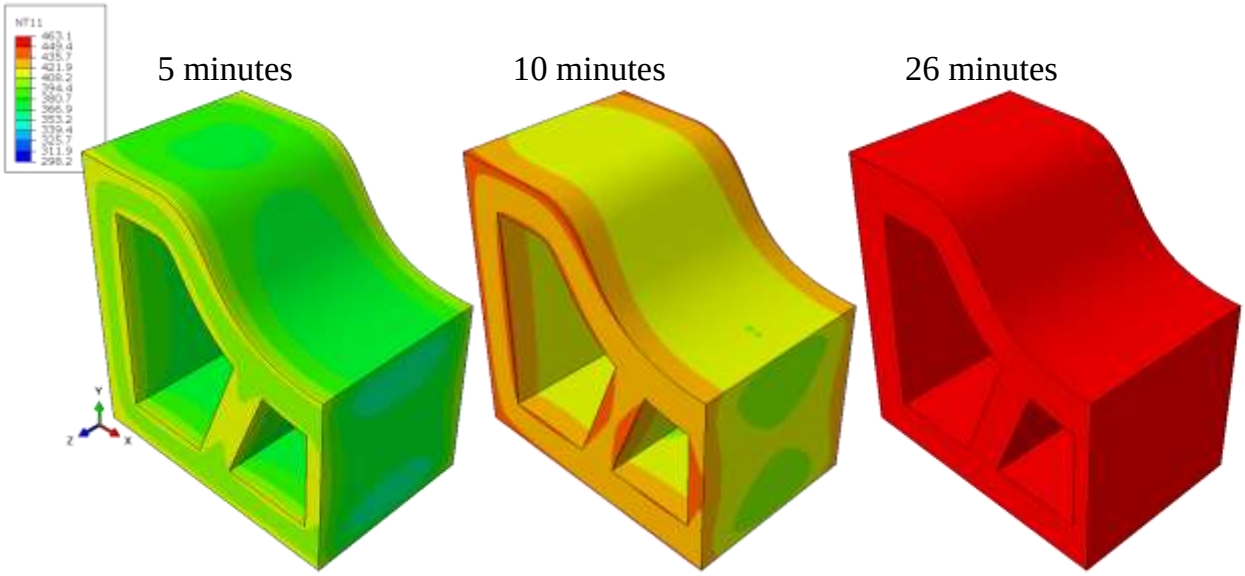

Figure 129 Transient heat transfer analysis of original u-shape mold design

Figure 130a shows the MTS-generated load versus crosshead displacement for the short fiber composite mold subjected to compressive loading. The aluminum plunger and composite mold are not completely in contact which is likely because of the thermal expansion difference and temperature differential between the two, the initial stiffening observed is a result of the contact between the mold and plunger settling into place. Some initial linear behavior is observed between 1mm and 2mm, nonlinear deformation is observed afterwards. The initial softening at the first peak load, corresponding to a load level of approximately 169KN, was observed to crack in the curved region and at the bottom-center. From the cameras, the cracks first formed and evolved at the base of the part, where the discontinuity lies. In the subsequent images, a macro-crack was observed on the tensile-loaded side of the curved portion, these cracked regions are highlighted in the figure below. Due to the fact that the load transmission was disrupted on the left-hand side of the mold (i.e., from the cracked curved region) and the center region, the left-hand side support as well as the center support could no longer sustain the required load. Consequently, the right-hand support essentially sustained the load post-initial peak until catastrophic fracture. The macro-crack that causes ultimate failure, passes through the discontinuity and terminates near the corner of the support, on the top-left side, and the contact surface. The duration of the test took approximately 5.5 minutes, this does not include the addition two or three minutes of setup time. The mold is believed to have substantially cooled down which explains the relatively large ultimate load.

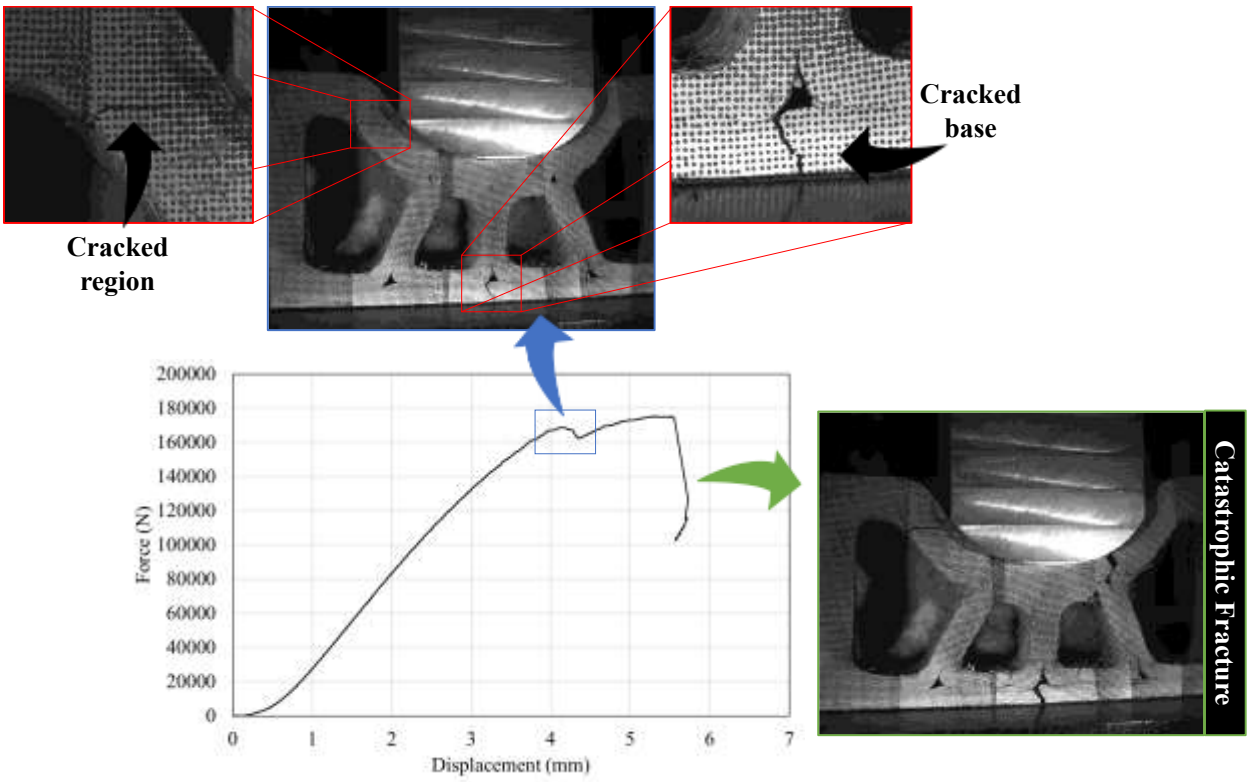

(a)

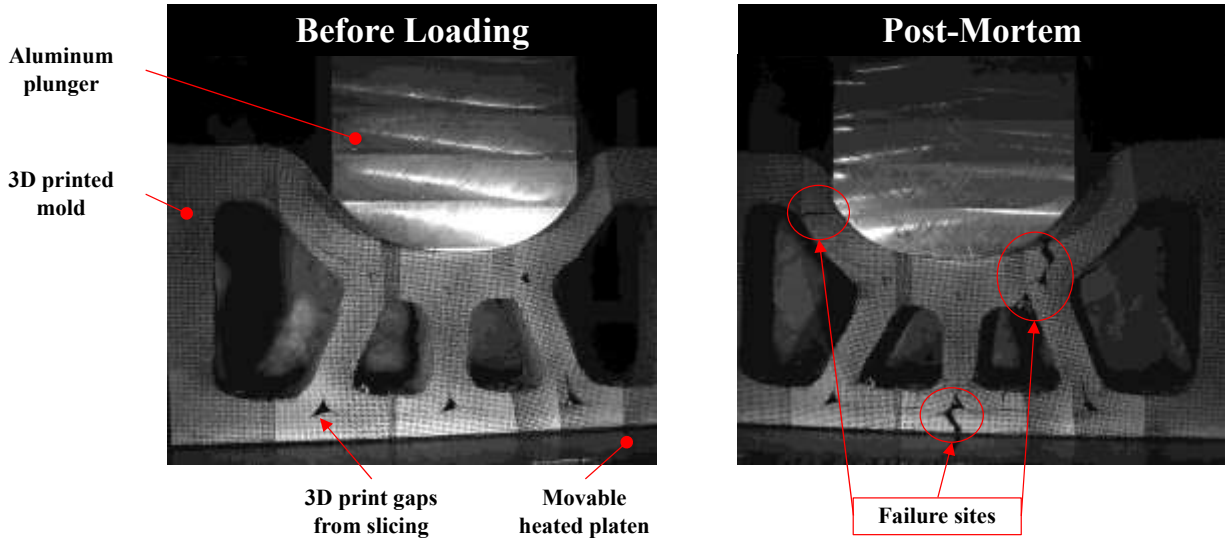

(b)

Figure 130 (a) MTS-generated load versus crosshead displacement for short fiber composite mold under compression, (b) images of composite mold before and after fracture

7. CONCLUSION

In summary of this dissertation, a novel viscoelastic damage modeling approach is developed for the analysis of extrusion deposition additive manufactured short fiber reinforced composites. The viscoelastic damage model is derived using thermodynamics and continuum damage mechanics principles. Two types of material models were considered, one with independent damage variables and another with three principle damage variables; moreover, critical damage values and a limited hardening function were also considered in the formulations. Experiments were conducted to understand the material behavior at ambient and elevated temperature; furthermore, stress versus strain behavior was analyzed for specimens subjected to uniaxial tensile, compressive, and shear deformations. The mechanical properties in tension and compression obtained from experiments were utilized to calibrate the material model, shear behavior was assumed based on experimental trends for the case with independent shear damage variables. The material model is verified using the experimental data, and it was shown to possess the ability to predict experimental trends observed at various temperatures or deformation modes. Lastly, the material model is integrated into the Additive3D framework and performance analyses were made for a compression molding tool.

Chapter 3 contains the derivation of the viscoelastic damage model used throughout this dissertation. The Helmholtz free energy potential is defined based on a Taylor series expansion of the viscoelastic internal state variables, damage is introduced through the principle energy equivalence. Thermodynamic consistency is enforced by satisfying the Clausius-Duhem inequality. Failure initiation and evolution is determined using the energy-norm surface function with a temperature-dependent isotropic hardening function; noteworthy to mention, the material-dependent damage interaction tensor also exhibits temperature-dependency and is dissociated into tensile and compressive parts. The material model is implemented in numerical form as a user-defined material subroutine for the commercial finite element analysis software Abaqus/Standard.

Chapter 4 includes the experimental characterization performed on a 25% wt. carbon fiber reinforced PESU. The viscoelastic properties were initially characterized using the three-point bending test for beams oriented along the print and in-plane transverse directions. Based on the results of the relaxation test, three temperatures were selected for elevated temperature mechanical tests with the intention to minimize relaxation nonlinearity within the span of the test. Unilateral

behavior is observed for tensile and compressive behaviors, with compression nonlinearity and strength being greater than the tensile performance irrespective of temperature or corresponding loading direction. A decreasing nonlinear onset strain value was observed for tensile and compressive specimens tested along the 2 and 3 directions. Furthermore, strength and stiffness were found to generally decrease as temperature increases for tensile and compressive specimens; however, shear modulus was not found to experience this decaying trend along the 2-3 and 1-3 directions. Overall, the experimental campaign has shown the need for an anisotropic damage model that can account for behavioral changes when temperature is changed.

Chapter 5 discusses the procedure used for calibrating the material model using experimental properties procured in Chapter 4. The Prony series is characterized and a modified WLF equation is adopted to better predict the shift factors at lower temperatures. The thermoelastic approach adopted in this work is used for defining the viscoelastic stiffness matrix. The model with three principal damage variables and critical damage values was calibrated using tensile experimental properties to obtain the temperature-dependent damage threshold and exponential of the hardening function. For the model with unilateral behavior, both tensile and compression properties are used for estimating the damage model parameters. Since the model parameters were determined using the uniaxial tensile and compressive data, the three shear-dependent components of the damage interaction tensors were adjusted to obtain reasonable correlation to the shear data. Overall, the material model is found capable of predicted the observed experimental trends such as reduced nonlinear onset strain and reduction in strength.

Chapter 6 presents the modification made to the Additive3D framework. The material model is used for predicting performance of an additive manufactured compression molding tool. The load versus displacement of the compression mold is predicted, where the damage modes are quantified. Several analyses were conducted to demonstrate the utility of process and performance simulations. Moreover, multiple performance analyses were made to illustrate the damage model capability to predict damage zones and the load versus displacement behavior.

In conclusion, this work shows a comprehensive effort in damage modeling for which there are several important results made from conducted research. Firstly, the short fiber composite exhibits anisotropic behavior and its stress versus strain behavior changes when temperature is changed, this behavior must be included in material models. Secondly, the stress versus strain for uniaxial tensile behavior can be predicted and shown to have good agreement with experiments by

using material model parameters calibrated from tensile properties. Predictions of the unilateral behavior requires additional normal damage variables alongside dissociated normal damage interaction components into tensile and compressive parts. Permanent deformation cannot be modeled using this approach; therefore, extensive deformation observed for shear properties at elevated temperatures are not well captured. The temperature-dependent isotropic hardening function is capable of capturing changes in intrinsic and extrinsic material properties, its parameters were deduced from elevated temperature tensile data. Performance analyses can be made using the material model to predict load-displacement behavior and identify damage quantified regions.

7.1 Future Work

The presented research has numerous areas of improvement, the author would like to recommend possible future work for this research as listed below.

1. Include a permanent or plastic deformation potential to model irreversible strains to complement damage.
2. Consider replacing the isotropic hardening function with an anisotropic hardening function with softening defined as a function of the fracture energy and strains.
3. Consider using the gradient-enhanced non-local approach to mitigate mesh-dependency caused by material softening.
4. Develop a searching algorithm for 3D printed geometries to specify enriched interface damage zones which act with interfacial damage properties.
5. Develop a micromechanics approach to obtain homogenized viscoelastic stiffness matrix from micro-constituent elastic and viscoelastic properties.
6. Conduct additional experiments aimed at quantifying damage and further validate the material model.
    a. Obtain X-ray computed tomography for a loaded specimen under tension or compression to quantify damage at different strain or stress levels.
    b. Obtain loading/unloading tensile and shear data to compare with CT-scan data and the current approach taken in this research.
    c. Perform a three-point bending under quasi-static loading to obtain creep rupture and ultimate strength to compare with simulations.

APPENDIX A. MATHEMATICAL FORMULATION AND CODES

A.1 Definition of Second and Fourth Order Tensors

In this dissertation, tensors are defined in 3-dimensional space; therefore, the rank of any tensor is defined by n and the total number of components is computed by 3^n. Summation notation is used to describe these tensors, it is also known as the Einstein summation convention. The total number of independent indices denote the rank of the tensor. Second and fourth order tensors are then composed of 9 and 81 components, respectively. An example of a generic second-order tensor is shown in Eq. A.1. The tensors presented here are Cartesian tensors, this means they are defined by a set of rectangular axes or orthonormal bases, $\hat{e}_1$, $\hat{e}_2$, and $\hat{e}_3$. Tensor transformation from one coordinate system to another follow the usual procedure, that is, they are transformed by the rotation or directional cosine matrix, as given by Yu [142].

$$\mathbf{T} = \mathrm{T_{mn}} = \begin{pmatrix} T_{11} & T_{12} & T_{13} \\ T_{21} & T_{22} & T_{23} \\ T_{31} & T_{32} & \boldsymbol{T_{33}} \end{pmatrix} \tag{A.1}$$

Another example of a second-rank tensor is the stress tensor, shown in Eq. A.2. The tensors presented here are Cartesian tensors, this means they are defined by a set of rectangular axes which are labeled the 1, 2 and 3 axes. The Cauchy stress tensor is used in this dissertation and it has symmetric properties, as shown in Eq. A.3, which can be derived through the equations of motion. Symmetry of second-order tensors means that it contains 6 independent components. To denote it is symmetric, its indices can be interchanged, $\sigma_{ij} = \sigma_{ji}$. Moreover, it can be written as a 6x1 vector as shown in Eq. A.4, this tensorial notation is known as the Voigt notation and it is used throughout this dissertation. The infinitesimal strain tensor, ε_{ij}, is also used throughout this work; moreover, the strain tensor follows similar convention, with the symmetry condition, $\varepsilon_{ij} = \varepsilon_{ji}$, still valid. Noteworthy to mention, there are many definitions of the strain tensor; however, for infinitesimal theory, such tensors are indistinguishable. The strain tensor can be written as shown in Eq. A.5, with γ_{12} or $2\varepsilon_{12}$ denoting the engineering shear strain, these are equivalent.

$$\sigma_{\mathrm{ij}} = \begin{pmatrix} \sigma_{11} & \sigma_{12} & \sigma_{13} \\ \sigma_{21} & \sigma_{22} & \sigma_{23} \\ \sigma_{31} & \sigma_{32} & \sigma_{33} \end{pmatrix} \tag{A.2}$$

$$\sigma_{ij} = \begin{pmatrix} \sigma_{11} & \sigma_{12} & \sigma_{13} \\ & \sigma_{22} & \sigma_{23} \\ symm & & \sigma_{33} \end{pmatrix} \tag{A.3}$$

$$\sigma_i = \begin{bmatrix} \sigma_1 \\ \sigma_2 \\ \sigma_3 \\ \sigma_4 \\ \sigma_5 \\ \sigma_6 \end{bmatrix} = \begin{bmatrix} \sigma_1 \\ \sigma_{22} \\ \sigma_{33} \\ \sigma_{23} \\ \sigma_{13} \\ \sigma_{12} \end{bmatrix} \tag{A.4}$$

$$\varepsilon_i = \begin{bmatrix} \varepsilon_1 \\ \varepsilon_2 \\ \varepsilon_3 \\ 2\varepsilon_4 \\ 2\varepsilon_5 \\ 2\varepsilon_6 \end{bmatrix} = \begin{bmatrix} \varepsilon_{11} \\ \varepsilon_{22} \\ \varepsilon_{33} \\ 2\varepsilon_{23} \\ 2\varepsilon_{13} \\ 2\varepsilon_{12} \end{bmatrix} = \begin{bmatrix} \varepsilon_{11} \\ \varepsilon_{22} \\ \varepsilon_{33} \\ \gamma_{23} \\ \gamma_{13} \\ \gamma_{12} \end{bmatrix} \tag{A.5}$$

A generic fourth-order tensor is shown in Eq. A.6. These types of tensors can have major and minor symmetry; for example, major symmetry implies the following $T_{ijkl} = T_{klij}$, where the first two pair of indices and the last two pairs are swapped. For the case of minor symmetry, the individual indices are permuted, $T_{ijkl} = T_{jikl} = T_{ijlk} = T_{jilk}$. Without symmetry, a fourth-order tensor indeed contains 81 independent components. On the other hand, minor symmetry curtails the number of independent components to 36, and further drops to 21 with both major and minor symmetry properties. In the latter case, the tensor can be written as a 6x6 matrix as shown in Eq. A.7. The indices are written in Voigt notation, and are related to the forth-order tensor indices by substituting each number to the corresponding fourth-order notation pair (e.g., $1 \rightarrow 11$, $2 \rightarrow 22$, $3 \rightarrow 33$, $4 \rightarrow 23$, $5 \rightarrow 13$, and $6 \rightarrow 12$).

$$T_{ijkl} = \begin{pmatrix} \begin{pmatrix} T_{11} & T_{12} & T_{13} \\ T_{21} & T_{22} & T_{23} \\ T_{31} & T_{32} & T_{33} \end{pmatrix}_{11} & \begin{pmatrix} T_{11} & T_{12} & T_{13} \\ T_{21} & T_{22} & T_{23} \\ T_{31} & T_{32} & T_{33} \end{pmatrix}_{12} & \begin{pmatrix} T_{11} & T_{12} & T_{13} \\ T_{21} & T_{22} & T_{23} \\ T_{31} & T_{32} & T_{33} \end{pmatrix}_{13} \\ \begin{pmatrix} T_{11} & T_{12} & T_{13} \\ T_{21} & T_{22} & T_{23} \\ T_{31} & T_{32} & T_{33} \end{pmatrix}_{21} & \begin{pmatrix} T_{11} & T_{12} & T_{13} \\ T_{21} & T_{22} & T_{23} \\ T_{31} & T_{32} & T_{33} \end{pmatrix}_{22} & \begin{pmatrix} T_{11} & T_{12} & T_{13} \\ T_{21} & T_{22} & T_{23} \\ T_{31} & T_{32} & T_{33} \end{pmatrix}_{23} \\ \begin{pmatrix} T_{11} & T_{12} & T_{13} \\ T_{21} & T_{22} & T_{23} \\ T_{31} & T_{32} & T_{33} \end{pmatrix}_{31} & \begin{pmatrix} T_{11} & T_{12} & T_{13} \\ T_{21} & T_{22} & T_{23} \\ T_{31} & T_{32} & T_{33} \end{pmatrix}_{32} & \begin{pmatrix} T_{11} & T_{12} & T_{13} \\ T_{21} & T_{22} & T_{23} \\ T_{31} & T_{32} & T_{33} \end{pmatrix}_{33} \end{pmatrix} \tag{A.6}$$

$$\mathrm{T}_{pq} = \begin{pmatrix} T_{11} & T_{12} & T_{13} & T_{14} & T_{15} & T_{16} \\ & T_{22} & T_{23} & T_{24} & T_{25} & T_{26} \\ & & T_{33} & T_{35} & T_{35} & T_{36} \\ & & & T_{44} & T_{45} & T_{46} \\ & & & & T_{55} & T_{56} \\ symm & & & & & T_{66} \end{pmatrix} = \begin{pmatrix} T_{1111} & T_{1212} & T_{1313} & T_{1123} & T_{1113} & T_{1112} \\ & T_{2222} & T_{2233} & T_{2223} & T_{2213} & T_{2212} \\ & & T_{3333} & T_{3313} & T_{3313} & T_{3312} \\ & & & T_{2323} & T_{2313} & T_{2312} \\ & & & & T_{1313} & T_{1312} \\ symm & & & & & T_{1212} \end{pmatrix} \quad \text{(A.7)}$$

A.2 Constitutive Relations – Pristine and Damaged Relations

In linear elastic solid mechanics, the stiffness matrix relates stress and strain as shown in Eq. A.8, this is the constitutive relation. The stiffness matrix, C_{ijkl}, is a fourth-order tensor which exhibits major and minor symmetries. An important relation in solid mechanics is that of the strain energy density, shown in Eq. A.9, for a uniaxial case, it can be expressed as $\mathrm{W} = \int_0^{\varepsilon} \sigma d\varepsilon$. The stiffness matrix needs to satisfy positive-definiteness for material stability since the strain-energy density is always positive [142]; consequently, the diagonals of the matrix in addition to all of its eigenvalues must be positive.

$$\sigma_{\mathrm{ij}} = C_{ijkl}\varepsilon_{kl} \quad \text{(A.8)}$$

$$\mathrm{W} = \frac{1}{2} C_{ijkl}\varepsilon_{ij}\varepsilon_{kl} \quad \text{(A.9)}$$

Orthotropic material definition

An elastic or viscoelastic material is recognized as orthotropic if it exhibits three orthogonal planes of symmetry [142]. Due to these planes of symmetry, an orthotropic stiffness matrix will contain 9 independent components and can be written as shown below in Eq. A.10. The compliance matrix exhibits the same symmetry. The compliance matrix can be written in terms of the nine independent elastic constants, assuming the linear elastic case, as shown in Eq. A.11. Since the compliance matrix is the inverse of the stiffness matrix, $S_{ijkl} = C_{ijkl}^{-1}$, the stiffness matrix can be written in terms of the elastic constants with the components defined as shown in Eq. A.12 [142].

$$\mathrm{C_{rs}} = \begin{pmatrix} C_{11} & C_{12} & C_{13} & 0 & 0 & 0 \\ & C_{22} & C_{23} & 0 & 0 & 0 \\ & & C_{33} & 0 & 0 & 0 \\ & & & C_{44} & 0 & 0 \\ & & & & C_{55} & 0 \\ symm & & & & & C_{66} \end{pmatrix} \tag{A.10}$$

$$S_{pq}(E_1, E_2, E_3, \nu_{23}, \nu_{13}, \nu_{12}, G_{23}, G_{13}, G_{12}) = \begin{pmatrix} \frac{1}{E_1} & -\frac{\nu_{12}}{E_1} & -\frac{\nu_{13}}{E_1} & 0 & 0 & 0 \\ & \frac{1}{E_2} & -\frac{\nu_{23}}{E_2} & 0 & 0 & 0 \\ & & \frac{1}{E_3} & 0 & 0 & 0 \\ & & & \frac{1}{G_{23}} & 0 & 0 \\ & & & & \frac{1}{G_{13}} & 0 \\ symm & & & & & \frac{1}{G_{12}} \end{pmatrix} \tag{A.11}$$

$$\begin{gathered} \mathrm{C_{11}} = E_1(1 - \nu_{23}\nu_{32})/\Delta \\ \mathrm{C_{12}} = E_2(\nu_{12} - \nu_{13}\nu_{32})/\Delta \\ \mathrm{C_{13}} = E_3(\nu_{13} - \nu_{12}\nu_{23})/\Delta \\ \mathrm{C_{22}} = E_2(1 - \nu_{13}\nu_{31})/\Delta \\ \mathrm{C_{23}} = E_3(\nu_{23} - \nu_{13}\nu_{21})/\Delta \\ \mathrm{C_{33}} = E_3(1 - \nu_{12}\nu_{21})/\Delta \\ \mathrm{C_{44}} = G_{23} \\ \mathrm{C_{55}} = G_{13} \\ \mathrm{C_{66}} = G_{12} \\ \Delta = 1 - \nu_{12}\nu_{21} - \nu_{23}\nu_{32} - \nu_{13}\nu_{31} - 2\nu_{21}\nu_{13}\nu_{32} \end{gathered} \tag{A.12}$$

In the viscoelastic case, the constitutive relation form is similar, and the stiffness matrix remains similar. The stresses are defined by the Duhamel's integral as shown in Eq. A.13. The viscoelastic stiffness, $C^*_{ijkl}\big(\xi(t) - \xi(s)\big)$, is composed of an equilibrated, C^e_{ijkl}, and un-relaxed portion, $C^V_{ijkl,m}$, shown in Eq. A.14. The comma notation does not signify differentiation as typically interpreted using the summation convention, rather, it is reserved for denoting the m^{th} Prony term. Each stiffness tensor takes the form shown in Eq. A.10; however, the tensors within the summation, have the exponential multiplied to each component. Indeed, this assumes each component is affected by the relaxation time in the same manner. These are the pristine relations, for which damage is not embedded within the elastic or viscoelastic constitutive relation.

$$\sigma_{ij} = \int_0^t C^*_{ijkl}(\xi(t) - \xi(s)) \frac{\partial \varepsilon_{kl}}{\partial s} ds \tag{A.13}$$

$$\bar{C}^*_{ijkl}(\xi(t)) = \bar{C}^e_{ijkl} + \sum_{m=1}^{M} \bar{C}^V_{ijkl,m} e^{-\xi/\tau_m} \tag{A.14}$$

Following the formulations laid out by Barbero [170], the damage tensor, which is a second-order tensor, can be written as shown in Eq. A.15, where δ_{ij} is the well-known Kronecker delta defined in Eq. A.16. The second-order damage tensor is also symmetry and it is commonly assumed to coincide with the material coordinate axes. The values of d_i are the Eigenvalues of D_{ij}. An integrity tensor can be defined from the second-order tensor, using the relation shown in Eq. A.17. The damage effect tensor, which is defined as a fourth-order tensor, can be formulated with the integrity tensor as shown in Eq. A.18. The damage effect tensor in this form coincides with the material coordinate system. In terms of the damage variable, the damage effect tensor can be re-written as shown in Eq. A.19. The form shown in Eq. A.18, can be re-written as $P_{ijkl} = \Omega_i \Omega_j I_{ijkl}$ with no sum on i or j, and $I_{ijkl} = \frac{1}{2}(\delta_{ik}\delta_{jl} + \delta_{il}\delta_{jk})$. Following this

$$\mathbf{D} = \mathrm{D_{ij}} = D_i \delta_{ij} = \begin{pmatrix} d_1 & 0 & 0 \\ 0 & d_2 & 0 \\ 0 & 0 & d_3 \end{pmatrix}, \qquad (no \text{ sum on i}) \tag{A.15}$$

$$\delta_{\mathrm{ij}} = \begin{pmatrix} 1 & 0 & 0 \\ 0 & 1 & 0 \\ 0 & 0 & 1 \end{pmatrix} \tag{A.16}$$

$$\Omega_{\mathrm{ij}} = \sqrt{1 - d_i}\delta_{ij} = \begin{pmatrix} \Omega_1 & 0 & 0 \\ 0 & \Omega_2 & 0 \\ 0 & 0 & \Omega_3 \end{pmatrix}, \qquad (\text{no sum on i}) \tag{A.17}$$

$$\mathrm{P_{ijkl}} = \frac{1}{2}(\Omega_{ik}\Omega_{jl} + \Omega_{il}\Omega_{jk}) = \begin{pmatrix} \Omega_1^2 & 0 & 0 & 0 & 0 & 0 \\ 0 & \Omega_2^2 & 0 & 0 & 0 & 0 \\ 0 & 0 & \Omega_3^2 & 0 & 0 & 0 \\ 0 & 0 & 0 & \Omega_2\Omega_3 & 0 & 0 \\ 0 & 0 & 0 & 0 & \Omega_1\Omega_3 & 0 \\ 0 & 0 & 0 & 0 & 0 & \Omega_1\Omega_2 \end{pmatrix} \tag{A.18}$$

$$\mathrm{P_{ijkl}} = \begin{pmatrix} 1-d_1 & 0 & 0 & 0 & 0 & 0 \\ 0 & 1-d_2 & 0 & 0 & 0 & 0 \\ 0 & 0 & 1-d_3 & 0 & 0 & 0 \\ 0 & 0 & 0 & \sqrt{1-d_2}\sqrt{1-d_3} & 0 & 0 \\ 0 & 0 & 0 & 0 & \sqrt{1-d_1}\sqrt{1-d_3} & 0 \\ 0 & 0 & 0 & 0 & 0 & \sqrt{1-d_1}\sqrt{1-d_2} \end{pmatrix} \tag{A.19}$$

A general form of the damage tensor can be used for added flexibility in modeling shear degradation modes alongside the normal degradation modes. The second-order damage tensor then takes on the form shown in Eq. A.20. When the integrity tensor definition is used, it can be defined as shown in Eq. A.21. Through a similar procedure as shown above, the general form of the damage effect tensor can be defined as shown in Eq. A.22.

$$\mathrm{D_{ij}} = \begin{pmatrix} D_{11} & D_{12} & D_{13} \\ & D_{22} & D_{23} \\ symm & & D_{33} \end{pmatrix} = \begin{pmatrix} D_1 & D_6 & D_5 \\ & D_2 & D_4 \\ symm & & D_3 \end{pmatrix} \tag{A.20}$$

$$\Omega_{\mathrm{ij}} = \sqrt{1-D_{ij}} = \begin{pmatrix} \sqrt{1-D_1} & \sqrt{1-D_6} & \sqrt{1-D_5} \\ & \sqrt{1-D_2} & \sqrt{1-D_4} \\ symm & & \sqrt{1-D_3} \end{pmatrix} \tag{A.21}$$

$$\mathrm{P_{ijkl}} = \Omega_{\mathrm{ij}}\Omega_{kl}I_{ijkl} = \begin{pmatrix} 1-D_1 & 0 & 0 & 0 & 0 & 0 \\ 0 & 1-D_2 & 0 & 0 & 0 & 0 \\ 0 & 0 & 1-D_3 & 0 & 0 & 0 \\ 0 & 0 & 0 & 1-D_4 & 0 & 0 \\ 0 & 0 & 0 & 0 & 1-D_5 & 0 \\ 0 & 0 & 0 & 0 & 0 & 1-D_6 \end{pmatrix} \tag{A.22}$$

From the energy equivalence principle, the damaged stiffness matrix taken the form shown in Eq. A.23. Each stiffness tensor is contracted by the same general damage effect tensor shown above; therefore, damage affects the viscoelastic modes (i.e., equilibrated and un-relaxed) in the same manner. For instance, the equilibrated damaged stiffness part takes the form shown in Eq. A.24.

$$C^*_{ijkl}(\xi(t)) = P_{ijab}C^e_{abcd}P_{cdkl} + \sum_{m=1}^{M} P_{ijab}C^V_{abcd,m}P_{cdkl}e^{-\xi/\tau_m} \tag{A.23}$$

$$P_{ijab}C^{e}_{abcd}P_{cdkl} =$$

$$\begin{pmatrix} (1-D_1)^2C^e_{11} & (1-D_1)(1-D_2)C^e_{12} & (1-D_1)(1-D_3)C^e_{13} & 0 & 0 & 0 \\ & (1-D_2)^2C^e_{22} & (1-D_2)(1-D_3)C^e_{23} & 0 & 0 & 0 \\ & & (1-D_3)^2C^e_{33} & 0 & 0 & 0 \\ & & & (1-D_4)^2C^e_{44} & 0 & 0 \\ & & & & (1-D_5)^2C^e_{55} & 0 \\ symm & & & & & (1-D_6)^2C^e_{66} \end{pmatrix} \tag{A.24}$$

A3. Damage Formulations

Thermodynamic force conjugated to damage

The thermodynamic force that drive damage is defined below as shown in Eq. A.25, the strains used in the definition are the elastic strains. Elastic strains are obtained by subtracting any thermal strains from the total strains, it also does not include plastic strains. The components of the thermodynamic forces conjugated to damage are defined in Eq. A.26. Solving for the damage multiplier (i.e., Lagrange multiplier) requires differentiation of the thermodynamic force tensor with respect to damage or strain. The differentiation with respect to damage is shown in Eq. A.27 – A.33. For the differentiation with respect to strain, see Eqns. A.34 – A.40.

$$\mathrm{Y_{ij}} = \frac{\partial \psi}{\partial D_{ij}} = -\frac{1}{2}\varepsilon_{ij}\frac{\partial C^{*}_{ijkl}\left(\xi(t)\right)}{\partial D_{mn}}\varepsilon_{kl} = \begin{pmatrix} Y_{11} & Y_{12} & Y_{13} \\ & Y_{22} & Y_{23} \\ symm & & Y_{33} \end{pmatrix} \tag{A.25}$$

$$\begin{aligned} Y_{11} &= (1-D_1)\left[\bar{C}^e_{11} + \sum_{m=1}^{M}\bar{C}^V_{11,m}e^{-\frac{\xi}{\tau_m}}\right]\varepsilon_{11}^2 + (1-D_2)\left[\bar{C}^e_{12} + \sum_{m=1}^{M}\bar{C}^V_{12,m}e^{-\frac{\xi}{\tau_m}}\right]\varepsilon_{11}\varepsilon_{22} \\ &\quad + (1-D_3)\left[\bar{C}^e_{13} + \sum_{m=1}^{M}\bar{C}^V_{13,m}e^{-\frac{\xi}{\tau_m}}\right]\varepsilon_{11}\varepsilon_{33} \\ Y_{22} &= (1-D_1)\left[\bar{C}^e_{12} + \sum_{m=1}^{M}\bar{C}^V_{12,m}e^{-\frac{\xi}{\tau_m}}\right]\varepsilon_{11}\varepsilon_{22} + (1-D_2)\left[\bar{C}^e_{22} + \sum_{m=1}^{M}\bar{C}^V_{22,m}e^{-\frac{\xi}{\tau_m}}\right]\varepsilon_{22}^2 \\ &\quad + (1-D_3)\left[\bar{C}^e_{23} + \sum_{m=1}^{M}\bar{C}^V_{23,m}e^{-\frac{\xi}{\tau_m}}\right]\varepsilon_{22}\varepsilon_{33} \\ Y_{33} &= (1-D_1)\left[\bar{C}^e_{13} + \sum_{m=1}^{M}\bar{C}^V_{13,m}e^{-\frac{\xi}{\tau_m}}\right]\varepsilon_{11}\varepsilon_{33} + (1-D_2)\left[\bar{C}^e_{23} + \sum_{m=1}^{M}\bar{C}^V_{23,m}e^{-\frac{\xi}{\tau_m}}\right]\varepsilon_{22}\varepsilon_{33} \\ &\quad + (1-D_3)\left[\bar{C}^e_{33} + \sum_{m=1}^{M}\bar{C}^V_{33,m}e^{-\frac{\xi}{\tau_m}}\right]\varepsilon_{33}^2 \\ Y_{23} &= 4(1-D_4)\left[\bar{C}^e_{44} + \sum_{m=1}^{M}\bar{C}^V_{44,m}e^{-\frac{\xi}{\tau_m}}\right]\varepsilon_{23}^2 \end{aligned} \tag{A.26}$$

$$Y_{13} = 4(1-D_5)\left[\bar{C}^e_{55} + \sum_{m=1}^{M} \bar{C}^V_{55,m} e^{-\frac{\xi}{\tau_m}}\right]\varepsilon^2_{13}$$

$$Y_{12} = 4(1-D_6)\left[\bar{C}^e_{66} + \sum_{m=1}^{M} \bar{C}^V_{66,m} e^{-\frac{\xi}{\tau_m}}\right]\varepsilon^2_{12}$$

$$\frac{\partial Y_{pq}}{\partial D_{rs}} = \begin{pmatrix} T_{11rs} & T_{12rs} & T_{13rs} \\ & T_{22rs} & T_{23rs} \\ symm & & T_{33rs} \end{pmatrix} \tag{A.27}$$

$$\mathrm{T}_{11\mathrm{rs}} = \begin{pmatrix} -\left[\bar{C}^e_{11} + \sum_{m=1}^{M} \bar{C}^V_{11,m} e^{-\frac{\xi}{\tau_m}}\right]\varepsilon^2_{11} & 0 & 0 \\ 0 & -\left[\bar{C}^e_{12} + \sum_{m=1}^{M} \bar{C}^V_{12,m} e^{-\frac{\xi}{\tau_m}}\right]\varepsilon_{11}\varepsilon_{22} & 0 \\ 0 & 0 & -\left[\bar{C}^e_{13} + \sum_{m=1}^{M} \bar{C}^V_{13,m} e^{-\frac{\xi}{\tau_m}}\right]\varepsilon_{11}\varepsilon_{33} \end{pmatrix}$$

(A.28)

$$\mathrm{T}_{22\mathrm{rs}} = \begin{pmatrix} -\left[\bar{C}^e_{12} + \sum_{m=1}^{M} \bar{C}^V_{12,m} e^{-\frac{\xi}{\tau_m}}\right]\varepsilon_{11}\varepsilon_{22} & 0 & 0 \\ 0 & -\left[\bar{C}^e_{22} + \sum_{m=1}^{M} \bar{C}^V_{22,m} e^{-\frac{\xi}{\tau_m}}\right]\varepsilon^2_{22} & 0 \\ 0 & 0 & -\left[\bar{C}^e_{23} + \sum_{m=1}^{M} \bar{C}^V_{23,m} e^{-\frac{\xi}{\tau_m}}\right]\varepsilon_{22}\varepsilon_{33} \end{pmatrix}$$

(A.29)

$$\mathrm{T}_{33\mathrm{rs}} = \begin{pmatrix} -\left[\bar{C}^e_{13} + \sum_{m=1}^{M} \bar{C}^V_{13,m} e^{-\frac{\xi}{\tau_m}}\right]\varepsilon_{11}\varepsilon_{33} & 0 & 0 \\ 0 & -\left[\bar{C}^e_{23} + \sum_{m=1}^{M} \bar{C}^V_{23,m} e^{-\frac{\xi}{\tau_m}}\right]\varepsilon_{22}\varepsilon_{33} & 0 \\ 0 & 0 & -\left[\bar{C}^e_{33} + \sum_{m=1}^{M} \bar{C}^V_{33,m} e^{-\frac{\xi}{\tau_m}}\right]\varepsilon^2_{33} \end{pmatrix}$$

(A.30)

$$\mathrm{T}_{23\mathrm{rs}} = \begin{pmatrix} 0 & 0 & 0 \\ 0 & 0 & -4\left[\bar{C}^{e}_{23} + \sum_{m=1}^{M} \bar{C}^{V}_{23,m} e^{-\frac{\xi}{\tau_m}}\right]\varepsilon^{2}_{23} \\ 0 & -4\left[\bar{C}^{e}_{23} + \sum_{m=1}^{M} \bar{C}^{V}_{23,m} e^{-\frac{\xi}{\tau_m}}\right]\varepsilon^{2}_{23} & 0 \end{pmatrix} \tag{A.31}$$

$$\mathrm{T}_{13\mathrm{rs}} = \begin{pmatrix} 0 & 0 & -4\left[\bar{C}^{e}_{13} + \sum_{m=1}^{M} \bar{C}^{V}_{13,m} e^{-\frac{\xi}{\tau_m}}\right]\varepsilon^{2}_{13} \\ 0 & 0 & 0 \\ -4\left[\bar{C}^{e}_{13} + \sum_{m=1}^{M} \bar{C}^{V}_{13,m} e^{-\frac{\xi}{\tau_m}}\right]\varepsilon^{2}_{13} & 0 & 0 \end{pmatrix} \tag{A.32}$$

$$\mathrm{T}_{12\mathrm{rs}} = \begin{pmatrix} 0 & -4\left[\bar{C}^{e}_{12} + \sum_{m=1}^{M} \bar{C}^{V}_{12,m} e^{-\frac{\xi}{\tau_m}}\right]\varepsilon^{2}_{12} & 0 \\ -4\left[\bar{C}^{e}_{12} + \sum_{m=1}^{M} \bar{C}^{V}_{12,m} e^{-\frac{\xi}{\tau_m}}\right]\varepsilon^{2}_{12} & 0 & 0 \\ 0 & 0 & 0 \end{pmatrix} \tag{A.33}$$

$$\frac{\partial Y_{mn}}{\partial \varepsilon_{pq}} = \begin{pmatrix} W_{11pq} & W_{12pq} & W_{13pq} \\ & W_{22pq} & W_{23pq} \\ symm & & W_{33pq} \end{pmatrix} \tag{A.34}$$

$$\mathrm{W}_{11\mathrm{rs}} = \begin{pmatrix} 2(1-D_1)\bar{C}^{*}_{11}\varepsilon_{11} + (1-D_2)\bar{C}^{*}_{12}\varepsilon_{22} + (1-D_3)\bar{C}^{*}_{13}\varepsilon_{33} & 0 & 0 \\ 0 & (1-D_2)\bar{C}^{*}_{12}\varepsilon_{11} & 0 \\ 0 & 0 & (1-D_3)\bar{C}^{*}_{13}\varepsilon_{11} \end{pmatrix} \tag{A.35}$$

$$\mathrm{W}_{22\mathrm{rs}} = \begin{pmatrix} (1-1)\bar{C}^{*}_{12}\varepsilon_{22} & 0 & 0 \\ 0 & (1-D_1)\bar{C}^{*}_{12}\varepsilon_{11} + 2(1-D_2)\bar{C}^{*}_{22}\varepsilon_{22} + (1-D_3)\bar{C}^{*}_{23}\varepsilon_{33} & 0 \\ 0 & 0 & (1-D_3)\bar{C}^{*}_{23}\varepsilon_{22} \end{pmatrix} \tag{A.36}$$

$$\mathrm{W}_{33\mathrm{rs}} = \begin{pmatrix} (1-D_1)\bar{C}^{*}_{13}\varepsilon_{33} & 0 & 0 \\ 0 & (1-D_2)\bar{C}^{*}_{23}\varepsilon_{33} & 0 \\ 0 & 0 & (1-D_1)\bar{C}^{*}_{13}\varepsilon_{11} + (1-D_2)\bar{C}^{*}_{23}\varepsilon_{22} + 2(1-D_3)\bar{C}^{*}_{33}\varepsilon_{33} \end{pmatrix} \tag{A.37}$$

$$\mathrm{W}_{23\mathrm{rs}} = \begin{pmatrix} 0 & 0 & 0 \\ 0 & 0 & 8(1-D_4)\bar{C}^*_{44}\varepsilon_{23}) \\ 0 & 8(1-D_4)\bar{C}^*_{44}\varepsilon_{23} & 0 \end{pmatrix} \tag{A.38}$$

$$\mathrm{W}_{13\mathrm{rs}} = \begin{pmatrix} 0 & 0 & 8(1-D_5)\bar{C}^*_{55}\varepsilon_{13} \\ 0 & 0 & 0 \\ 8(1-D_5)\bar{C}^*_{55}\varepsilon_{13} & 0 & 0 \end{pmatrix} \tag{A.39}$$

$$\mathrm{W}_{12\mathrm{rs}} = \begin{pmatrix} 0 & 8(1-D_6)\bar{C}^*_{66}\varepsilon_{12} & 0 \\ 8(1-D_6)\bar{C}^*_{66}\varepsilon_{12} & 0 & 0 \\ 0 & 0 & 0 \end{pmatrix} \tag{A.40}$$

Damage surface

The damage surface is defined using the relation below in Eq. A.41. The J-tensor is assumed non-interacting, this means it has only diagonal components as shown in Eq. A.42, it is also symmetric and can be reduced to a 6x6 matrix, similar to the stiffness tensor. The thermodynamic force tensors can be written as a 6x1 matrix, similar to the stress or strain tensors. The differentiated damage surface with respect to the thermodynamic forces is given in Eq. A. 44. The numerator of L_d is given in Eq. A.45.

$$\mathrm{g}\left(\mathrm{Y}_{\mathrm{ij}}, J_{ijkl}\right) = \sqrt{\frac{1}{2} Y_{ij} J_{ijkl} Y_{kl}} = \sqrt{\frac{1}{2} Y_m J_{mn} Y_n} \tag{A.41}$$

$$J_{mn} = \mathrm{J}_{\mathrm{ijkl}} = \begin{pmatrix} J_{11} & 0 & 0 & 0 & 0 & 0 \\ 0 & J_{22} & 0 & 0 & 0 & 0 \\ 0 & 0 & J_{33} & 0 & 0 & 0 \\ 0 & 0 & 0 & J_{44} & 0 & 0 \\ 0 & 0 & 0 & 0 & J_{55} & 0 \\ 0 & 0 & 0 & 0 & 0 & J_{66} \end{pmatrix} \tag{A.42}$$

$$g = \frac{\sqrt{\mathrm{Y}_{11}^2 \mathrm{J}_{11} + 4\mathrm{X}_{12}^2 \mathrm{J}_{66} + 4\mathrm{X}_{13}^2 \mathrm{J}_{55} + \mathrm{X}_{22}^2 \mathrm{J}_{22} + 4\mathrm{X}_{23}^2 \mathrm{J}_{44} + \mathrm{X}_{33}^2 \mathrm{J}_{33}}}{\sqrt{2}} \tag{A.43}$$

$$\frac{\partial g}{\partial Y_{ij}} = \begin{pmatrix} \frac{J_{11}Y_{11}}{\Delta_1} & \frac{2\sqrt{2}J_{66}Y_{12}}{\Delta_2} & \frac{2\sqrt{2}J_{55}Y_{13}}{\Delta_2} \\ \frac{2\sqrt{2}J_{66}Y_{12}}{\Delta_2} & \frac{J_{22}Y_{22}}{\Delta_1} & \frac{2\sqrt{2}J_{44}Y_{23}}{\Delta_2} \\ \frac{2\sqrt{2}J_{55}Y_{13}}{\Delta_2} & \frac{2\sqrt{2}J_{44}Y_{23}}{\Delta_2} & \frac{J_{33}Y_{33}}{\Delta_1} \end{pmatrix} \tag{A.44}$$

Where

$$\Delta_1 = \sqrt{2}\sqrt{J_{11}Y_{11}^2 + 4J_{66}Y_{12}^2 + 4J_{55}Y_{13}^2 + J_{22}Y_{22}^2 + 4J_{44}Y_{23}^2 + J_{33}Y_{33}^2}$$

And

$$\Delta_2 = \sqrt{J_{11}Y_{11}^2 + 4J_{66}Y_{12}^2 + 4J_{55}Y_{13}^2 + J_{22}Y_{22}^2 + 4J_{44}Y_{23}^2 + J_{33}Y_{33}^2}$$

$$\frac{\partial g}{\partial Y_{ij}}\frac{\partial Y_{ij}}{\partial \varepsilon_{kl}} = \begin{pmatrix} Q_{11} & Q_{12} & Q_{13} \\ & Q_{22} & Q_{23} \\ symm & & Q_{33} \end{pmatrix} \tag{A.45}$$

with

$$Q_{11} = \frac{J_{11}Y_{11}(-2(\mathrm{D}_1 - 1)\bar{\mathrm{C}}_{11}^*\varepsilon_{11} - (\mathrm{D}_2 - 1)\bar{\mathrm{C}}_{12}^*\varepsilon_{22} - (\mathrm{D}_3 - 1)\bar{\mathrm{C}}_{13}^*\varepsilon_{33}) - (\mathrm{D}_1 - 1)(\bar{\mathrm{C}}_{12}^*J_{22}Y_{22}\varepsilon_{22} + \bar{\mathrm{C}}_{13}^*J_{33}Y_{33}\varepsilon_{33})}{\Delta_1}$$

$$Q_{22} = \frac{-(\mathrm{D}_2 - 1)\bar{\mathrm{C}}_{12}^*J_{11}Y_{11}\varepsilon_{11} - (\mathrm{D}_2 - 1)\bar{\mathrm{C}}_{23}^*J_{33}Y_{33}\varepsilon_{33} + J_{22}Y_{22}(-(\mathrm{D}_1 - 1)\bar{\mathrm{C}}_{12}^*\varepsilon_{11} - 2(\mathrm{D}_2 - 1)\bar{\mathrm{C}}_{22}^*\varepsilon_{22} - (\mathrm{D}_3 - 1)\bar{\mathrm{C}}_{23}^*\varepsilon_{33})}{\Delta_1}$$

$$Q_{33} = \frac{-(\mathrm{D}_3 - 1)\bar{\mathrm{C}}_{13}^*J_{11}Y_{11}\varepsilon_{11} - (\mathrm{D}_3 - 1)\bar{\mathrm{C}}_{23}^*J_{22}Y_{22}\varepsilon_{22} + J_{33}Y_{33}(-(\mathrm{D}_1 - 1)\bar{\mathrm{C}}_{13}^*\varepsilon_{11} - (\mathrm{D}_2 - 1)\bar{\mathrm{C}}_{23}^*\varepsilon_{22} - 2(\mathrm{D}_3 - 1)\bar{\mathrm{C}}_{33}^*\varepsilon_{33})}{\Delta_1}$$

$$Q_{23} = -\frac{32\sqrt{2}(\mathrm{D}_4 - 1)\bar{\mathrm{C}}_{44}^*J_{44}Y_{23}\varepsilon_{23}}{\Delta_2}$$

$$Q_{13} = -\frac{32\sqrt{2}(\mathrm{D}_5 - 1)\bar{\mathrm{C}}_{55}^*J_{55}Y_{13}\varepsilon_{13}}{\Delta_2}$$

$$Q_{12} = -\frac{32\sqrt{2}(\mathrm{D}_6 - 1)\bar{\mathrm{C}}_{66}^*J_{66}Y_{12}\varepsilon_{12}}{\Delta_2}$$

A.4 Location of UMAT and MATLAB codes

The codes are made available on the GitHub page below:

https://github.com/mramirez975/viscoelasticDamage

APPENDIX B. SUPPLEMENTARY EXPERIMENTAL DATA

B.1 SEM Fracture Images

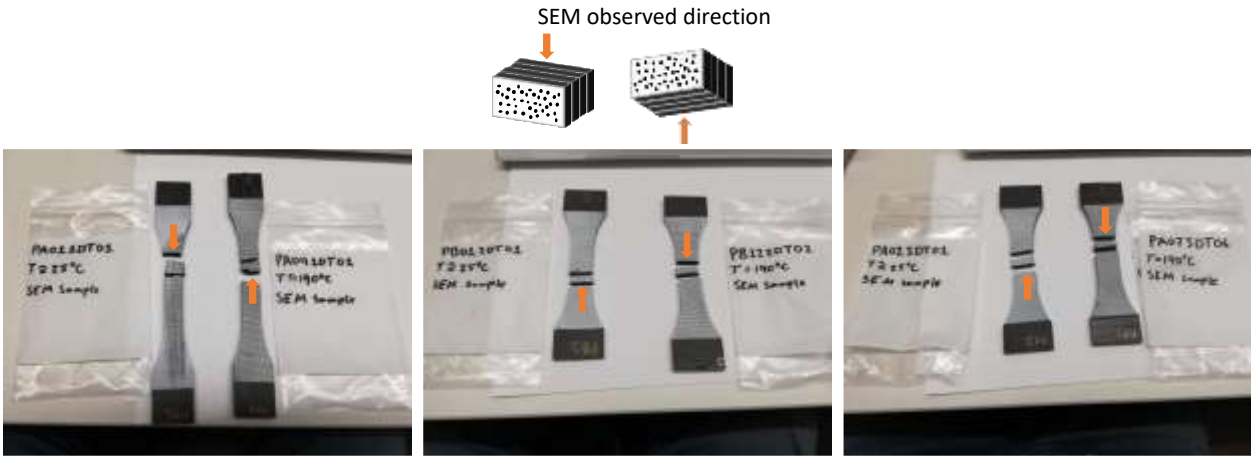

Fig B.1 Illustration of selected surface for investigation under SEM

1D_25

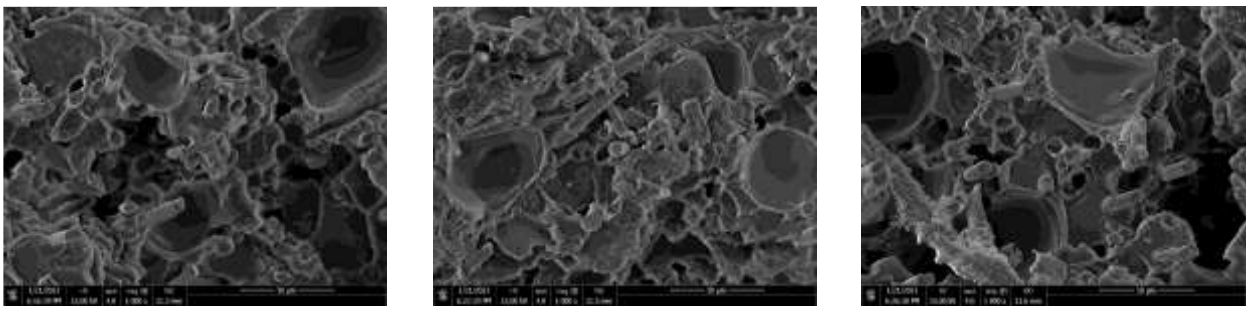

RS1 RS2 RS3

Fig B.2 SEM images from print direction fractured surface at room temperature, at three different locations, 1000x

1D_25

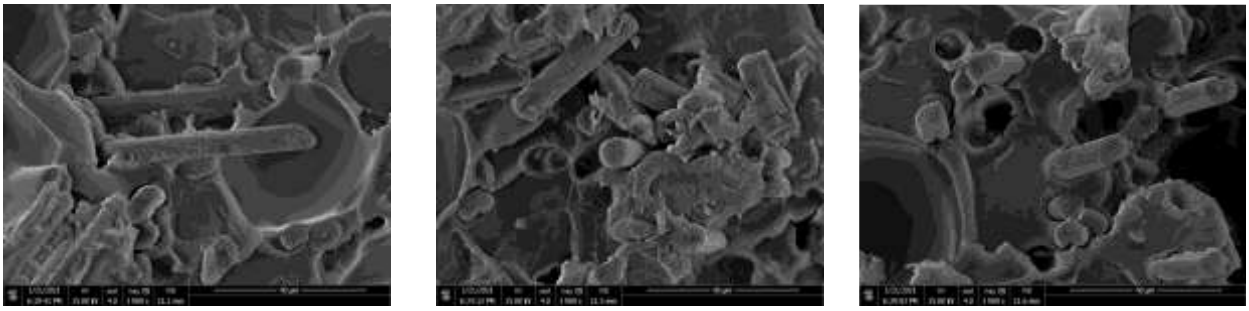

RS1 RS2 RS3

Fig B.3 SEM images from print direction fractured surface at room temperature, at three different locations, 2000x

1D_25

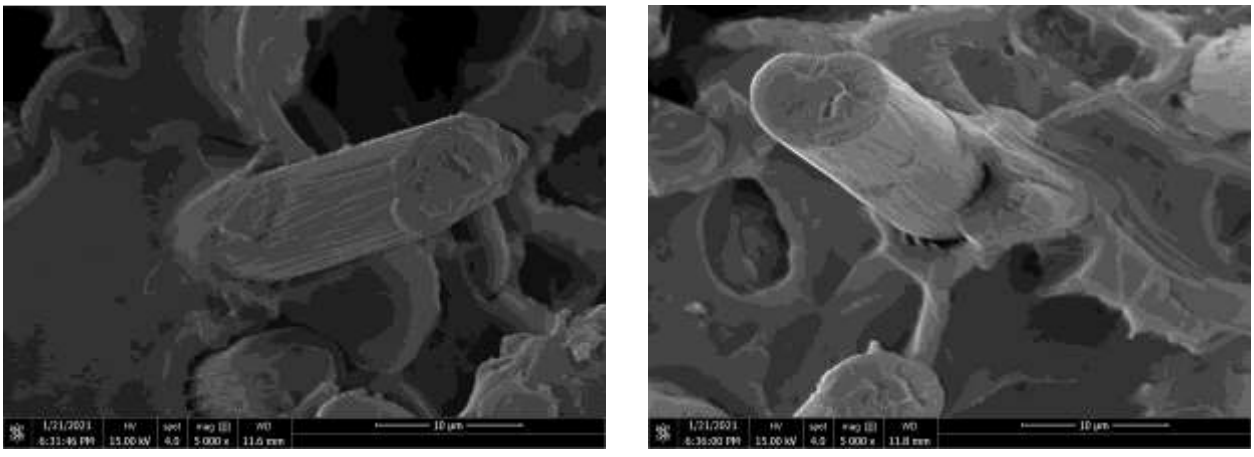

RS3 RS1

Fig B.4 SEM images from print direction fractured surface at room temperature, at selected locations, 5000x

1D_25

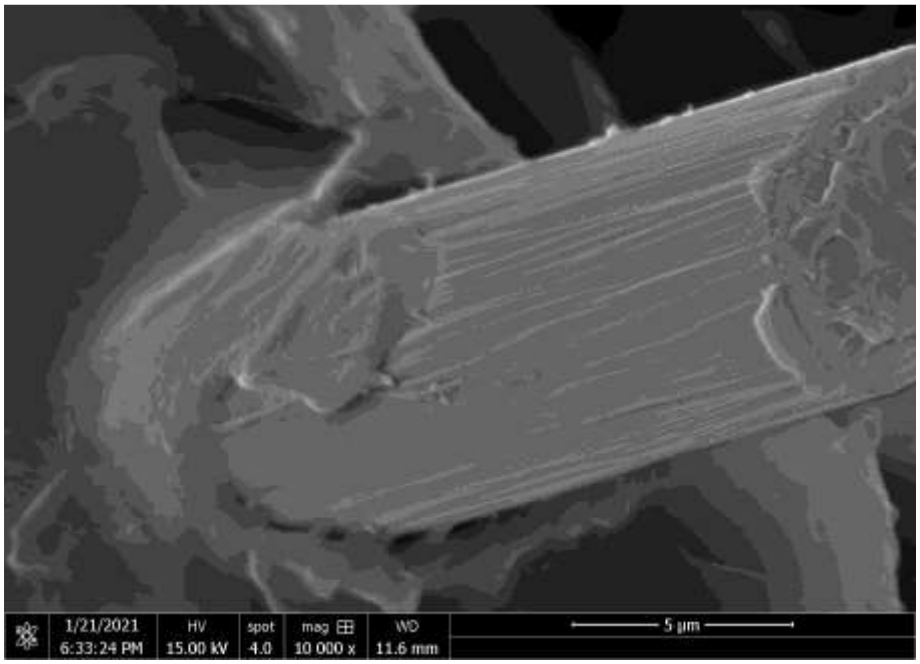

RS3

Fig B.5 SEM image from print direction fractured surface at room temperature, fiber-matrix bond, 10000x

1D_190

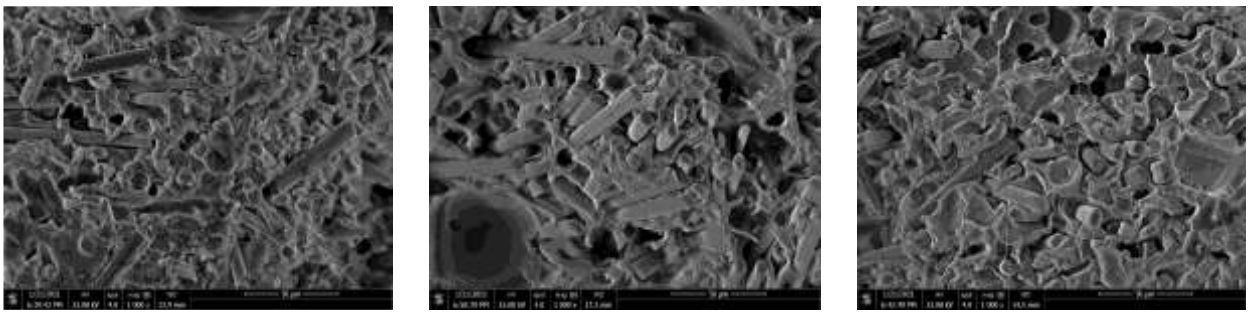

RS1 RS2 RS3

Fig B.6 SEM images from print direction fractured surface at 190°C, at three different locations, 1000x

1D_190

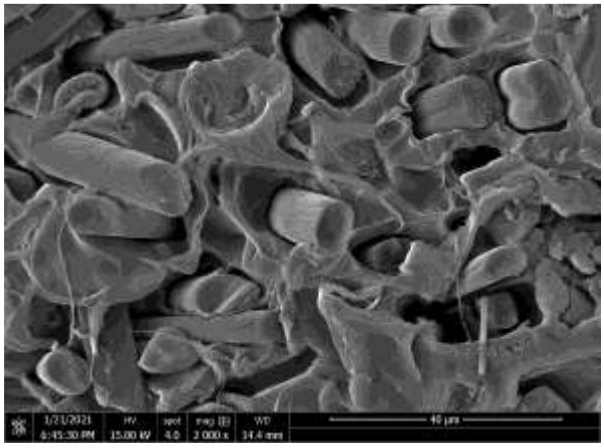

RS3

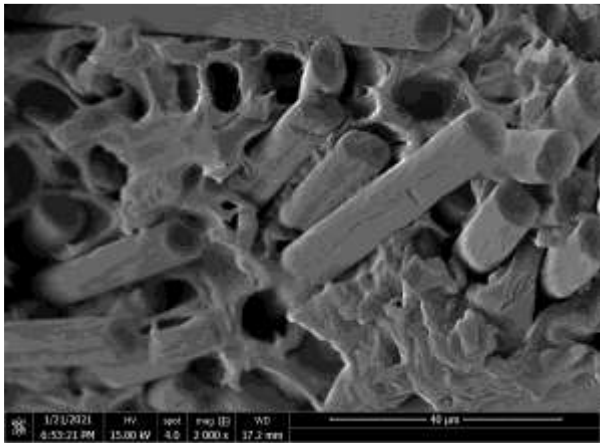

RS1

Fig B.7 SEM images from print direction fractured surface at 190°C, at selected locations, 2000x

1D_190

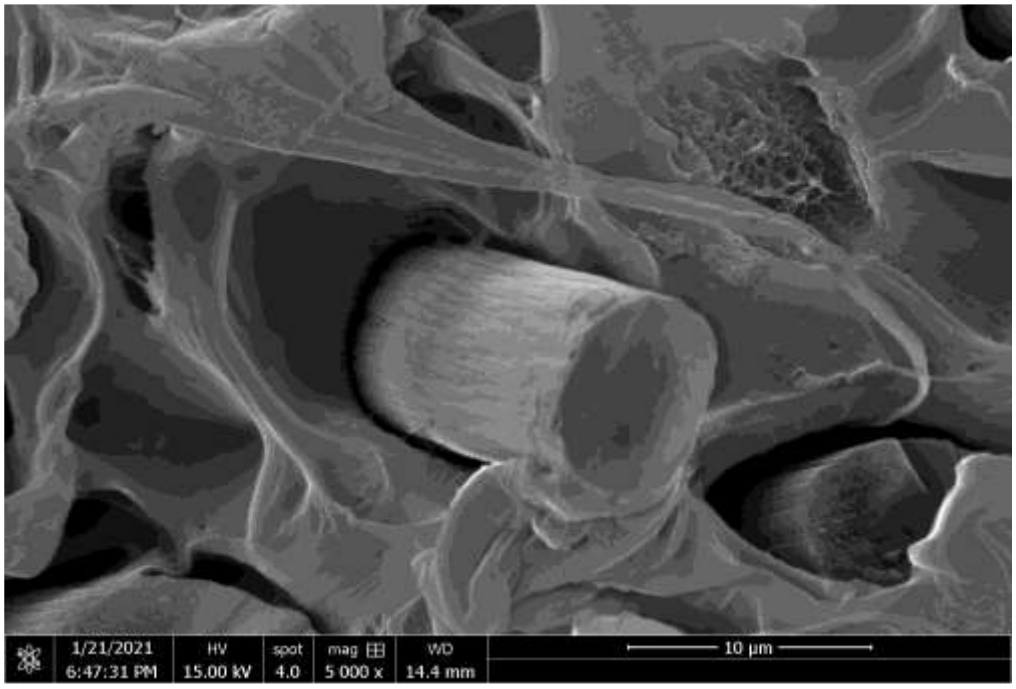

Fig B.8 SEM image from print direction fractured surface at 190°C, fiber-matrix bond, 5000x

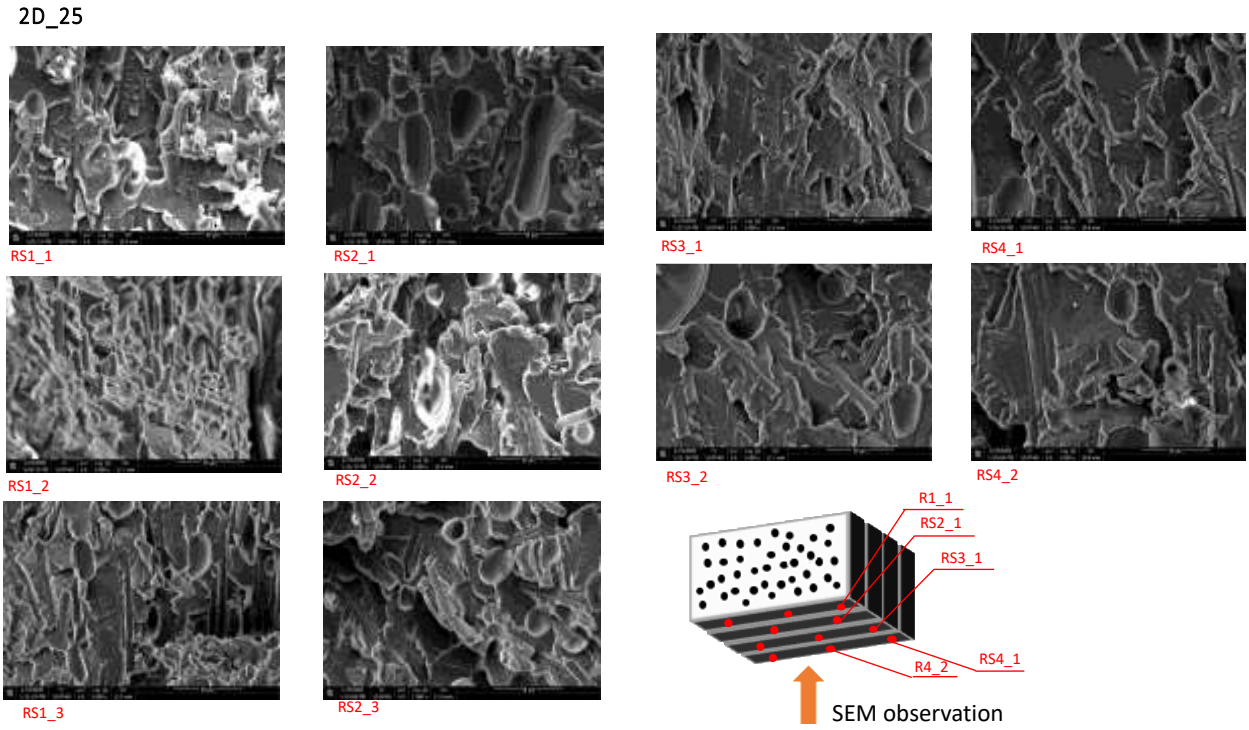

Fig B.9 SEM images from 2 direction fractured surface at room temperature, at several points illustrated in the schematic on the lower-right side, 1000x

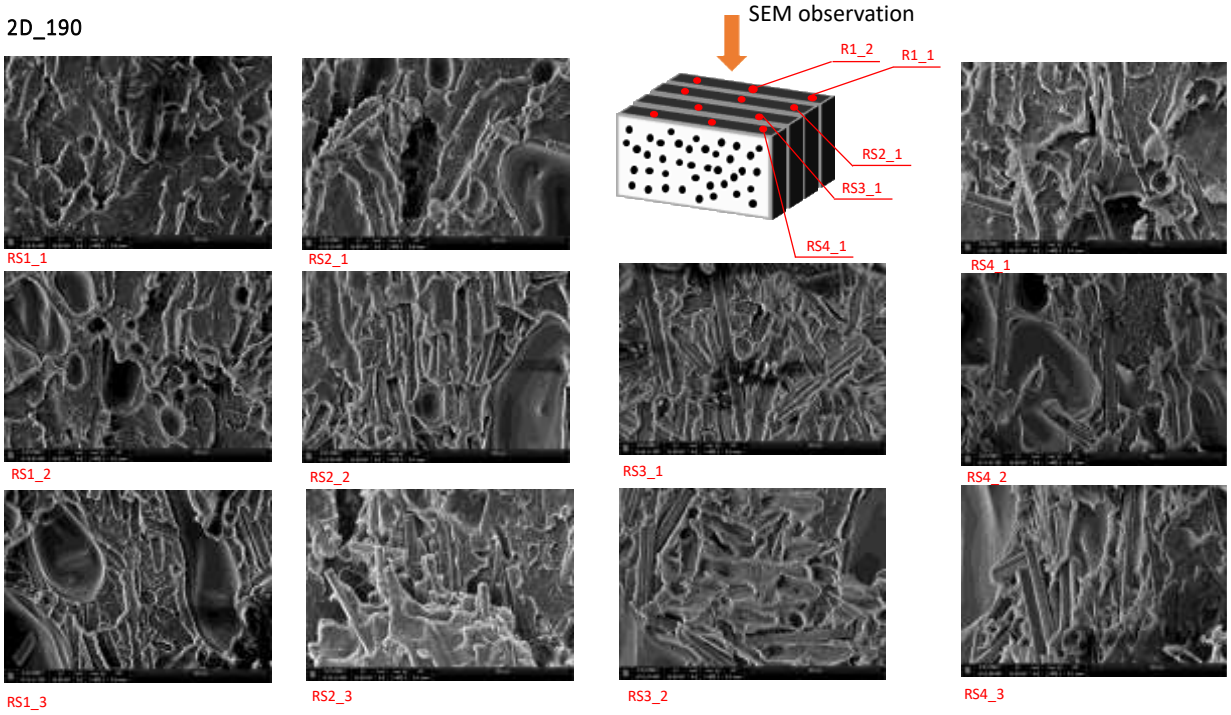

Fig B.10 SEM images from 2 direction fractured surface at 190°C, at several points illustrated in the schematic at the upper-middle region, 1000x

2D_190

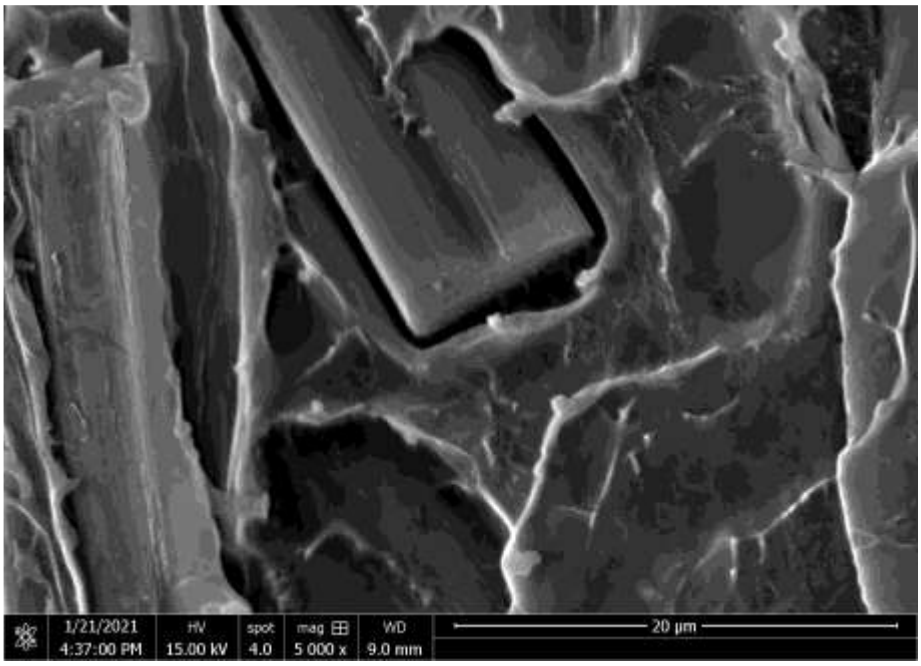

RS1

Fig B.11 SEM image from 2 direction fractured surface at 190°C, fiber-matrix detach, 5000x

3D_25

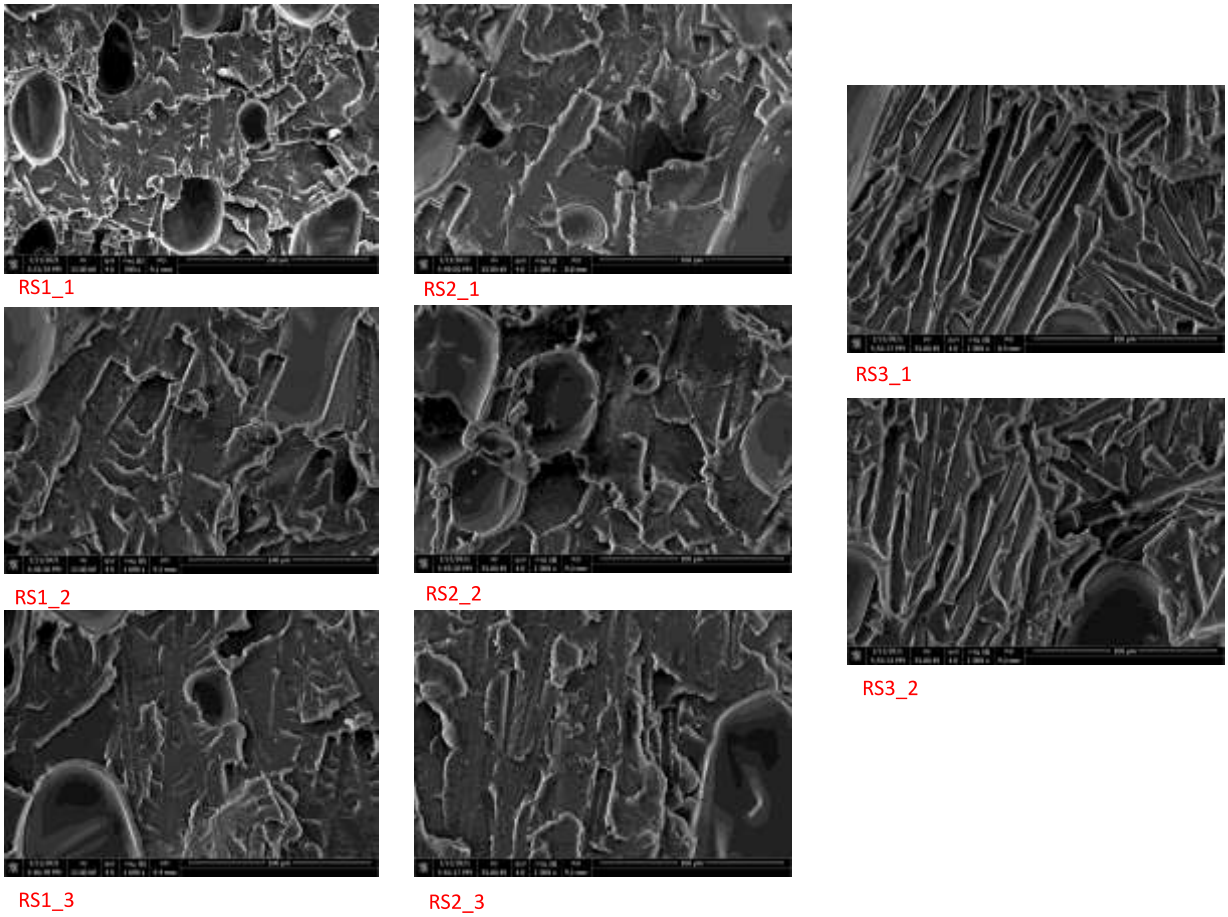

Fig B.12 SEM images from 3 direction fractured surface at room temperature, at several points, 1000x

3D_190

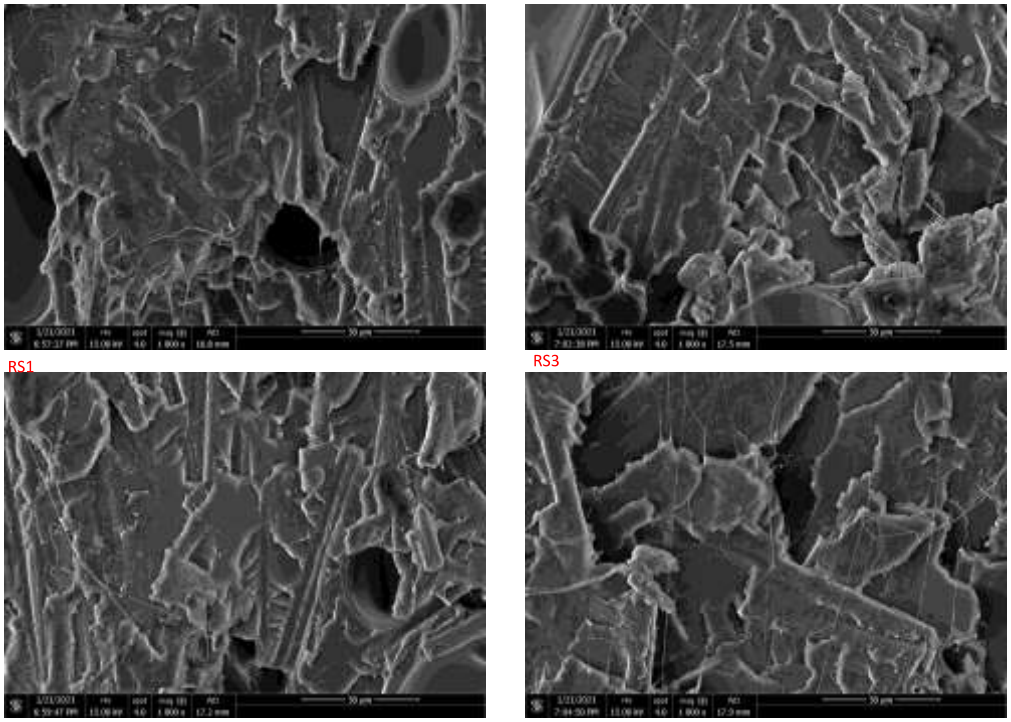

Fig B.13 SEM images from 3 direction fractured surface at 190°C, at several points, 1000x

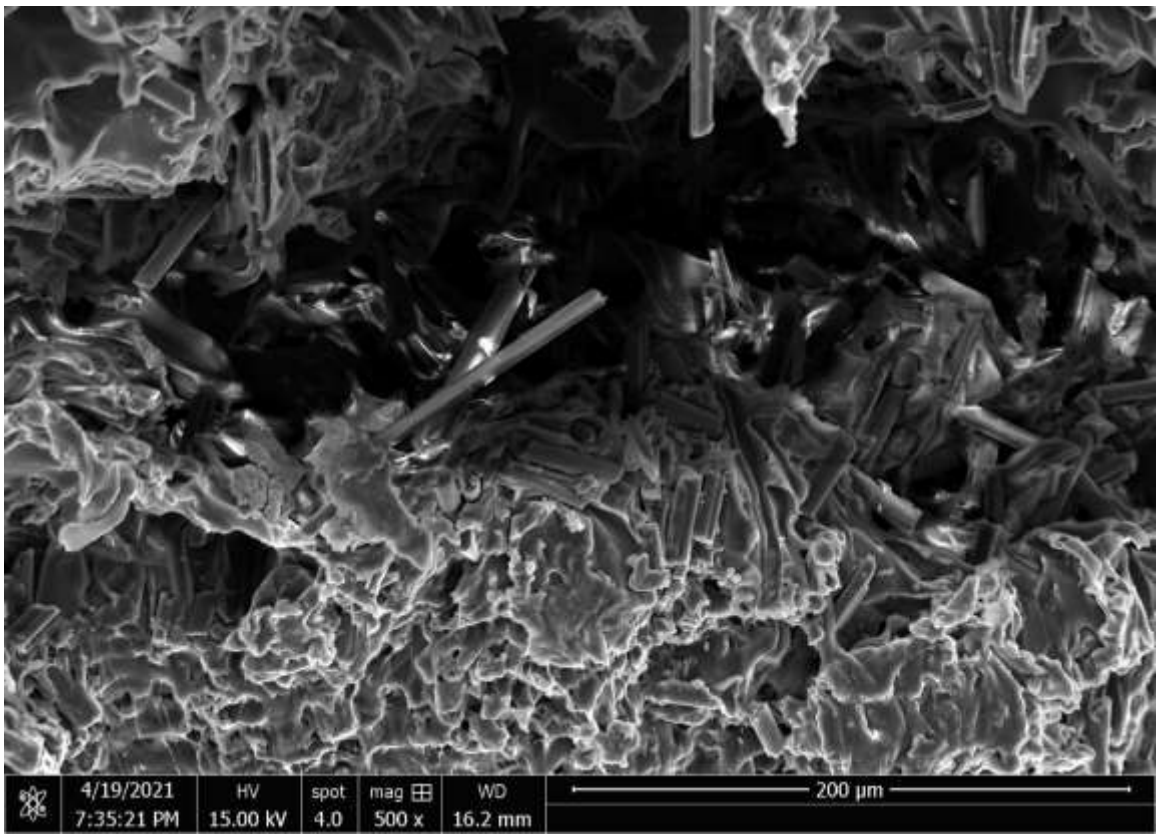

Fig B.14 PA081DC05RT, PanelA 1 direction compression sample 05 at room temperature fracture surface

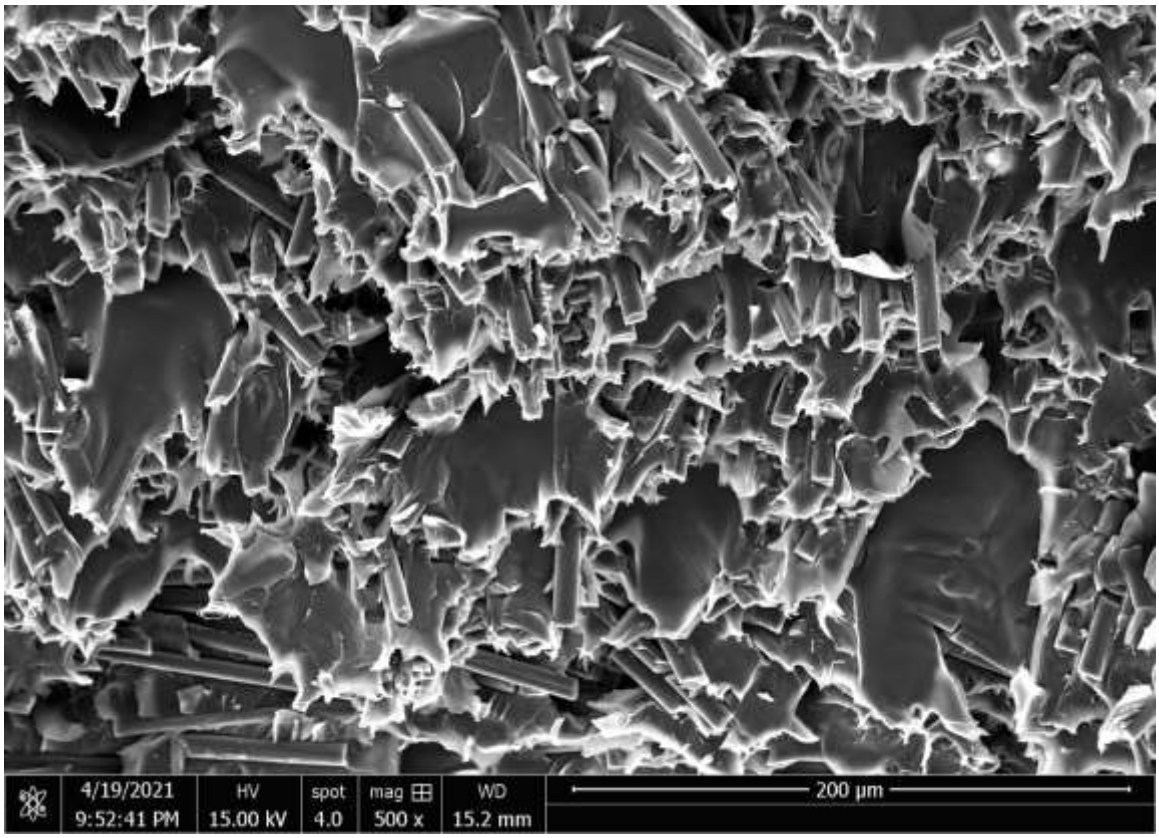

Fig B.14 PA081DC05RT, PanelA 1 direction compression sample 16 at 190°C fracture surface

B.2 Viscoelastic Measurements

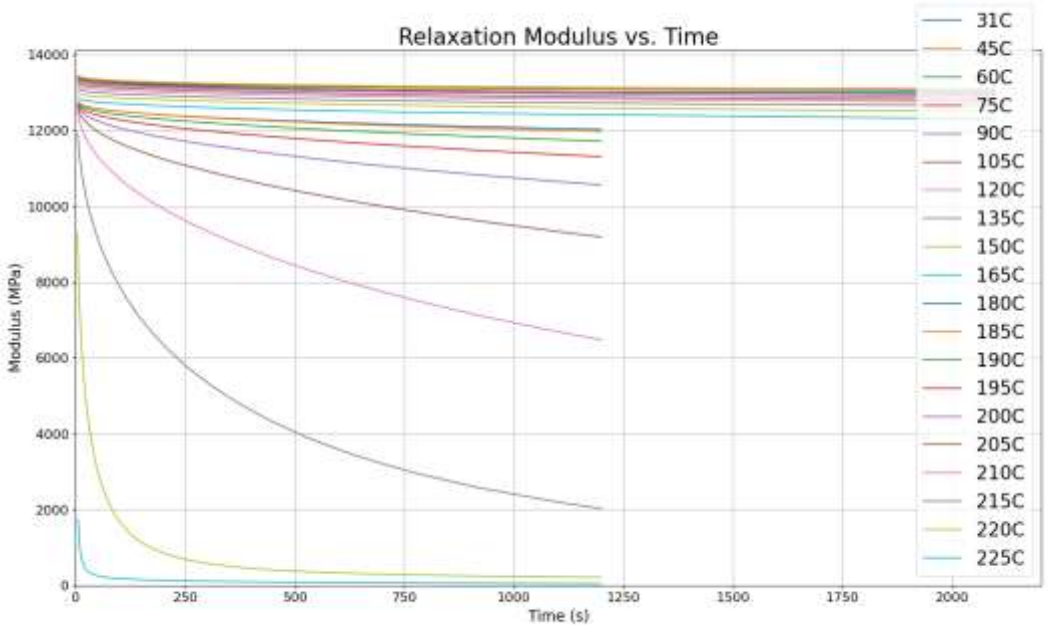

Fig B.15 Relaxation modulus versus time along the print direction for CF/PESU

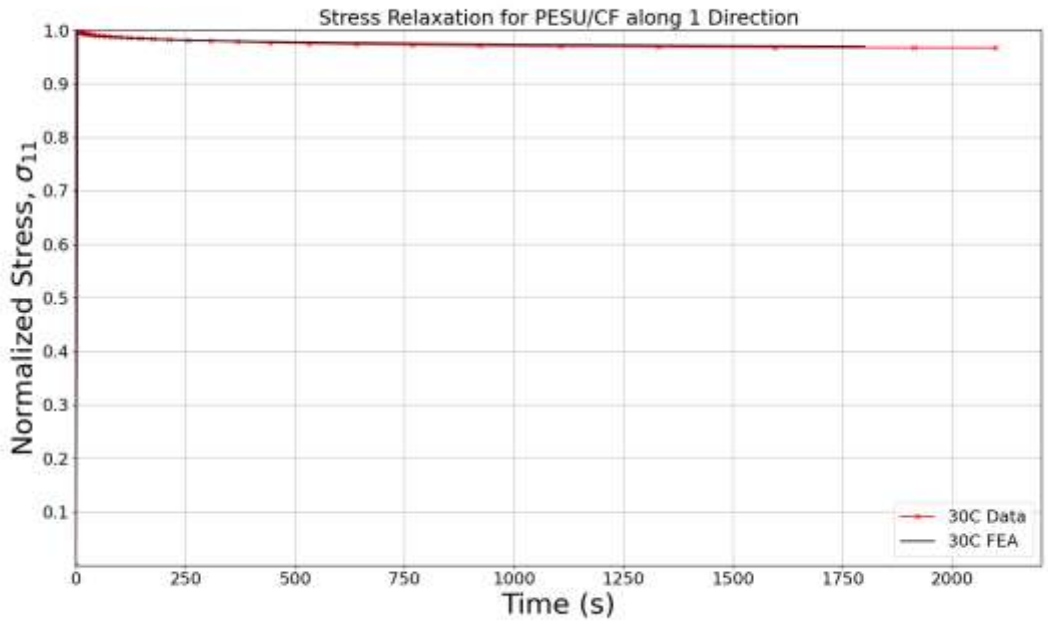

Fig B.16 Normalized stress along print direction versus time, comparison between FEA and Data at 30°C

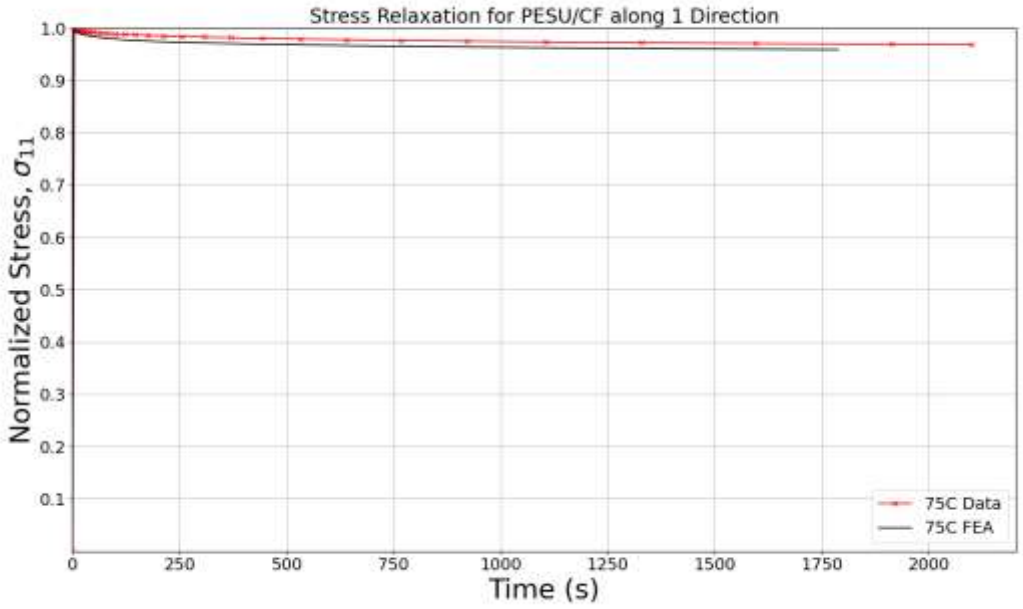

Fig B.17 Normalized stress along print direction versus time, comparison between FEA and Data at 75°C

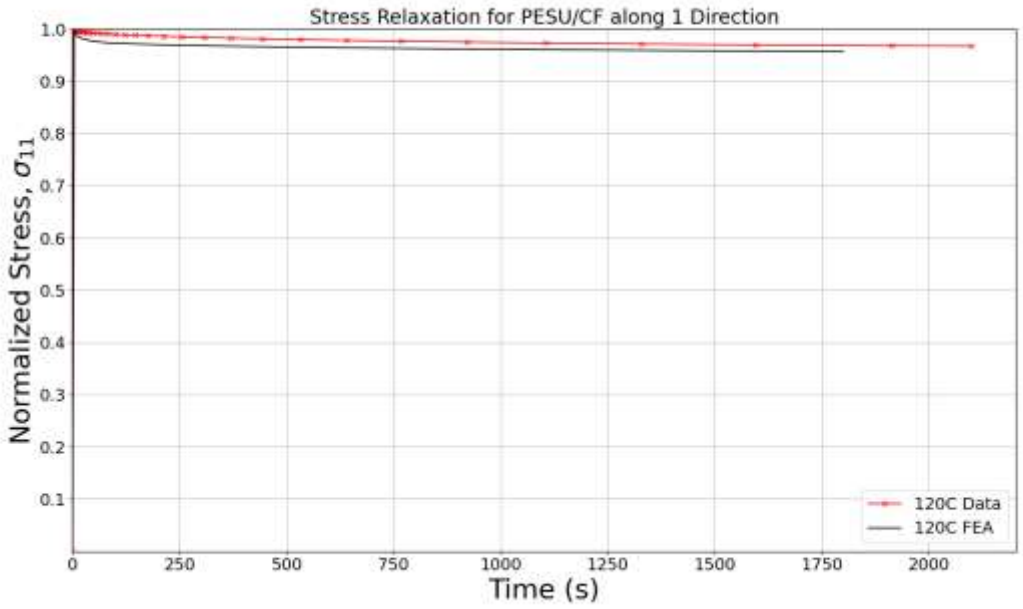

Fig B.18 Normalized stress along print direction versus time, comparison between FEA and Data at 120°C

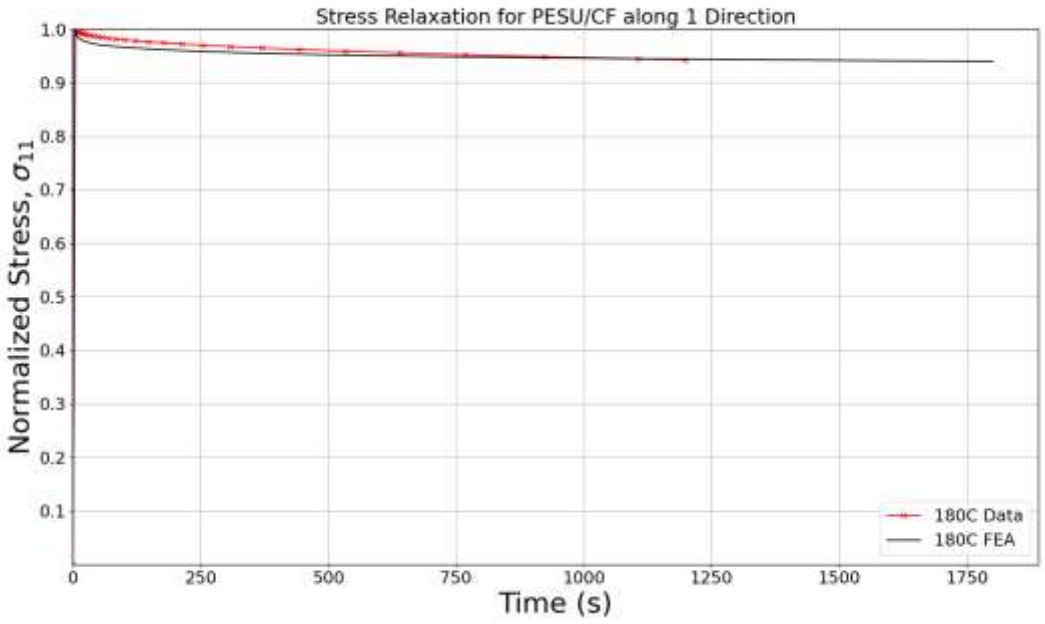

Fig B.19 Normalized stress along print direction versus time, comparison between FEA and Data at 180°C

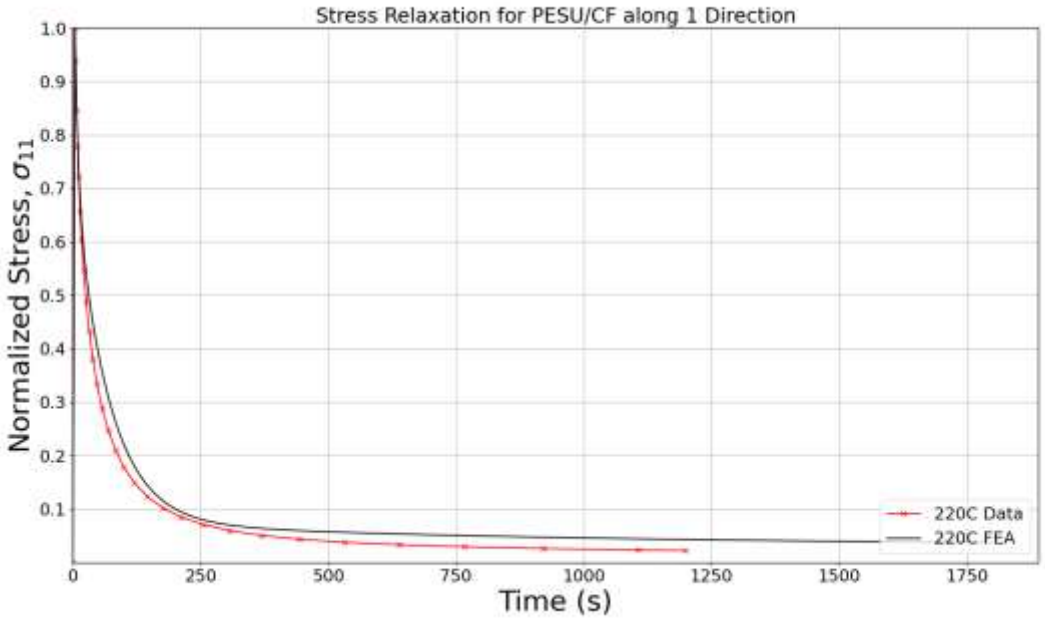

Fig B.20 Normalized stress along print direction versus time, comparison between FEA and Data at 220°C

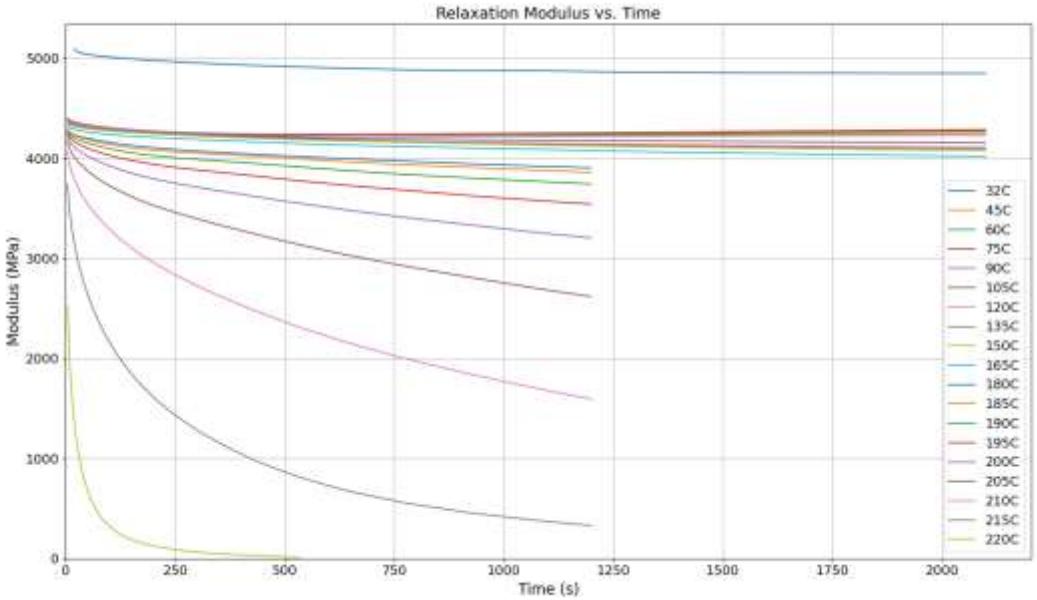

Fig B.21 Relaxation modulus versus time along the 2 direction for CF/PESU

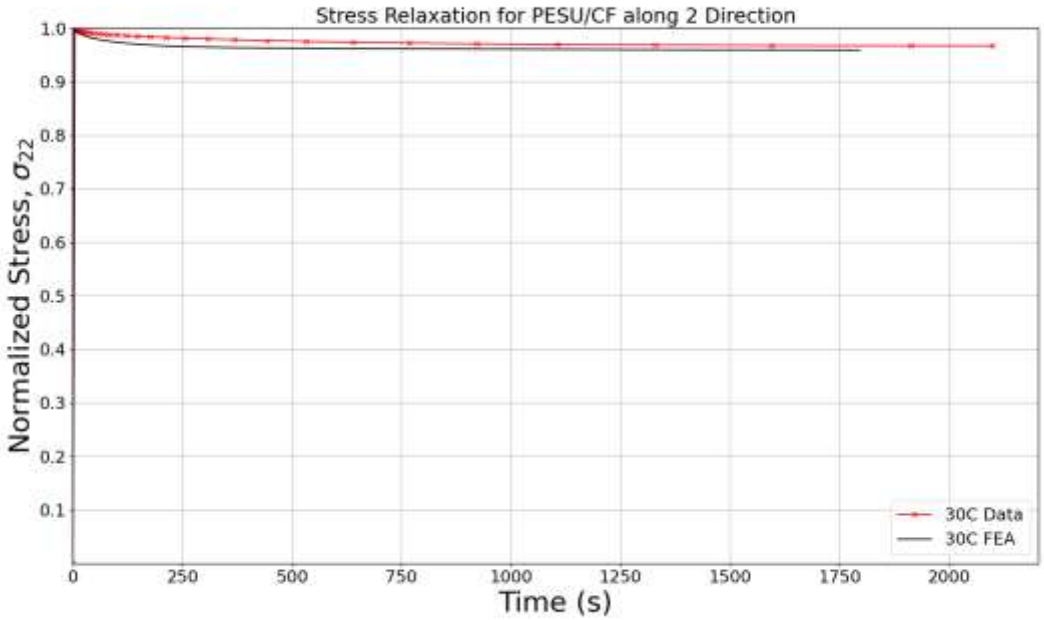

Fig B.22 Normalized stress along 2 direction versus time, comparison between FEA and Data at 30°C

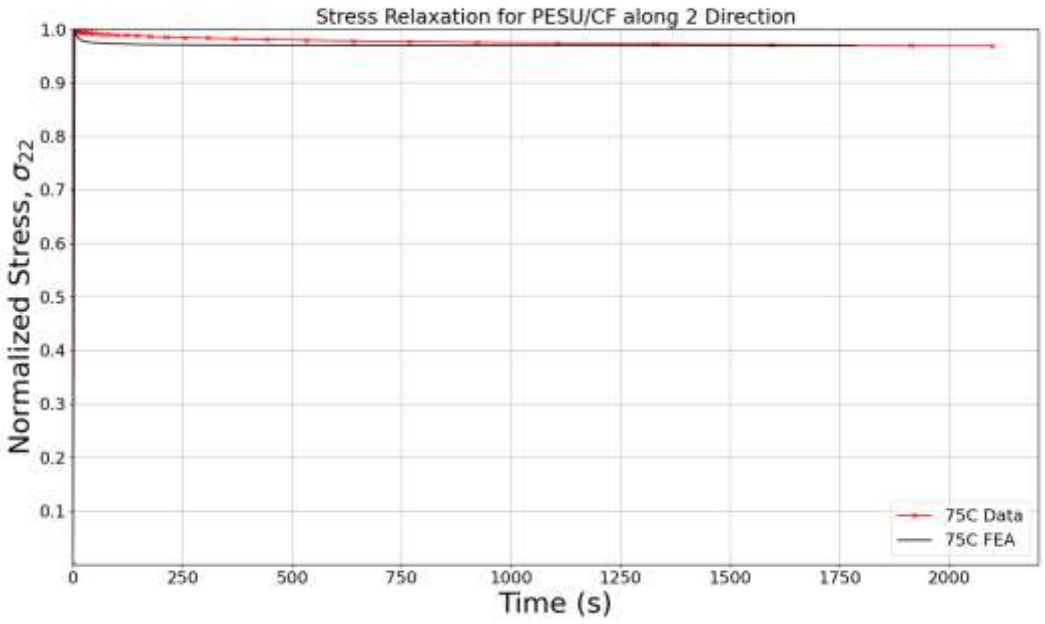

Fig B.23 Normalized stress along 2 direction versus time, comparison between FEA and Data at 75°C

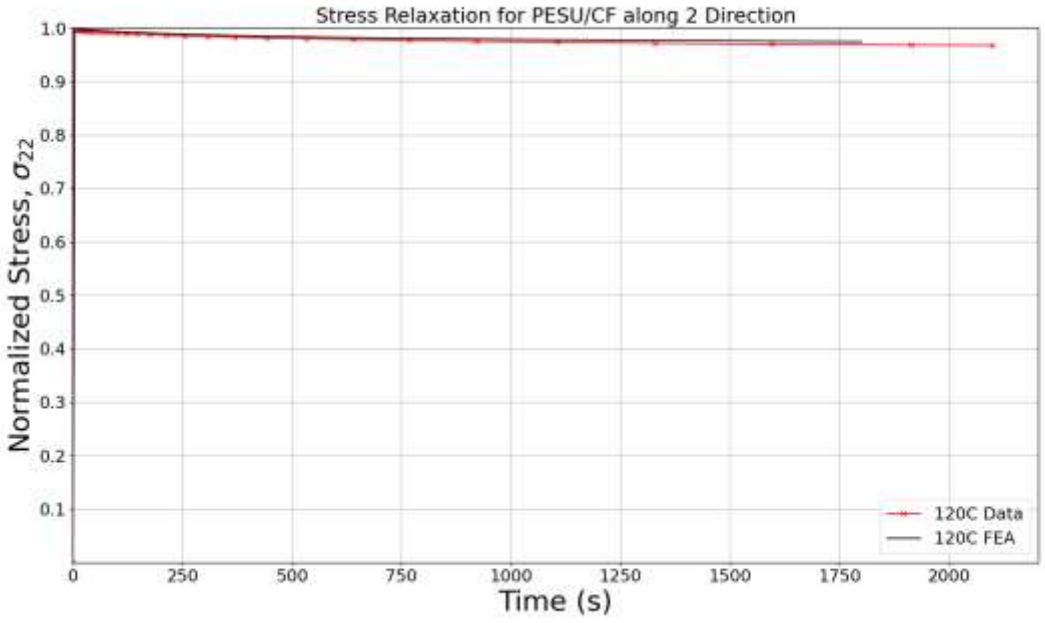

Fig B.24 Normalized stress along 2 direction versus time, comparison between FEA and Data at 120°C

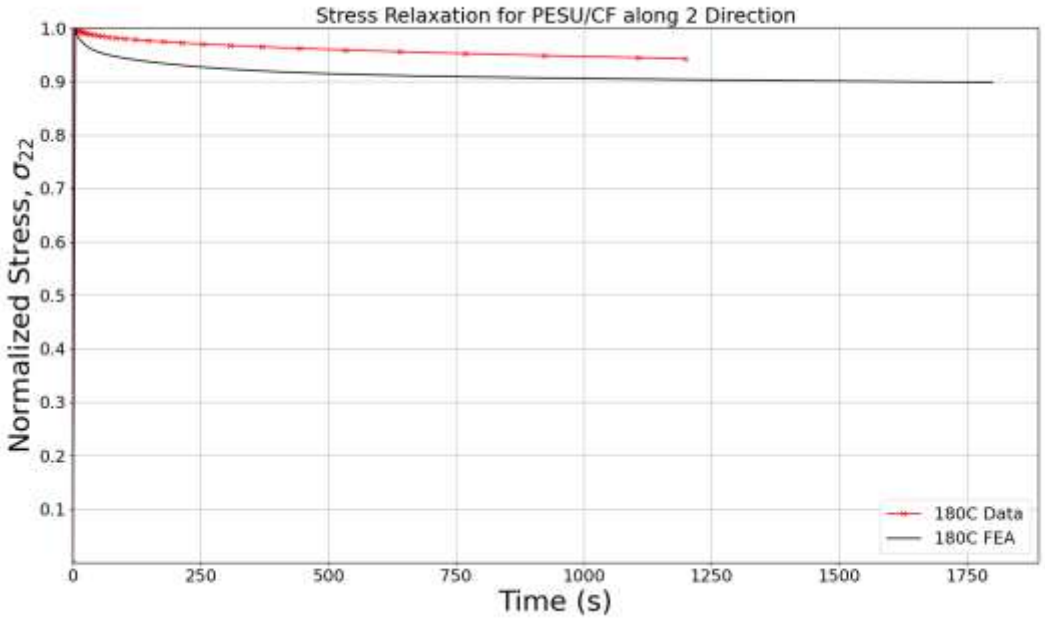

Fig B.25 Normalized stress along 2 direction versus time, comparison between FEA and Data at 180°C

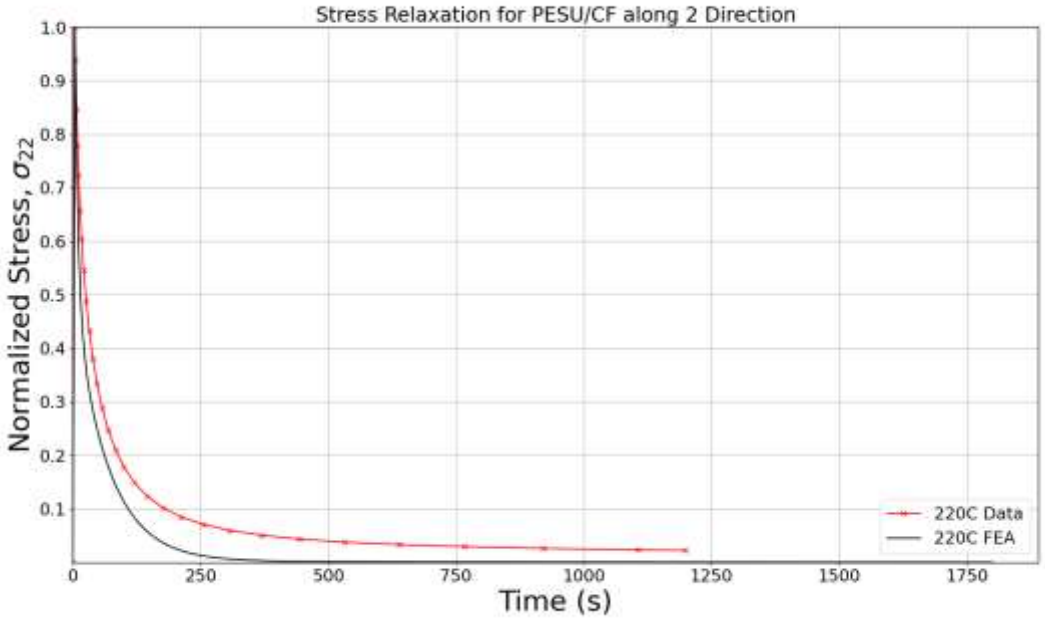

Fig B.22 Normalized stress along 2 direction versus time, comparison between FEA and Data at 220°C

B.3 Selected DIC Strain Field Plots

PB0112DS01RT

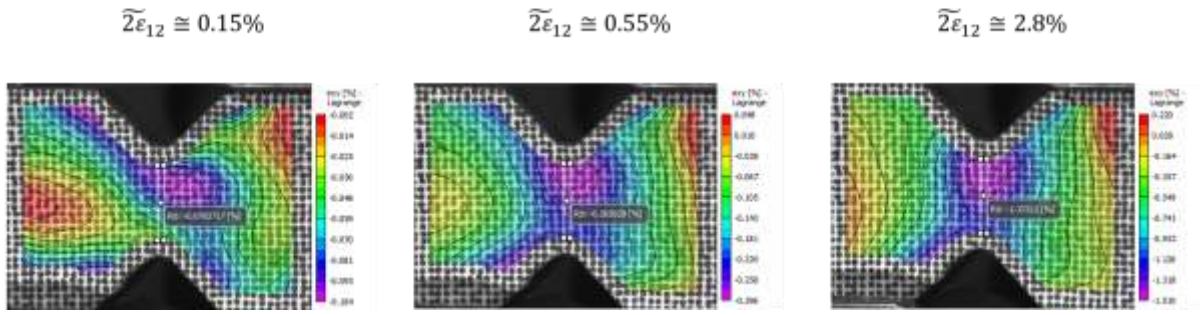

Fig B.23 PB0112DS01RT, V-notch specimen along 1-2 plane, under shear deformation at three strain levels at room temperature

PA0113DS01RT

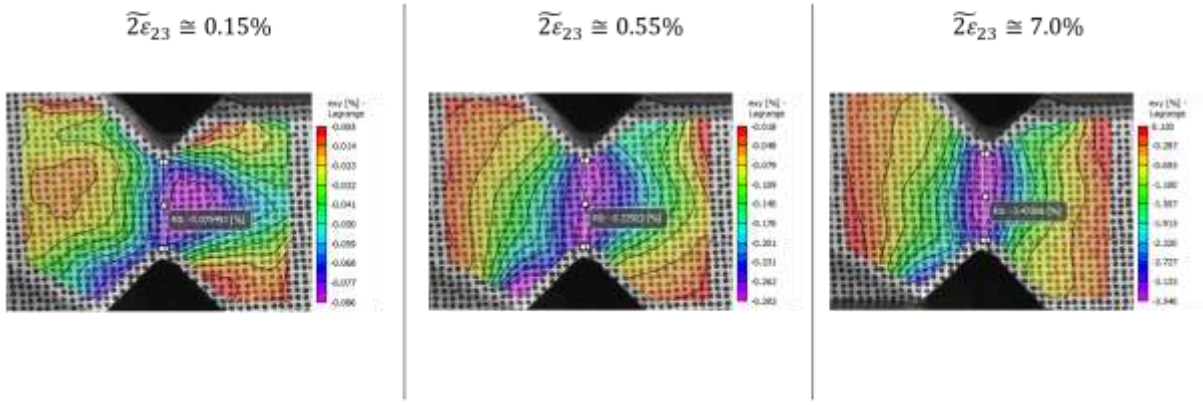

Fig B.24 PA0113DS01RT, V-notch specimen along 2-3 plane, under shear deformation at three strain levels at room temperature

BA0123DS01RT

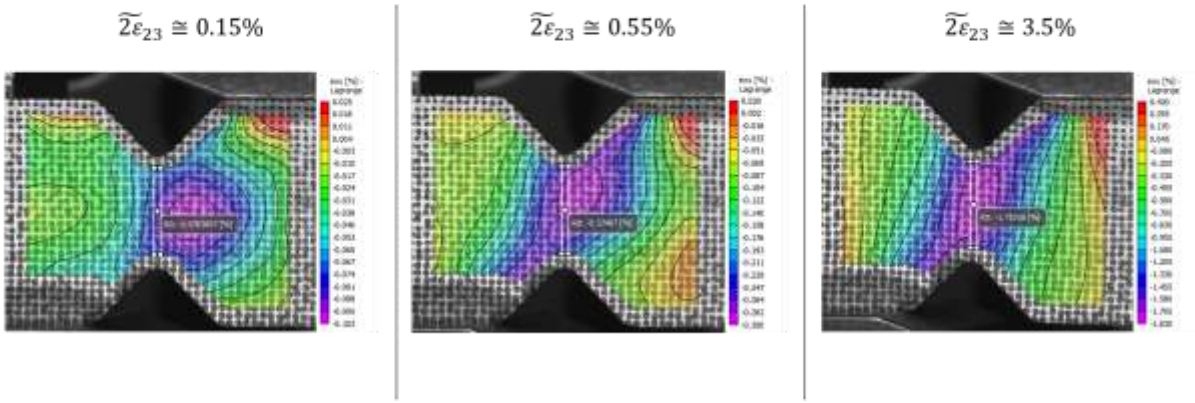

Fig B.25 BA0123DS01RT, V-notch specimen along 2-3 plane, under shear deformation at three strain levels at room temperature

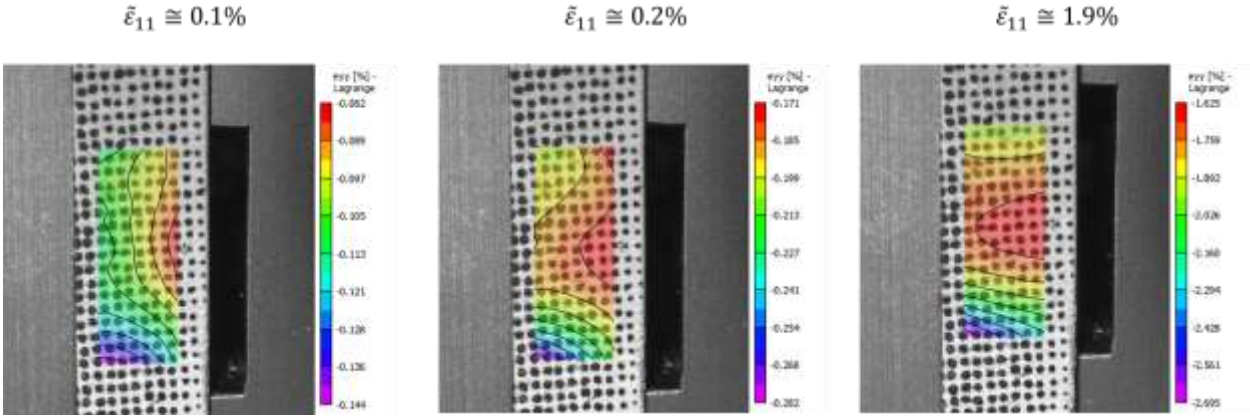

Fig B.26 PA081DC02RT, print direction compression sample at room temperature, at three average strain levels

PB022DC04RT

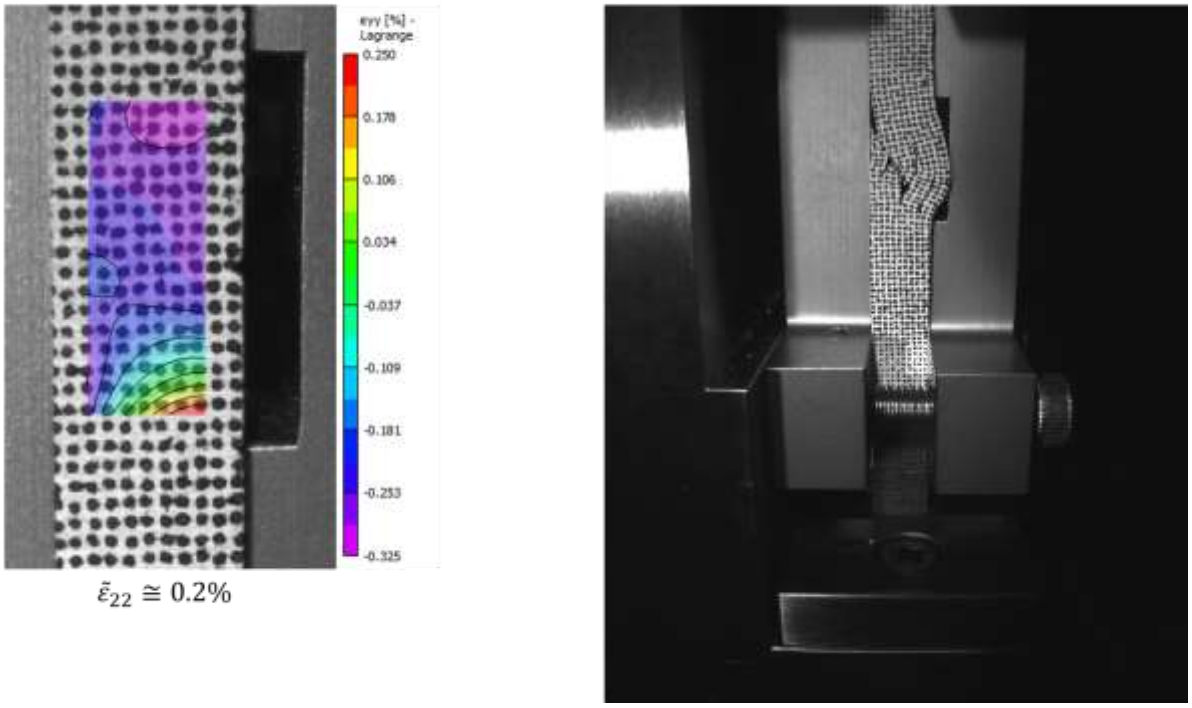

Fig B.27 PB022DC04RT, 2 direction compression sample at room temperature, DIC-computed strain-field (left) and post-mortem sample (right)

PA083DC01RT

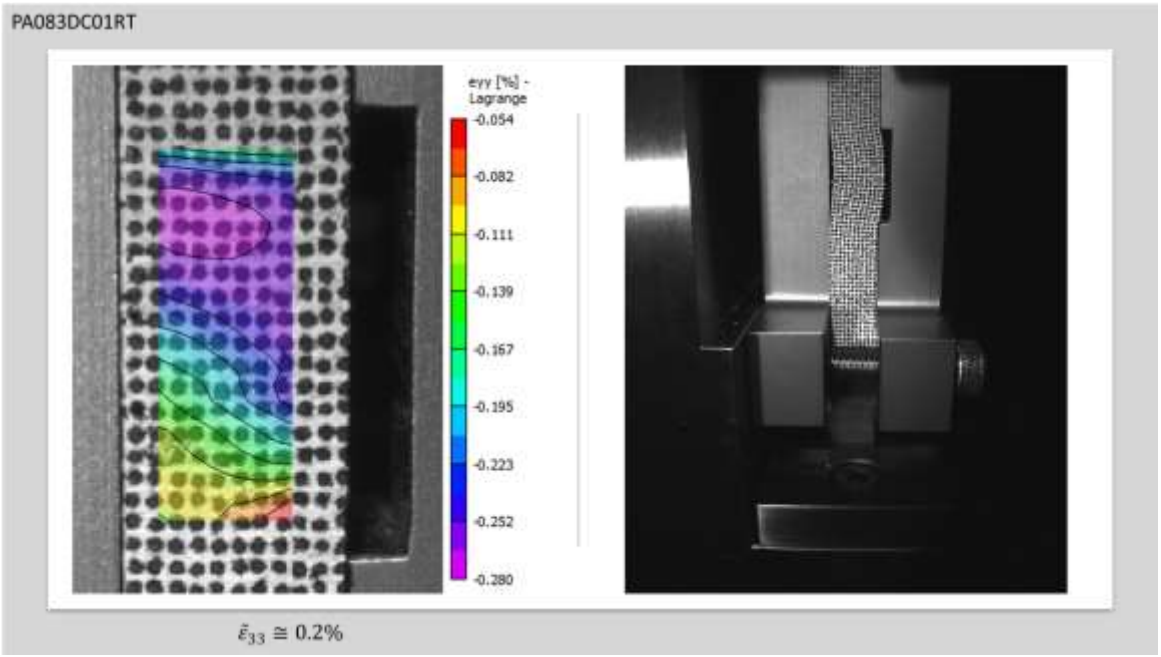

Fig B.28 PA083DC01RT, stacking direction compression sample at room temperature, DIC-computed strain-field (left) and post-mortem sample (right)

REFERENCES

[1] ASTM International, "ISO/ASTM52900-15 Standard Terminology for Additive Manufacturing," West Conshohocken, PA, 2015.

[2] Thermwood Corporation, "Large Scale Additive Manufacturing," 2017. [Online]. Available: http://thermwood.com/lsam/lsam_main.htm. [Accessed: 29-Jun-2018].

[3] Cincinnati Incorporated, "Big Area Additive Manufacturing," 2021. [Online]. Available: https://www.e-ci.com/baam. [Accessed: 28-Mar-2021].

[4] L. J. Love, V. Kunc, O. Rios, C. E. Duty, A. M. Elliott, B. K. Post, R. J. Smith, and C. A. Blue, "The importance of carbon fiber to polymer additive manufacturing," *J. Mater. Res.*, vol. 29, no. 17, pp. 1893–1898, 2014.

[5] T. Vialva, "AFRL, Boeing, Thermwood apply large scale additive manufacturing to autoclave tools," *3dprintingindustry.com*. [Online]. Available: https://3dprintingindustry.com/news/arfl-boeing-therwood-apply-large-scale-additive-manufacturing-to-autoclave-tools-160022/. [Accessed: 20-Mar-2020].

[6] T. Jackson, "Navy Partnership Goes to New Depths with First 3D-Printed Submersible," *Energy.gov*. [Online]. Available: https://www.energy.gov/eere/articles/navy-partnership-goes-new-depths-first-3d-printed-submersible. [Accessed: 20-Mar-2020].

[7] B. Post, P. D. Lloyd, J. Lindahl, R. F. Lind, L. J. Love, and V. Kunc, "The Economics of Big Area Addtiive Manufacturing." Oak Ridge National Laboratory (ORNL), Oak Ridge, TN (United States). Manufacturing Demonstration Facility (MDF), 2016.

[8] E. Barocio, "Fusion Bonding Of Fiber Reinforced Semi-Crystalline Polymers In Extrusion Deposition Additive Manufacturing," Ph.D. Dissertation, School of Mat. Eng., Purdue Univ., West Lafayette, IN, 2018.

[9] E. Barocio, B. Brenken, A. Favaloro, and R. B. Pipes, "Extrusion deposition additive manufacturing of composite molds for high-temperature applications," in *Proceedings of the Int. SAMPE Tech. Conf., Seattle, WA, USA*, 2017, pp. 22–25.

[10] M. S. Alsoufi and A. E. Elsayed, "How surface roughness performance of printed parts manufactured by desktop FDM 3D printer with PLA+ is influenced by measuring direction," *Am. J. Mech. Eng.*, vol. 5, no. 5, pp. 211–222, 2017.

[11] I. Gibson, D. W. Rosen, and B. Stucker, "Design for additive manufacturing," in *Additive manufacturing technologies*, Springer, 2010, pp. 299–332.

[12] E. Barocio, "Examples of EDAM part manufacture compression mold in PPS/CF," in *Additive Manufacturing Workshop*, West Lafayette, IN., 2018.

[13] E. Barocio, B. Brenken, A. Favaloro, M. Bogdanor, and R. B. Pipes, "Extrusion deposition additive manufacturing with fiber-reinforced thermoplastic polymers," in *Woodhead Publishing Series in Composites Science and Engineering*, K. Friedrich, R. Walter, C. Soutis, S. G. Advani, and I. H. B. B. T.-S. and P. of A. M. P. C. Fiedler, Eds. Woodhead Publishing, 2020, pp. 191–219.

[14] B. Brenken, "Extrusion Deposition Additive Manufacturing of Fiber Reinforced Semi-Crystalline Polymers," Ph.D. Dissertation, School of Aero. & Astro. Eng., Purdue Univ., West Lafayette, IN, 2017.

[15] B. Brenken, E. Barocio, A. Favaloro, V. Kunc, and R. B. Pipes, "Development and validation of extrusion deposition additive manufacturing process simulations," *Addit. Manuf.*, vol. 25, pp. 218–226, 2019.

[16] E. Barocio, B. Brenken, A. J. Favaloro, M. Ramirez, J. Ramirez, and R. B. Pipes, "Prediction of the degree of bonding in the extrusion deposition additive manufacturing process of semi-crystalline polymer composites," *Proc. Dassault Syst. Sci. Age Exp. Boston, MA, USA*, pp. 18–21, 2018.
[17] A. J. Favaloro, B. Brenken, E. Barocio, and R. B. Pipes, "Simulation of Polymeric Composites Additive Manufacturing using Abaqus," in *Sience in the Age of Experience conference*, 2017, pp. 15–18.
[18] Dassault Systemes Simulia Corp., "ABAQUS 2017 Documentation," 2017. [Online]. Available: https://help.3ds.com/2017/English. [Accessed: 30-Mar-2021].
[19] F. Yang and R. Pitchumani, "Nonisothermal healing and interlaminar bond strength evolution during thermoplastic matrix composites processing," *Polym. Compos.*, vol. 24, no. 2, pp. 263–278, 2003.
[20] J. Nixon, B. Dryer, D. Chiu, I. Lempert, and D. I. Bigio, "Three parameter analysis of fiber orientation in fused deposition modeling geometries," *72nd Annu. Tech. Conf. Soc. Plast. Eng. Plast. Conf. ANTEC 2014*, vol. 2, no. January, pp. 985–995, 2014.
[21] Dimensional Innovations, "Las Vegas Raiders Al Davis Memorial Torch," 2019. [Online]. Available: https://dimin.com/work/las-vegas-raiders-al-davis-memorial-torch. [Accessed: 01-Apr-2021].
[22] M. R. Talagani, S. DorMohammadi, R. Dutton, C. Godines, H. Baid, F. Abdi, V. Kunc, B. Compton, S. Simunovic, and C. Duty, "Numerical simulation of big area additive manufacturing (3D printing) of a full size car," *SAMPE J.*, vol. 51, no. 4, pp. 27–36, 2015.
[23] B. G. Compton, B. K. Post, C. E. Duty, L. Love, and V. Kunc, "Thermal analysis of additive manufacturing of large-scale thermoplastic polymer composites," *Addit. Manuf.*, vol. 17, pp. 77–86, 2017.
[24] A. International, "ASTM D638-14, Standard Test Method for Tensile Properties of Plastics," ASTM International, 2015.
[25] N. G. McCrum, C. P. Buckley, C. B. Bucknall, and C. B. Bucknall, *Principles of polymer engineering*. Oxford University Press, USA, 1997.
[26] H. F. Brinson and L. C. Brinson, "Characteristics, applications and properties of polymers," in *Polymer Engineering Science and Viscoelasticity*, Springer, 2015, pp. 57–100.
[27] E. F. Rybicki and M. F. Kanninen, "The effect of different behavior in tension than in compression on the mechanical response of polymeric materials," in *Deformation and Fracture of High Polymers*, Springer, 1973, pp. 417–427.
[28] A. J. Kinloch and R. J. Young, "Shear Yielding BT - Fracture Behaviour of Polymers," A. J. Kinloch and R. J. Young, Eds. Dordrecht: Springer Netherlands, 1995, pp. 107–146.
[29] H. F. Brinson and L. C. Brinson, "Polymer engineering science and viscoelasticity," *An Introd.*, 2008.
[30] H. F. Brinson and L. C. Brinson, "Hereditary integral representations of stress and strain," in *Polymer Engineering Science and Viscoelasticity*, Springer, 2015, pp. 211–230.
[31] S. P. C. Marques and G. J. Creus, *Computational viscoelasticity*. Springer Science & Business Media, 2012.
[32] H. F. Brinson and L. C. Brinson, "Differential Constitutive Equations," in *Polymer Engineering Science and Viscoelasticity*, Springer, 2015, pp. 169–209.
[33] H. F. Brinson and L. C. Brinson, "Time and temperature behavior of polymers," in *Polymer Engineering Science and Viscoelasticity*, Springer, 2015, pp. 231–285.

[34] E. T. J. Klompen and L. E. Govaert, “Nonlinear viscoelastic behaviour of thermorheologically complex materials,” *Mech. Time-Dependent Mater.*, vol. 3, no. 1, pp. 49–69, 1999.
[35] F. Schwarzl and A. J. Staverman, “Time-temperature dependence of linear viscoelastic behavior,” *J. Appl. Phys.*, vol. 23, no. 8, pp. 838–843, 1952.
[36] J. Dealy and D. Plazek, “Time-temperature superposition—a users guide,” *Rheol. Bull*, vol. 78, no. 2, pp. 16–31, 2009.
[37] N. I. M. Yusoff, E. Chailleux, and G. D. Airey, “A comparative study of the influence of shift factor equations on master curve construction,” *Int. J. Pavement Res. Technol.*, vol. 4, no. 6, p. 324, 2011.
[38] S. Ropers, M. Kardos, and T. A. Osswald, “A thermo-viscoelastic approach for the characterization and modeling of the bending behavior of thermoplastic composites,” *Compos. Part A Appl. Sci. Manuf.*, vol. 90, pp. 22–32, 2016.
[39] B. Fan and D. O. Kazmer, “Low-temperature modeling of the time-temperature shift factor for polycarbonate,” *Adv. Polym. Technol. J. Polym. Process. Inst.*, vol. 24, no. 4, pp. 278–287, 2005.
[40] P. E. Rouse Jr, “A theory of the linear viscoelastic properties of dilute solutions of coiling polymers,” *J. Chem. Phys.*, vol. 21, no. 7, pp. 1272–1280, 1953.
[41] F. Bueche, “Viscosity, self-diffusion, and allied effects in solid polymers,” *J. Chem. Phys.*, vol. 20, no. 12, pp. 1959–1964, 1952.
[42] J. D. Ferry, *Viscoelastic properties of polymers*. John Wiley & Sons, 1980.
[43] T. Hobbiebrunken, B. Fiedler, M. Hojo, S. Ochiai, and K. Schulte, “Microscopic yielding of CF/epoxy composites and the effect on the formation of thermal residual stresses,” *Compos. Sci. Technol.*, vol. 65, no. 10, pp. 1626–1635, 2005.
[44] S. Deng, M. Hou, and L. Ye, “Temperature-dependent elastic moduli of epoxies measured by DMA and their correlations to mechanical testing data,” *Polym. Test.*, vol. 26, no. 6, pp. 803–813, 2007.
[45] C. E. Duty, V. Kunc, B. Compton, B. Post, D. Erdman, R. Smith, R. Lind, P. Lloyd, and L. Love, “Structure and mechanical behavior of Big Area Additive Manufacturing (BAAM) materials,” *Rapid Prototyp. J.*, vol. 23, no. 1, pp. 181–189, 2017.
[46] H. L. Tekinalp, V. Kunc, G. M. Velez-Garcia, C. E. Duty, L. J. Love, A. K. Naskar, C. A. Blue, and S. Ozcan, “Highly oriented carbon fiber–polymer composites via additive manufacturing,” *Compos. Sci. Technol.*, vol. 105, pp. 144–150, Dec. 2014.
[47] R. Takahashi, I. Shohji, Y. Seki, and S. Maruyama, “Effect of fiber direction and temperature on mechanical properties of short fiber-reinforced PPS,” in *2014 International Conference on Electronics Packaging (ICEP)*, 2014, pp. 778–781.
[48] P. T. Curtis, M. G. Bader, and J. E. Bailey, “The stiffness and strength of a polyamide thermoplastic reinforced with glass and carbon fibres,” *J. Mater. Sci.*, vol. 13, no. 2, pp. 377–390, 1978.
[49] N. Sato, T. Kurauchi, S. Sato, and O. Kamigaito, “Microfailure behaviour of randomly dispersed short fibre reinforced thermoplastic composites obtained by direct SEM observation,” *J. Mater. Sci.*, vol. 26, no. 14, pp. 3891–3898, 1991.
[50] R. W. Lang, J. A. Manson, and R. W. Hertzberg, “Mechanisms of fatigue fracture in short glass fibre-reinforced polymers,” *J. Mater. Sci.*, vol. 22, no. 11, pp. 4015–4030, 1987.

[51] K. Friedrich and J. Karger-Kocsis, “Fractography and failure mechanisms of unfilled and short fiber reinforced semi-crystalline thermoplastics,” *Elsevier Sci. Publ. Ltd., Fractography Fail. Mech. Polym. Compos.*, pp. 437–494, 1989.
[52] N. Takeda, D. Y. Song, K. Nakat, and T. Shioya, “The effect of fiber surface treatment on the micro-fracture progress in glass fiber/Nylon 6 composites,” *Compos. Interfaces*, vol. 2, no. 2, pp. 143–155, 1994.
[53] B. Z. Jang and Y. K. Lieu, “Fracture behavior of short fiber reinforced thermoplastics I. Crack propagation mode and fracture toughness,” *J. Appl. Polym. Sci.*, vol. 30, no. 9, pp. 3925–3942, 1985.
[54] J. Lindhagen and L. Berglund, “Microscopical damage mechanisms in glass fiber reinforced polypropylene,” *J. Appl. Polym. Sci.*, vol. 69, no. 7, pp. 1319–1327, 1998.
[55] J. K. Wells and P. W. R. Beaumont, “Debonding and pull-out processes in fibrous composites,” *J. Mater. Sci.*, vol. 20, no. 4, pp. 1275–1284, 1985.
[56] H. Rolland, N. Saintier, and G. Robert, “Damage mechanisms in short glass fibre reinforced thermoplastic during in situ microtomography tensile tests,” *Compos. Part B Eng.*, vol. 90, pp. 365–377, 2016.
[57] X. Hu, J. Fang, F. Xu, B. Dong, Y. Xiao, and L. Wang, “Real internal microstructure based key mechanism analysis on the micro-damage process of short fibre-reinforced composites,” *Sci. Rep.*, vol. 6, no. 1, p. 34761, 2016.
[58] A. Kelly and amd W. R. Tyson, “Tensile properties of fibre-reinforced metals: copper/tungsten and copper/molybdenum,” *J. Mech. Phys. Solids*, vol. 13, no. 6, pp. 329–350, 1965.
[59] S. Fara and A. Pavan, “Fracture Mechanisms in Short Fibre Polymer Composites: The Influence of External Variables on Critical Fibre Angle,” vol. 32, B. R. K. Blackman, A. Pavan, and J. G. B. T.-E. S. I. S. Williams, Eds. Elsevier, 2003, pp. 387–398.
[60] M. R. Piggott, M. Ko, and H. Y. Chuang, “Aligned short-fibre reinforced thermosets: Experiments and analysis lend little support for established theory,” *Compos. Sci. Technol.*, vol. 48, no. 1, pp. 291–299, 1993.
[61] R. B. Nath, D. N. Fenner, and C. Galiotis, “Finite element modelling of interfacial failure in model carbon fibre-epoxy composites,” *J. Mater. Sci.*, vol. 31, no. 11, pp. 2879–2883, 1996.
[62] S. Sirivedin, D. N. Fenner, R. B. Nath, and C. Galiotis, “Matrix crack propagation criteria for model short-carbon fibre/epoxy composites,” *Compos. Sci. Technol.*, vol. 60, no. 15, pp. 2835–2847, 2000.
[63] A. Forghani, M. Shahbazi, N. Zobeiry, A. Poursartip, and R. Vaziri, “6 - An overview of continuum damage models used to simulate intralaminar failure mechanisms in advanced composite materials,” in *Woodhead Publishing Series in Composites Science and Engineering*, P. P. Camanho and S. R. B. T.-N. M. of F. in A. C. M. Hallett, Eds. Woodhead Publishing, 2015, pp. 151–173.
[64] C. Rose, C. Dávila, and F. Leone, *Analysis Methods for Progressive Damage of Composite Structures*. Technical report NASA/TM-2013-218024, 2013.
[65] Z. Yuan and J. Fish, “Are the cohesive zone models necessary for delamination analysis?,” *Comput. Methods Appl. Mech. Eng.*, vol. 310, pp. 567–604, 2016.
[66] J.-L. Chaboche, “Continuous damage mechanics — A tool to describe phenomena before crack initiation,” *Nucl. Eng. Des.*, vol. 64, no. 2, pp. 233–247, 1981.

[67] J. Lemaitre and R. Desmorat, “Background on continuum damage mechanics,” *Eng. Damage Mech. Ductile, Creep, Fatigue Brittle Fail.*, pp. 1–76, 2005.
[68] M. Jirásek, “Damage and Smeared Crack Models BT - Numerical Modeling of Concrete Cracking,” G. Hofstetter and G. Meschke, Eds. Vienna: Springer Vienna, 2011, pp. 1–49.
[69] L. M. Kachanov, “On the rupture time under the condition of creep,” *Izv. Akad. Nauk SSSR, Otd. Tekh. Nauk*, vol. 8, p. 26, 1958.
[70] Y. N. Rabotnov, “Creep problems in structural members,” 1969.
[71] D. R. Hayhurst, “Creep rupture under multi-axial states of stress,” *J. Mech. Phys. Solids*, vol. 20, no. 6, pp. 381–382, 1972.
[72] F. A. Leckie and D. R. Hayhurst, “Creep rupture of structures,” *Proc. R. Soc. London. A. Math. Phys. Sci.*, vol. 340, no. 1622, pp. 323–347, 1974.
[73] J.-L. Chaboche and C. JL, “Une loi differentielle d’endommagement de fatigue avec cumulation non lineaire.,” 1974.
[74] J. L. Chaboche, “Sur l’utilisation des variables d’état interne pour la description du comportement viscoplastique et de la rupture par endommagement,” *Probl. Non-Lineaires Mec.*, pp. 137–159, 1977.
[75] M. Chrzanowski, “Use of the damage concept in describing creep-fatigue interaction under prescribed stress,” *Int. J. Mech. Sci.*, vol. 18, no. 2, pp. 69–73, Jan. 1976.
[76] J. Lemaitre and J.-L. Chaboche, “Aspect phénoménologique de la rupture par endommagement,” *J Méc Appl*, vol. 2, no. 3, 1978.
[77] A. A. Vakulenko and M. L. Kachanov, “Continuum theory of cracked media,” *Mekh. Tverd. Tela*, vol. 6, p. 159, 1971.
[78] S. Murakami, *Continuum damage mechanics: a continuum mechanics approach to the analysis of damage and fracture*, vol. 185. Springer Science & Business Media, 2012.
[79] S. Murakami and N. Ohno, “A continuum theory of creep and creep damage,” in *Creep in structures*, Springer, 1981, pp. 422–444.
[80] D. Krajcinovic and G. U. Fonseka, “The Continuous Damage Theory of Brittle Materials, Part 1: General Theory,” *J. Appl. Mech.*, vol. 48, no. 4, pp. 809–815, Dec. 1981.
[81] G. U. Fonseka and D. Krajcinovic, “The Continuous Damage Theory of Brittle Materials, Part 2: Uniaxial and Plane Response Modes,” *J. Appl. Mech.*, vol. 48, no. 4, pp. 816–824, Dec. 1981.
[82] J.-L. Chaboche, “Continuum damage mechanics: Part I—General concepts,” 1988.
[83] J.-L. Chaboche, “Continuum damage mechanics: Part II—Damage growth, crack initiation, and crack growth,” 1988.
[84] P. Germain, P. Suquet, and Q. S. Nguyen, “Continuum thermodynamics,” *ASME Trans. Ser. E J. Appl. Mech.*, vol. 50, pp. 1010–1020, 1983.
[85] S. Murakami, “Notion of Continuum Damage Mechanics and its Application to Anisotropic Creep Damage Theory,” *J. Eng. Mater. Technol.*, vol. 105, no. 2, pp. 99–105, Apr. 1983.
[86] P. Ladevèze, *Sur une théorie de l’endommagement anisotrope*. Laboratoire de Mécanique et Technologie, 1983.
[87] J. Lemaitre, “How to use damage mechanics,” *Nucl. Eng. Des.*, vol. 80, no. 2, pp. 233–245, Jul. 1984.
[88] D. K. Krajcinovic, “Continuum damage mechanics.,” *Appl. Mech. Rev.*, vol. 37, no. 1, pp. 1–6, 1984.
[89] M. Ortiz, “A constitutive theory for the inelastic behavior of concrete,” *Mech. Mater.*, vol. 4, no. 1, pp. 67–93, Mar. 1985.

[90] R. Talreja, “A continuum mechanics characterization of damage in composite materials,” *Proc. R. Soc. London. A. Math. Phys. Sci.*, vol. 399, no. 1817, pp. 195–216, Jun. 1985.
[91] J. Mazars, “A model of a unilateral elastic damageable material and its application to concrete,” *Fract. toughness Fract. energy Concr.*, pp. 61–71, 1986.
[92] C. L. Chow and J. Wang, “An anisotropic theory of continuum damage mechanics for ductile fracture,” *Eng. Fract. Mech.*, vol. 27, no. 5, pp. 547–558, Jan. 1987.
[93] J. C. Simo, “On a fully three-dimensional finite-strain viscoelastic damage model: formulation and computational aspects,” *Comput. Methods Appl. Mech. Eng.*, vol. 60, no. 2, pp. 153–173, 1987.
[94] C. L. Chow and T. J. Lu, “On evolution laws of anisotropic damage,” *Eng. Fract. Mech.*, vol. 34, no. 3, pp. 679–701, Jan. 1989.
[95] J. W. Ju, “On energy-based coupled elastoplastic damage theories: Constitutive modeling and computational aspects,” *Int. J. Solids Struct.*, vol. 25, no. 7, pp. 803–833, 1989.
[96] J. L. Chaboche, “Le Concept de Contrainte Effective Appliqué à l’Élasticité et à la Viscoplasticité en Présence d’un Endommagement Anisotrope BT - Mechanical Behavior of Anisotropic Solids / Comportment Méchanique des Solides Anisotropes,” 1982, pp. 737–760.
[97] J. Lemaitre, “Evaluation of dissipation and damage in metals,” in *In Proc. 1st International Conference on Mechanical Behavior of Materials*, 1971, vol. 1.
[98] J. P. Cordebois and F. Sidoroff, “Anisotropie élastique induite par endommagement,” *Comport. mécanique des solides anisotropes*, no. 295, pp. 761–774, 1979.
[99] N. R. Hansen and H. L. Schreyer, “A thermodynamically consistent framework for theories of elastoplasticity coupled with damage,” *Int. J. Solids Struct.*, vol. 31, no. 3, pp. 359–389, 1994.
[100] Y. Y. Zhu and S. Cescotto, “A fully coupled elasto-visco-plastic damage theory for anisotropic materials,” *Int. J. Solids Struct.*, vol. 32, no. 11, pp. 1607–1641, 1995.
[101] E. J. Barbero and L. De Vivo, “A constitutive model for elastic damage in fiber-reinforced PMC laminae,” *Int. J. Damage Mech.*, vol. 10, no. 1, pp. 73–93, 2001.
[102] E. J. Barbero and P. Lonetti, “An inelastic damage model for fiber reinforced laminates,” *J. Compos. Mater.*, vol. 36, no. 8, pp. 941–962, 2002.
[103] E. J. Barbero and P. Lonetti, “Damage model for composites defined in terms of available data,” *Mech. Compos. Mater. Struct.*, vol. 8, no. 4, pp. 299–315, 2001.
[104] P. Lonetti, R. Zinno, F. Greco, and E. J. Barbero, “Interlaminar damage model for polymer matrix composites,” *J. Compos. Mater.*, vol. 37, no. 16, pp. 1485–1504, 2003.
[105] R. Talreja and C. V. Singh, *Damage and failure of composite materials*. Cambridge University Press, 2012.
[106] J. Besson, G. Cailletaud, J.-L. Chaboche, and S. Forest, *Non-linear mechanics of materials*, vol. 167. Springer Science & Business Media, 2009.
[107] W. Zhang and Y. Cai, *Continuum damage mechanics and numerical applications*. Springer Science & Business Media, 2010.
[108] J. Lemaitre, *A course on damage mechanics*. Springer Science & Business Media, 2012.
[109] L. M. Kachanov, *Introduction to continuum damage mechanics*. 1986.
[110] Z. P. Bažant and B. H. Oh, “Crack band theory for fracture of concrete,” *Matériaux Constr.*, vol. 16, no. 3, pp. 155–177, 1983.
[111] Z. P. Bazant, “Recent advances in failure localization and non-local models,” *Micromechanics Fail. quasi-brittle Mater.*, pp. 12–32, 1990.

[112] B. A. Bilby, I. C. Howard, and Z. H. Li, “Mesh independent cell models for continuum damage theory,” *Fatigue Fract. Eng. Mater. Struct.*, vol. 17, no. 10, pp. 1221–1233, Oct. 1994.
[113] S. Pietruszczak and Z. Mróz, “Finite element analysis of deformation of strain-softening materials,” *Int. J. Numer. Methods Eng.*, vol. 17, no. 3, pp. 327–334, Mar. 1981.
[114] J. C. Simo, “Strain softening and dissipation: a unification of approaches,” *Crack. damage strain localization size Eff.*, pp. 440–461, 1989.
[115] R. De Borst, L. J. Sluys, H.-B. Muhlhaus, and J. Pamin, “Fundamental issues in finite element analyses of localization of deformation,” *Eng. Comput.*, vol. 10, no. 2, pp. 99–121, 1993.
[116] P. Gilles and B. Z. P., “Nonlocal Damage Theory,” *J. Eng. Mech.*, vol. 113, no. 10, pp. 1512–1533, Oct. 1987.
[117] B. Z. P. and G. Pijaudier-Cabot, “Nonlocal Continuum Damage, Localization Instability and Convergence,” *J. Appl. Mech.*, vol. 55, no. 2, pp. 287–293, Jun. 1988.
[118] K. Saanouni, J. L. Chaboche, and P. M. Lesne, “On the creep crack-growth prediction by a non local damage formulation,” *Eur. J. Mech. A. Solids*, vol. 8, no. 6, pp. 437–459, 1989.
[119] R. K. Abu Al-Rub, M. K. Darabi, and E. A. Masad, “A straightforward numerical technique for finite element implementation of non-local gradient-dependent continuum damage mechanics theories,” *Int. J. Theor. Appl. Multiscale Mech.*, vol. 1, no. 4, pp. 352–385, 2010.
[120] J. C. Simo and J. W. Ju, “Strain- and stress-based continuum damage models—I. Formulation,” *Int. J. Solids Struct.*, vol. 23, no. 7, pp. 821–840, 1987.
[121] J. C. Simo and J. W. Ju, “Strain- and stress-based continuum damage models—II. Computational aspects,” *Int. J. Solids Struct.*, vol. 23, no. 7, pp. 841–869, 1987.
[122] G. Duvaut and J. L. Lions, *Inequalities in Mechanics and Physics*, vol. 219. Berlin, Heidelberg: Springer Berlin Heidelberg, 1976.
[123] P. Maimí, P. P. Camanho, J. A. Mayugo, and C. G. Dávila, “A continuum damage model for composite laminates: Part II – Computational implementation and validation,” *Mech. Mater.*, vol. 39, no. 10, pp. 909–919, 2007.
[124] R. W. Sullivan and S. M. Arnold, “An annotative review of multiscale modeling and its application to scales inherent in the field of ICME,” *Model. databases, Simul. tools needed Realiz. Integr. Comput. Mater. Eng.*, pp. 6–23, 2011.
[125] J. Aboudi, S. M. Arnold, and B. A. Bednarcyk, “Chapter 1 - Introduction,” J. Aboudi, S. M. Arnold, and B. A. B. T.-M. of C. M. Bednarcyk, Eds. Oxford: Butterworth-Heinemann, 2013, pp. 1–18.
[126] H. L. Cox, “The elasticity and strength of paper and other fibrous materials,” *Br. J. Appl. Phys.*, vol. 3, no. 3, p. 72, 1952.
[127] H. Krenchel, “Fibre reinforcement; theoretical and practical investigations of the elasticity and strength of fibre-reinforced materials,” 1964.
[128] J. C. Halpin and N. J. Pagano, “The laminate approximation for randomly oriented fibrous composites,” *J. Compos. Mater.*, vol. 3, no. 4, pp. 720–724, 1969.
[129] J. C. Halpin, “Stiffness and expansion estimates for oriented short fiber composites,” *J. Compos. Mater.*, vol. 3, no. 4, pp. 732–734, 1969.
[130] J. C. H. Affdl and J. L. Kardos, “The Halpin-Tsai equations: A review,” *Polym. Eng. Sci.*, vol. 16, no. 5, pp. 344–352, May 1976.
[131] S.-Y. Fu and B. Lauke, “The elastic modulus of misaligned short-fiber-reinforced polymers,” *Compos. Sci. Technol.*, vol. 58, no. 3–4, pp. 389–400, 1998.

[132] M. A. Ramirez, “In-silico Tensile Testing of Additively Manufactured Short Fiber Composite,” M.S. Thesis, School of Aero. & Astro. Eng. Purdue University, West Lafayette, IN., 2018.
[133] Y. Pan and A. A. Pelegri, “Progressive Damage Analysis of Random Chopped Fiber Composite Using Finite Elements,” *J. Eng. Mater. Technol.*, vol. 133, no. 1, p. 011018, 2011.
[134] L. T. Harper, C. Qian, T. A. Turner, S. Li, and N. A. Warrior, “Representative volume elements for discontinuous carbon fibre composites–Part 1: Boundary conditions,” *Compos. Sci. Technol.*, vol. 72, no. 2, pp. 225–234, 2012.
[135] L. T. Harper, C. Qian, T. A. Turner, S. Li, and N. A. Warrior, “Representative volume elements for discontinuous carbon fibre composites–Part 2: Determining the critical size,” *Compos. Sci. Technol.*, vol. 72, no. 2, pp. 204–210, 2012.
[136] S. K. Ha, L. Xu, C. Zhao, and M. DeMonte, “Progressive failure prediction of short fiber reinforced composites using a multi-scale approach,” *J. Compos. Mater.*, p. 0021998318770252, 2018.
[137] M. G. Pike and C. Oskay, “XFEM modeling of short microfiber reinforced composites with cohesive interfaces,” *Finite Elem. Anal. Des.*, vol. 106, pp. 16–31, 2015.
[138] P. Ladevèze, “Multiscale modelling and computational strategies for composites,” *Int. J. Numer. Methods Eng.*, vol. 60, no. 1, pp. 233–253, May 2004.
[139] Y. W. Kwon, D. H. Allen, and R. Talreja, *Multiscale modeling and simulation of composite materials and structures*, vol. 47. Springer, 2008.
[140] J. Fish, *Multiscale Methods*. Oxford University Press, 2009.
[141] J. Aboudi, S. M. Arnold, and B. A. Bednarcyk, “Chapter 3 - Fundamentals of the Mechanics of Multiphase Materials,” J. Aboudi, S. M. Arnold, and B. A. B. T.-M. of C. M. Bednarcyk, Eds. Oxford: Butterworth-Heinemann, 2013, pp. 87–145.
[142] W. Yu, *MULTISCALE STRUCTURAL MECHANICS Top-Down Modeling of Composite Structures using Mechanics of Structure Genome*. Hoboken, New Jersey, 2019.
[143] L. Onsager, “Reciprocal Relations in Irreversible Processes. I.,” *Phys. Rev.*, vol. 37, no. 4, pp. 405–426, Feb. 1931.
[144] L. Onsager, “Reciprocal Relations in Irreversible Processes. II.,” *Phys. Rev.*, vol. 38, no. 12, pp. 2265–2279, Dec. 1931.
[145] A. J. Staverman and F. Schwarzl, “Thermodynamics of viscoelastic behavior,” *Proceeding Acad. Sci.*, vol. 55, pp. 474–492, 1952.
[146] A. J. Staverman, “Thermodynamics of linear viscoelastic behavior,” in *Proceedings of second international congress on rheology. Academic Press, New York*, 1954, pp. 134–138.
[147] J. Meixner, “Die thermodynamische Theorie der Relaxationserscheinungen und ihr Zusammenhang mit der Nachwirkungstheorie,” *Kolloid-Zeitschrift*, vol. 134, no. 1, pp. 3–20, 1953.
[148] M. A. Biot, “Theory of stress-strain relations in anisotropic viscoelasticity and relaxation phenomena,” *J. Appl. Phys.*, vol. 25, no. 11, pp. 1385–1391, 1954.
[149] M. A. Biot, “Variational Principles in Irreversible Thermodynamics with Application to Viscoelasticity,” *Phys. Rev.*, vol. 97, no. 6, pp. 1463–1469, Mar. 1955.
[150] M. A. Biot, “Thermoelasticity and Irreversible Thermodynamics,” *J. Appl. Phys.*, vol. 27, no. 3, pp. 240–253, Mar. 1956.
[151] M. A. Biot, “Mechanics of Deformation and Acoustic Propagation in Porous Media,” *J. Appl. Phys.*, vol. 33, no. 4, pp. 1482–1498, Apr. 1962.

[152] R. A. Schapery, “Application of thermodynamics to thermomechanical, fracture, and birefringent phenomena in viscoelastic media,” *J. Appl. Phys.*, vol. 35, no. 5, pp. 1451–1465, 1964.
[153] R. A. Schapery, “On the characterization of nonlinear viscoelastic materials I. Theoretical development,” *Polym. Eng. Sci.*, vol. 9, no. 4, pp. 295–310, 1969.
[154] R. A. Schapery, “Viscoelastic behavior and analysis of composite materials,” *Mech. Compos. Mater.*, 1974.
[155] R. A. Schapery, “A theory of crack initiation and growth in viscoelastic media,” *Int. J. Fract.*, vol. 11, no. 1, pp. 141–159, 1975.
[156] R. A. Schapery, “A theory of crack initiation and growth in viscoelastic media II. Approximate methods of analysis,” *Int. J. Fract.*, vol. 11, no. 3, pp. 369–388, 1975.
[157] R. A. Schapery and S. RA, “A theory of crack initiation and growth in viscoelastic media III. Analysis of continuous growth.,” 1975.
[158] R. A. Schapery, “On viscoelastic deformation and failure behavior of composite materials with distributed flaws,” *1981 Adv. Aerosp. Struct. Mater.*, pp. 5–20, 1981.
[159] R. A. Schapery, “Correspondence principles and a generalized J integral for large deformation and fracture analysis of viscoelastic media,” *Int. J. Fract.*, vol. 25, no. 3, pp. 195–223, 1984.
[160] R. A. Schapery, “Nonlinear viscoelastic constitutive equations for composites based on work potentials,” 1994.
[161] R. A. Schapery, “Characterization of nonlinear, time-dependent polymers and polymeric composites for durability analysis,” *Prog. Durab. Anal. Compos. Syst.*, pp. 21–38, 1996.
[162] Y. Weitsman, “Stress assisted diffusion in elastic and viscoelastic materials,” *J. Mech. Phys. Solids*, vol. 35, no. 1, pp. 73–93, 1987.
[163] J. Lubliner, “On the thermodynamic foundations of non-linear solid mechanics,” *Int. J. Non. Linear. Mech.*, vol. 7, no. 3, pp. 237–254, 1972.
[164] K. Abdel-Tawab and Y. J. Weitsman, “A Coupled Viscoelasticity/Damage Model with Application to Swirl-Mat Composites,” *Int. J. Damage Mech.*, vol. 7, no. 4, pp. 351–380, Oct. 1998.
[165] K. Abdel-Tawab and Y. J. Weitsman, “A strain-based formulation for the coupled viscoelastic/damage behavior,” *J. Appl. Mech.*, vol. 68, no. 2, pp. 304–311, 2000.
[166] R. Clausius, *The mechanical theory of heat*. Macmillan, 1879.
[167] J. Kestin and J. R. Rice, *Paradoxes in the application of thermodynamics to strained solids*. Citeseer, 1969.
[168] R. A. Schapery, *Irreversible thermodynamics and variational principles with applications to viscoelasticity*, vol. 62, no. 418. California Institute of Technology., 1962.
[169] F. Sidoroff, “Description of anisotropic damage application to elasticity,” in *Physical Non-Linearities in Structural Analysis*, Springer, 1981, pp. 237–244.
[170] E. J. Barbero, *Finite element analysis of composite materials*. CRC press, 2007.
[171] J. L. Curiel Sosa, N. Petrinic, and J. Wiegand, “A three-dimensional progressive damage model for fibre-composite materials,” *Mech. Res. Commun.*, vol. 35, no. 4, pp. 219–221, 2008.
[172] P. Maimí, P. P. Camanho, J. A. Mayugo, and C. G. Dávila, “A continuum damage model for composite laminates: Part I – Constitutive model,” *Mech. Mater.*, vol. 39, no. 10, pp. 897–908, 2007.

[173] K. V Williams, R. Vaziri, and A. Poursartip, “A physically based continuum damage mechanics model for thin laminated composite structures,” *Int. J. Solids Struct.*, vol. 40, no. 9, pp. 2267–2300, 2003.
[174] B. A. Bednarcyk, B. Stier, J.-W. Simon, S. Reese, and E. J. Pineda, “Meso-and micro-scale modeling of damage in plain weave composites,” *Compos. Struct.*, vol. 121, pp. 258–270, 2015.
[175] J.-W. Simon, D. Höwer, B. Stier, S. Reese, and J. Fish, “A regularized orthotropic continuum damage model for layered composites: intralaminar damage progression and delamination,” *Comput. Mech.*, vol. 60, no. 3, pp. 445–463, 2017.
[176] E. J. Barbero, F. A. Cosso, R. Roman, and T. L. Weadon, “Determination of material parameters for Abaqus progressive damage analysis of E-glass epoxy laminates,” *Compos. Part B Eng.*, vol. 46, pp. 211–220, 2013.
[177] A. L. Matzenmiller, J. Lubliner, and R. L. Taylor, “A constitutive model for anisotropic damage in fiber-composites,” *Mech. Mater.*, vol. 20, no. 2, pp. 125–152, Apr. 1995.
[178] J. Cordebois and F. Sidoroff, “Anisotropic damage in elasticity and plasticity,” *J. Mec. Theor. Appl.*, pp. 45–60, 1982.
[179] J. F. Maire and J. L. Chaboche, “A new formulation of continuum damage mechanics (CDM) for composite materials,” *Aerosp. Sci. Technol.*, vol. 1, no. 4, pp. 247–257, 1997.
[180] F. Ning, W. Cong, J. Qiu, J. Wei, and S. Wang, “Additive manufacturing of carbon fiber reinforced thermoplastic composites using fused deposition modeling,” *Compos. Part B Eng.*, vol. 80, pp. 369–378, 2015.
[181] C. Hill, K. Rowe, R. Bedsole, J. Earle, and V. Kunc, “Materials and process development for direct digital manufacturing of vehicles,” in *SAMPE Long Beach 2016 Conference and Exhibition*, 2016.
[182] C. E. Duty, T. Drye, and A. Franc, “Material development for tooling applications using big area additive manufacturing (BAAM),” *ORNL Tech. Rep. ORNL/TM-2015/78*, 2015.
[183] V. Kunc, “Advances and challenges in large scale polymer additive manufacturing,” in *Proceedings of the 15th SPE Automotive Composites Conference, Novi, MI, USA*, 2015, vol. 9.
[184] N. M. DeNardo, “Additive manufacturing of carbon-fiber-reinforced thermoplastic composites,” 2016.
[185] A. R. Torrado Perez, D. A. Roberson, and R. B. Wicker, “Fracture surface analysis of 3D-printed tensile specimens of novel ABS-based materials,” *J. Fail. Anal. Prev.*, vol. 14, no. 3, pp. 343–353, 2014.
[186] P. Yeole, A. A. Hassen, S. Kim, J. Lindahl, V. Kunc, A. Franc, and U. Vaidya, “Mechanical Characterization of High-Temperature Carbon Fiber-Polyphenylene Sulfide Composites for Large Area Extrusion Deposition Additive Manufacturing,” *Addit. Manuf.*, p. 101255, 2020.
[187] H. L. Tekinalp, V. Kunc, G. M. Velez-Garcia, C. E. Duty, L. J. Love, A. K. Naskar, C. A. Blue, and S. Ozcan, “Highly oriented carbon fiber–polymer composites via additive manufacturing,” *Compos. Sci. Technol.*, vol. 105, pp. 144–150, Dec. 2014.
[188] B. G. Compton and J. A. Lewis, “3D-printing of lightweight cellular composites,” *Adv. Mater.*, vol. 26, no. 34, pp. 5930–5935, 2014.
[189] F. Ning, W. Cong, Y. Hu, and H. Wang, “Additive manufacturing of carbon fiber-reinforced plastic composites using fused deposition modeling: Effects of process parameters on tensile properties,” *J. Compos. Mater.*, vol. 51, no. 4, pp. 451–462, Feb. 2017.

[190] B. Brenken, E. Barocio, A. Favaloro, V. Kunc, and R. B. Pipes, "Fused Filament Fabrication of Fiber-Reinforced Polymers: A Review," *Addit. Manuf.*, 2018.
[191] M. R. Talagani, S. Dormohammadi, R. Dutton, C. Godines, H. Baid, and F. Abdi, "Numerical Simulation of Big Area Additive Manufacturing (3D Printing) of a Full Size Car," no. July 2015, pp. 27–36, 2016.
[192] Techmer PM., "ELECTRAFIL® PESU 1810 3DP - Preliminary Data," Clinton, Tennessee, 2019.
[193] N. D. Sharp, J. E. Goodsell, and A. J. Favaloro, "Measuring Fiber Orientation of Elliptical Fibers from Optical Microscopy," *Journal of Composites Science* , vol. 3, no. 1. 2019.
[194] ASTM D3039/D3039M, "Standard Test Method for Tensile Properties of Polymer Matrix Composite Materials," 2014.
[195] K.-Y. Hour and H. Sehitoglu, "Damage development in a short fiber reinforced composite," *J. Compos. Mater.*, vol. 27, no. 8, pp. 782–805, 1993.
[196] D. E. Walrath, D. F. Adams, D. A. Riegner, and B. A. Sanders, "Mechanical behavior of three sheet molding compounds," in *Short Fiber Reinforced Composite Materials*, ASTM International, 1982.
[197] B. P. Heller, "Effects of nozzle geometry and extrudate swell on fiber orientation in Fused Deposition Modeling nozzle flow.," 2015.
[198] M.-L. Dano, G. Gendron, F. Maillette, and B. Bissonnette, "Experimental characterization of damage in random short glass fiber reinforced composites," *J. Thermoplast. Compos. Mater.*, vol. 19, no. 1, pp. 79–96, 2006.
[199] M. Oldenbo and J. Varna, "A constitutive model for non-linear behavior of SMC accounting for linear viscoelasticity and micro-damage," *Polym. Compos.*, vol. 26, no. 1, pp. 84–97, 2005.
[200] J. Varna and M. Oldenbo, "An incremental 2D constitutive model accounting for linear viscoelasticity and damage development in short fibre composites," *Int. J. Numer. Methods Eng.*, vol. 64, no. 11, pp. 1509–1528, 2005.
[201] A. Lion, "On the large deformation behaviour of reinforced rubber at different temperatures," *J. Mech. Phys. Solids*, vol. 45, no. 11–12, pp. 1805–1834, 1997.
[202] A. Lion, "A physically based method to represent the thermo-mechanical behaviour of elastomers," *Acta Mech.*, vol. 123, no. 1, pp. 1–25, 1997.
[203] N. Huber and C. Tsakmakis, "Finite deformation viscoelasticity laws," *Mech. Mater.*, vol. 32, no. 1, pp. 1–18, 2000.
[204] C. Miehe and J. Keck, "Superimposed finite elastic–viscoelastic–plastoelastic stress response with damage in filled rubbery polymers. Experiments, modelling and algorithmic implementation," *J. Mech. Phys. Solids*, vol. 48, no. 2, pp. 323–365, 2000.
[205] G. He, Y. Liu, D. J. Bammann, and M. F. Horstemeyer, "An Elastothermoviscoplasticity Anisotropic Damage Model for Short Fiber Reinforced Polymer Composites," in *ASME 2018 International Mechanical Engineering Congress and Exposition*, 2018.
[206] J.-L. Bouvard, D. K. Ward, D. Hossain, E. B. Marin, D. J. Bammann, and M. F. Horstemeyer, "A general inelastic internal state variable model for amorphous glassy polymers," *Acta Mech.*, vol. 213, no. 1, pp. 71–96, 2010.
[207] J.-L. Bouvard, D. K. Francis, M. A. Tschopp, E. B. Marin, D. J. Bammann, and M. F. Horstemeyer, "An internal state variable material model for predicting the time, thermomechanical, and stress state dependence of amorphous glassy polymers under large deformation," *Int. J. Plast.*, vol. 42, pp. 168–193, 2013.

[208] D. K. Francis, J.-L. Bouvard, Y. Hammi, and M. F. Horstemeyer, “Formulation of a damage internal state variable model for amorphous glassy polymers,” *Int. J. Solids Struct.*, vol. 51, no. 15–16, pp. 2765–2776, 2014.
[209] J. P. Cordebois, “Endommagement anisotrope en élasticité et plasticité,” 1982.
[210] M. Eftekhari and A. Fatemi, “Tensile, creep and fatigue behaviours of short fibre reinforced polymer composites at elevated temperatures: a literature survey,” *Fatigue Fract. Eng. Mater. Struct.*, vol. 38, no. 12, pp. 1395–1418, 2015.